Dissertation

submitted to the

Combined Faculties of Natural Sciences and Mathematics

of Heidelberg University, Germany

for the degree of

Doctor of Natural Sciences

Put forward by

M. Sc. Andreas Schaller

born in: Bad Mergentheim

Oral examination: 22.07.2021

Influence of nuclear moments on the decay of dielectric polarization echoes in glasses at low temperatures

Referees: Prof. Dr. Christian Enss
Prof. Dr. Heinz Horner

Einfluss von Kernmomenten auf den Zerfall von dielektrischen Polarisationsechos in Gläsern bei tiefen Temperaturen

Diese Arbeit untersucht den Einfluss von Kernmomenten auf den Zerfall von dielektrischen Zweipulspolarisationsechos in Gläsern bei tiefen Temperaturen anhand von zwölf Proben. Einige der Proben, die Atome mit Kernmomenten enthalten, zeigen einen sehr schnellen Zerfall der Echamplitude bei kurzen Pulsabständen, der einer Relaxation basierend auf Kernmomenten zugeschrieben werden kann. Ein detailierter Vergleich aller Zerfallskurven zeigt, dass die Modulation der Quadrupolkoppelkonstanten durch die Tunnelbewegung der entscheidende Parameter für einen starken Beitrag einer auf Kernmomenten basierenden Relaxation ist. Durch die zusätzliche Zeemanaufspaltung im Magnetfeld konnte für das Glas HY-1, entsprechend der Erwartung, der Einfluss der kernmomentbasierten Relaxation auf den Zerfall der Echoamplitude verringert werden. Die aktuellen theoretischen Modelle können den schnellen Zerfall der Echoamplitude bei kleinen Pulsabständen nicht beschreiben, was auf einen weiteren Relaxationsmechanismus, verursacht durch Kernmomente, hinweist. Zur weiteren Untersuchung des schnellen Zerfalls bei kleinen Pulsabständen wurde im Rahmen dieser Arbeit ein neuer Aufbau, basierend auf mikrostrukturierten supraleitenden planaren Resonatoren, entwickelt. Dies ermöglichte zum ersten Mal Pulsabstände nahe des theoretischen Limits und die Beobachtung des gaußförmigen Abflachens der Echoamplitude am Glas N-BK7, wie von der spektralen Diffusion vorhergesagt.

Influence of nuclear moments on the decay of dielectric polarization echoes in glasses at low temperatures

This thesis investigates the influence of nuclear moments on the decay of dielectric two-pulse polarization echoes in glasses at low temperatures based on twelve samples. Several samples, containing atoms carrying nuclear moments, show a very fast decay of the echo amplitude at short times, which can be attributed to a nuclear moment based relaxation. A detailed comparison of all decay curves shows, that the modulation of the quadrupole coupling constant during the tunneling motion is the decisive parameter for a significant contribution of a nuclear moment based relaxation. For the glass HY-1, the additional Zeeman splitting in a magnetic field reduces the influence of the nuclear moment based relaxation on the decay of the echo amplitude, as expected. The observed decay behavior cannot be described by current theoretical models, indicating another relaxation mechanism related to the relaxation due to nuclear moments. To further study the decay at very short pulse separation times, a novel setup, based on planar microfabricated superconducting resonators, was developed. This enabled for the first time pulse separation times close to the theoretical limit and the observation of the Gaussian shape like leveling-off of the echo amplitude of N-BK7 glass, as predicted by spectral diffusion theory.

Contents

1. Introduction

Although many models for describing the properties of solids are based on the assumption of perfect crystals, most materials appearing in everyday life are far from a perfect crystal and many even belong to the substance class of amorphous solids or glasses. In some fields, an amorphous structure can lead to unintended effects. For example, in solid-state quantum computing the presence of amorphous material in a qubit causes decoherence, limiting the performance of quantum computers [Sim04, Mar05, Sch19].
Compared to crystals, glasses exhibit only a short range order of their constituents, which is usually given by the chemical binding situation. The missing long range order leads not only to a reduced density of amorphous solids compared to their crystalline counterparts, but also to some extraordinary properties. In particular at low temperatures, the specific heat and the thermal conductivity of glasses showed unexpected temperature dependencies [Zel71] which deviate from the Debye model valid for crystals. Further measurements of the thermal properties of other glasses in [Ste73, Las75, Ste76] led to the same dependencies. Together with the observed similarities in other properties at low temperatures, like acoustic attenuation, the assumption that all amorphous solids behave similar at low temperatures, the so-called 'universality of glasses', evolved.
A phenomenological explanation for this behavior was given, independently of each other, by Anderson et al. [And72] and Phillips [Phi72] with the standard tunneling model. This model assumes additional low energetic excitations in amorphous solids and identifies them with atoms or groups of atoms which can populate two energetically almost equal positions, separated by a potential barrier. At low temperatures a change of position of these atoms is only possible by quantum mechanical tunneling. Although the standard tunneling model is purely based on the structure of amorphous solids and does not make any assumption about the composition of the glass, it describes the low temperature behavior of the specific heat and the thermal conductivity [Las75] as well as further properties like the dielectric function [Fre16, Woh01a, Luc16].
However, the model could not explain the observations of the hole-burning experiments in [Arn75], since it takes no interaction between the low energetic exicitations, called tunneling systems, into account. This observation encouraged an expansion of the standard tunneling model describing the interaction of the tunneling systems with each other, the spectral diffusion theory [Kla62, Hu74, Bla77]. Over time, additional extensions and modifications of the model were introduced to describe measured data. For example, collective excitations [Bur98, Esq98] and a sub-system of only weakly interacting tunneling systems [Bur13, Fic13].
Compared to the deviations from the standard tunneling model, which could often be modeled by a modified distribution function or by a modification of the interactions

between the tunneling systems, the observation of magnetic field effects in the dielectric function in [Str98] was unexpected and required new explanations. Also in subsequent dielectric polarization echoes on various multicomponent glasses, a variation of the echo amplitude with applied magnetic field was visible [Lud02, Lud03]. Furthermore, not every sample showed an influence of the magnetic field on its dielectric properties, which repealed the universality of glasses. It turned out that the dielectric properties of glasses at low temperatures depend not only on their amorphous structure but also on their composition. Finally, detailed studies of polarization echoes, in which the isotope effect was exploited, showed that the magnetic field dependence is caused by atoms carrying nuclear quadrupole moments being part of tunneling systems [Bra04b, Nag04]. The corresponding theories [Wür02, Wür04, Par04] explain the measured data well. Another addition to the existing theory resulted from the observation, that not only nuclear quadrupole moments but also nuclear magnetic dipole moments influence the echo amplitude [Baz07, Baz08]. These discoveries revealed that tunneling systems, which were usually treated as two-level systems, are actually multi-level systems if they contain nuclear moments.
Besides the magnetic field dependence, several glasses containing atoms carrying nuclear quadrupole moments showed a decay of the echo amplitude faster than expected [Ens02a, Lud03]. Since dielectric polarization echoes are sensitive to the phase coherence of the probed ensemble of tunneling systems, a decay of the echo amplitude faster than expected indicates an additional relaxation mechanism of the tunneling systems. The missing relaxation channel was detected in measurements of the dielectric function of glasses containing very large nuclear quadrupole moments [Luc16]. There an additional non-phononic relaxation mechanism, being dominant at low temperatures, was observed, which was attributed to the nuclear moments.

As stated above, dielectric polarization echoes are a suitable method for the study of relaxation mechanisms. In the present thesis this technique is used to systematically study the influence of nuclear moments on the decay of tunneling systems. Therefore the decay behavior of twelve glasses is compared to each other. The samples cover a broad range of different glass types, like organic and inorganic samples and contain different amounts and kinds of quadrupole carrying atoms. In our study the amount of atoms with nuclear quadrupole moments covers a range between zero and 40 at.% and quadrupole moments of about 0.02 barn to approximately 3.6 barn. Thus the selected materials are suitable for a further investigation of the nuclear moments based relaxation.
To tackle the criteria for a significant contribution of the nuclear moment based relaxation, a detailed comparison of the echo amplitudes' decay behavior, with respect to the fraction of quadrupole carrying atoms, the size of the quadrupole moments and the size of the quadrupole coupling constant, is carried out. Whether the observed fast relaxation is actually caused by nuclear moments is verified by measurements in magnetic fields. For a more elaborate examination of the nuclear moment based relaxation, measurements at very small pulse separation times are required. To enable such measurements, a novel resonator technique is developed within this thesis.

This thesis is structured as follows:
In chapter 2, the structural properties of the different examined glass types within this thesis are addressed. The focus is on the multicomponent oxide glasses and the implementation of different elements in these materials.
Subsequently, chapter 3 introduces the standard tunneling model, the theory of the echo experiment and the known relaxation processes of tunneling systems.
Chapter 4 deals with the interaction of tunneling systems and nuclear moments. Therefore, at first a short introduction into nuclear quadrupole resonance is given, before the coupling mechanism of the tunneling systems and the nuclear quadrupole moments and its consequences for the echo amplitude are discussed. Furthermore, the observed increased relaxation rate of nuclear moments in amorphous samples as well as the relaxation of tunneling systems due to interactions with nuclear moments are discussed.
The experimental methods used in the framework of this thesis are presented in chapter 5. Besides the experimental setup, the limitations and error sources of the experiment as well as the investigated samples within this thesis are depicted.
In chapter 6, the experimental results are presented. At first, the preparations to ensure reliable measurement conditions are discussed. Then, the decay behavior of the different samples is analyzed. Finally, the measurements with magnetic fields are presented.
The novel resonator technique, together with first test measurements, is introduced in chapter 7.
In chapter 8 the results obtained in this thesis are summarized and an outlook on future measurements is given.

2. Structure of dielectric glasses

When talking about glass, most people will think of window glass or drinking glasses, materials that appear in everyday life. But the substance class of glasses or amorphous solids, both terms are used synonymously in the following, contains significantly more materials such as metallic or organic glasses.
This thesis deals with a variety of dielectric glasses, inorganic and organic ones. For interpreting the obtained data, it is helpful to have a basic understanding of the structural properties of glasses. Therefore, a rough overview of this topic is given in the following chapter, based on [Vog92, Sch91].

2.1 Basic properties of glasses

Most glasses are made by rapidly cooling their melt. Exceptions are for example vapour-deposited glasses and some organic materials. When a melt is cooled slowly, its volume decreases and at a certain temperature, called melting temperature T_m, crystallization starts. This is a first order phase transition accompanied by a jump in the volume (compare figure 2.1). However, if the melt is cooled rapidly, solidification does not occur at T_m, instead vitrification takes place at a lower temperature, which is referred to as the glass transition temperature T_g (for most glasses applies: $T_\mathrm{g} \simeq {}^2\!/_3 T_\mathrm{m}$ [Hun87]). In a microscopic picture the constituents of the melt are rearranging very fast, on picosecond timescale [Roy15], such that the system is always

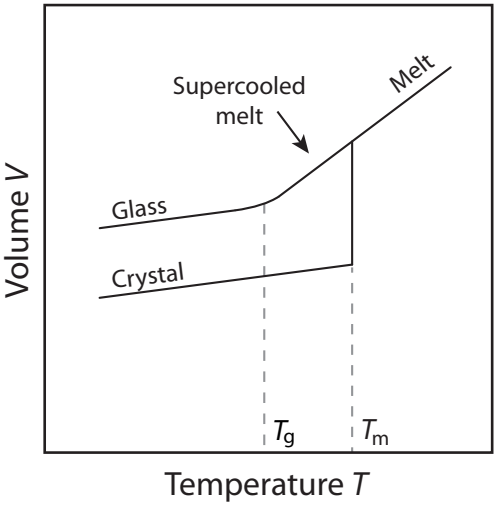

Figure 2.1: Schematic illustation of the change in volume during crystallization and vitrification of a one-component melt. T_m marks the crystallation temperature of the melt and T_g the glass transition temperature. Adapted from [Hun11].

in equilibrium. If the melt is cooled, the structural relaxation time becomes larger and the viscosity increases. In case of crystallization, the constituents start to rearrange in an ordered way at the melting temperature, such that the system stays in equilibrium. If the cooling is too fast, the individual components of the melt cannot arrange in an crystalline manner and solidification does not happen at T_m. The system is in some kind of metastable-equilibrium, called supercooled melt. In this state the viscosity increases further and at the arbitrarily defined viscosity of 10^{13} Poise [Sch91], corresponding to relaxation times in the order of 100 s [Roy15], the material is called solid. In this context solid means that in experimentally accessible timescales no return to equilibrium can be achieved.[1] This is also the reason why glasses are sometimes called frozen liquids. In the V/T diagram, shown in figure 2.1, this process appears as a transformation area at T_g and not as a classical phase transition. Whether a melt develops an amorphous or a crystalline structure upon cooling strongly depends on the composition of the melt and on the cooling rate. For good glass formers 10^{-6} K/s are sufficient to develop an amorphous structure, but for bad ones cooling rates up to 10^{6} K/s are needed [Hun11].

The two classes of solids, crystal and glass, differ significantly in their physical properties. One significant difference can be seen in figure 2.1. At the same temperature, the volume of the amorphous material is larger compared to its crystalline counterpart. Consequently, both materials have different densities even though they consist of the same constituents. This leads to the question of the actual structural properties of both materials. For an ideal crystal it is well known that it is built-up of unit cells, in which every atom has its exclusive place. This leads to an ordered lattice with short and long range order. In contrast, a hypothetical ideal amorphous solid would have a completely statistical distribution of its constituents leading to no detectable order. In reality it is very hard to obtain a single crystal of very high quality and an amorphous solid will show a certain amount of short range order

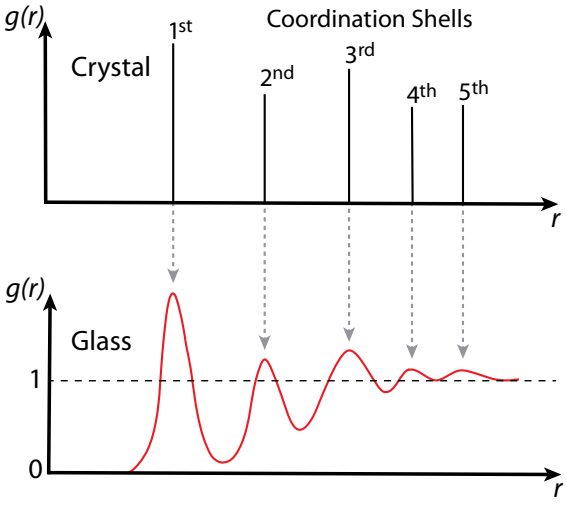

Figure 2.2: Schematic illustration of the pair correlation function of an ideal crystalline and its corresponding amorphous solid. The crystal shows distinct lines, representing its short and long range order. The amorphous material shows broad maxima just at short distances, indicating short but no longe range order. Adapted from [Hu15].

[1] According to [Roy15] 10-100 relaxation times are needed before the system is in equilibrium.

defined amongst others by the chemical binding situation of its constituents.
A possibility to visualize the structural difference of these two kinds of solids is the so-called pair correlation function $g(r)$, which is a measure of the particle number density in the distance r to a reference atom. In figure 2.2 the pair correlation function of an ideal crystalline and its corresponding amorphous solid are shown. The crystal shows due to its long range order delta peak like maxima up to large distances r. Instead of the delta peak like structure, the vitreous material shows broad maxima at small r. Towards larger r they smear out very fast such that the pair correlation function saturates at one. This indicates that some short but no long range order exists in the glass. The resulting structural properties are introduced in the following section.

2.2 Structural properties of dielectric glasses

The materials studied in the framework of this thesis are all dielectric glasses. They can be roughly classified into two big groups as shown in figure 2.3. The organic glasses are based on covalently bound carbon atoms. The samples of this group can be further divided into molecular and polymer glasses. The former are monomeric materials and the latter are composed of repeating subunits. The second group of dielectric glasses are inorganic glasses, which can be separated into those based on different oxides and those without oxygen. In the following chapters, inorganic glasses are considered first. Afterwards organic glasses are discussed.

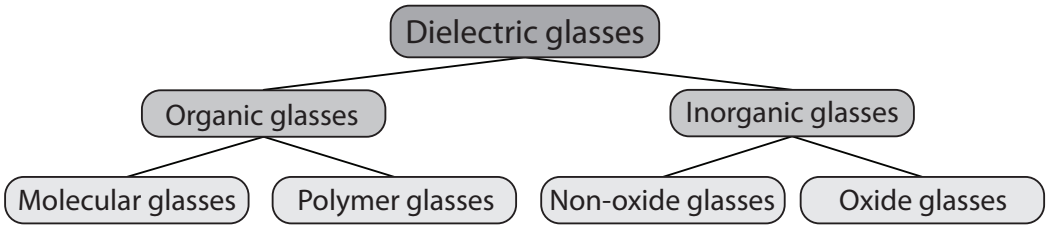

Figure 2.3: Classification of the glasses examined in the framework of this thesis.

2.2.1 Inorganic glasses

Not only the manufacture of a glass can be a difficult task, which often depends on details.[2] Once a glass is made, it is another challenge to determine the structural properties or rather the arrangement of its constituents. There are two approaches to investigate this. One of them is following the guiding principle that glass is a frozen liquid. Thus by studying the melt, information on the actual structure of the solid can be obtained. Another possibility is to look at the corresponding crystal

[2]For instance the exact mixing ratio of the individual constituents and the cooling rate.

and try to draw conclusions about the amorphous version of the solid. This method was used in 1932 by Zachariasen to successfully judge the glass forming ability of oxides and to describe the structure of the corresponding glasses [Zac32]. Therefore the following chapter will focus on this approach.

Oxide glasses

The so-called 'Random Network Theory' by Zachariasen [Zac32] describes the glass forming ability of the at this time known oxide glasses and was used by Warren to successfully describe his X-ray measurements [War41]. The theory is based on the idea that atoms in glasses and crystals are linked together by the same forces. Consequently, the binding situations found in crystals should also hold for glasses. Based on this theory amorphous solids consisting of oxides A_xO_y are random three dimensional networks of oxygen polyhedra around an atom A. Requirements for such structures are: One oxygen atom is linked to no more than two atoms A, the coordination number of atom A must be small and the oxygen polyhedra share only corners with each other. For three dimensional networks not less than three corners of each polyhedra must be shared. This leads to the assumption that A_2O_3 oxides, forming oxygen triangles around atom A, as well as AO_2 and A_2O_5 oxides, forming tetrahedra around atom A, are able to form glasses. In those glasses the orientation of the polyhedra varies in rather large limits, such that just a short range order is present, defined by the polyhedra itself and possibly the nearest environment. In the corresponding crystalline materials, the polyhedra are arranged in an ordered way to enable short and long range order to develop.

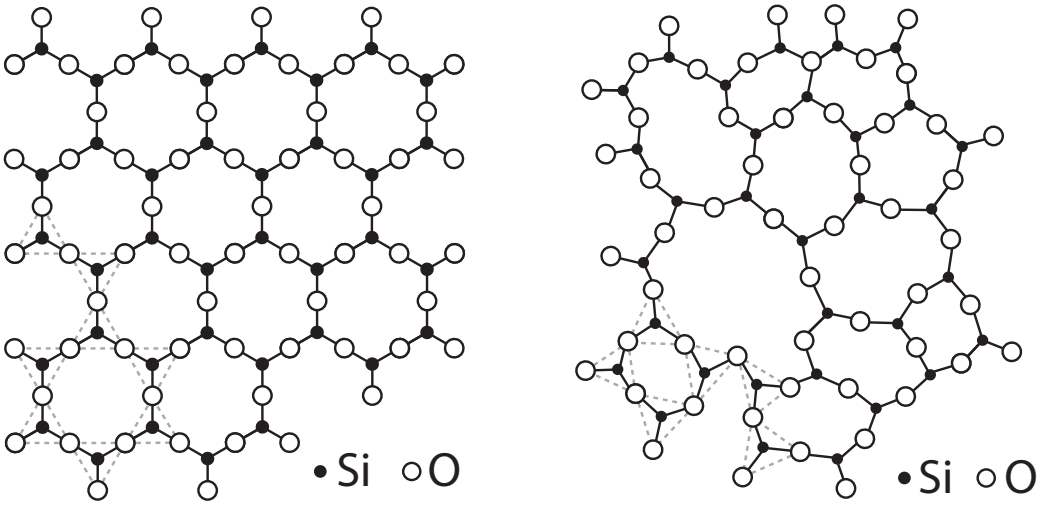

Figure 2.4: Schematic two dimensional representation of crystalline (left) and amorphous (right) SiO_2. One oxygen atom of each tetraheder is lying above or below the plain of projection. The dashed lines show edges of the tetrahedron. Sketch derived from [Zac32, Vog92].

For crystalline and amorphous SiO_2 the basic building module is the [SiO_4] tetrahedra, consisting of the Si^{4+} cation in the centre and four O^{2-} anions in the corners. It is common practice to speak of ions even though there is no proper ionic bond. In reality each bond is a mixture of a covalent and an ionic bond. The mix of a directed (covalent) and undirected (ionic) bond is a typical feature of glass networks. A schematic two dimensional representation of crystalline and amorphous SiO_2 is shown in figure 2.4. One oxygen atom of each tetrahedra is lying above or below the plain of projection. In the crystalline material rings of six tetrahedra are visible whereas in the disordered structure rings of different sizes occur. According to Zachariasen's theory additional cations of a multicomponent glass (for example from alkali or alkaline earth oxides) are placed within the holes of the amorphous structure. In order to form a stable glass, the added cations need to have a large ionic radius and a small charge to avoid repulsive forces between them and the cations forming the network. However, it turned out that various observations, like the glass forming properties of binary mixtures of well known glass formers, could not be explained with Zachariasen's theory [Vog92].

To improve the theory, Dietzel developed an extension taking also into account the actual field strengths between the cation and the anion [Vog92, Sch91]. For oxide glasses the field strength F of the cation at the position of the anion, the O^{2-} ion, is relevant. It can be derived from Coulomb's law. Omitting constant factors, it is given by

$$F = \frac{Z}{a^2}, \tag{2.1}$$

with the valence Z of the cation in units of the elementary charge and the distance of the ions $a = r_{\mathrm{Cation}} + r_{\mathrm{O^{2-}}}$ in Å. r_i is representing the radius of the respective ion and depends slightly on the coordination number CN. The cations can be classified depending on their field strengths into three groups: network former, modifier and intermediate oxides.
Typical network formers are listed in table 2.1. They usually have a small ionic radius and coordination numbers of 3 or 4. Their field strengths vary from 1 [Sch91] or 1.4 [Vog92] to 2. The difference in field strengths depending on the reference already

Network former					
Element	Valence of ion Z	Ionic radius [Å]	Coordination number CN	Cation oxygen distance a [Å]	Field strength at O^{2-} ion Z/a^2
B	3	0.25	3	1.36	1.62
			4	1.44	1.45
Si	4	0.39	4	1.60	1.56
P	5	0.34	4	1.55	2.08

Table 2.1: List of cations that traditionally serve as network formers and their field strengths according to Dietzel. The shown data is a selection of those listed in [Sch91].

Network modifier					
Element	Valence of ion Z	Ionic radius [Å]	Coordination number CN	Cation oxygen distance a [Å]	Field strength at O^{2-} ion Z/a^2
K	1	1.33	8	2.76	0.13
Na	1	0.98	6	2.30	0.19
			8	2.42	0.17
Ba	2	1.43	8	2.86	0.24
Ca	2	1.06	6	2.38	0.35
			8	2.48	0.33
Pb	2	1.32	6	2.64	(0.34)
			8	2.74	(0.32)

Table 2.2: List of cations that serve as network modifiers and their field strengths according to Dietzel. The values in parentheses are raised by 20 % due to the highly polarizing effects on the anions [Sch91]. The shown data is a selection of those listed in [Sch91].

indicates that it is not easy to establish a general set of rules for glass chemistry or to give a fixed role to a certain cation. Consequently, the conclusions based on these field strengths are only valid to a certain extent. In a glass, network formers build the three dimensional network. In the case of silicon, the basic unit of the network is the already introduced [SiO_4] tetrahedra and for boron the basic module is a [BO_3] group.

Another import group of cations are the so-called network modifier. Several examples, frequently present in glasses, are shown in table 2.2. These ions have a comparably large radius and a small charge. Usually, network modifier have a coordination number greater than or equal 6 and their field strength is between 0.1 and 0.4 [Vog92] or not larger than 0.35 [Sch91]. If such oxides are added to a silicate glass

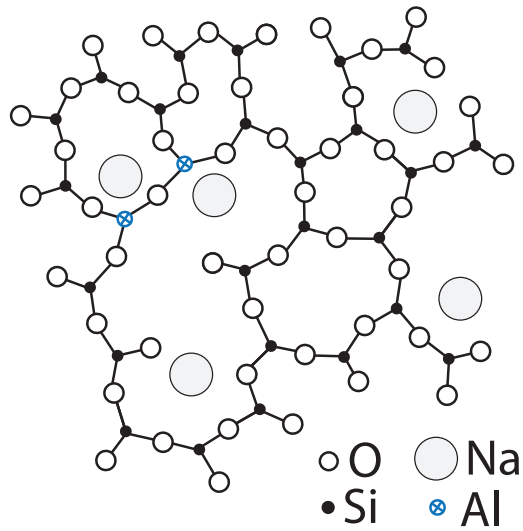

Figure 2.5: Schematic two dimensional representation of the integration of network modifiers and intermediate oxides into a silicate glass. The introduced network modifiers have broken the oxygen bonds and are sitting in the holes of the glass matrix. The intermediate oxide aluminum strengthens the network. Adapted from [Sch91]

network, they split up the so-called bridging oxygen bonds between neighbouring silicon atoms. The additionally introduced oxygen of the oxide is taken by one of the silicon atoms, such that two non-bridging oxygen atoms arise. The network modifier cation itself is placed in the hole of the structure. Figure 2.5 illustrates a silicate glass with added network modifiers. The introduced cation is not lying loosely in the network but is weakly ionically bound to the negatively charged non-bridging oxygen. By breaking the bridging bonds, the inserted cations loosen up the network, which has an effect on many macroscopically measurable properties of the glass. For example, the glass transition temperature is lowered and the electrical conductivity increases. Conversely, measurements of different physical properties can give insights into the embedding of various cations.
The third group of cations are intermediate oxides. A selection of these cations is shown in table 2.3. Their coordination number is typically between 4 and 6 and

Intermediate Oxides					
Element	Valence of ion Z	Ionic radius [Å]	Coordination number CN	Cation oxygen distance a [Å]	Field strength at O^{2-} ion Z/a^2
Ho	3^b	1.04^b	6^b	2.44	0.50
	3^b	1.16^b	8^b	2.56	0.46
Zn	2	0.83	4	2.03	(0.59)
			6	2.15	(0.52)
Ta	3^b	0.86^b	6^b	2.26	0.59
	4^b	0.82^b	6^b	2.22	0.81
	5^b	0.78^b	6^b	2.18	1.05
	5^b	0.88^b	8^b	2.28	0.96
Sb	5	0.63	4	1.84	(1.76)
	3	0.90	6	2.22	(0.73)
Zr	4	0.87	6	2.19	0.84
			8	2.28	0.77
Ti	4	0.64	6	1.96	(1.25)
	3	0.69	6	2.01	(0.89)
Al	3	0.57	4	1.76	0.97
			6	1.89	0.84
Nb	5^b	0.62^b	4^b	2.02	1.23
		0.78^b	6^b	2.18	1.05
		0.88^b	8^b	2.28	0.96

Table 2.3: List of cations from intermediate oxides and their field strengths according to Dietzel. The values in parentheses are raised by 20 % due to their highly polarizing effects on the anions [Sch91]. The shown data is a selection of those listed in [Sch91]. The data marked with superscript b is taken from [Web] and the corresponding distance is calculated with an O^{2-} radius of 1.4 Å^b.

their field strength is the range from 0.5 to 1 [Vog92] or between 0.35 and 1 [Sch91]. Unlike network formers, intermediate oxides alone do not vitrify, nor do they behave like classical network modifiers. When they are added into a glass matrix they can act in different ways. Depending amongst others on the composition of the glass, they can either break bonds and act as network modifiers or they can be built into the glass matrix and strengthen the network. A widely used example is Al_2O_3. If this oxide is added to a pure SiO_2 glass the Al^{3+} ion is usually in coordination 6 and acts as a network modifier. However, if other network modifiers, such as sodium, are present in the glass, the aluminium ion can go into coordination 4. Thereby the valence compensation of the Al^{3+} ion is established by the additional network modifier ion. This way, aluminium ions can be implemented into the glass matrix and close the non-bridging oxygen bonds broken by network modifier. This process strengthens the glass network (compare figure 2.5).

The rules introduced above serve as general guidelines for the structural properties of oxide glasses. They allow to establish a rough picture of the structure of many glasses. In 2011 the atomic structure of amorphous dielectric glass was resolved for the first time. Lichtenstein et al. [Lic12] measured the structure of a disordered two dimensional silica bilayer, grown on Ru(001), using scanning tunneling microscopy. The observed arrangement of atoms agrees well with Zachariasen's random network model and it could be confirmed that the glass is built from $[SiO_4]$ tetrahedra. The observed ring sizes in the amorphous structure varied between 4 and 9 silicon atoms, most rings had a size of 6. In 2012, Huang et al. [Hua12] obtained similar results by transmission electron microscopy of a two dimensional silica glass on graphene. Figure 2.6 shows the taken picture from this publication. The rings of different sizes, which are according to Zachariasen typical for a disordered structure, can be seen clearly. Furthermore, rearrangements in such glasses could be visualized [Hua13], offering a promising way to investigate vitrification. In reverse Monte Carlo modelling of high energy X-ray and neutron diffraction measurements on three dimensional data of vitreous SiO_2 [Koh05] a slightly different distribution of ring sizes was found

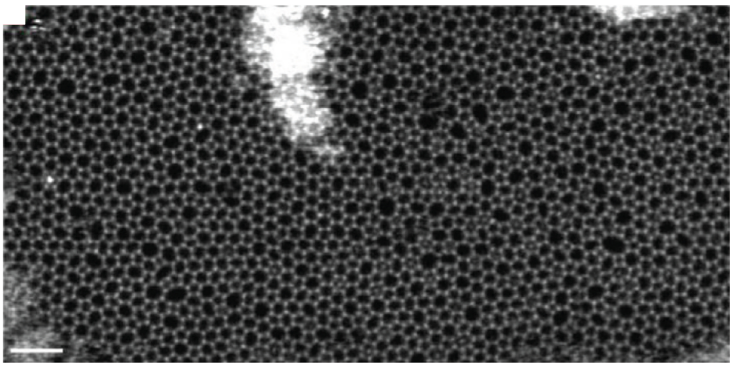

Figure 2.6: Transmission electron microscope picture of a two dimensional silica glass on graphene. The rings of $[SiO_4]$ tetrahedra as predicted by the random network model of Zachariasen can be seen. Picture taken from [Hua12]

compared to the two dimensional materials. The ring sizes vary between 3 and 10, but the most common one is also 6. All of these measurements support the general guidelines introduced in this chapter. However, these simple ideas do not always provide the right approach for complex glass mixtures.

Non-oxide glasses

In addition to the group of oxide glasses, there are two other big groups. The so-called halide glasses, having a halogen (F, Cl, Br,...) as anion, and the chalcogenide glasses which have an element of the sixth group of the periodic table of the elements excluding oxygen (S, Se, Te,...) as anion. The non-oxide glass investigated in the framework of this thesis is arsenic trisulfide (As_2S_3) and thus belonging to the second mentioned group. Since the structural properties of chalcogenide glasses are manifold just those of the investigated sample will be discussed in the following. In general, it can be said that the glass forming ability of the chalcogenides decreases with increasing atomic mass of the anion [Sch91]. Arsenic trisulfide is such a good glass former that it is difficult to make a crystalline sample in a laboratory [Yan86]. The guiding principles from Zachariasen and Dietzel, introduced in the framework of the oxide glasses, also hold for glasses with a chalcone or a halide as anion. However, the field strengths of Dietzel have to be calculated with respect to the particular anion. For arsenic trisulfide the field strength of the As^{3+} cation in the distance of the S^{2-} anion is 1.88, directly implying the good glass forming ability.[2] Concerning the actual structure of the solid it is assumed that the chemical binding situation of the crystal is conserved. However, the bond angles are different, resulting in a disordered structure. Hence, the basic building unit of the glass is a [AsS_3] group, which is three dimensionally networked. Attempts to describe the structure of amorphous As_2S_3 via a computer simulation can be found in [Bra91].

2.2.2 Organic glasses

Organic glasses are made of carbon-based chemical compounds ranging from small molecules to large polymers. The structure of those compounds or the repeating units of polymers are usually well known from organic chemistry. Since the variety of organic materials is very large, it is not possible to establish a simple rule for the arrangement of the molecules in a solid. However, some aspects are similar for all organic glasses and are discussed in the following, based on the books [Sch05, Hun11, Sta15]. The majority of the mentioned properties apply to small molecules and polymers, hence they are only separated into these groups where necessary. In the context of this thesis, the term molecular glass is used for all samples that are not polymers.

[2] The values needed for the calculation are taken from [Web]

The group of organic glasses differs not only in the kind of constituents from inorganic solids but also in the way they are connected. For the inorganic glasses discussed within this chapter, the constituents, neglecting network modifier, are bound by mixed bonds (covalent and ionic), where the covalent part often dominates. Therefore, inorganic glasses are also called covalent solids. In organic glasses the atoms that build the molecules or polymers are connected via covalent bonds, too (intramolecular forces). However, the individual molecules and polymers in the solid are not hold together by covalent bonds but by various weaker forces (intermolecular forces). Therefore, organic glasses are also called molecular solids. The intermolecular forces have significant influence on some macroscopic properties of organic glasses. For example, the melting temperature of inorganic glasses is usually significantly higher than for organic ones. Since the intermolecular forces in the organic glasses are very weak compared to the intramolecular ones, the physical properties of the individual molecules are conserved to a large extend. This is useful, for example, when discussing nuclear effects. The most dominant intermolecular forces are:

- Van-der-Waals forces between
  - two non-polar molecules,
  - two polar molecules,
  - a polar and a non-polar molecule.

  These forces are of short range and depend on the polarizability of the non-polar molecules.
- Coulomb forces, if both molecules are charged (ionic bond).
- Hydrogen bonds, if a hydrogen atom is covalently bound to a strong electronegative atom (O, F, ...) in one of the molecules.

The collapse of the solid is prevented by the Pauli exclusion principle and Coulomb repulsion. For a neutral molecule with filled molecular orbitals the interaction potential is described by the Lennard-Jones-potential.

If an organic melt is cooled, the constituents try to arrange to an energetically favorable state (crystalline structure). For large enough cooling rates, this state cannot fully achieved and the melt vitrifies, similar to inorganic melts. There are also materials, where the melt is vitrifying even at smallest cooling rates. An example are large polymers, where the large size of the molecule and the associated spatial obstacle prevent crystallization. A two dimensional scheme of how a polymer glass could look like is shown in figure 2.7. The individual polymer chains are building a kind of static bundle.
Another peculiarity of organic glasses is that they can also be made by a chemical reaction. In this process covalent bonds are created which connect the molecules with each other. Examples for this kind of glass are so-called thermosetting polymers.

Those materials are often made by a reaction of a resin with a hardener. When thermosetting polymers are heated, they do not become liquid again, but they are dissociated at a certain temperature.

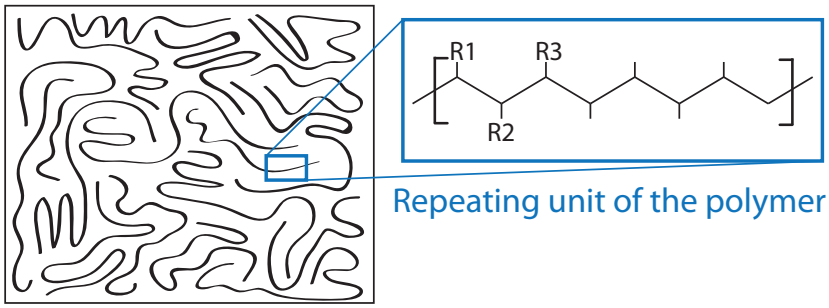

Figure 2.7: Schematic representation of a polymer glass. The individual polymer chains consist of a carbon backbone and possbile functional sidegroups R_i. Adapted from [Sch17].

3. Dielectric glasses at low temperatures

Based on the structural characteristics of glasses discussed in chapter 2, the following sections address some of the physical properties of these materials at low temperatures. First, the influence of the disordered structure on heat capacity and thermal conductance is discussed. The observations in those measurements resulted in the development of the 'standard tunneling model', which is introduced in section 3.2. The standard tunneling model is the foundation for polarization echo experiments, which were performed within this thesis. The theory behind these measurements is introduced in section 3.3. Occurring relaxation processes in dielectric glasses are described in section 3.4.

3.1 Thermal properties

Due to the missing long rang order in glasses well established methods, like the Brillouin zone, cannot be used to describe physical properties. However, the concept of the phonon should be applicable, as long as its wavelength is large enough, such that the disordered structure can be neglected and the material can be seen as a continuum [Hun11]. Consequently, the physical properties determined by phonons should coincide for crystalline and amorphous solids at low enough temperatures. Nevertheless, experiments showed that this is not the case as outlined in the following.

The specific heat capacity $c(T) \propto {\mathrm{d}Q}/{\mathrm{d}T}$ of a sample at a certain temperature T is defined by the amount of heat $\mathrm{d}Q$ needed to change the temperature of the sample by $\mathrm{d}T$. It is thus a measure for the excitable degrees of freedom in a material at the temperature T. For dielectric crystalline materials the specific heat at low temperatures is defined by phonons. It can be described by the Debye approximation, which assumes an isotropic solid with a monoatomic basis [Deb12]. It holds:

$$c_{\mathrm{phonon}}(T) \propto T^3 \tag{3.1}$$

In figure 3.1 the measured specific heat capacities of crystalline and vitreous silicon dioxide are shown. It is clearly visible that the crystalline material follows the predicted T^3 dependence very well. However, the glass is showing a $T^{1.3}$ dependence and an absolute value which is considerably larger compared to the crystal. This implies another excitable degree of freedom in addition to phonons at low temperatures in disordered materials, so that $c = c_{\mathrm{phonon}} + c_{\mathrm{additional}}$.

The thermal conductivity κ in a dielectric solid is determined by phonons and can be calculated with the dominant phonon approximation in analogy to the kinetic gas theory via

$$\kappa_{\mathrm{phonon}}(T) = \frac{1}{3} c_{\mathrm{phonon}}(T) v_{\mathrm{s}} l(T). \tag{3.2}$$

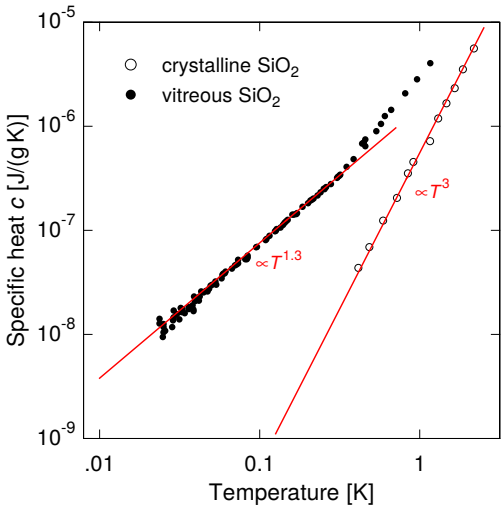

Figure 3.1: Comparison of the specific heat capacity C of vitreous and crystalline SiO_2 as a function of temperature [Zel71, Las75]. The specific heat of the amorphous sample is significantly larger and shows a $T^{1.3}$ dependency instead of the expected T^3, indicating an additional contribution at low temperatures.

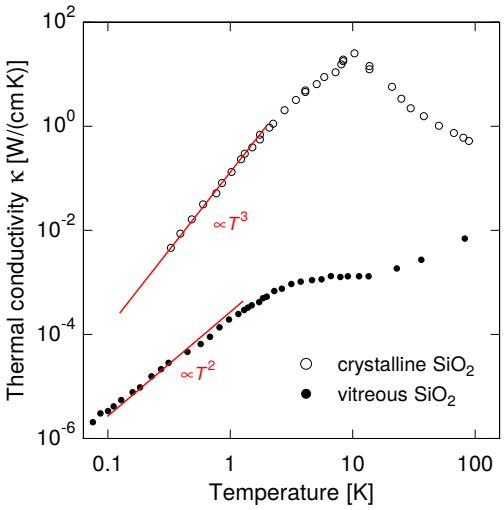

Figure 3.2: Comparison of the thermal conductivity κ of vitreous and crystalline SiO_2 as a function of temperature [Zel71]. The absolute value of the amorphous sample is smaller over the whole temperature range and shows a T^2 dependency instead of the expected T^3 at low temperatures, indicating additional scattering centers.

In this equation v_s represents the speed of sound of the dominant phonons and l their mean free path. Thus by studying the thermal conductivity of solids insights into scattering processes, limiting l, are gained. The temperature dependence of the thermal conductivity of crystalline and amorphous SiO_2 is shown in figure 3.2. The shape of the crystalline curve from high to low temperatures can be explained by the extinction of Umklapp scattering, leading to an increase of the mean free path and thus to a higher conductivity. At a certain temperature a maximum is reached. The subsequent reduction of the thermal conductivity is a consequence of the mean free path becoming temperature independent. In this regime, it is only determined by the sample dimension or internal defects (Casimir regime) and from equation 3.2 it follows $\kappa_{\text{phonon}}(T) \propto c_{\text{phonon}}(T) \propto T^3$. In comparison, the course of the thermal conductivity of vitreous SiO_2 is completely different. The absolute value is distinctly lower than the one of the crystalline counterpart and starting from high temperatures it continuously drops with an plateau at around 10 K. This plateau is not related to the maximum in the crystalline material, since the flattening is independent of the sample size or purity. The exact origin for the behavior at temperatures higher than approximately 1 K is still matter of research [Hun11]. For low temperatures it can be seen, that κ_{phonon} is proportional to about T^2, hence the Casimir regime cannot be reached. This indicates that additional scattering centers must be present in the amorphous material, limiting the mean free path of the phonons.

The presented differences between crystalline and vitreous silicon dioxide are not special features of this material but can be found in all amorphous solids, independent of their composition, at temperatures below about 3 K [Sch18a]. This can be well seen in figure 3.3, where the the specific heat (left) and the thermal conductivity (right) of various inorganic and organic dielectrics is shown. Considering the thermal conductivity, it should ne noted that not only the temperature dependencies of the different materials are equal, but also the absolute values lie within about one order of magnitude. This striking similarity of the thermal and other properties of glasses, like acoustic attenuation, at low temperatures led to the often referred to 'universality of glasses' [Ber88, Leg91, Poh02, Sch18a]. For the sake of completeness, it should already be mentioned at this point that not all low-temperature properties of glasses are universal, compare e.g. [Dra77, And86, Lud03, Nag04, Luc16] and the further course of this work.
A more detailed introduction to the thermal properties of amorphous solids including the peculiarities and differences in relation to crystals can be found in [Hun11].

It has been shown that the thermal behavior of amorphous solids at low temperatures is an universal property. Therefore it is reasonable to assume that the cause for the additional heat capacity and the reduced thermal conductivity compared to crystals lies in the disordered structure of these materials. This observation led to the development of the so-called standard tunneling model [And72, Phi72] introduced in the next section.

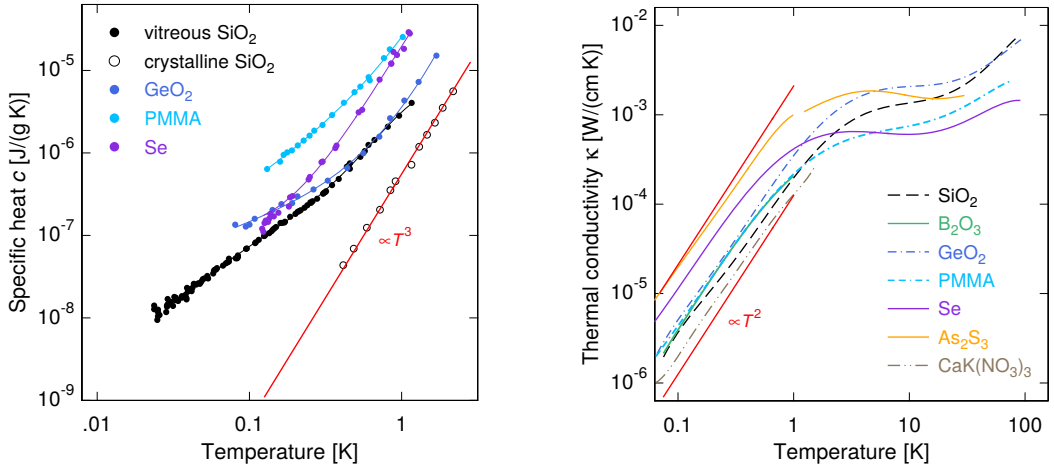

Figure 3.3: Specific heat (left) and thermal conductivity (right) of various amorphous dielectric solids as a function of temperature [Zel71, Ste73, Las75, Ste76]. The data of the different samples has a similar course, indicating universality at low temperatures.

3.2 Standard tunneling model

Due to their lower density, which is caused by the lack of long range order, glasses are less densely packed compared to their crystalline counterparts. This circumstance enables different atoms or groups of atoms to occupy several energetically almost equal sites. These atoms or groups of atoms can change their position thermally activated at high temperatures. However, at sufficiently low temperatures a change in position is only possible by quantum mechanical tunneling through the potential barrier, separating the two local minima. Different conceivable realizations of this movement are exemplified for amorphous SiO_2 in figure 3.4 with colored circles. As shown, the so-called tunneling system can consist of just one atom or a whole group of atoms. In a multicomponent glass the large number of different atoms (see chapter 2) is most likely also reflected in a large number of possible tunneling systems. It is conceivable, that parts of the glass network, network modifiers in their gaps, dangling bonds (e.g. non-bridging oxygen) or a mixture of them tunnel. These tunneling systems can be identified as the low energy excitations providing the additional degree of freedom seen in the measurements of the specific heat (section 3.1). In addition, they act as immobile scattering centers for phonons, thus reducing the thermal conductivity of glasses.
Anderson et al. [And72] and Phillips [Phi72], independently of each other, developed a microscopic model, the so-called standard tunneling model. This model is based on these tunneling atoms and is able to describe the behavior of amorphous solids at low temperatures well. Although the model is based on the atomic level of the solid, the exact nature of the tunneling particle remains usually unknown. Finally, it is a phenomenological model. Until today, the nature of the tunneling system is in most glasses unknown with the exception of for example [Baz08, Bar13].

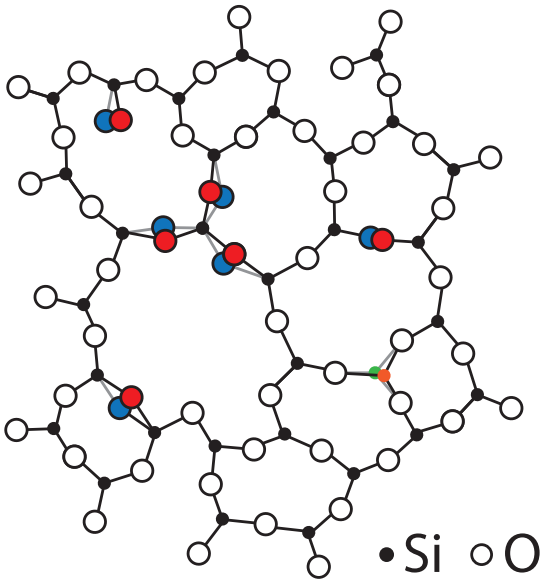

Figure 3.4: Schematic two dimensional illustration of vitreous SiO_2 with possible tunneling systems. The two different equilibrium positions are indicated by red and blue for oxygen and orange and green for silicon. Sketch derived from [Zac32, Hun11, Luc16].

3.2.1 Two-level tunneling system

In the standard tunneling model, Anderson et al. and Phillips approximated the potential landscape of the glass at the tunneling atom or group of atoms, hereinafter referred to as tunneling particle of mass m, as a double well potential. This potential is composed of two harmonic potentials V_{harm}, which are separated by a distance d in configuration space. The configuration space is chosen since the actual tunneling process can be a translation, rotation or a combination of both. The overlap of the two harmonic potentials leads to a potential barrier of height V. The minima of the two potentials differ in energy by the asymmetry energy Δ. This quantity takes the disordered structure and the resulting potential landscape of the glass into account. Furthermore, it is assumed that the individual tunneling systems within the glass do not interact with each other. A schematic representation of the described double well potential is shown in figure 3.5. In principle, there could also be potentials with a larger number of minima in the glass. However, shortly after the standard tunneling model was introduced, various measurements, e.g. [Gol73, Hun72, Hun73, Pic74], showed that the low temperature properties of glasses can be described by two-level systems which arise from double well potentials.
To motivate the calculation of the energy levels of the double well potential, the case of a particle in a single harmonic potential is considered. Solving the corresponding time independent Schrödinger equation gives the following energy eigenvalues

$$E^{(n)}_{\mathrm{harm,a}} = \hbar\Omega\left(n+\frac{1}{2}\right)+\Delta; \qquad E^{(n)}_{\mathrm{harm,b}} = \hbar\Omega\left(n+\frac{1}{2}\right) \tag{3.3}$$

with the eigenfrequency [Gro18]

$$\Omega = \sqrt{\frac{k}{m}} = \sqrt{\frac{(\partial^2 V_{\mathrm{harm}}(x)/\partial x^2)_{x=x_0}}{m}}. \tag{3.4}$$

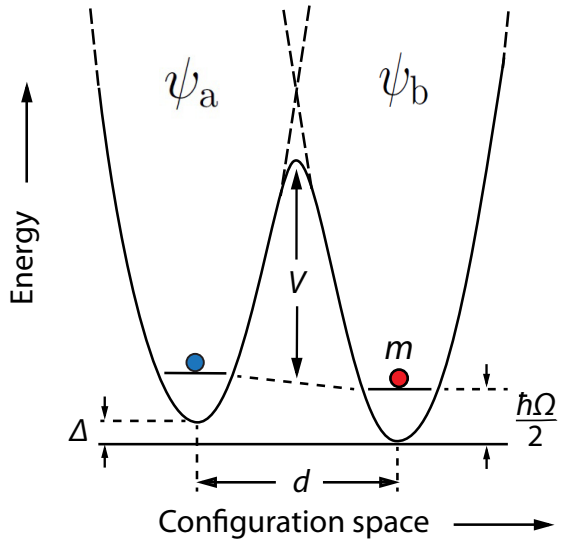

Figure 3.5: Schematic illustration of a tunneling particle of mass m in a double well potential with asymmetry energy Δ, barrier height V and zero point energy $\hbar\Omega/2$. The minima are a distance d in configuration space apart from each other. Illustration based on [Ens10].

Equation 3.3 results in the zero point energy of $E^{(0)}_{\mathrm{harm}} = {}^{\hbar\Omega}/_{2}$ for the tunneling particle in either of the isolated wells. The energetic difference to the next excitable level is $\Delta E_{\mathrm{harm}} = \hbar\Omega$. In amorphous SiO_2, it can be assumed, for a rough estimate, that the tunneling particle is an oxygen atom, which oscillates in one of the harmonic wells with a frequency of about 10^{13} to 10^{14} Hz [Kän94]. Therefore the energy difference ΔE_{harm} is about ${}^{\Delta E_{\mathrm{harm}}}/_{k_{\mathrm{B}}} \approx 10^2$ to 10^3 K. Even if the tunneling particle is heavier, resulting in a lower eigenfrequency (equation 3.4), the energy difference between the ground and the first exited state is still large. Since the temperatures used in the framework of this thesis are well below 1 K, it is justified to consider only the ground states of the individual wells when calculating the energy eigenvalues E of the double well potential.

Turning to the double well potential, the normalized wave functions of the isolated left and right well are ψ_{a} and ψ_{b}, respectively. If the two wells are close enough to each other, it is possible that the wave function of the particle located in one of the two wells still has a finite value in the other one. In this case, the particle can tunnel through the barrier. Thus, a superposition of ψ_{a} and ψ_{b} are a reasonable ansatz for the wave function of the coupled system

$$\Psi = \alpha\psi_{\mathrm{a}} + \beta\psi_{\mathrm{b}} \qquad\qquad \alpha, \beta \in \mathbb{R}. \tag{3.5}$$

To get the energy eigenvalues, the time independent Schrödinger equation $\hat{H}\Psi = E\Psi$ is solved via the Rayleigh Ritz method. In the following, only the results and the used methods according to [Ens10] are presented.

$$E = \frac{\int \Psi^* \hat{H} \Psi \,\mathrm{d}^3x}{\int \Psi^* \Psi \,\mathrm{d}^3x} = \frac{\alpha^2 H_{\mathrm{aa}} + \beta^2 H_{\mathrm{bb}} + 2\alpha\beta H_{\mathrm{ab}}}{\alpha^2 + \beta^2 + 2\alpha\beta S} \tag{3.6}$$

with $H_{\mathrm{aa}} = \int \psi_{\mathrm{a}}^* \hat{H} \psi_{\mathrm{a}} \,\mathrm{d}^3x$ and $H_{\mathrm{bb}} = \int \psi_{\mathrm{b}}^* \hat{H} \psi_{\mathrm{b}} \,\mathrm{d}^3x$ being the eigenvalues of the tunneling particle in the isolated wells, $H_{\mathrm{ab}} = \int \psi_{\mathrm{a}}^* \hat{H} \psi_{\mathrm{b}} \,\mathrm{d}^3x = \int \psi_{\mathrm{b}}^* \hat{H} \psi_{\mathrm{a}} \,\mathrm{d}^3x$ representing the exchange energy and $S = \int \psi_{\mathrm{a}}^* \psi_{\mathrm{b}} = \int \psi_{\mathrm{b}}^* \psi_{\mathrm{a}}$ describing the overlap of the isolated wave functions. The energy eigenvalues of the double well potential are calculated by minimizing E with respect to α and β (${}^{\partial E}/_{\partial\alpha} = 0$, ${}^{\partial E}/_{\partial\beta} = 0$).
By setting the energetic zero point in the middle of the potential minima, the eigenvalues of the individual wells can be expressed by $H_{\mathrm{aa}} = {}^{\hbar\Omega+\Delta}/_{2}$ and $H_{\mathrm{bb}} = {}^{\hbar\Omega-\Delta}/_{2}$. In addition, it is assumed that the overlap of the wave functions is weak, so that $S \approx 0$. The resulting energy eigenvalues of the total wave function are given by

$$E_{\mathrm{e,g}} = \frac{1}{2}\left(\hbar\Omega \pm \sqrt{\Delta^2 + \Delta_0^2}\right) \tag{3.7}$$

with the ground state energy splitting

$$E = E_{\mathrm{e}} - E_{\mathrm{g}} = \sqrt{\Delta^2 + \Delta_0^2}. \tag{3.8}$$

The variable Δ_0 is the so-called tunnel splitting and calculated via the WKB method[1]

$$\Delta_0 \approx \hbar\Omega \mathrm{e}^{-\lambda}. \tag{3.9}$$

[1] after **W**entzel, **K**ramers, and **B**rillouin

The tunnel splitting depends on the frequency Ω and the tunnel probability $e^{-\lambda}$. The latter is determined by the tunnel parameter λ which takes the actual shape of the potential and the mass of the tunneling particle into account. For the considered double well potential λ it is given by

$$\lambda \approx \frac{d}{2\hbar}\sqrt{2mV}. \tag{3.10}$$

Thus the tunneling particle in the double well potential, the tunneling system, can be described by a two-level system with energy splitting E.
For further calculations it is suitable to switch to the matrix notation. Redefining the zero energy point between the ground state E_g and the exited state E_e, the tunneling system in the basis of the individual wells (ψ_a, ψ_b) is represented by the Hamiltonian

$$\hat{H}_0 = \frac{1}{2}\begin{pmatrix} \Delta & -\Delta_0 \\ -\Delta_0 & -\Delta \end{pmatrix}. \tag{3.11}$$

Using the eigenvalues of the total wave function from equation 3.8 yields the Hamiltonian in the basis of the double well potential (Ψ_g, Ψ_e)

$$\hat{\mathcal{H}}_0 = \frac{1}{2}\begin{pmatrix} E & 0 \\ 0 & -E \end{pmatrix}. \tag{3.12}$$

The eigenfunctions for a double well potential with $\Delta = 0$ are given by a symmetric (ground state) and an antisymmetric (excited state) superposition of the wave functions of the isolates wells. A schematic illustration of a double well potential with $\Delta, \Delta_0 \neq 0$ is shown in figure 3.6.

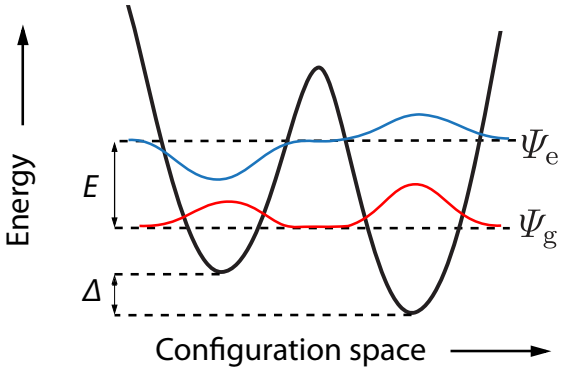

Figure 3.6: Schematic illustration of the eigenvalues and corresponding eigenstates of a double well potential with $\Delta, \Delta_0 \neq 0$. The symmetric ground state Ψ_g and the antisymmetric excited state Ψ_e are separated by the energy E. Scheme in analogy to [Phi81].

3.2.2 Occupation difference of two-level systems

For the analysis of experiments at low temperatures the occupation difference between the two energy levels Ψ_g and Ψ_e is important. Assuming an ensemble of N tunneling systems with an energy splitting E the occupation difference can be calculated by means of statistical physics. Defining the ground state energy to zero

($E_\mathrm{g} = 0$) and the excited state energy as E ($E_\mathrm{e} = E$), the partition function of a single two-level system is given by

$$Z = \sum_{i=1}^{2} \mathrm{e}^{-\frac{E_i}{k_\mathrm{B}T}} = 1 + \mathrm{e}^{-\frac{E}{k_\mathrm{B}T}} \tag{3.13}$$

with the Boltzmann constant k_B. This leads to the two possible micro states

$$p_\mathrm{g} = \frac{1}{Z}\mathrm{e}^{-\frac{E_\mathrm{g}}{k_\mathrm{B}T}} = \frac{1}{1+\mathrm{e}^{-\frac{E}{k_\mathrm{B}T}}} \quad \text{and} \quad p_\mathrm{e} = \frac{1}{Z}\mathrm{e}^{-\frac{E_\mathrm{e}}{k_\mathrm{B}T}} = \frac{\mathrm{e}^{-\frac{E}{k_\mathrm{B}T}}}{1+\mathrm{e}^{-\frac{E}{k_\mathrm{B}T}}} \tag{3.14}$$

and a difference in occupation probability of

$$\Delta p = p_\mathrm{g} - p_\mathrm{e} = \frac{1-\mathrm{e}^{-\frac{E}{k_\mathrm{B}T}}}{1+\mathrm{e}^{-\frac{E}{k_\mathrm{B}T}}} = \frac{\mathrm{e}^{\frac{E}{k_\mathrm{B}T}}-1}{\mathrm{e}^{\frac{E}{k_\mathrm{B}T}}+1} = \tanh\left(\frac{E}{2k_\mathrm{B}T}\right). \tag{3.15}$$

For an ensemble of N non-interacting tunneling systems, all with the energy splitting E, the resulting occupation difference ΔN in thermal equilibrium is

$$\Delta N = N \tanh\left(\frac{E}{2k_\mathrm{B}T}\right). \tag{3.16}$$

3.2.3 Distribution function of the tunneling systems

Up to this point only tunneling systems with a well defined energy splitting were considered. However, due to the disordered structure of amorphous solids the actual shape of the double well potential described through V, d, Δ as well as the mass m of the tunneling particle are widely distributed. To describe the macroscopic properties of glasses all tunneling systems have to be considered. The standard tunneling model takes this into account by an uniform distribution function $P(\lambda, \Delta)$ of the independent parameters Δ and $\lambda\,(V, d, m)$

$$P(\Delta, \lambda)\,\mathrm{d}\Delta\,\mathrm{d}\lambda = P_0\,\mathrm{d}\Delta\,\mathrm{d}\lambda. \tag{3.17}$$

The parameter P_0 is a constant which depends on the sample, for instance its glass transition temperature [Hun87], and must be determined experimentally. The choice of a flat distribution function might seem arbitrary, but it successfully describes the temperature dependence of the thermal properties of different glasses (shown in section 3.1) and also many other experiments, compare [Zim81, Esq98].

For the further course of the thesis, it is useful to express the distribution function in terms of Δ and E. This is achieved with a Jacobi transformation while making use of equation 3.8 and 3.9 and yields

$$P(\Delta, E)\,\mathrm{d}\Delta\,\mathrm{d}E = P(\Delta, \lambda)\left|\frac{\partial\lambda}{\partial E}\right|\mathrm{d}\Delta\,\mathrm{d}E = P_0\,\frac{E}{E^2-\Delta^2}\,\mathrm{d}\Delta\,\mathrm{d}E. \tag{3.18}$$

In addition, it is helpful to describe the distribution function by E and the dimensionless asymmetry parameter $q = \Delta/E$ as

$$P(q, E)\,\mathrm{d}q\,\mathrm{d}E = P(\Delta, E)\left|\frac{\partial \Delta}{\partial q}\right|\mathrm{d}q\,\mathrm{d}E = P_0\,\frac{1}{1-q^2}\,\mathrm{d}q\,\mathrm{d}E. \tag{3.19}$$

The distribution function $P(q, E)$ is shown in figure 3.7 for an arbitrary, but fixed energy splitting E as a function of the asymmetry parameter q. For a fixed energy splitting, there are more asymmetric ($q = \Delta/E \to \pm 1$) than symmetric ($q = \Delta/E \to 0$) tunneling systems in the glass. The divergence of the distribution function for highly

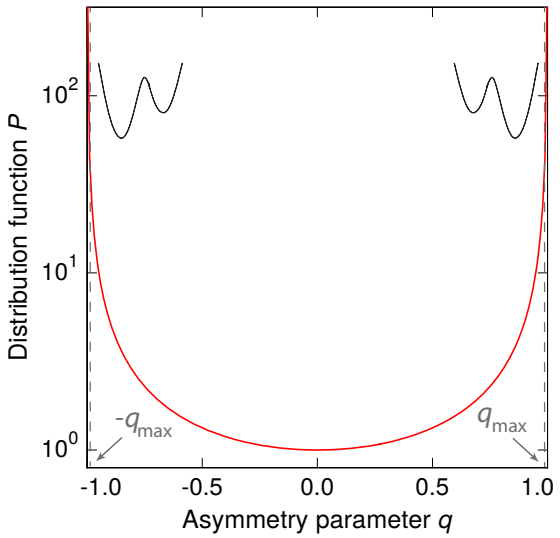

Figure 3.7: Illustration of the distribution function $P(q, E)$ for an arbitrary, but fixed energy splitting E, as a function of the asymmetry parameter q as predicted by the standard tunneling model. The parameter P_0 was set to one. The indicated upper and lower limit $\pm q_{\mathrm{max}}$ prevent non integrable singularities.

asymmetric tunneling systems is contradictory to the finite number of tunneling systems in an amorphous material. To solve this and to avoid a divergence when integrating over $P(q, E)$ a lower and upper limit $\pm q_{\mathrm{max}}$ is introduced[2]. These integration limits are motivated by the existence of a tunneling system with a minimal tunnel splitting[3] Δ_0^{min}, corresponding to a maximal tunnel parameter λ_{max}, present in every glass sample. Systems with even larger λ may not be treated as double well potentials, but as individual wells which do not contribute to the dielectric response of the sample. However, in real systems the distribution function will end smoothly and not abruptly [Ens10].

3.2.4 Interaction of tunneling systems with external (electric) fields

Since the tunneling systems in an amorphous solid affect the solid's properties (compare 3.1), it is obvious that tunneling systems are no isolated systems within a solid.

[2]For the physical properties only the absolute value of the asymmetry energy Δ and thus of q is relevant and not whether the right or left well is at lower energy. Therefore, as also shown later, an integration over the distribution function is usually performed as $\int_{-q_{\mathrm{max}}}^{q_{\mathrm{max}}} = 2\int_0^{q_{\mathrm{max}}}$, exploiting the symmetry of the distribution.

[3]According to [Luc16], $\Delta_0^{\mathrm{min}} \approx {}^1/_{1000} \cdot T_{\mathrm{m}}$, where T_{m} represents the lowest temperatures used in the experiment, is a feasible choice.

For the physical properties discussed in section 3.1 the interaction of the tunneling systems with the strain field or rather phonons is decisive. All tunneling systems are embedded in the solid, such that all can interact with phonons.

In the framework of this thesis the coupling of the tunneling systems to the strain field is relevant in terms of the relaxation processes described in section 3.4. For the generation of the examined polarization echo the coupling to alternating electric fields, rather photons, is decisive. For this interaction it is essential that the tunneling particle carries a permanent electric dipole moment. It does not matter whether it is caused by ions, like for an OH^- ion, or an intrinsic dipolar unit as it can be formed for example by the SiO_4 tetrahedrons in the irregular environment of a silica glass [Sch76]. Usually only a fraction of all tunneling systems in a solid carries a permanent electric dipole moment. The size of this fraction is to some extend determined by the materials composition [Sch75]. Hence the ensemble of tunneling systems probed with dielectric techniques is a sub-ensemble of the one probed with acoustic techniques.

Quantum mechanically the interaction of the tunneling systems with an external field can under the assumption of a sufficiently small perturbation be described by first order perturbation theory. The resulting total Hamiltonian describing the disturbed tunneling system is thus given by $\hat{H} = \hat{H}_0 + \hat{H}_{\mathrm{pert}}$, with $\hat{H}_0$ from equation 3.11, and the perturbation Hamiltonian

$$\hat{H}_{\mathrm{pert}} = \frac{1}{2}\begin{pmatrix} \delta\Delta & -\delta\Delta_0 \\ -\delta\Delta_0 & -\delta\Delta \end{pmatrix} \tag{3.20}$$

in the basis $(\psi_{\mathrm{a}}, \psi_{\mathrm{b}})$. According to [Phi81], it is assumed that the weak perturbation changes the asymmetry energy Δ, but the variation $\delta\Delta_0$ of the tunnel splitting is exponentially suppressed. Thus the perturbation Hamiltonian simplifies to

$$\hat{H}_{\mathrm{pert}} \approx \frac{1}{2}\begin{pmatrix} \delta\Delta & 0 \\ 0 & -\delta\Delta \end{pmatrix}. \tag{3.21}$$

This assumption is reasonable, since an external field does not significantly influence the shape of the double well potential (m, V, d), which determines the tunnel splitting (compare equation 3.9 and 3.10). However, the local environment of the tunneling system can vary and thus the asymmetry energy. Accordingly, the energy splitting of the tunneling system changes with an external applied field to

$$E = \sqrt{(\Delta + \delta\Delta)^2 + \Delta_0^2}. \tag{3.22}$$

This hyperbolic dependence of the energy splitting was observed in various measurements with strain and electric fields or a combination of both [Gra12, Lis15, Sar16, Lis19] and supports above introduced approximation.
A transformation into the basis of the double well potential $(\Psi_{\mathrm{g}}, \Psi_{\mathrm{e}})$ results in[4]

$$\hat{\mathcal{H}}_{\mathrm{pert}} \approx \frac{1}{2E}\begin{pmatrix} \Delta & \Delta_0 \\ \Delta_0 & -\Delta \end{pmatrix}\delta\Delta. \tag{3.23}$$

[4]Using the transformation $\hat{\mathcal{H}}_{\mathrm{pert}} = \hat{H}_{\mathrm{pert}} \cdot T_\psi^\Psi$ with $T_\psi^\Psi = \frac{1}{E}\begin{pmatrix} \Delta & \Delta_0 \\ -\Delta_0 & \Delta \end{pmatrix}$

Using the Pauli matrizes[5], the total Hamiltonian of the disturbed tunneling system in the basis of the double well potential is given by

$$\hat{\mathcal{H}} = \hat{\mathcal{H}}_0 + \hat{\mathcal{H}}_{\text{pert}} \approx \frac{1}{2}\left(E + \frac{\Delta}{E}\delta\Delta\right)\hat{\sigma}_{\text{z}} + \frac{1}{2}\frac{\Delta_0}{E}\delta\Delta\hat{\sigma}_{\text{x}}. \tag{3.24}$$

This representation shows that a tunneling system can be described by the same formalism as a spin $1/2$ particle in an external magnetic field. In addition, it can be seen that an external field results in a change of the energy splitting of the tunneling system by

$$\delta E = \frac{\Delta}{E}\delta\Delta. \tag{3.25}$$

The off-diagonal elements of the Hamiltonian 3.24 ($\hat{\sigma}_{\text{x}}$-term) cause transitions between the two eigenstates of the tunneling system. Due to the Δ_0/E proportionality this is especially pronounced for symmetric tunneling systems ($\Delta \to 0 \Rightarrow \Delta_0 \to E$).

If the external field is an electric field $\vec{F} = \vec{F}_0 \cos(\omega_{\text{ef}} t)$ and the perturbation is sufficiently small, the asymmetry energy $\delta\Delta$ of a tunneling system varies linearly with the strength of the applied field [Ens10]

$$\delta\Delta = 2\delta\vec{p} \cdot \vec{F}, \tag{3.26}$$

$\delta\vec{p}$ denotes the difference of the dipole moment of the tunneling particle between the right and left potential well. In the framework of this thesis the tunneling systems are excited by an alternating electric field with the frequency ω_{ef}. The total Hamiltonian of a tunneling system exposed to such an alternating electric field is given by

$$\mathcal{H} = \mathcal{H}_0 + \mathcal{H}_{\text{pert}} \approx \frac{1}{2}\begin{pmatrix} E & 0 \\ 0 & -E \end{pmatrix} \underbrace{+\frac{1}{E}\begin{pmatrix} \Delta & \Delta_0 \\ \Delta_0 & -\Delta \end{pmatrix}\delta\vec{p}}_{\hat{P}} \cdot \vec{F}_0 \cos(\omega_{\text{ef}} t), \tag{3.27}$$

with the dipole or polarization operator $\hat{P}$ [Esq98].

Spin 1/2 analogy - Bloch sphere representation

In the following the above mentioned analogy of a tunneling system and a spin $1/2$ particle in an external magnetic field is demonstrated and used to introduce the Bloch sphere representation. This concrete illustration is used later in the description of the dielectric polarization echo in section 3.3. The following argumentation is based on [Hun76, Jäc76, Esq98].

Unlike a spin $1/2$ particle, which needs an additional static magnetic field to become a two-level system, a tunneling system is an intrinsic two-level system. However, it has no real spin, therefore the term 'pseudo spin' is used [Ens10]. The Hamiltonian

[5] $\hat{\sigma}_{\text{x}} = \begin{pmatrix} 0 & 1 \\ 1 & 0 \end{pmatrix}$, $\hat{\sigma}_{\text{y}} = \begin{pmatrix} 0 & -i \\ i & 0 \end{pmatrix}$, $\hat{\sigma}_{\text{z}} = \begin{pmatrix} 1 & 0 \\ 0 & -1 \end{pmatrix}$, $\vec{\hat{\sigma}} = (\hat{\sigma}_{\text{x}}, \hat{\sigma}_{\text{y}}, \hat{\sigma}_{\text{z}})$

of a particle with spin $\vec{S} = 1/2$ and gyromagnetic ratio γ_{gy} in a magnetic field $\vec{B}(t) = \vec{B}_0 + \vec{B}'(t)$ is given by

$$\hat{\mathcal{H}}_{\mathrm{s}} = -\hbar\gamma_{\mathrm{gy}} \left(\vec{B}(t) \cdot \vec{S}\right) = -\hbar\gamma_{\mathrm{gy}} \left(\vec{B}_0 \cdot \vec{S}\right) - \hbar\gamma_{\mathrm{gy}} \left(\vec{B}'(t) \cdot \vec{S}\right). \tag{3.28}$$

$\vec{B}_0$ represents the static magnetic field, defined along the z-direction, and $\vec{B}'(t)$ an alternating magnetic field perturbing the spin. With $\vec{S} = 1/2\,\vec{\sigma}$ the equation simplifies to

$$\hat{\mathcal{H}}_{\mathrm{s}} = -\frac{\hbar\gamma_{\mathrm{gy}}}{2} B_{\mathrm{z}} \hat{\sigma}_{\mathrm{z}} - \frac{\hbar\gamma_{\mathrm{gy}}}{2} \left(B'_{\mathrm{x}}(t)\hat{\sigma}_{\mathrm{x}} + B'_{\mathrm{y}}(t)\hat{\sigma}_{\mathrm{y}} + B'_{\mathrm{z}}(t)\hat{\sigma}_{\mathrm{z}}\right). \tag{3.29}$$

Rewriting equation 3.27 to

$$\hat{\mathcal{H}} \approx \frac{E}{2}\hat{\sigma}_{\mathrm{z}} + \frac{1}{E}\delta\vec{p} \cdot \vec{F}_0 \cos(\omega_{\mathrm{ef}} t) \left(\Delta_0 \hat{\sigma}_{\mathrm{x}} + \Delta\hat{\sigma}_{\mathrm{z}}\right) \tag{3.30}$$

allows for a coefficient comparison

$$\begin{aligned} -\hbar\gamma_{\mathrm{gy}}\vec{B}_0 &= (0, 0, E) \\ -\hbar\gamma_{\mathrm{gy}}\vec{B}'(t) &= \tfrac{2}{E}\delta\vec{p} \cdot \vec{F}_0 \cos(\omega_{\mathrm{ef}} t) \left(\Delta_0, 0, \Delta\right). \end{aligned} \tag{3.31}$$

This formal equivalence shows that a tunneling system can be described by the same formalism as a spin $1/2$ particle in a magnetic field, perturbed by a magnetic field in x- and z-direction. In case of a spin, the static magnetic field in z-direction leads to a Larmor precession around the z-axis unless the spin is aligned parallel or anti-parallel to the magnetic field.

The Bloch sphere representation, introduced in the following, is an illustrative way to show the time evolution of a two-level system, often a spin $1/2$ particle in a magnetic field, and therefore used by many authors e.g. [Hah50, Lös57, Fuk81, Ens10, Fic13]. The orientation of a spin vector on a unit sphere describes the current state of the system under investigation. In figure 3.8 a Bloch sphere with an arbitrary pseudo spin vector $\vec{R}$ precessing around the z-axis is shown. Following the analogy of the spin $1/2$ particle and the tunneling system derived above, the state with higher energy Ψ_{e} corresponds to the spin-up state in the spin formalism and the Bloch sphere picture [Jäc76]. Accordingly, Ψ_{g} corresponds to the spin-down state. Therefore the expectation value $\langle\hat{\sigma}_{\mathrm{z}}\rangle$ determines the occupation number of the higher energy state Ψ_{e}. Transferred to the Bloch sphere picture, a pseudo spin vector $\vec{R}$ pointing downwards represents a tunneling system in its ground state Ψ_{g} and a vector pointing upwards describes a tunneling system in its excited state Ψ_{e}. All other positions, for example the one shown in figure 3.8, correspond to a superposition of Ψ_{e} and Ψ_{g}. Considering figure 3.6, a subtraction of both eigenfunctions results in a localization of the tunneling particle in the left potential well, an addition to one in the right potential well. In case of a symmetric tunneling system a pure state Ψ_{g} or Ψ_{e}, results in a complete delocalization. A precession movement of $\vec{R}$ around the z-axis is thus interpretable as a microscopic back and forth motion of the tunneling particle. If such a back and forth motion is carried out in phase by an ensemble of

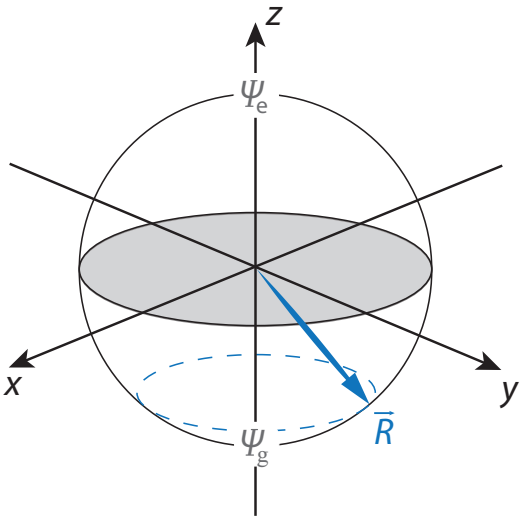

Figure 3.8: Bloch sphere representation of an arbitrary state of a tunneling system, represented by the pseudo spin $\vec{R}$ precessing around the z-axis. The expectation value $\langle\hat{\sigma}_z\rangle$ determines the occupation number of the state Ψ_e whereas $\langle\hat{\sigma}_y\rangle$ and $\langle\hat{\sigma}_x\rangle$ define the polarization. Illustration created according to [Fic13].

tunneling systems where every system carries a permanent electric dipole moment a macroscopic measurable polarization of the glass occurs. The polarization of a single tunneling system is given by the phase dependent expectation values $\langle\hat{\sigma}_x\rangle$ and $\langle\hat{\sigma}_y\rangle$.

In general, the wave function of a tunneling system is a superposition of the symmetric Ψ_g and antisymmetric Ψ_e eigenfunctions of the Hamiltonian 3.12

$$\Psi = c_1(t)\Psi_g + c_2(t)\Psi_e \tag{3.32}$$

with $|c_1(t)|^2 + |c_2(t)|^2 = 1$. To calculate the effect of an alternating electric field onto a tunneling system the time-dependent Schrödinger equation

$$\hat{\mathcal{H}}\Psi = i\hbar\frac{\partial\Psi}{\partial t} \tag{3.33}$$

needs to be solved. Equivalent to the spin formalism, the time dependence of the Hamiltonian can be removed by a transformation to a rotating frame of reference, which is rotating with an appropriate frequency around the z-axis ($\Psi \mapsto \Psi^{\mathrm{rot}}$, $\hat{\mathcal{H}} \mapsto \hat{\mathcal{H}}^{\mathrm{rot}}$).
Following [Bra04a, Baz08, Haa18a], in the reference frame rotating with the frequency ω_{ef}, the application of an alternating electric field with the same frequency ω_{ef} to a tunneling system is determined by the propagator

$$\mathrm{e}^{-i\frac{\hat{\mathcal{H}}^{\mathrm{rot}}_{\mathrm{pert}}t}{\hbar}} \propto \mathrm{e}^{-i\frac{\Omega_R t}{2}\hat{\sigma}_x} = \hat{\mathbb{1}}\cos\left(\frac{\Omega_R t}{2}\right) - i\hat{\sigma}_x\sin\left(\frac{\Omega_R t}{2}\right), \tag{3.34}$$

with the identity matrix $\hat{\mathbb{1}}$ and the Rabi frequency

$$\Omega_R = \frac{\delta\vec{p}\vec{F}_0}{\hbar}\left(\frac{\Delta_0}{E}\right). \tag{3.35}$$

This propagator describes a rotation of the pseudo spin vector $\vec{R^{\mathrm{rot}}}$ around the x-axis of the rotating frame of reference. The Rabi frequency is the rate of transition

between the two energy levels of the tunneling system caused by the applied alternating electric field. In the formula it can be seen that the transition rate depends on the tunneling system's dipole moment, the electric field and the angle between those two quantities. Furthermore the Δ_0/E dependence shows that symmetric tunneling systems ($\Delta \to 0 \Rightarrow \Delta_0 \to E$) have a higher transition rate compared to asymmetric ones.
If no alternating electric field is applied, the evolution of the tunneling system in the rotating frame of reference is given by the propagator

$$\mathrm{e}^{-i\frac{\hat{\mathcal{H}}_0^{\mathrm{rot}} t}{\hbar}} \propto \mathrm{e}^{i\frac{\omega_\mathrm{d} t}{2}\hat{\sigma}_\mathrm{z}} \tag{3.36}$$

with $\omega_\mathrm{d} = \omega_\mathrm{ef} - \omega_\mathrm{ts}$ and $\omega_\mathrm{ts} = E/\hbar$ the eigenfrequency of the tunneling system. For $\omega_\mathrm{ef} = \omega_\mathrm{ts}$, the pseudo spin vector keeps its position in the Bloch sphere. For $\omega_\mathrm{ef} \neq \omega_\mathrm{ts}$, the pseudo spin vector precesses with the difference frequency ω_d around the z-axis.

3.3 Dielectric two-pulse polarization echo

Echo experiments were triggered by Hahn in 1950 with the discovery of a coherent effect of nuclear induction signals of protons and flourine in liquids [Hah50]. He called this effect 'Spin-echo'. It was followed by the observation of a photon echo in a ruby crystal in 1964 [Kur64, Abe66]. The first phonon echo was measured in 1976 by Golding et al. in a fused silica glas [Gol76, Gra79].
Even though the investigated systems (proton/ fluorine spins, dipoles in ruby crystal, tunneling systems) are very different, the principle behind all the experiments is the same. An echo signal is a macroscopic measure and thus an echo experiment probes no single systems but a multitude of them. In an echo measurement the respective sample or rather the systems within the sample to be examined are exposed to a special sequence of pulses. With a suitable choice of the pulse sequence a macroscopically measurable quantity, called echo, appears. To observe a coherent effect like the echo, the relaxation times of the studied systems need to be sufficiently long. Therefore, investigating the dependence of the echo signal on e.g. temperature, magnetic field or pulse sequence is a suitable method to investigate relaxation times in solids and liquids.

In amorphous solids, as in all other materials, coherence is destroyed by interactions with the environment. As mentioned in section 3.2.4, tunneling systems can, amongst others, interact with phonons. If this interaction is sufficiently strong, it can prevent the observation of coherent effects. To avoid this, echo measurements on glass samples are carried out at very low temperatures to reduce the number of phonons and thus weakening the interaction with the heat bath. Another requirement for the observation of echoes is a suitable occupation difference of the two energy levels. Following equation 3.16 this is also achieved by employing very low temperatures, such that $k_\mathrm{B}T < E$ (with E being the energy splitting of the considered tunneling systems).

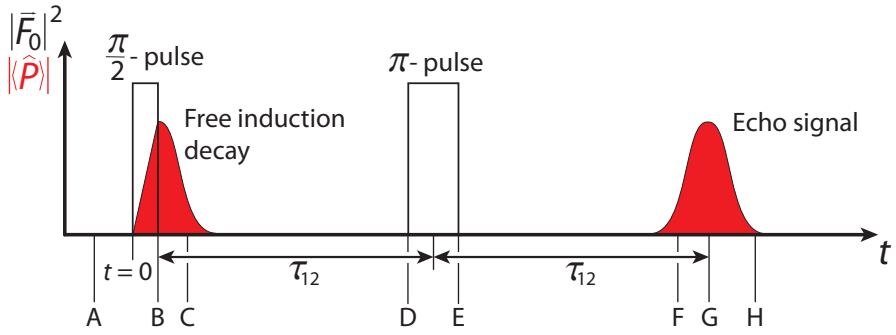

Figure 3.9: Schematic illustration of the pulse sequence used in the framework of this thesis. It consists of two high frequency electric field pulses (shown in black), which are called $\pi/2$ and π pulse, separated by the pulse separation time τ_{12}. In red the envelopes of the dielectric polarization of the sample, which is induced by the two-pulse sequence, is shown. The time stamps are used for the explanation in section 3.3.1.

In this thesis the two-pulse $\pi/2 - \pi$ technique, called Hahn or spontaneous echo, is used which is in particular sensitive to so-called transversal relaxation processes (see section 3.4.2). During this echo sequence the examined glass sample is exposed to two high frequency electric field pulses of frequency ω_{ef}, separated by the pulse separation time τ_{12}. Tunneling systems that carry a permanent electric dipole moment and that have an energy splitting of $E \approx \hbar\omega_{\mathrm{ef}}$ are resonantly excited. This leads to a macroscopically measurable polarization after twice the pulse separation time τ_{12}, called echo. In figure 3.9 the respective pulse sequence is shown in black. The rectangles in this illustration represent the envelopes of the high frequency electric field pulses. In red the envelopes of the resulting polarizations of the sample are visible.

The following sections present first a phenomenological derivation of the echo using the Bloch sphere representation. Afterwards, a quantum mechanical motivation is presented and the path diagram representation is introduced.

3.3.1 Phenomenological description - Bloch sphere representation

The Bloch sphere representation, introduced in section 3.2.4, offers an easy comprehensible way to explain the formation of the dielectric polarization echo. However, it is necessary to keep in mind that tunneling systems and thus pseudo spins are considered and not actual spins. This circumstance will be particularly emphasized at the relevant points. The explanation is based on [Baz08, Ens10, Fic13].
For simplicity the following assumptions are made:

- All considered tunneling systems have the same Rabi frequency, such that they experience the same rotation around the x-axis by an applied alternating electric field.

- Relaxation processes are not considered. They will be introduced in section 3.4.
- The reference frame of the Bloch spheres (figure 3.10) is rotating with the frequency of the applied alternating electric field ω_{ef} around the z-axis, such that the precession motion of the tunneling systems is compensated.

In the following the occurrence of the echo is explained on the basis of figure 3.9 and the therein shown timestamps. First, the influence of the two-pulse sequence on the wave function of the tunneling system is phenomenologically discussed. Afterwards, it is transferred to the corresponding Bloch sphere, shown in figure 3.10. The wave function of a tunneling system is given by a superposition of the symmetric ground state Ψ_{g} and the antisymmetric excited state Ψ_{e} (compare equation 3.32, figure 3.6). The current state of the individual tunneling systems that contribute to the echo are represented by small blue arrows in figure 3.10. The thick red arrow corresponds to the macroscopic property of the sample (= sum/ integral over all participating tunneling systems). This discrimination is necessary since the polarization echo is a macroscopic property at which a lot of tunneling systems participate.

Prior to the first pulse ('A' in figure 3.9 and 3.10) it is assumed that all tunneling systems are in their ground state Ψ_{g}. Thus, all individual pseudo spin vectors and the macroscopic one point downwards in the Bloch sphere. There is no coherent movement of the tunneling systems and due to the arbitrary orientation of their dipole moments the macroscopic polarization is zero.
The first alternating electric field pulse ($\pi/2$ pulse) at the time $t = 0$ forces a coherent tunneling motion of the tunneling systems with the frequency of the electric field (ω_{ef}). Consequently, the ground and excited state mix, causing an increase of the antisymmetric part of the tunneling system's wave function. The associated addition/ subtraction of Ψ_{g} and Ψ_{e} leads to an oscillating wave function with a higher amplitude in either of the wells. This coherent increasing localization results in a non-zero dipole moment average and thus an oscillating macroscopic polarization emerges. With a suitable $\pi/2$ pulse the localization is maximized at the end of the pulse, leading to a maximal oscillating polarization of the sample. In the Bloch sphere picture, the application of an alternating electric field pulse and the subsequent mixing of the ground and excited state is associated with a rotation around the x-axis (compare equation 3.34). Thereby the expectation value in y-direction increases, corresponding to a growing polarization of the tunneling systems and the sample. To maximize the polarization of the tunneling systems and the sample the $\pi/2$ pulse is chosen such that the rotation is 90°. This state corresponds to state 'B' in figure 3.9 and 3.10. The precession motion around the z-axis, which can be interpreted as the oscillation of the polarization, is not visible in the Bloch sphere due to its visualization in a rotating frame of reference.
After the alternating electric field is switched off, the forced tunneling motion of the tunneling systems ends and they oscillate with their eigenfrequencies $\omega_{\mathrm{ts}}^i = E^i/\hbar$, collecting the phase $\Phi_1^i = \omega_{\mathrm{ts}}^i t$. Since the $\pi/2$ pulse is very short ($\approx 100 - 200\,\mathrm{ns}$) its

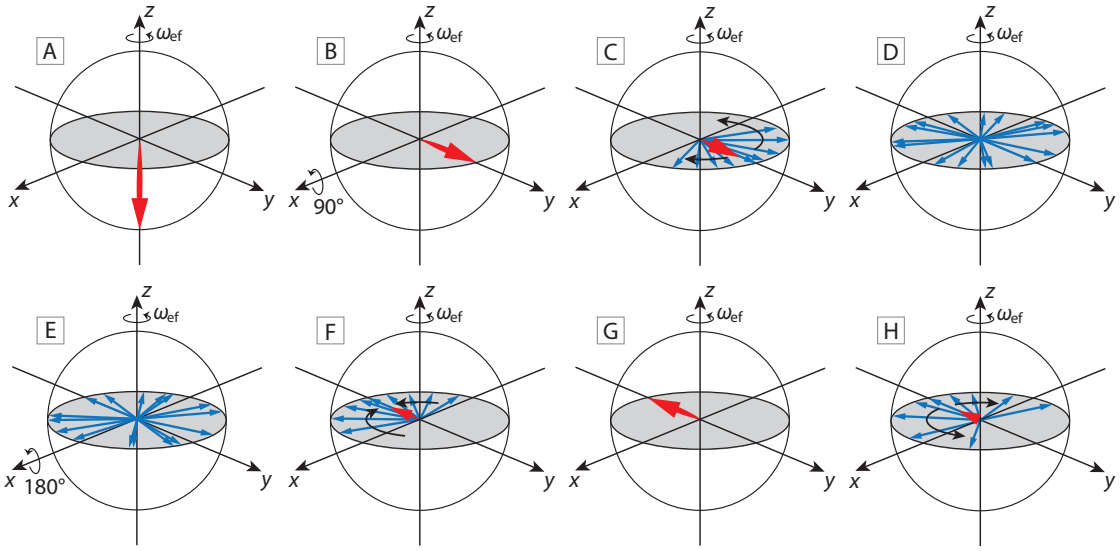

Figure 3.10: Bloch spheres in a rotating frame of reference representing the different stages of echo formation. The labels 'A' to 'H' correspond to the time stamps shown in figure 3.9. The thick red arrow indicates the current macroscopic property of the sample (sum/ integral over all tunneling systems) and the thin blue arrows show the current state of the individual tunneling systems. The stages are: '**A**' $t = 0$, all tunneling systems are assumed to be in the ground state prior to the first pulse; '**B**' after application of the $\pi/2$ pulse; '**C**' free induction decay; '**D**' distribution of the pseudo spins of the individual tunneling systems in the xy-plane right before the π pulse; '**E**' right after the π pulse; '**F**' common phase is more and more restored; '**G**' spontaneous echo; '**H**' loss of common phase after the echo. Illustration created according to [Ens10, Fic13]

frequency composition is broad and not monochromatic. Therefore not only tunneling systems with exactly $E = \hbar\omega_{\mathrm{ef}}$ are resonantly excited, but also those within a certain energy range around E. Due to the individually developing wave functions of the tunneling systems the corresponding localizations get out of step and the macroscopic polarization of the sample decays. In other words, the common phase of the tunneling systems is gradually lost. This process is called 'free induction decay' (time stamp 'C'). In the Bloch sphere 'C' this corresponds to the clockwise and counterclockwise precession of the individual tunneling systems with the frequencies $\omega_{\mathrm{d}}^{i} = \omega_{\mathrm{ef}} - \omega_{\mathrm{ts}}^{i}$ of the individual tunneling systems around the z-axis. The increasing distribution of the individual pseudo spin vectors in the xy-plane leads to a reduction of the polarization of the sample since the sum over all dipole moments shrinks and finally disappears.

Time stamp 'D' shows the situation before the application of the second pulse. The individual tunneling systems collected different phases $\Phi_1^i = \omega_{\mathrm{ts}}^i \tau_{12}$ and thus the current localizations are arbitrary such that no macroscopic polarization is detectable. In the Bloch sphere 'D' this is indicated by the spread of the pseudo spin vectors over the complete xy-plane.

The second alternating electric field pulse, applied after the pulse separation time

τ_{12}, is chosen such that during its application the wave functions of the tunneling systems experience a phase change of 180° or π. In the pulse sequence, shown in figure 3.9, this is realized by a pulse twice as long as the $\pi/2$ pulse. By the application of the π pulse (time stamp 'E'), the development of the phase of the individual tunneling system changes sign, which is equal to a time reversal. After the pulse, the wave functions of the tunneling systems evolve freely again and collect the phase $\Phi_2^i = \omega_{\mathrm{ts}}^i(t - \tau_{12})$. In the Bloch sphere 'E' the application of the second alternating electric field pulse causes similar to the first pulse a rotation around the x-axis by 180°. Since the precession motions are continued with the same frequencies ω_{d}^i afterwards, this rotation is equivalent to a time reversal of the phase evolution.
By the time marked with 'F', nearly one pulse separation time τ_{12} passed after the second pulse. Thus the phase differences $\Delta\Phi^i = \Phi_1^i - \Phi_2^i$ decline again and the oscillating wave functions and the corresponding localizations of the individual tunneling systems gradually adapt to each other. Consequently, a macroscopic polarization of the sample evolves. At the time $t = 2\tau_{12}$ (time stamp 'G') $\Phi_1^i = \Phi_2^i$ holds and the oscillating wave functions of the tunneling systems are in phase causing a recovery of the maximal macroscopic polarization of the sample, called 'spontaneous echo'. In the Bloch sphere 'F' this polarization is visible by the convergence of the individual pseudo spin vectors. The growing macroscopic expectation value in -y-direction illustrates the occurrence of the polarization of the sample. In sphere 'G' all pseudo spins are aligned again, forming the maximal macroscopic polarization.
After the maximal echo occurred the individual wave functions loose due to their free evolution their common phase again, which leads to a decrease and finally a vanishing macroscopic polarization (time stamp 'H'). In the Bloch sphere 'H' this is visualized by the spread of the pseudo spin vectors similar to 'C' and 'D', leading to the reduction of the macroscopic expectation value in -y-direction.

3.3.2 Quantum mechanical motivation - Path diagram visualization

A detailed calculation of the two-pulse echo in a two-level system has already been performed by several authors, e.g. [Dur89, Gur90, Bra04a, Baz08, Haa18a]. This paragraph gives a short overview of the calculation and introduces the path diagram representation, which was established by Parshin in 2004 [Par04]. These diagrams are a descriptive visualization of the wave function of a single tunneling system and allow to deduce the echo amplitude. Especially when considering the echo in a multilevel system, as in section 4.3.3, this representation is helpful. Finally, the influence of the pulse duration on the echo amplitude will be shortly addressed.
For the calculation a general two-pulse sequence with pulses of same field strength F_0 and the lengths t_1 and t_2 is assumed. The two pulses are separated by the pulse separation time τ_{I}. The time window after the second pulse is represented by the time τ_{II}. In figure 3.11 the corresponding time ranges are shown. It is further assumed that the pulse durations t_1 and t_2 are much smaller than the pulse separation time τ_{I} such that they can be treated as delta-like pulses. This assumption allows to neglect the

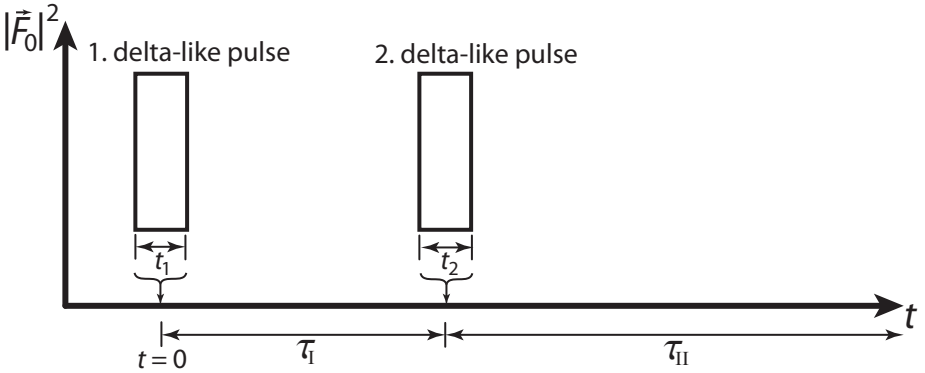

Figure 3.11: Scheme of a general two-pulse sequence with pulse duration t_1 and t_2, pulse separation time τ_I and the time window τ_{II} after the second pulse. The pulse durations t_1 and t_2 are assumed to be very small in comparison to the pulse separation time such that they can be treated as delta-like pulses. Illustration adapted from [Sch16a]

precession motion during the pulses and still provides the correct proportionalities for the echo amplitude. The following outline is mainly based on [Haa18a].

The calculation is performed for one single arbitrary tunneling system and finally applied to an ensemble of tunneling systems via an integration over the distribution function. Like in section 3.2.4, it is advantageous to use a reference frame rotating with the frequency of the alternating electric field of the pulses (ω_{ef}). The wave function of a single tunneling system is then given by $\Psi^{\mathrm{rot}}(t)$, the propagator describing the evolution of the wave function during the application of a pulse by

$$U_{\mathrm{ef}}(t) \propto \hat{\mathbb{1}} \cos\left(\frac{\Omega_{\mathrm{R}} t}{2}\right) - i\hat{\sigma}_{\mathrm{x}} \sin\left(\frac{\Omega_{\mathrm{R}} t}{2}\right) \tag{3.37}$$

(compare equation 3.34) and the time in between the two pulses is described by

$$U_{\mathrm{nf}}(t) \propto \mathrm{e}^{i\frac{\omega_{\mathrm{d}} t}{2}\hat{\sigma}_{\mathrm{z}}} \tag{3.38}$$

(compare equation 3.36). At the time $t = 0$, right before the first alternating electric field pulse is applied, the tunneling system is in its ground state

$$\Psi^{\mathrm{rot}}(0) = \begin{pmatrix} c_2^{\mathrm{rot}}(0) \\ c_1^{\mathrm{rot}}(0) \end{pmatrix} = \begin{pmatrix} 0 \\ 1 \end{pmatrix}. \tag{3.39}$$

The time evolution of the wave function during the pulse is obtained by applying the propagator U_{ef} to $\Psi^{\mathrm{rot}}(0)$. This results for the coefficients c_1^{rot} and c_2^{rot} in

$$\begin{aligned} c_1(t_1)^{\mathrm{rot}} &= -i \sin\left(\tfrac{\Omega_{\mathrm{R}} t_1}{2}\right) \\ c_2(t_1)^{\mathrm{rot}} &= \cos\left(\tfrac{\Omega_{\mathrm{R}} t_1}{2}\right). \end{aligned} \tag{3.40}$$

In the time interval τ_I between the two pulses the tunneling system evolves freely. The application of the propagator U_{nf} results in

$$\begin{aligned} c_1^{\mathrm{rot}}(t_1 + \tau_I) &= -i \sin\left(\tfrac{\Omega_{\mathrm{R}} t_1}{2}\right) \mathrm{e}^{i\frac{\omega_{\mathrm{d}} \tau_I}{2}} \\ c_2^{\mathrm{rot}}(t_1 + \tau_I) &= \cos\left(\tfrac{\Omega_{\mathrm{R}} t_1}{2}\right) \mathrm{e}^{-i\frac{\omega_{\mathrm{d}} \tau_I}{2}}. \end{aligned} \tag{3.41}$$

The second electric field pulse of duration t_2 leads to

$$\begin{aligned} c_1^{\mathrm{rot}}(t_{\mathrm{sp}}) &= -i \sin\left(\tfrac{\Omega_{\mathrm{R}} t_1}{2}\right) \cos\left(\tfrac{\Omega_{\mathrm{R}} t_2}{2}\right) \mathrm{e}^{i\frac{\omega_{\mathrm{d}}\tau_{\mathrm{I}}}{2}} - i \cos\left(\tfrac{\Omega_{\mathrm{R}} t_1}{2}\right) \sin\left(\tfrac{\Omega_{\mathrm{R}} t_2}{2}\right) \mathrm{e}^{-i\frac{\omega_{\mathrm{d}}\tau_{\mathrm{I}}}{2}} \\ c_2^{\mathrm{rot}}(t_{\mathrm{sp}}) &= \cos\left(\tfrac{\Omega_{\mathrm{R}} t_1}{2}\right) \cos\left(\tfrac{\Omega_{\mathrm{R}} t_2}{2}\right) \mathrm{e}^{-i\frac{\omega_{\mathrm{d}}\tau_{\mathrm{I}}}{2}} - \sin\left(\tfrac{\Omega_{\mathrm{R}} t_1}{2}\right) \sin\left(\tfrac{\Omega_{\mathrm{R}}}{2}\right) \mathrm{e}^{i\frac{\omega_{\mathrm{d}}\tau_{\mathrm{I}}}{2}} \end{aligned} \tag{3.42}$$

with $t_{\mathrm{sp}} = t_1 + \tau_{\mathrm{I}} + t_2$. After the pulse the tunneling system evolves freely again. The coefficients at the time $t_{\mathrm{e}} = t_1 + \tau_{\mathrm{I}} + t_2 + \tau_{\mathrm{II}}$ are given by

$$\begin{aligned} c_1^{\mathrm{rot}}(t_{\mathrm{e}}) = &\underbrace{-i \sin\left(\frac{\Omega_{\mathrm{R}} t_1}{2}\right) \cos\left(\frac{\Omega_{\mathrm{R}} t_2}{2}\right) \mathrm{e}^{i\frac{\omega_{\mathrm{d}}(\tau_{\mathrm{I}}+\tau_{\mathrm{II}})}{2}}}_{\mathrm{a}} \\ &\underbrace{-i \cos\left(\frac{\Omega_{\mathrm{R}} t_1}{2}\right) \sin\left(\frac{\Omega_{\mathrm{R}} t_2}{2}\right) \mathrm{e}^{-i\frac{\omega_{\mathrm{d}}(\tau_{\mathrm{I}}-\tau_{\mathrm{II}})}{2}}}_{\mathrm{b}} \end{aligned}$$

$$\begin{aligned} c_2^{\mathrm{rot}}(t_{\mathrm{e}}) = &\underbrace{\cos\left(\frac{\Omega_{\mathrm{R}} t_1}{2}\right) \cos\left(\frac{\Omega_{\mathrm{R}} t_2}{2}\right) \mathrm{e}^{-i\frac{\omega_{\mathrm{d}}(\tau_{\mathrm{I}}+\tau_{\mathrm{II}})}{2}}}_{\mathrm{c}} \\ &\underbrace{-\sin\left(\frac{\Omega_{\mathrm{R}} t_1}{2}\right) \sin\left(\frac{\Omega_{\mathrm{R}} t_2}{2}\right) \mathrm{e}^{i\frac{\omega_{\mathrm{d}}(\tau_{\mathrm{I}}-\tau_{\mathrm{II}})}{2}}}_{\mathrm{d}} . \end{aligned} \tag{3.43}$$

The braces with the labels 'a' to 'd' are used later for the path diagram visualization. To obtain the polarization of the tunneling system at the time $t = t_{\mathrm{e}}$ the expectation value of the polarization operator, defined in equation 3.27, has to be calculated. Beforehand this operator needs to be transformed into the rotating reference frame. It follows

$$\langle \hat{P}^{\mathrm{rot}} \rangle \propto \underbrace{\frac{\Delta_0}{E} \langle \hat{\sigma_{\mathrm{x}}} \rangle}_{P_{\mathrm{x}}} - \underbrace{\frac{\Delta_0}{E} \langle \hat{\sigma_{\mathrm{y}}} \rangle}_{P_{\mathrm{y}}} + \underbrace{\frac{\Delta}{E} \langle \hat{\sigma_{\mathrm{z}}} \rangle}_{P_{\mathrm{z}}} \tag{3.44}$$

with the polarization $P_{\mathrm{x,y,z}}$ in the x, y and z-direction. An evaluation results in

$$\begin{aligned} P_{\mathrm{x}} = &\frac{\Delta_0}{E} \sin\left(\Omega_{\mathrm{R}} t_1\right) \cos^2\left(\frac{\Omega_{\mathrm{R}} t_2}{2}\right) \underbrace{\sin\left(\omega_{\mathrm{d}}(\tau_{\mathrm{I}} + \tau_{\mathrm{II}})\right)}_{\mathrm{Phase}} \\ &+ \frac{\Delta_0}{E} \sin\left(\Omega_{\mathrm{R}} t_1\right) \sin^2\left(\frac{\Omega_{\mathrm{R}} t_2}{2}\right) \underbrace{\sin\left(\omega_{\mathrm{d}}(\tau_{\mathrm{I}} - \tau_{\mathrm{II}})\right)}_{\mathrm{Phase}} \\ &+ \frac{\Delta_0}{E} \cos\left(\Omega_{\mathrm{R}} t_1\right) \sin\left(\Omega_{\mathrm{R}} t_2\right) \underbrace{\sin\left(\omega_{\mathrm{d}} \tau_{\mathrm{II}}\right)}_{\mathrm{Phase}} \end{aligned} \tag{3.45}$$

$$
\begin{aligned}
P_\mathrm{y} = &\frac{\Delta_0}{E}\sin\left(\Omega_\mathrm{R}t_1\right)\cos^2\left(\frac{\Omega_\mathrm{R}t_2}{2}\right)\underbrace{\cos\left(\omega_\mathrm{d}(\tau_\mathrm{I}+\tau_\mathrm{II})\right)}_{\text{Phase}} \\
&-\frac{\Delta_0}{E}\sin\left(\Omega_\mathrm{R}t_1\right)\sin^2\left(\frac{\Omega_\mathrm{R}t_2}{2}\right)\underbrace{\cos\left(\omega_\mathrm{d}(\tau_\mathrm{I}-\tau_\mathrm{II})\right)}_{\text{Phase}} \\
&+\frac{\Delta_0}{E}\cos\left(\Omega_\mathrm{R}t_1\right)\sin\left(\Omega_\mathrm{R}t_2\right)\underbrace{\cos\left(\omega_\mathrm{d}\tau_\mathrm{II}\right)}_{\text{Phase}}
\end{aligned}
\tag{3.46}
$$

$$
P_\mathrm{z} = \frac{\Delta}{E}\left(\sin\left(\Omega_\mathrm{R}t_1\right)\sin\left(\Omega_\mathrm{R}t_2\right)\underbrace{\cos\left(\omega_\mathrm{d}\tau_\mathrm{I}\right)}_{\text{Phase}} - \cos\left(\Omega_\mathrm{R}t_1\right)\cos\left(\Omega_\mathrm{R}t_2\right)\right). \tag{3.47}
$$

Due to the delta-like pulses the tunneling system collects its phase only during the times $\tau_\mathrm{I,II}$, like in the Bloch sphere representation. The corresponding factors in equation 3.45 to 3.47 are marked by braces. From the previous discussions it is known, that the tunneling systems need to oscillate with the same phase to form an echo. Due to the different precession frequencies of the tunneling systems ω_d this condition is only fulfilled when each tunneling system collects the same phase before and after the second pulse. Looking at the trigonometric functions in equation 3.45 to 3.47, just the second term of P_x and P_y can become zero independent of ω_d, which is synonymous to the afore mentioned condition. This is reached when $\tau_\mathrm{I} = \tau_\mathrm{II}$ which is why the echo appears after twice the pulse separation time τ_I. At this time only the P_y term remains due to the cosine function. Thus, the second term of P_y is the one representing the polarization of the tunneling system during the echo. By choosing appropriate pulse durations the terms not contributing to the echo amplitude can be suppressed. An analysis yields

$$
\Omega_\mathrm{R}t_1 = \frac{\pi}{2} \quad \text{and} \quad \Omega_\mathrm{R}t_2 = \pi. \tag{3.48}
$$

By choosing such pulses all terms except the second one of P_y vanish and the polarization is maximized. Summarizing, for every single tunneling system in a glass holds

$$
\langle\hat{P}^\mathrm{rot}\rangle \propto \underbrace{\frac{\Delta_0}{E}\sin\left(\Omega_\mathrm{R}t_1\right)\sin^2\left(\frac{\Omega_\mathrm{R}t_2}{2}\right)}_{\propto\text{Amplitude } A_\mathrm{Echo,ts}}\underbrace{\cos\left(\omega_\mathrm{d}\left(\tau_\mathrm{I}-\tau_\mathrm{II}\right)\right)}_{\text{Phase}}. \tag{3.49}
$$

The expectation value consists of a part describing the actual polarization of the tunneling system ($A_\mathrm{Echo,ts}$) and a part representing the phase. The echo amplitude, equivalent to the macroscopic polarization of an ensemble of tunneling systems can thus be calculated by summing up or integrating the single amplitudes over all values of Δ_0, according to the distribution function introduced in section 3.2.3.

The obtained result for the echo amplitude is in accordance with the spin $^1/_2$ picture and the Bloch sphere representation. With the pulses defined in equation 3.48, the expectation value P_z becomes zero, which is equivalent to a rotation by 90° and 180°. At the time $2\tau_\mathrm{I}$, the polarization in y-direction is maximal and the echo appears.

In equation 3.48, considering the definition of the Rabi frequency in equation 3.35, it can be seen that the $\pi/2 - \pi$ condition cannot only be fulfilled by $t_2 = 2t_1$ as shown in figure 3.9. It is also possible to use different field strengths F_0 for the two pulses, which would lead to an altered Rabi frequency, or a combination of different field strength and pulse duration. To fulfill the $\pi/2 - \pi$ condition, the area of the pulse is the relevant part. Assuming very small pulses with $t_2 = 2t_1$, such that the approximation $\sin(x) \approx x$ can be used, the echo amplitude (equation 3.49) at the time $\tau_{\mathrm{II}} = \tau_{\mathrm{I}}$ can be rewritten to

$$A_{\mathrm{Echo,ts}} \propto \frac{\Delta_0}{E} \left(\Omega_{\mathrm{R}} t_1\right)^3 \propto \left(\frac{\Delta_0}{E}\right)^4 \left(\delta\vec{p}\vec{F}_0 t_1\right)^3. \tag{3.50}$$

This approximation is called 'small angle approximation'. Since the measured echo is a sum over the polarization amplitudes of all participating tunneling systems, a F_0^3 behavior is expected for small field strengths, when measuring the echo amplitude at fixed pulse separation time τ and with constant pulse duration t_1 in dependence of the electric field strength F_0. Similarly, a t_1^3 dependence is expected when measuring at constant electric field in dependence of the pulse duration. This behavior is observed in several measurements, e.g. [Sch78, Ber79] for dielectric polarization echoes or [Gra79] for phonon echoes in which similar relations are valid. When measuring such that the small angle approximation is valid the $\pi/2-\pi$ condition is not fulfilled for the tunneling system. This means that the other terms of the expectation value of the polarization operator (equation 3.45 to equation 3.47) may not vanish. However, due to the multitude of different tunneling systems with different precession frequencies ω_{d} in a glass which participate in the echo formation those contributions average out. Finally, just the term shown in equation 3.49, which is independent of ω_{d} at the time $\tau_{\mathrm{I}} = \tau_{\mathrm{II}}$, is observable.
Another point, which can be seen in equation 3.50, is the $(\Delta_0/E)^4$ dependence. It shows that symmetric tunneling systems contribute more to the echo amplitude.

Path diagram visualization

In equation 3.43 it can be seen that the wave function of the tunneling system consists of four terms at the time t_{e} after the second pulse. Each term describes a possible response of the tunneling system to the two-pulse sequence. Considering the propagators given in equation 3.37 and 3.38 the different constituents of the four terms can be evaluated:

- $\sin\left(\frac{\Omega_{\mathrm{R}} t_i}{2}\right)$: Off-diagonal element of the electric field propagator corresponding to a mixing of the two energy levels of the tunneling system during the pulses.
- $\cos\left(\frac{\Omega_{\mathrm{R}} t_i}{2}\right)$: On-diagonal element of the electric field propagator representing no mixing of the two energy states of the tunneling system during the pulses.
- $\mathrm{e}^{\pm i\frac{\omega_{\mathrm{d}}}{2}(\tau_{\mathrm{I}} \pm \tau_{\mathrm{II}})}$: Phase accumulated by the free evolution in the time window τ_{I} and τ_{II}.

Based on this classification, the term labelled 'a' in equation 3.43 represents the possibility of a mixing up during the first pulse and no mixing during the second one. The term 'b' corresponds to no mixing throughout the first and a mixing up throughout the second pulse. Term 'c' stands for no mixing at all and term 'd' shows a mixing up during the first and a mixing down during the second pulse. This evolution of the wave function of one single tunneling system can nicely be represented in a path diagram. In 2004 Parshin [Par04] introduced this representation without explicitly using a rotating frame of reference. However, this is not important since this representation is only used to get basic proportionalities (e.g. $A_{\mathrm{Echo,TS}} \propto F_0^3$) and the echo amplitude as a function of the pulse separation time. Therefore the path diagram representation is directly applicable to the results obtained above. Detailed information like the shape of the echo signal require detailed calculations as they can be found e.g. in [Gur90].
In figure 3.12 the path diagram representing equation 3.43 is shown. The vertical lines indicate a mixing of energy levels and the horizontal lines a free evolution of the tunneling system. Analogous to [Baz08], the wave function of the tunneling system at times $t > \tau_{\mathrm{I}}$ can be constructed via

$$\Psi^{\mathrm{path}}(t > \tau_{\mathrm{I}}) = \sum_i \pi_i(t > \tau_{\mathrm{I}}) \tag{3.51}$$

where i refers to one of the four paths and π_i being the corresponding path ('a' to 'd'). If path i ends in the ground state, π_i contributes to $|\Psi_{\mathrm{g}}\rangle$. If the path ends in the excited state, it contributes to $|\Psi_{\mathrm{e}}\rangle$. As before, the polarization of the tunneling system is given by the expectation value of the polarization operator

$$\langle \hat{P} \rangle = \langle \Psi^{\mathrm{path}} | \hat{P} | \Psi^{\mathrm{path}} \rangle = \sum_{i,j} \langle \pi_i | \hat{P} | \pi_j \rangle. \tag{3.52}$$

It can be seen that the calculation of the expectation value can be reduced to a sum over pairs of paths. From previous considerations it is already known that a tunneling system has to collect the same phase before and after the second pulse to

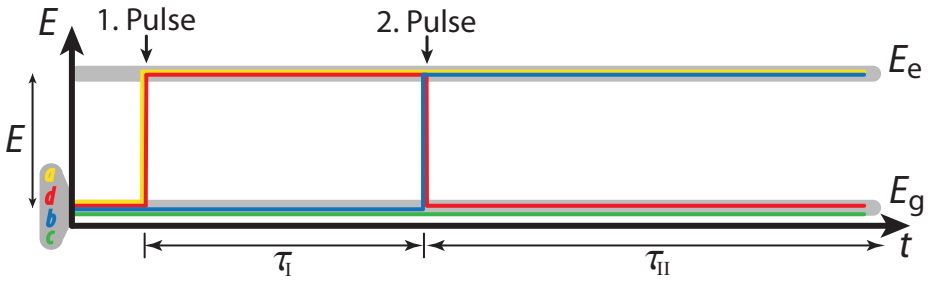

Figure 3.12: Path diagram representing the four terms of equation 3.43. Each path represents one possible response of the tunneling system to the two-pulse sequence. A vertical line indicates a level mixing. A horizontal line represents a free evolution of the wave function. Illustration adapted from [Sch16a]

contribute to the macroscopic polarization of the sample. Considering all possible path pairs only the combinations bd* and db* are contributing to the polarization of the tunneling system during the echo. All others contain phases which do not vanish at $\tau_{\mathrm{II}} = \tau_{\mathrm{I}}$ independently of ω_{d}, analogous to the equations 3.45 to 3.47. In figure 3.13 the path combination db* is shown. The dashed line in this illustration indicates the complex conjugation of the path (compare equation 3.52). The area below a path in the path diagram can be interpreted as the accumulated phase of the corresponding path during the two-pulse sequence. The phase of the relevant path pair is marked by $\Phi_{\mathrm{I,II}}$ in the figure. It can be seen that Φ_{I} and Φ_{II} are equally large such that the phase of the pair will vanish at $t = 2\tau_{\mathrm{I}}$. When calculating the expectation value with the relevant path pair combinations bd* and db*, the same proportionalities as in equation 3.49 are obtained.

As already mentioned, the benefit of the path diagram visualization is not only the visualization of the previous quantum mechanical calculation, but also to derive the polarization of a single tunneling system as a function of the pulse separation time. This is shown for the two-pulse echo in a two-level system. The derivation follows the rules [Par04]:

- To each vertical line, representing a transition from level k to level l, a factor $(-iF_{0,(1,2)})\alpha_{lk}$ is ascribed. $F_{0,(1,2)}$ represents the electric field strength during the first and second pulse and $\vec{F}_{0,(1)} \parallel \vec{F}_{0,(2)}$. The factors α_{lk} are the off-diagonal transition matrix elements projections on the direction of the electric field $\alpha_{lk} = (\vec{e}\cdot\delta\vec{p})^{\Delta_0}/_{E}$, with $\vec{e}$ being the unit vector in the direction of the electric field $\vec{F}_0 = F_0\vec{e}$. It holds $\alpha_{lk} = \alpha^*_{kl}$. It can easily be seen that α_{lk} is defined similar to the Rabi frequency (see equation 3.35) just without the field strength dependence and thus α_{lk} is proportional to the transition matrix elements of the quantum mechanical calculation when assuming negligible short pulses.

- To each horizontal line, corresponding to a free evolution of the tunneling system, a factor $\mathrm{e}^{-iE_l t/\hbar}$ is ascribed. E_l represents the energy level of the path during the free evolution.

Applying those rules to the path pair shown in figure 3.13 results in

$$\begin{aligned}
\langle\hat{P}\rangle(t > \tau_{\mathrm{I}}) \propto & \underbrace{(-iF_{0,(1)})\alpha_{\mathrm{eg}} \cdot \mathrm{e}^{-i\frac{E_{\mathrm{e}}}{\hbar}\tau_{\mathrm{I}}} \cdot (-iF_{0,(2)})\alpha_{\mathrm{ge}} \cdot \mathrm{e}^{-i\frac{E_{\mathrm{g}}}{\hbar}(t-\tau_{\mathrm{I}})}}_{\text{Path d}} \\
& \times \underbrace{\left[\mathrm{e}^{-i\frac{E_{\mathrm{g}}}{\hbar}\tau_{\mathrm{I}}} \cdot (-iF_{0,(2)})\alpha_{\mathrm{eg}} \cdot \mathrm{e}^{-i\frac{E_{\mathrm{e}}}{\hbar}(t-\tau_{\mathrm{I}})}\right]^*}_{\text{Path b}^*} \underbrace{\alpha_{\mathrm{eg}}}_{\text{Echo}} + c.c. \qquad (3.53) \\
= & -iF_{0,(1)}F^2_{0,[2]}|\alpha_{\mathrm{eg}}|^2|\alpha_{\mathrm{ge}}|^2 \mathrm{e}^{i\frac{(E_{\mathrm{e}}-E_{\mathrm{g}})}{\hbar}(t-\tau_{\mathrm{I}})-i\frac{(E_{\mathrm{e}}-E_{\mathrm{g}})}{\hbar}\tau_{\mathrm{I}}} + c.c. \\
= & \underbrace{-iF_{0,(1)}F^2_{0,(2)}|\alpha_{\mathrm{eg}}|^2|\alpha_{\mathrm{ge}}|^2}_{\propto A_{\mathrm{echo,TS}}} \underbrace{\mathrm{e}^{i\frac{E}{\hbar}(t-2\tau_{\mathrm{I}})}}_{\propto \text{ Phase}} + c.c..
\end{aligned}$$

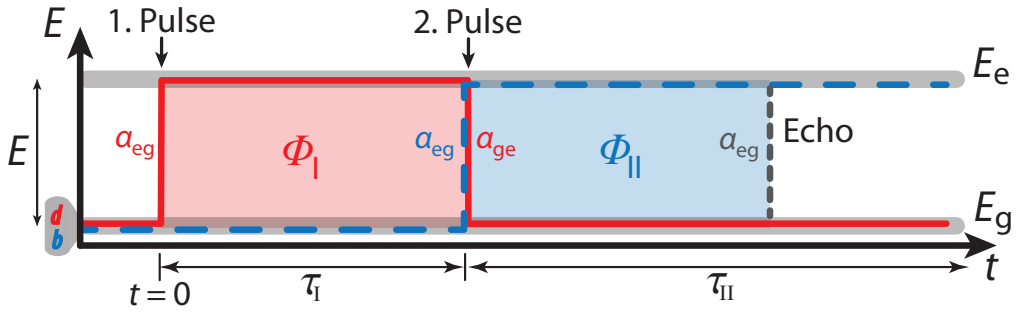

Figure 3.13: One of the path pairs contributing to the polarization of the tunneling system during the echo. The areas marked with $\Phi_{\mathrm{I,II}}$ reprsent the phase accumulated during the two-pulse sequence by the corresponding path. The $\alpha_{eg,ge}$ are needed for the derivation of the polarization of the tunneling system.

The *c.c.* indicates the complex conjugate path pair bd*, which needs to be considered as well to get the complete polarization of the tunneling system. The result is in agreement with the quantum mechanical calculation, see equation 3.49 and 3.50. Under the assumption of $F_{0,(1)} = F_{0,(2)} = F_0$ the cubic field dependency is visible and the $(\Delta_0/E)^4$ dependence follows from the two α^2 factors. Furthermore, the phase factor becomes one at the time $t = 2\tau_{\mathrm{I}}$, independent of E. This shows, that the path diagram representation can be used to derive the correct dependencies of the echo. It is especially helpful when the echo in a multi-level system is discussed in section 4.3.3.

Influence of the pulse duration on the echo signal

Until now, the two pulses of the two-pulse sequence were treated as delta-like pulses such that the precession motion during the pulses could be neglected in all calculations. In a real measurement the tunneling systems precess already during the pulses. This does not influence the above obtained proportionalities of the echo amplitude, but it affects the actual pulse separation time. Thereby the size of the echo amplitude is also altered due to already acting relaxation processes (see section 3.4). In figure 3.9 the pulse separation time is defined between the end of the first pulse and the middle of the second one. This definition of the pulse separation time is also used within this thesis. However, in a real measurement it is difficult to define the exact pulse separation time, since the shape and duration of the pulses are influenced by the properties of the employed resonator, e.g. its rise and fall time. Thus, in measurements of the echo amplitude in dependence of the pulse separation time a slight systematic offset is expectable.

Another effect of the pulse duration on the echo signal is related to the spectral width of the pulse. During the electric field pulses not only the tunneling systems with $E = \hbar\omega_{\mathrm{ef}}$ are excited, but also those within a certain energy range around E

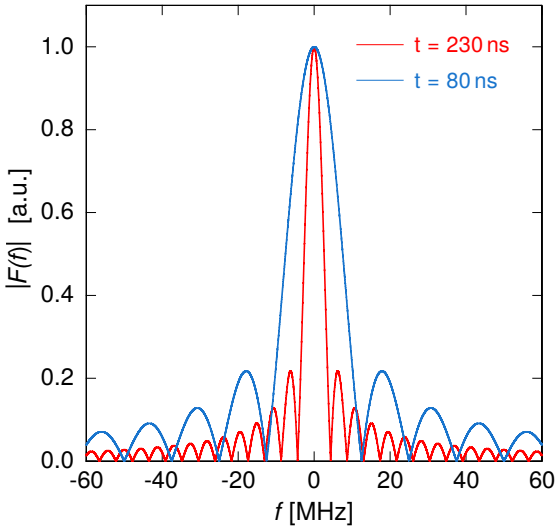

Figure 3.14: Absolute values of the Fourier transformations of two rectangular pulses with the durations 80 ns and 230 ns. It can be seen that the frequency composition becomes narrower for longer pulses.

according to the spectral width of the pulses. This leads to the different precession frequencies $\omega_{\mathrm{d}}^{i} = \omega_{\mathrm{ef}} - \omega_{\mathrm{ts}}^{i}$, which are required to observe an echo. According to [Par04] the spectral width of the pulses is given by:

$$\Delta E = \frac{\hbar}{t_j} \quad \Leftrightarrow \quad \Delta f = \frac{1}{2\pi t_j} \qquad (j = 1, 2). \tag{3.54}$$

Consequently, the shorter the pulse, the broader its spectral width and thus the more widely distributed and accordingly higher are the precession frequencies ω_{d}^{i}. This leads to a faster de- and re-phasing of the individual tunneling systems and thus to a narrower echo signal. Conversely holds, the broader the pulse, the broader the echo signal. The connection between the pulse duration and the spectral width is visualized in figure 3.14 by means of the absolute value of the Fourier transformation[6] of normalized pulses with durations of 80 ns and 230 ns.
In a real measurement the pulses cannot be made arbitrarily short due to the rise and fall time of the used resonator. The frequency composition of the pulses is in particular important when discussing the echo in a multi-level system, see section 4.3.3.

3.4 Relaxation and interactions between tunneling systems

Up to this point interactions of tunneling systems with photons and phonons were only discussed in terms of the excitation of those system for the generation of echo

[6] According to [Fuk81] the Fourier transformation of a normalized rectangular pulse of duration t_{pulse}, starting at $t = -t_{\mathrm{pulse}}/2$ is given by

$$F(f) = \frac{2}{t_{\mathrm{pulse}}} \int_{0}^{t_{\mathrm{pulse}}/2} \cos(2\pi f)\,\mathrm{d}t = \frac{\sin(\pi f t_{\mathrm{pulse}})}{\pi f t_{\mathrm{pulse}}}. \tag{3.55}$$

signals. However, every excitation channel is also a possible relaxation channel. Considering the spin 1/2 analogy, Bloch introduced the so-called Bloch equations to describe the motion of a spin 1/2 in a magnetic field and added the relaxation times T_1 and T_2 to describe the relaxation processes [Blo46]. Transforming those equations into a reference frame, rotating with frequency ω, and translating them to the case of tunneling systems, it holds [Ens95]

$$\begin{aligned}
\frac{\mathrm{d}\hat{S}_\mathrm{x}(t)}{\mathrm{d}t} &= -\frac{1}{T_2}\hat{S}_\mathrm{x}(t) - (\omega - \omega_\mathrm{ts})\,\hat{S}_\mathrm{y}(t) \\
\frac{\mathrm{d}\hat{S}_\mathrm{y}(t)}{\mathrm{d}t} &= (\omega - \omega_\mathrm{ts})\,\hat{S}_\mathrm{x}(t) - \frac{1}{T_2}\hat{S}_\mathrm{y}(t) - \Omega_\mathrm{R}\hat{S}_\mathrm{z}(t) \\
\frac{\mathrm{d}\hat{S}_\mathrm{z}(t)}{\mathrm{d}t} &= \Omega_\mathrm{R}\hat{S}_\mathrm{y}(t) - \frac{1}{T_1}\left(\hat{S}_\mathrm{z} - S_\mathrm{z}^\mathrm{th}\right)
\end{aligned} \tag{3.56}$$

with the pseudo spin operators[7] $\hat{S}_\mathrm{x,y,z}$ and the thermal equilibrium value of the population difference S_z^th. The longitudinal relaxation time T_1 describes the time an ensemble of spins needs to return to its thermal equilibrium value after a perturbation. T_2 is the so-called transversal relaxation time and governed by processes destroying the phase coherence of an ensemble of systems. The two processes can be explained considering the Bloch sphere representation. A longitudinal process changes the occupation difference given by the expectation value in z-direction. A transversal relaxation process influences, for example, the precession motion of the individual spins in the xy-plane and thereby the expectation value in y-direction, which is proportional to the polarization of the sample. The two-pulse echo sequence used in the framework of this thesis is in particular sensitive to T_2. T_1 can for example be studied in more detail by three-pulse echoes (also called stimulated echo).
In the following, the two most relevant relaxation processes for this thesis are introduced, the one-phonon process (longitudinal relaxation) and spectral diffusion (transversal relaxation). At the end of the chapter other possible relaxation processes are shortly addressed.

3.4.1 One-phonon process

According to the standard tunneling model (see section 3.2) the one-phonon process is the dominating relaxation process at very low temperatures $T < 2\,\mathrm{K}$ [Esq98], when the thermal energy becomes comparable to the energy splitting of the tunneling systems $k_\mathrm{B}T \lesssim E$. This process is characterized by the interaction of the tunneling systems with the heat bath of the glass via single thermal phonons as shown in figure 3.15.
The corresponding time constant T_1 was calculated by [Jäc76]. In the following the notation of [Ens10] is employed. The probability for a transition of a single tunneling

[7] $\hat{S}_\mathrm{x} = \frac{1}{2}\hat{\sigma}_\mathrm{x}$, $\hat{S}_\mathrm{y} = \frac{1}{2}\hat{\sigma}_\mathrm{y}$, $\hat{S}_\mathrm{z} = \frac{1}{2}\hat{\sigma}_\mathrm{z}$

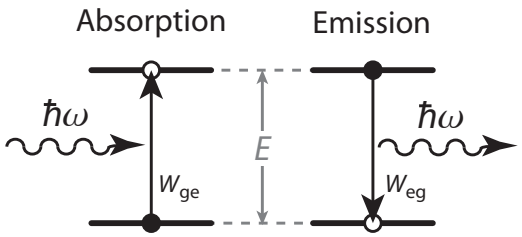

Figure 3.15: Schematic representation of the so-called 'one phonon process'. The transitions between the energy levels are caused by single thermal phonons of energy $E = \hbar\omega$. Illustration created according to [Ens10].

system from one level to the other W_{eg} (and W_{ge}) can be calculated using Fermi's golden rule. The transition from the ground to the excited state is accompanied by the absorption of a phonon of energy $\hbar\omega = E$ and given by

$$W_{\mathrm{ge}} = \frac{2\pi}{\hbar}|\langle\Psi_{\mathrm{e}}|\hat{\mathcal{H}}_{\mathrm{pert}}|\Psi_{\mathrm{g}}\rangle|^2 D(E) f(E) \delta(\hbar\omega = E). \tag{3.57}$$

$\hat{\mathcal{H}}_{\mathrm{pert}}$ represents the perturbation Hamiltonian, given in equation 3.23, for the coupling to phonons with $\delta\Delta = 2\gamma\tilde{e}$. The tensorial character of the deformation potential γ and the strain field $\tilde{e}$ is neglected. $D(E)$ is the density of states of the phonons in the Debye model and $f(E)$ the Bose-Einstein distribution function. The relaxation rate T_1^{-1} is given by $T_1^{-1} = W_{\mathrm{ge}} + W_{\mathrm{eg}}$. When calculating W_{eg} the Bose-Einstein distribution function $f(E)$ has to be replaced by $[1 + f(E)]$ to take into account the emitted phonon in this process.
The total relaxation rate is then given by

$$T_1^{-1} = \left(\frac{\gamma_{\mathrm{l}}^2}{v_{\mathrm{l}}^5} + 2\frac{\gamma_{\mathrm{t}}^2}{v_{\mathrm{t}}^5}\right)\left(\frac{\Delta_0}{E}\right)^2 \frac{E^3}{2\pi\rho\hbar^4} \coth\left(\frac{E}{2k_{\mathrm{B}}T}\right) \tag{3.58}$$

with the speed of sound v and the density ρ. The subscripts 'l' and 't' indicate the longitudinal and the two transversal phonon branches. For a fixed energy splitting E, the $(\Delta_0/E)^2$ dependence shows that the relaxation rate is maximal for symmetric tunneling systems ($\Delta \to 0 \;\Rightarrow\; \Delta_0/E \to 1$). The temperature dependence of the relaxation rate through $\coth(E/2k_{\mathrm{B}}T)$ is caused by the rising number of phonons with increasing temperature. For $E \leq k_{\mathrm{B}}T$ the approximation $\coth(E/2k_{\mathrm{B}}T) \approx T$ holds, such that for the temperature dependence of the relaxation time

$$T_1^{-1} \propto T \tag{3.59}$$

is expected.
A decay governed by T_1 follows the exponential law e^{-t/T_1} with $t = 2\tau_{12}$. Thus by rewriting equation 3.58 to

$$T_1^{-1} = T_{1,\mathrm{min}}^{-1}(E)\left(\frac{\Delta_0}{E}\right)^2, \tag{3.60}$$

the contribution of the one-phonon process for a tunneling system with fixed E and Δ_0 to the echo amplitude is given by

$$W_{1\mathrm{Phonon}}(2\tau_{12}) = \mathrm{e}^{-2\tau_{12}T_{1,\mathrm{min}}^{-1}(E)\left(\frac{\Delta_0}{E}\right)^2}. \tag{3.61}$$

The variable $T_{1,\min}^{-1}$ corresponds to the relaxation rate of a symmetric double-well potential with $\Delta = 0$ and $\Delta_0 = E$ [Esq98].
To describe the whole glass sample equation 3.61 has to be integrated according to the distribution function given in section 3.2.3. Thus there is no simple exponential decay in a real measurement. An example for the one-phonon decay of an ensemble of tunneling systems is shown in figure 3.17

3.4.2 Spectral diffusion

The transversal relaxation rate T_2^{-1} describes the loss of phase coherence and is in general given by [Phi81]

$$\frac{1}{T_2} = \frac{1}{2T_1} + \frac{1}{T_\Phi}, \tag{3.62}$$

with the phase memory time T_Φ. Not only processes influencing directly the precession motion of the tunneling systems in the xy-plane lead to a loss of phase coherence as mentioned in the introduction. But also longitudinal processes, described by T_1, cause via de-excitations of tunneling systems a loss of phase coherence. However, in the temperature range considered within this thesis processes influencing the precession motion directly, described by the phase memory time T_Φ, dominate compared to the one-phonon relaxation. Consequently, the approximation $T_2 \approx T_\Phi$ applies.

The precession motion during the free evolution and the accompanied collection of phase of a tunneling system during an echo sequence is determined by the eigenfrequency of the system and thus by its energy splitting (compare section 3.3). According to section 3.2.4, the energy splitting of a tunneling system can be changed by a variation of its asymmetry energy Δ through an interaction with an external field. During the free evolution of a tunneling system in an echo sequence no electric field is present, such that the strain field has to be considered. An interaction with a thermal phonon of appropriate energy would lead to the already introduced T_1 process. A direct interaction between adjacent tunneling systems, mediated via virtual phonons, is not considered within the standard tunneling model. However, this direct interaction was observed in 1975 by Arnold and Hunklinger [Arn75] during a hole-burning experiment. They measured a strong broadening of the hole in the acoustic absorption spectrum which could not be explained by the natural linewidth. A theoretical explanation for this observation is given by the elastic dipole-dipole interaction of the tunneling systems, known as spectral diffusion. This theory was initially developed for spin echoes by [Kla62] and later transferred to polarization echoes in amorphous solids by [Bla77].

The total amount of tunneling systems in the range $0 < {}^{E}/_{k_\mathrm{B}} \approx 1\,\mathrm{K}$ is about 10^{17} to 10^{18} per cubic centimeter [Ens10]. The density of resonantly excited tunneling systems during a pulse sequence is approximately 10^{12} per cubic centimeter [Phi81]. Consequently, the amount of non-excited tunneling systems during an echo sequence is several orders of magnitude larger than the one of the excited ones. Therefore every

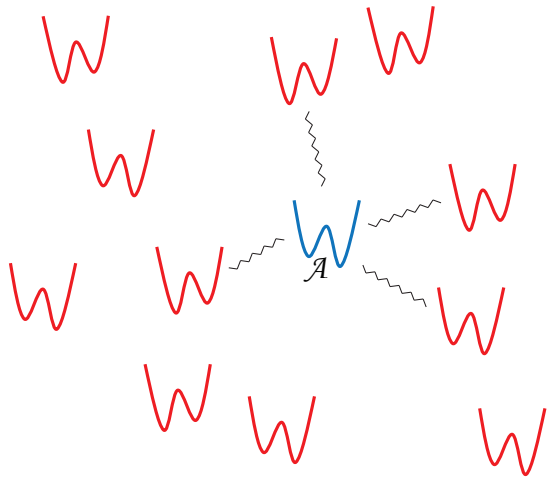

Figure 3.16: Simplified representation of spectral diffusion. A resonantly excited $\mathcal{A}$-system (blue) is surrounded by non-excited $\mathcal{B}$-systems (red). The springs represent the interaction via the strain field. Illustration based on [Esq98].

excited tunneling system, from now on labelled as $\mathcal{A}$-system, is surrounded by several non-excited ones, called $\mathcal{B}$-systems. A schematic illustration of this situation is shown in figure 3.16. The $\mathcal{A}$-system (blue) is interacting via the strain field (illustrated by the springs) with several $\mathcal{B}$ systems (red). If one of the $\mathcal{B}$-systems undergoes a transition between its energy states, via an absorption or emission of a phonon, the strain field in its proximity is altered. This change of the elastic field is experienced by a nearby $\mathcal{A}$-system and causes a shift of its asymmetry energy Δ and thus of its energy splitting. Therefore its eigenfrequency ω_{ts} changes and the $\mathcal{A}$-system loses phase coherence to the other resonantly excited tunneling systems since it does not collect the same phase before and after the second pulse. Hence the $\mathcal{A}$-system can no longer contribute to the macroscopic polarization of the sample. According to [Esq98], two tunneling systems with a distance of 10 nm alter each other's asymmetry energy by about 20 mK $\widehat{\approx}$ 0.4 GHz[8]. With increasing pulse separation time the probability for transitions of the $\mathcal{B}$-systems increases and thus the echo amplitude decays.

In the following a short motivation of the theoretical calculation is given mainly based on [Bla77]. Like before, the spin $^1/_2$ analogy is employed. The Hamiltonian of the dipole-dipole interaction of two pseudo spins i and j is given by

$$\hat{H}_{\mathrm{spin}\leftrightarrow\mathrm{spin}} = \sum_{i>j} U_{ij} \hat{S}_{\mathrm{z}}^{i} \hat{S}_{\mathrm{z}}^{j} \tag{3.63}$$

with the coupling energy U_{ij} defined as

$$U_{ij} = C_{ij} \left(\frac{\Delta}{E}\right)_i \left(\frac{\Delta}{E}\right)_j \frac{1}{r_{ij}^3}. \tag{3.64}$$

C_{ij} represents a material dependent parameter which depends amongst others on the deformation potential γ at site i and j. In the further calculation an averaged value

[8] For the interaction energy holds $E_{\mathrm{int}} = \frac{\gamma^2}{\rho v^2} \frac{1}{r^3}$. The value was calculated with typical values for the sound velocity v and density ρ. The deformation potential γ is in the order of 1 eV [Esq98].

for γ will be used. r_{ij} is the distance between spin i and j. The total Hamiltonian of the $\mathcal{A}$-system i surrounded by $\mathcal{B}$-systems j in the basis $(\Psi_\mathrm{g}, \Psi_\mathrm{e})$ is thus given by

$$\hat{\mathcal{H}}^i_\mathrm{eff} = E^i_\mathrm{eff} \hat{S}^i_\mathrm{z} \tag{3.65}$$

with

$$E^i_\mathrm{eff} = E^i + \sum_{i \neq j} U_{ij} \hat{S}^j_\mathrm{z}. \tag{3.66}$$

If $\hat{S}^j_\mathrm{z}$ is time independent for all $\mathcal{B}$-systems ($\partial \hat{S}^j_\mathrm{z} / \partial t = 0$) the interaction leads to a time independent shift of the energy splitting E^i of the $\mathcal{A}$-system. However, such a (time independent) shift can be assumed to be already included in the definition of E^i, since the energy splitting of the tunneling systems in an amorphous solid is a wide distribution (compare section 3.2.3). If $\hat{S}^j_\mathrm{z}$ is time dependent ($\partial \hat{S}^j_\mathrm{z} / \partial t \neq 0$) the spin flips of the $\mathcal{B}$-systems cause a change of the energy splitting $E^i_\mathrm{eff}(t)$ of the $\mathcal{A}$-system with time. It will drift away from its initial value $E^i_\mathrm{eff}(0) = \hbar\omega_0$ to $E^i_\mathrm{eff}(t) = \hbar\omega$ in the time t.
In a lengthy calculation, given in [Bla77], the effect of the introduced interaction between tunneling systems onto the decay of the echo amplitude is determined. In the derivation the spectral diffusion kernel $D(\omega - \omega_0, t)$, which gives the probability that $E^i_\mathrm{eff} = \hbar\omega$ at time t, is analyzed. Thereby it is taken into account that $\mathcal{B}$-systems with an appropriate energy in relation to the sample temperature can flip so-called thermal tunneling systems with $E \approx k_\mathrm{B}T$. Systems with a too large energy splitting are frozen in their ground state. In addition, only tunneling systems that went through an odd number of flips until the time t are relevant for the calculation. The process leading to flips of the $\mathcal{B}$-systems is the one-phonon relaxation.
In the short time limit, where the pulse separation time τ_{12} is much smaller than the shortest T_1 of the $\mathcal{B}$-systems ($\tau_{12} \ll T^{\mathcal{B}}_{1,\mathrm{min}}$), the contribution of the spectral diffusion for a single tunneling system is given by

$$W_{\mathrm{specDiff,st}}(2\tau_{12}) = \mathrm{e}^{-\left(\frac{2\tau_{12}}{T_2}\right)^2} = \mathrm{e}^{-m_\mathrm{st}(T, \frac{\Delta}{E})\tau_{12}^2} \tag{3.67}$$

with

$$m_\mathrm{st}(T, \frac{\Delta}{E}) = \frac{\Delta}{E} m(T) \propto \frac{\Delta}{E} T^4 \tag{3.68}$$

[Bla77, Ens96b, Fic13]. The Δ/E dependence of m shows that the contribution of tunneling systems with a large asymmetry energy Δ to the echo amplitude decays fast with increasing pulse separation time. Symmetric tunneling systems with $\Delta \to 0$ are almost unaffected by spectral diffusion. The strong temperature dependence of m_st is caused by the increasing amount of thermal phonons with rising temperature. The phase memory time $T_\Phi \approx T_2$ shows a

$$T_2 \propto T^{-2} \tag{3.69}$$

dependence [Bla77, Ens96b]. This behavior was experimentally confirmed for example in the glass Suprasil I down to about 13 mK [Ens96a]. In addition, the decay of

the polarization echo amplitude measured on the multicomponent glass BK7 can be well described at short pulse separation times with the model of spectral diffusion [Ens96b].
According to equation 3.67, a Gaussian shape like leveling-off of the polarization echo is expected for a single tunneling system towards small pulse separation times. During a measurement an ensemble of tunneling systems is studied such that the obtained contribution for a single tunneling system has to be integrated with respect to the distribution function given in section 3.2.3. Thus, the shape of the decay of the echo amplitude with increasing pulse separation time is a summation of various different Gaussian like functions. The Gaussian shape like leveling-off of the echo amplitude towards short pulse separation times was first observed on the glass Suprasil I [Ens96b].

Estimations of the minimal relaxation time of $\mathcal{B}$-systems $T_{1,\min}^{\mathcal{B}}$ vary. Based on acoustic experiments the minimal relaxation time of $\mathcal{B}$-systems $T_{1,\min}^{\mathcal{B}}$ in vitreous silica at 10 mK is about 5 ms, but echo measurements on the glass Suprasil I yielded significantly shorter times [Ens02b]. A general estimation of $T_{1,\min}^{\mathcal{B}}$ in [Bla77] yields 99 µs at 20 mK for thermal $\mathcal{B}$-systems. Towards higher temperatures the relaxation times of thermal tunneling systems decrease proportional to T^{-3} [Bla77, Esq98].[9] However, most measurements in the framework of this thesis were performed at a temperature of 10 mK and pulse separation times of $2\tau_{12} < 100\,\mu s$. Thus the short time limit should be valid for these measurements.

In the intermediate time regime, after the short time limit, the echo amplitude falls more slowly. It holds

$$W_{\text{specDiff,it}}(2\tau_{12}) = \mathrm{e}^{-\frac{2\tau_{12}}{T_2}} = \mathrm{e}^{-\sqrt[3]{\pi} m_{\text{it}}(T) \frac{\Delta}{E} T_{1,\min}^{\mathcal{B}}(T) \tau_{12}} \tag{3.70}$$

[Bla77, Hu74, Ens96b]. In this limit the phase memory time T_2 shows a T^{-1} dependence [Ens96b]. An approximation for the long time limit can be found in the same publications but is not discussed here due to the short pulse separation times used in this thesis.

The course of the decay of the echo amplitude caused by spectral diffusion in the short time limit, the one-phonon process as well as a combination of both is shown in figure 3.17. For comparability the decays are plotted relative to the maximal values. These curves are obtained by integrating the echo amplitude in the small angle approximation and the contributions of the two relaxation processes over the

[9] The T^{-3} proportionality results from equation 3.58 and the thermal tunneling system assumption $E \approx \Delta_0 \approx k_{\mathrm{B}}T$. Setting $E \approx \Delta_0$ ($\Rightarrow \Delta \approx 0$) is caused by the $1/\Delta_0^2$ dependence of T_1 whereby tunneling systems with this characteristic flip most efficiently (compare section 3.4.1) [Esq98].

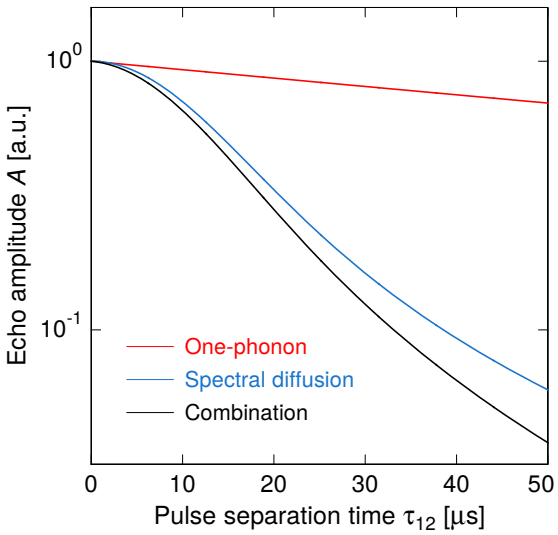

Figure 3.17: Numerical calculation of the echo amplitude A in dependence of the pulse separation time τ_{12} for an ensemble of tunneling systems follwing the distribution function given in section 3.2.3. In the calculations only the one-phonon relaxation, spectral diffusion in the short time limit or both were considered to illustrate their influence on the echo decay. The used parameters are $T_{1,\mathrm{min}}$ of 220 µs and $m = 10 \cdot 10^9\,{}^1/_{\mathrm{s}^2} \Rightarrow T_{2,\mathrm{min}} = \sqrt{4m^{-1}} = 20\,\mu\mathrm{s}$. They are motivated by the results obtained in [Fic13] for the glass N-BK7.

distribution function.

$$A(\tau_{12}) \propto \int A_{\mathrm{Echo,ts}} P\left(E,q\right) W_{\mathrm{1Phonon}} W_{\mathrm{specDiff,st}} \mathrm{d}q \tag{3.71}$$
$$= A_0 \int_0^1 \sqrt{1-q^2}^4 \frac{1}{1-q^2} \mathrm{e}^{-2\tau_{12} T_1^{-1}(T_{1,\mathrm{min}}^{-1},q)} \mathrm{e}^{-mq\tau_{12}^2} \mathrm{d}q$$

In this formula the relation $\Delta_0/E = \sqrt{1-q^2}$ was used to rewrite the echo amplitude and the contributions of the relaxation processes. The factor A_0 contains all parameters which are independent of q as well as the thermal occupation difference. In the curves shown in figure 3.17 this parameter is set to one. In addition, no maximal value for q must be considered in the integration since there is no discontinuity for $q \to 1$. The integral was calculated numerically with the software Mathematica[10]. For the used parameters (see caption) spectral diffusion dominates the course of the echo decay.

3.4.3 Further relaxation processes

This section gives an overview of other possible relaxation processes of tunneling systems. The here listed processes are either relevant at pulse separation times not reached within this thesis or their influence onto the decay of the echo amplitude is expected to be weak at the used temperatures compared to other relaxation processes. Thus, this chapter is more an enumeration than a detailed explanation. For further insights references are given. Note, that the list of processes might not be complete.

[10] Wolfram Research Inc., The Wolfram Centre, Lower Road, Long Hanborough Oxfordshire OX29 8FD, United Kingdom

Spectral diffusion caused by electric field variations

Using the terminology from section 3.4.2 the $\mathcal{A}$-system can interact with the surrounding $\mathcal{B}$-systems, if they carry large enough dipole moments, via the exchange of virtual phonons [Esq98]. A transition of a $\mathcal{B}$-system changes the electric field configuration at the position of the $\mathcal{A}$-system and thus influences the $\mathcal{A}$-systems energy splitting E and precession frequency ω_{ts}. Classically, spectral diffusion considers the interaction via the strain field, since the tunneling systems carrying an electric dipole moment are a sub-ensemble of all tunneling systems in a sample. However, the effect of the electric mechanism is qualitatively identical [Esq98] to the elastic mechanism and can thus be understood as included into the relaxation time T_2 when it is determined for a given data set.

Tunneling systems with weak coupling to phonons

In [Bur13] and [Fic13] it is shown that at large pulse separation times the echo amplitude in the multicomponent glass N-BK7 is determined by a small sub-ensemble of tunneling systems with a negligible relaxation and decoherence due to a very weak coupling to phonons. Theoretically this is modeled by introducing a distribution of the deformation potential γ. The distribution function is Gaussian like with a modified asymptotic behavior to take the tunneling systems with the negligible deformation potential ($x \to 0$) and thus very weak coupling to phonons into account. A plot of the corresponding function is shown in figure 3.18. This distribution of the deformation potential is added to the derivation of relaxation processes which involve the coupling of tunneling systems to the strain field (e.g. one-phonon relaxation (section 3.4.1), spectral diffusion (section 3.4.2)) and collective excitation (see this section). Without this theory a mean value of the deformation potential is used for the calculation of the relaxation processes. Since the sub-ensemble of weakly interacting tunneling systems determines the shape of the echo decay curve at very

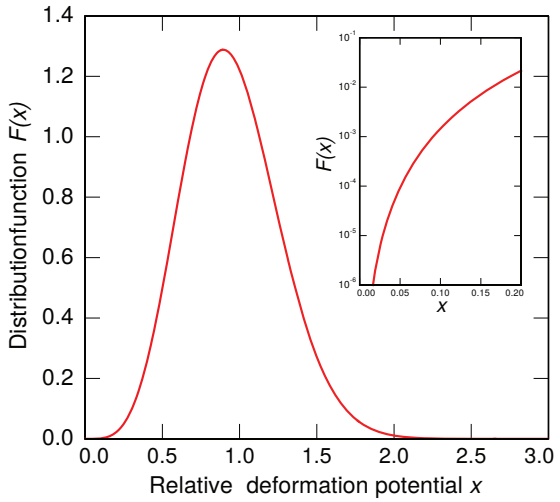

Figure 3.18: Plot of the distribution function $F(x)$ of the relative deformation potential $x = |\gamma_i|/\gamma_0$ with γ_0 being the deformation potential of a 'standard' tunneling system. The inset shows the same function for small values of x semilogarithmically. Plot taken from [Fic13].

large pulse separation times this distribution of the deformation potential is not considered in the present thesis, which focuses on short pulse separation times.

Direct interaction of two tunneling systems

The direct interaction of two resonant tunneling systems is discussed in [Bla77] and [Fic13]. In this process one tunneling system is excited or deexcited by a change of state of another nearby tunneling system via the exchange of a virtual phonon. A schematic illustration of this relaxation mechanism is shown in figure 3.19.

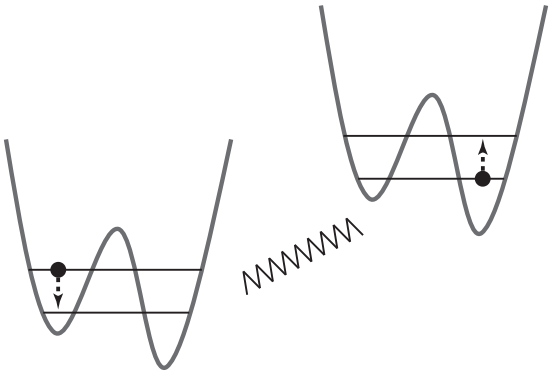

Figure 3.19: Visualization of the interaction of two resonant tunneling systems via the strain field (illustrated by the spring). One tunneling system changes its state due to the excitation or deexcitation of the other one. The excitation energy is transmitted via a virtual phonon.

The corresponding Hamiltonian describing the interaction of tunneling system i and j is given by

$$\hat{H}_{\text{flip-flop},ij} = K_{ij}\hat{S}_{\text{x}}^{i}\hat{S}_{\text{x}}^{j} \qquad \text{with} \qquad K_{ij} \propto \frac{1}{r_{ij}^{3}} \tag{3.72}$$

with the coupling constant K_{ij} similar to the one given in equation 3.64. Since the density of resonant tunneling systems is comparatively low, this kind of interaction is very weak. According to the numbers given in section 3.4.2 the distance between two resonant systems in an amorphous solid is approximately 1 µm. Due to the $1/r_{ij}^{3}$ dependency of the coupling constant K_{ij} this interaction is negligible compared to spectral diffusion.

Collective excitation

In the previous section it was argued that the interaction of two resonant tunneling systems is negligibly small. However, interacting resonant pairs of tunneling systems are considered relevant at lowest temperatures, as described in [Bur98]. The actual existence of such coupled tunneling systems was experimentally confirmed in defect spectroscopy of single tunneling systems using a superconducting qubit [Lis15]. In the following, a short motivation of this interaction process and its influence onto the relaxation of tunneling systems is given, based on [Esq98].

In the corresponding theory the tunneling systems are, as in spectral diffusion theory, no longer treated as non-interacting. The strength of the interaction of tunneling

system i and j is analogous to equation 3.63 given by the coupling energy

$$U_{ij} = \pm\frac{U_0}{r_{ij}^3}. \tag{3.73}$$

The coupling strength U_0 is assumed to be isotropic for all tunneling systems and depends on the kind of interaction (strain or electric dipole interaction).
It is assumed that two tunneling systems, referred to as tunneling system 1 and 2, can form a resonant pair in a so-called flip-flop configuration[11] under certain requirements:

- The lifetime of the individual tunneling systems is longer than the time needed for one coherent oscillation of the pair ($\Delta_{0,\mathrm{pair}} < \hbar T_1^{-1}$). If one of the tunneling systems decays earlier the coherent coupling is destroyed.
- Within a cutoff radius R_c around tunneling system 1 another appropriate tunneling system (tunneling system 2) exists with which it can couple resonantly. For thermal tunneling systems ($E, \Delta_0 \approx k_\mathrm{B}T$), which are most relevant for this process, it holds
$$R_\mathrm{c} \propto \frac{1}{T}. \tag{3.74}$$
Thus the cutoff radius increases with decreasing temperature.

The probability for a tunneling system to find an appropriate other tunneling system within R_c is proportional to P_0U_0, with the tunneling system density P_0 from section 3.2.3. Since $P_0U_0 \approx 10^{-3} \ll 1$ holds for all known glasses [Bur98], the probability to find a resonant partner is very low. Thus every tunneling system participates at most in one pair.
A formed resonant pair can be treated as 'new' two-level system with asymmetry energy Δ_pair and tunnel splitting $\Delta_{0,\mathrm{pair}}$. A derivation of the distribution function of the pairs yields

$$P_\mathrm{pair}(\Delta_\mathrm{pair}, \Delta_{0,\mathrm{pair}}) \approx (P_0 k_\mathrm{B}T)(P_0U_0)\frac{1}{\Delta_{0,\mathrm{pair}}^2}. \tag{3.75}$$

This distribution function has a stronger singularity for small tunnel splittings than the one of the individual tunneling systems[12], leading for $\Delta_{0,\mathrm{pair}} < k_\mathrm{B}T(P_0U_0)$ to a larger density of low-energy flip-flop pairs compared to isolated tunneling systems.

[11] Flip-flop configuration means that one of the system is in its ground state and the other one in its excited. A transition of one of the systems leads to a transition of the other one. The energy is thereby transmitted in dependence of the coupling via a virtual phonon or photon (compare figure 3.19). In general a coupled pair has, similar to two coupled spins, four different states $|\uparrow\uparrow\rangle$, $|\uparrow\downarrow\rangle$, $|\downarrow\uparrow\rangle$, $|\downarrow\downarrow\rangle$. However, the levels $|\uparrow\uparrow\rangle$ and $|\downarrow\downarrow\rangle$ are energetically separated from the flip-flop configuration ($|\uparrow\downarrow\rangle$, $|\downarrow\uparrow\rangle$) and coupled only weakly to them.

[12] For comparison the distribution function given in equation 3.17 can be rewritten to: $P(\Delta, \Delta_0) = \frac{P_0}{\Delta_0}$

Therefore at low enough temperatures the dominant low-energy excitations are flip-flop pairs. In this case their high density, compared to isolated tunneling systems, can lead to delocalized excitations between different pairs.
In the further derivation the pairs are considered as effective tunneling systems and interactions between them are studied analogous to before (equation 3.63 and 3.73). This results in the following conditions for the appearance of interacting resonant pairs, so-called clusters, whose occurance enables delocalized excitations.

- The coherent coupling within the pairs $\Delta_{0,\mathrm{pair}}$ is smaller or equal the coupling between the resonant pairs Δ_*.
- The distance between pairs R_* is smaller than the cutoff radius R_c.

From the last requirement the characteristic temperature below which delocalized excitations are expected can be derived to be

$$T_* \approx \frac{1}{k_\mathrm{B}} \sqrt{\frac{v^3\hbar^3}{U_0}}\,(P_0U_0) \tag{3.76}$$

with the sound velocity v.

The appearance of delocalized excitations influences the longitudinal and transversal relaxation time of the tunneling systems which are excited during an echo sequence. Similar to the argumentation for the case of spectral diffusion (section 3.4.2), transitions within a cluster of resonant pairs as well as breaking and reformation of pairs change the elastic and electric (if the respective tunneling systems carry electric dipole moments) field at the positions of the $\mathcal{A}$-systems. The characteristic time scale is no longer given by the tunneling system phonon interaction ($\propto T_{1,\mathrm{min}}^{\mathcal{B}}$) but by diffusive transport of the excitations within the cluster. Thus the transversal relaxation time $T_{2,\mathrm{pair}}$ is given by

$$\frac{1}{T_2^{\mathrm{pair}}} \approx \frac{\Delta_*}{\hbar} \propto \frac{k_\mathrm{B}T(P_0U_0)^2}{\hbar} = bT \qquad \text{with} \qquad b \approx 10^6\,\frac{1}{\mathrm{sK}}. \tag{3.77}$$

Comparing this linear temperature dependence of the relaxation rate with the quadratic of spectral diffusion theory (equation 3.69), it can be seen that at very low temperatures the de-phasing of the $\mathcal{A}$-systems is governed by delocalized excitations.

In addition, the clusters affect the longitudinal relaxation time. As already introduced, the transitions within a cluster change the elastic and possibly electric fields at the positions of the $\mathcal{A}$-systems. Besides the influence onto the de-phasing these rearrangements can also stimulate transitions within the $\mathcal{A}$-systems. For thermal tunneling systems it holds

$$\frac{1}{T_{1,\mathrm{th}}^{\mathrm{pair}}} \approx \frac{10k_\mathrm{B}T}{\hbar}(P_0U_0)^3. \tag{3.78}$$

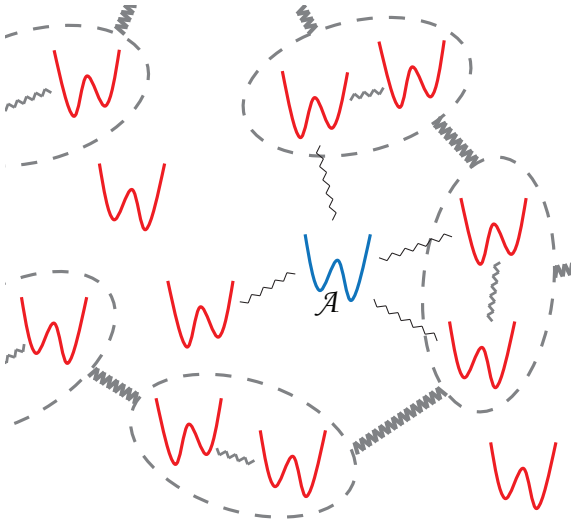

Figure 3.20: Simplified representation of the influence of delocalized excitations onto an $\mathcal{A}$-system. The ellipses illustrate resonant pairs and the springs the coupling between the tunneling systems and resonant pairs. Illustration based on [Esq98].

This linear temperature dependence of the relaxation rate dominates at very low temperatures the cubic dependence of the one-phonon process for symmetric thermal tunneling systems (equation 3.58).

The influence of a cluster of resonant pairs onto an $\mathcal{A}$-system, excited during an echo sequence, is schematically shown in figure 3.20.

In measurements of the polarization echo amplitude on the multicomponent glass N-BK7 up to very large pulse separation times a transition in the temperature dependence of T_2^{-1} was observed at about 28 mK from $T_2^{-1} \propto T^2$, as expected according to spectral diffusion theory, to a reduced exponent. This observation can be attributed to delocalized excitations. By considering those excitations and the above introduced distribution of the deformation potential the course of the echo decay can be described [Bur13, Fic13]. However, measurements down to even lower temperatures ($T < 7.5\,\mathrm{mK}$) are needed to clarify the influence of delocalized excitations. In addition, the possibility that another relaxation mechanism, probably based on nuclear quadrupole moments, could cause this behavior is shortly addressed in [Fic13].

4. Tunneling systems with nuclear quadrupole moments

The influence of nuclear moments on the properties of dielectric glasses at low temperatures is the main topic of this thesis. The necessary theoretical background to follow the discussion of the measured data is conveyed in this chapter. First a brief outline of the discoveries showing the crucial influence of nuclear quadrupole moments on the properties of dielectric glasses at low temperatures is given. It follows an introduction into nuclear quadrupole resonance and the relevant energy and frequency scales. In the subsequent section, the influence of nuclear moments on the two-pulse echo amplitude is depicted. Finally, possible relaxation mechanisms of and between nuclear moments and tunneling systems are discussed.

4.1 Magnetic properties of non-magnetic glasses

In 1998, [Str98] reported a magnetic field dependence of the dielectric function of the multicomponent glass Albasi (BaO-Al_2O_3-SiO_2) at temperatures between 5.84 mK and 0.72 mK and small magnetic fields up to 10 µT, as shown in figure 4.1. This observation was unexpected since the standard tunneling model predicts no magnetic field dependency and measurements on the quartz glass Suprasil and other glasses up to 6 T [Rei86], 9 T [Wie87] and 20 T [Pen95] supported this postulate down to temperatures of 4 mK [Wie87] and 16 mK [Pen95]. Later measurements, published in [Str00], showed that the observed magnetic field dependence in Albasi is not limited to small magnetic fields and very low temperatures. They actually measured a

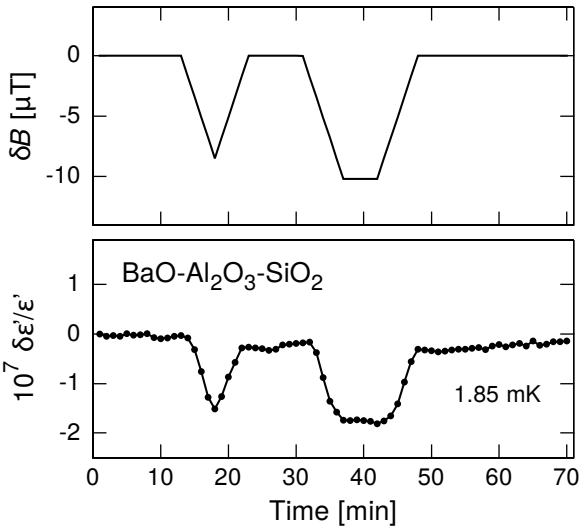

Figure 4.1: Influence of a magnetic field on the dielectric function of the multicomponent glass BaO-Al_2O_3-SiO_2. **Top:** Variation of the magnetic field with time. **Bottom:** Relative change of the dielectric constant at a temperature of 1.85 mK. Plot taken from [Str98].

change of the dielectric constant up to magnetic field strengths of about 100 mT and temperatures of circa 80 mK.
After the influence of magnetic fields on the dielectric properties of non-magnetic glasses was observed for the first time, it was quickly discovered in other glasses and experiments. In [Woh01b] the magnetic field dependence of the dielectric function of the multicomponent glass N-BK7 was reported and [Lud02] showed the influence of magnetic fields on the polarization echo amplitude of Albasi. Subsequent measurements on the multicomponent glasses N-BK7 and Duran exhibited qualitative similarities [Lud03], as shown in figure 4.2[1]. At small magnetic fields the echo amplitudes oscillate, while at larger field strengths the amplitudes increase and tend to level off. In contrast, Suprasil I shows no significant magnetic field dependence in accordance with the measurements at high magnetic fields mentioned at the beginning of this section. The observation of the magnetic field dependency of the echo amplitude also showed that the magnetic field effect involves the tunneling systems, since in echo experiments only tunneling systems contribute to the signal [Ens02b].

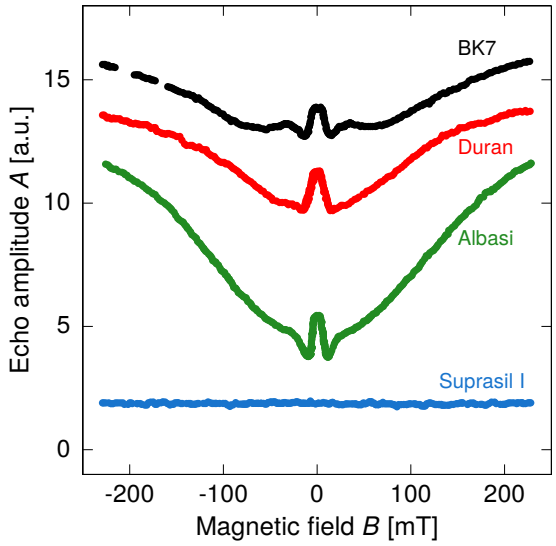

Figure 4.2: Influence of a magnetic field on the two-pulse echo amplitude of the multicomponent glasses BK7, Duran and Albasi as well as the one of the quartz glass Suprasil I. Data first published in [Lud03]. For the shown plot the data was digitized from [Baz08].

In the course of those observations various theories were developed to explain the magnetic field dependence of the dielectric function and the echo amplitude. Short summaries of these theories can for example be found in [Woh01b, Lud03]. Finally, investigations showed that nuclear quadrupole moments are the cause of the observed magnetic field effects in dielectric glasses. In the following, the underlying theory, based on [Wür02], together with the crucial supporting experiments, is shortly summarized. An extensive introduction is given in section 4.3.2.

A tunneling system usually consists of several atoms which can carry a nuclear magnetic dipole and an electric quadrupole moment. For simplicity only one atom is

[1] According to A. Fleischmann, the data shown in [Lud03] may have been shifted and scaled for a better illustration of the magnetic field effect. For later discussion the unshifted data is required, which is available in [Baz08].

considered in the following. The nuclear quadrupole moment couples to the electric field gradient caused by the binding of the corresponding atom in the solid and nearby charges. This coupling induces a splitting of the atom's nuclear spin states. Consequently, a tunneling system containing an atom with a nuclear quadrupole moment experiences a fine splitting of its two energy levels into two multiplets corresponding to the splitting of the nuclear quadrupole. In an amorphous solid the electric field gradients in the two wells of a tunneling system usually differ in size and orientation. Thus the quantization axis of the nuclear moment depends on the state of the tunneling system. Therefore the nuclear spin Hamiltonian does not commute with the tunneling system Hamiltonian, leading to a mixing of the nuclear states during the tunneling motion. If an external magnetic field is applied, the Zeeman interaction between the magnetic field and the nuclear magnetic moment lifts possible degeneracies and shifts the energy levels. The fine splitting of the tunneling system's energy levels and the subsequent mixing between the nuclear levels during an echo sequence changes the phase accumulation and leads to the oscillatory behavior of the echo amplitude at small magnetic fields, as shown in figure 4.2. At larger fields the nuclear magnetic moment aligns along the applied magnetic field, preventing the mixing of the nuclear levels. Thus, the behavior of a common two-level tunneling system is recovered and the echo amplitude saturates. The theory is confirmed by the fact, that only the three multicomponent glasses N-BK7, Duran and Albasi, which show an influence of the magnetic field, contain atoms which carry nuclear quadrupole moments. Whereas Suprasil I is free from atoms carrying nuclear quadrupole moments.

The experiments showing the crucial role of the nuclear quadrupole moments were published in [Bra04b] and [Nag04]. In the latter the magnetic field dependence of the echo amplitude was measured for ordinary glycerol-d0, which contains no quadrupole moments, and fully deuterated glycerol-d8, in which all hydrogen atoms are replaced

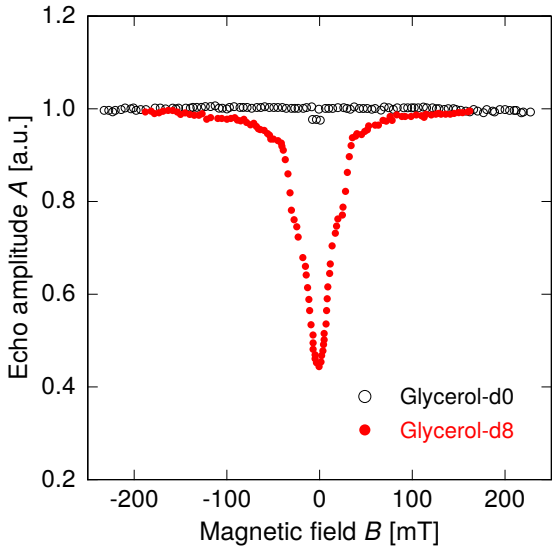

Figure 4.3: Magnetic field dependence of the two-pulse echo amplitude of Glycerol-d0 and Glycerol-d8. The curves were measured at a temperature of 13.4 mK, a pulse separation time of 3.5 µs and a frequency of the electric field of 1 GHz. Data taken from [Nag04].

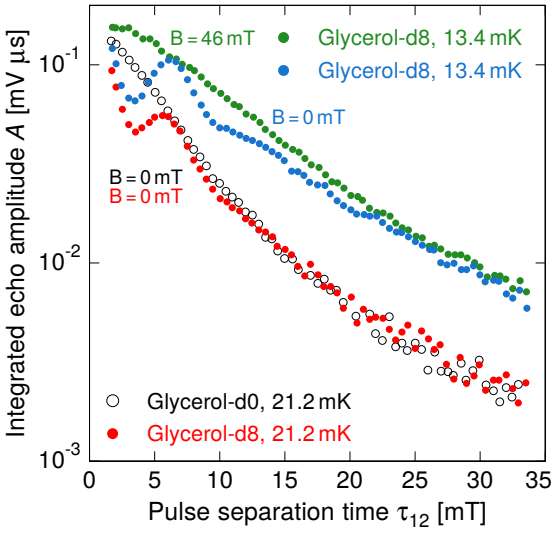

Figure 4.4: Integrated echo amplitude of deuterated and ordinary glycerol in dependence of the pulse separation time. The measurements were performed at different temperatures and magnetic fields. Data taken from [Nag04].

by the quadrupole carrying isotope deuterium. The observed curves are depicted in figure 4.3. As predicted by the model, the sample containing nuclear quadrupole moments shows a strong magnetic field dependence whereas the ordinary glycerol seems to be largely unaffected. Furthermore, the saturation of the glycerol-d8 curve at high magnetic fields, as predicted by the theory, can be seen. This isotope effect can be seen as proof for the nuclear quadrupole model, since only a single type of atom is replaced by another while the whole experiment as well as the structure of the sample remains the same. The small dip around 0 mT in the measurement of glycerol-d0 is caused by the interaction of magnetic dipole moments of the hydrogen nuclei, which will be shortly addressed in section 4.4.1. In addition to the magnetic field effect, a quantum beating is visible in the decay of the echo amplitude of glycerol-d8, which is not visible in the decay of glycerol-d0. This beating can be suppressed by applying a sufficiently strong magnetic field (compare figure 4.4). An explanation for this behavior is also possible considering the nuclear properties of the tunneling systems (compare section 4.3.3).

Above outline showed that the influence of nuclear quadrupole moments needs to be considered for a correct description of dielectric measurements of glasses at low temperatures. A closer examination of the influence of nuclear quadrupole moments on dielectric polarization echoes is given in section 4.3. The prerequisites, nuclear quadrupole resonance and the associated energy scales, are conveyed in the next section.

4.2 Nuclear quadrupole resonance

The following chapter is mainly based on the reviews [Smi71, Sui06]. Nuclei with a spin $I > 1/2$ have not only a magnetic dipole moment but also an electrical quadru-

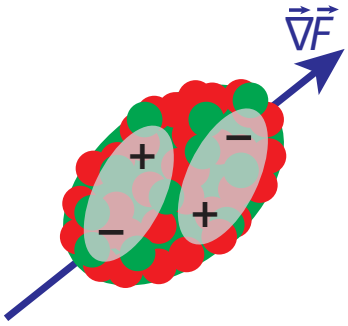

Figure 4.5: Schematic representation of a prolate nucleus with quadrupole moment aligned along the electric field gradient $\vec{\nabla}\vec{F}$. The two opposed dipoles precess around the direction of maximal field gradient.

pole moment. This means that the corresponding nucleus has not a spherical charge distribution. The deviation from spherical symmetry and thus the quadrupole moment Q are calculated via

$$eQ = \int \rho_n \left(3z_n^2 - r_n^2\right) \mathrm{d}r^3. \tag{4.1}$$

Here ρ_n represents the nuclear charge density in the volume $\mathrm{d}r^3$, e the elementary charge, z_n the axis along the direction of axial symmetry, usually given by the orientation of the nuclear spin, and r_n depicts the radius of the nucleus. For nuclei with I $\leq 1/2$ holds $z_n = r_n$. Consequently, it is spherical symmetric and has no quadrupolar moment. For those not being spherical symmetric the shape can either be prolate or oblate, corresponding to a positive or negative quadrupole moment, respectively. Usually, Q is given in barn: $1\,\mathrm{barn} \mathrel{\hat{=}} 10^{-24}\,\mathrm{cm}^2$.
In a classical picture, the charge distribution of a nucleus with a quadrupole moment can be imagined by two antiparallel dipoles (compare figure 4.5). If a nuclei with a nuclear quadrupole moment is at a position in a solid, at which all fields cancel out each other (for example in a cubic ionic crystal) or at which a homogeneous electric field is present, no impact is observable. In the first case there is no resulting field visible for the nucleus and in the latter case the torque of the individual 'dipoles' will be the same but with opposite direction and thus there is no net effect. However, in an electric field gradient the torque experienced by the two 'dipoles' differs and results in a torque. The emerging torque depends on the strength of the electric field gradient, the quadrupole moment as well as the orientation of those quantities with respect to each other. This leads to a precession of the nucleus around the maximum electric field gradient.
The anisotropy of the nuclear spin with respect to the electric field gradient results in a splitting of the nuclear ground state called quadrupole splitting or resonance.

The electric field gradient $\vec{\nabla}\vec{F}$ at the position of the nucleus, determined by the surrounding charge distribution, is calculated by the second derivative of the local electrostatic potential V,

$$\vec{\nabla}\vec{F} = -\frac{\partial^2 V}{\partial r_j \partial r_k}\bigg|_{\text{nucleus}} =: V_{jk} \tag{4.2}$$

with $\{r_i\} = \{x, y, z\}$. By using an appropriate set of coordinate axes, known as principal axes, the electric field gradient can be expressed as $\vec{\nabla}\vec{F} = V_{\mathrm{xx}} + V_{\mathrm{yy}} + V_{\mathrm{zz}}$.

If further $|V_{zz}| \geq |V_{xx}| \geq |V_{yy}|$ is chosen and the charge distribution within the nucleus is neglected, such that the Laplace equation $\Delta V = 0$ holds, it is possible to define the following parameters:

$$eq := V_{zz} \tag{4.3}$$

$$\eta := \frac{V_{xx} - V_{yy}}{V_{zz}}. \tag{4.4}$$

eq is the electric field gradient and defines for symmetric potentials the orientation of the quantization axis of the nuclear spin. The asymmetry parameter η is a positive number, $0 \leq \eta \leq 1$, and a measure of the electrical field gradient's deviation from cylindrical symmetry.

The interaction of the nuclear quadrupole moment with the electric field gradient can in the principal axes coordination system of the field gradient be expressed by the Hamiltonian [Abr61]

$$\hat{H}_Q = \frac{e^2qQ}{4I(2I-1)} \left[3\hat{I}_z^2 - I(I+1) + \frac{1}{2}\eta(\hat{I}_+^2 + \hat{I}_-^2) \right]. \tag{4.5}$$

The variable I is the nuclear spin quantum number, $\hat{I}_z$ the corresponding operator of the z-component of the nuclear spin and $\hat{I}_\pm = \hat{I}_x \pm i\hat{I}_y$, with $\hat{I}_x$, $\hat{I}_y$ being the spin operator components in x- and y-direction.
The so-called quadrupole coupling constant

$$C_Q = \frac{e^2qQ}{h}, \tag{4.6}$$

where h is Planck's constant, as well as the asymmetry factor η contain information about the environment surrounding the considered nucleus or nuclei. This is why nuclear quadrupole spectroscopy is used in material science to study the structure of matter. For further reading concerning glass structures [Vog92, Sch91] are recommended.

In the case of a complete axial symmetric electric field gradient ($\eta = 0$) the quadrupole Hamiltonian can be diagonalized using the eigenstates of $\hat{I}_z$ with the quantum numbers $m = -I,\ -I+1, ..., I-1,\ I$, leading to $2I+1$ energy levels. For the described circumstance m is a good quantum number and thus the magnetic dipole transition rules $\Delta m = 0, \pm 1$ are valid, leading to the transition frequencies

$$\nu_{m,m\pm1} = \nu_Q|(2m \pm 1)| \qquad \text{with} \qquad |m|,\ |m \pm 1| \leq I \tag{4.7}$$

with the frequency ν_Q

$$\nu_Q = \frac{3C_Q}{4I(2I-1)}. \tag{4.8}$$

For $\eta \neq 0$ there are analytic solutions for the energy levels and transition frequencies for $I = 1$ and $I = 3/2$. They are given by

$$I = 1: \quad \nu_0 = \frac{2}{3}\eta\nu_Q; \quad \nu_\pm = \nu_\mathrm{Q}(1 \pm \frac{\eta}{3}) \tag{4.9}$$

$$I = \frac{3}{2}: \quad \nu = 2\nu_\mathrm{Q}(1 + \frac{\eta^2}{3})^{\frac{1}{2}}. \tag{4.10}$$

For other nuclear spins the energy levels and transition frequencies usually have to be calculated numerically. In addition, more transitions than only $\Delta m = 0, \pm 1$ are allowed, but many have a small likelihood. Possible transitions for $I = 5/2,\ 7/2,\ 9/2$ are shown in [Sui06].

In table A.1 the quadrupole moments, coupling constants C_Q and splittings ν_Q are given for the isotopes relevant for this thesis. The corresponding studied material is always mentioned, since the quadrupole interaction strongly depends on the environment of the respective nucleus. For example, a small change in the binding situation or coordination number can already lead to a significant different coupling constant and thus frequency. Especially in inorganic glasses the disordered structure and the resulting varying bond lengths and field strengths lead to a comparably broad distribution of quadrupole frequencies compared to the same materials in a crystalline state. In addition, there are several isotopes where it is unclear how they are exactly implemented into the glass matrix (compare for example intermediate oxides in section 2.2.1). Thus if the quadrupole data is not measured in the same material as used in this thesis it is in general challenging to draw conclusions about the quadrupole coupling for those samples. Nevertheless, the listed values convey an overview of the magnitude of the quadrupole interactions. In contrast to inorganic glasses, organic glasses benefit from the strong intramolecular forces compared to the intermolecular ones. In those samples the binding situation within the molecule usually determines the quadrupole splitting.

4.2.1 Magnetic field effects

In the previous section it was shown that the splitting of the nuclear ground state of atoms carrying quadrupole moments exists intrinsically in materials with electrical field gradients. Thus, in contrast to nuclear magnetic resonance (NMR), no external magnetic field needs to be applied to study transition frequencies or relaxation times. Therefore, these measurements are also called pure or zero-field nuclear quadrupole resonance (NQR).
If an additional magnetic field is applied, it couples to the magnetic dipole moment of the nucleus. The resulting Zeeman interaction lifts degeneracies and shifts the nuclear energy levels as shown in figure 4.6. The associated Hamiltonian is given by [Abr61]

$$\hat{H}_\mathrm{Zee} = -\gamma_\mathrm{gy}\hbar\vec{B}\hat{\vec{I}}, \tag{4.11}$$

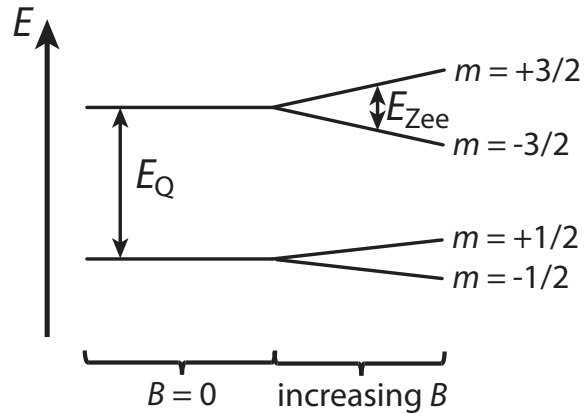

Figure 4.6: Illustration of the influence of a magnetic field on the level splitting of a nucleus with spin $I = 3/2$ and $\eta = 0$.

with the gyromagnetic ratio γ_{gy}, the magnetic field vector $\vec{B}$ and the nuclear spin operator $\hat{\vec{I}}$. The gyromagnetic ratios of the isotopes relevant for this thesis are given in table A.1.
Depending on the magnetic field strength two different effects are possible. The Zeeman interaction can be a small correction to the quadrupole splitting or, if the magnetic field is large enough, the quadrupole interaction can be a correction to the Zeeman splitting.

In addition to external magnetic fields the nuclei within a solid experience internal magnetic fields, caused by nearby magnetic moments of other atoms or the own electron shell. Those effects are especially strong for paramagnetic atoms and can dominate the quadrupole interaction.

4.3 Two-pulse echo under the influence of nuclear moments

In this section the influence of nuclear quadrupole moments and magnetic dipole moments on the dielectric two-pulse polarization echo is discussed. First, the general theory is introduced and the corresponding Hamiltonians are formulated before they are applied to the two-pulse echo. Finally, another effect based on the nuclear properties of the tunneling atoms, the so-called dipole effect, is shortly addressed.

4.3.1 Coupling of nuclear quadrupole moments and tunneling systems

The theory describing the coupling of nuclear quadrupole moments and tunneling systems was introduced by [Wür02]. In the following, this coupling mechanism is discussed with the simplification that only one of the atoms building the tunneling particle of a tunneling system carries a nuclear quadrupole moment. The obtained results are later generalized to a multitude of nuclear moments per tunneling particle. A detailed explanation of the coupling process and the consequences for the dielectric polarization echo is given in [Wür04, Par04].

Phenomenological explanation

Before the quantum mechanical calculation is shown a short phenomenological explanation of the coupling of tunneling systems and nuclear quadrupole moments is given based on [Wür02, Wür04, Nag04, Baz08, Bar13].
As shown schematically in figure 4.7, the effective electric field gradients $\vec{\nabla}\vec{F}^{\text{eff}}_{\text{l,r}}$ in the two wells of a double well potential, which are caused amongst others by the binding of the tunneling particle, usually differ in strength and orientation. If the tunneling particle contains a nuclear quadrupole moment, the coupling of the respective nucleus to the effective electric field gradient causes a splitting of the two-level system into a multi-level system according to the nuclear states (compare figure 4.8). Depending on the asymmetry energy of the tunneling system, as well as the type of tunneling motion (rotation, translation), this fine splitting of the tunneling system's energy levels causes different effects.
Considering the tunneling system with the finite asymmetry energy $\Delta \neq 0$ shown in figure 4.7, the tunneling particle has a higher probability to be in the right well in its ground state and in the left well in its excited state. Thus, the unperturbed tunneling particle with a nuclear quadrupole moment will at low enough temperatures be located mainly in the right well. The quantization axis of its nuclear spin is therefore given by an effective field gradient caused by a superposition of the field gradients in the right and left well. Since the tunneling particle's probability density is in the example of figure 4.7 higher in the right well, the effective electric field gradient will mainly be determined by the electric field gradient present in this well (e.g. $\vec{\nabla}\vec{F}_{\text{r}}$). If the tunneling system is excited, for example by the electric field pulse of an echo sequence, a mixing of its ground and excited energy level occurs. Assuming that the tunneling motion contains a rotary component and that the tunneling particle

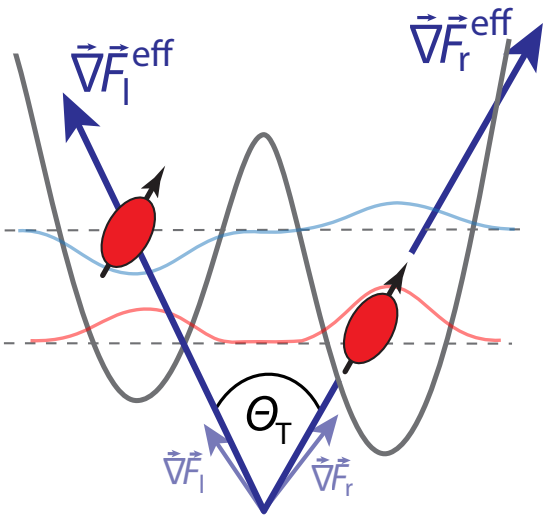

Figure 4.7: Illustration of a tunneling particle carrying a nuclear quadrupole moment in a double well potential. The rotating component of the tunneling motion is indicated by the angle Θ_{T}. The small black arrow indicates the quantization axis of the nuclear moment. The small arrows labeled $\vec{\nabla}\vec{F}_{\text{(r,l)}}$ represent the direction of the field strengths in the respective well. The field gradients $\vec{\nabla}\vec{F}^{\text{eff}}_{\text{(r,l)}}$ are the effective field gradients experienced by the nuclear moment. They are a superposition of $\vec{\nabla}\vec{F}_{\text{(r)}}$ and $\vec{\nabla}\vec{F}_{\text{(l)}}$ weighted by the probability density of the tunneling particle in the respective well.

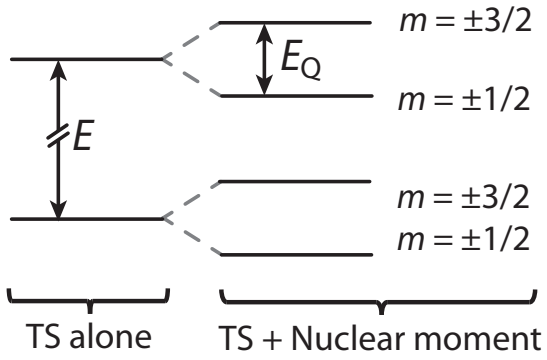

Figure 4.8: Schematic drawing of the level splitting caused by the interaction of a tunneling system (TS) with a nuclear spin of $I = 3/2$ and $\eta = 0$. The two-level system with energy splitting E is transformed into a multi-level system according to the nuclear quadrupole splitting $E_\mathrm{Q} = h\nu_{I=3/2}$.

is lifted to the excited state such that it is mainly located in the left well. Thus the direction of the effective field gradient with respect to the nuclear spin changes. The orientation of the nuclear spin is maintained, since its relaxation rate T_1^{-1} is at low temperature several orders of magnitude smaller than the tunneling frequency ω_ts of the tunneling systems considered in echo experiments ($\omega_\mathrm{ts} \approx \omega_\mathrm{ef} \propto 1\,\mathrm{GHz}$) [Sze75]. Given that the initial pure state is no longer conserved a mixing of different nuclear states happens. This mixing changes the time evolution of the tunneling system during an echo sequence and consequently the phase collection between the pulses leading to a quantum beating. For this mechanism it is important that the tunneling motion contains a rotary component (as shown in figure 4.7), since a pure translational motion would not change the orientation of the effective electric field gradient relative to the nuclear spin quantization axis.
If the tunneling system is symmetrical, $\Delta = 0$, the tunneling particle has the same probability of being in the right and left well in the ground as well as in the excited state. Thus, the nuclear spin of the tunneling particle experiences both electric field gradients equally often and its quantization axis is given by their superposition. Consequently, an excitation of the tunneling system does not lead to a change of the effective field gradient experienced by the nuclear spin. Therefore the initial pure state is conserved and no mixing of the nuclear states occurs.

In short, the finite asymmetry and the rotary component of the tunneling motion lead to a change of the effective field gradient seen by the tunneling particle and thus to a mixing of nuclear levels in dependence of the state of the tunneling system.
This phenomenological explanation shows that the unexpected properties of dielectric glasses containing nuclear quadrupole moments in dielectric polarization echoes are caused by the asymmetric tunneling systems with a rotary component in their tunneling motion. In the following the effective field gradient in the two wells is just called electric field gradient.

Quantum mechanical motivation

A detailed quantum mechanical description of the quadrupole interaction can be found in [Par04, Wür04, Bra04a]. Based on those publications, this chapter motivates

the calculation and summarizes the results.

The coupled system, tunneling system and nuclear quadrupole moment, is described by a new Hamiltonian. This Hamiltonian has to take into account that with the tunneling motion not only the direction of the field gradient changes, but maybe also its strength in the two wells, leading to different quadrupole coupling constants C_Q. The resulting Hamiltonian is given by

$$\hat{H}_\mathrm{res} = \hat{H}_0 \otimes \hat{\mathbb{1}}_\mathrm{Q} + \begin{pmatrix} 1 & 0 \\ 0 & 0 \end{pmatrix} \otimes \hat{H}_\mathrm{Qr} + \begin{pmatrix} 0 & 0 \\ 0 & 1 \end{pmatrix} \otimes \hat{H}_\mathrm{Ql}. \tag{4.12}$$

Here $\hat{H}_0$ is the Hamiltonian of the tunneling system in the basis of the individual wells $(\psi_\mathrm{a}, \psi_\mathrm{b})$ from equation 3.11, $\hat{H}_\mathrm{Qr,l}$ the quadrupole Hamiltonian from equation 4.5 in the right and left well, $\hat{\mathbb{1}}_\mathrm{Q}$ the identity matrix in the space of the nuclear spin and $\otimes$ denotes the Kronecker product. If the tunneling motion contains no rotary component and just the strength of the electric field gradient varies, for example, because the nuclear quadrupole moment is changing its distance to the electric field gradient's source, only the factor C_Q of $\hat{H}_\mathrm{Q}$ changes. Since C_Q is a scalar prefactor of the Hamiltonians $\hat{H}_\mathrm{Qr,l}$ they are diagonalizable simultaneously and no mixing of nuclear states happens during this tunneling motion.
To get the energy eigenstates of the coupled system, the Hamiltonian $\hat{H}_\mathrm{res}$ has to be diagonalized. However, the informations needed for calculations with this Hamiltonian, e.g. the electric field gradient strength and thus the quadrupole coupling constant in the individual wells, are usually not available since these quantities cannot be measured separately. In general, from nuclear quadrupole resonance only an average value of the whole ensemble of nuclear spins is obtained. Thus, for the further evaluation of the Hamiltonian some assumptions need to be made and the distribution of the quadrupole parameters can later be added e.g. by a certain width of the quadrupole resonance.

In the simplified picture it is assumed that the electric field gradients in the two wells have the same strength and only differ in their orientation. The angle, enclosed by the two principal axes of the field gradients is denoted $\Theta_\mathrm{T} = 2\Theta$ (compare fig 4.7 and 4.9).
For the further calculation the reference frame of the nuclear moments is changed from the one defined by the respective principal axes of the electric field gradient (x, y, z systems) to a common one with the z-component of the spin vector along the halving axis of the electric field gradient vectors ($\tilde{x}, \tilde{y}, \tilde{z}$ system). This corresponds to a frame of reference which is rotated by an angle $\pm\Theta$ with respect to the principal axes of the electric field gradients, as illustrated in figure 4.9. Thus in the right well the projection of $\hat{I}_\mathrm{z}$ on the new coordinate system $(\tilde{x}, \tilde{y}, \tilde{z})$ is given by (compare also [Abr61])

$$\hat{I}_\mathrm{z}(\Theta) = \hat{I}_\tilde{\mathrm{z}} \cos(\Theta) + \hat{I}_\tilde{\mathrm{x}} \sin(\Theta). \tag{4.13}$$

For the left well Θ has to be substituted by $-\Theta$. If further $\eta = 0$ is assumed, equation

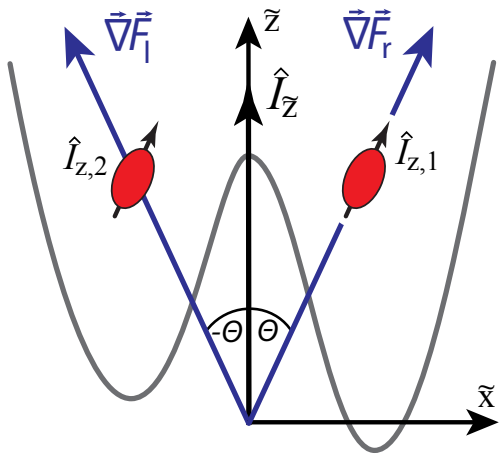

Figure 4.9: Illustration of a tunneling particle carrying a nuclear quadrupole moment in a double well potential. The electric field gradients differ only in orientation. The black arrows represent the orientation of the z-component of $\hat{I}_{z,\tilde{z}}$. Illustration based on [Bra04a, Baz08].

4.12 simplifies to

$$\hat{H}_{\mathrm{res}} = \underbrace{\hat{H}_0 \otimes \hat{\mathbb{1}}_{\mathrm{Q}}}_{\text{Tunneling system alone}} + \underbrace{\begin{pmatrix} 1 & 0 \\ 0 & 0 \end{pmatrix} \otimes \hat{H'}_{\mathrm{Q}}(\Theta)}_{\text{Quadrupole interaction right well}} + \underbrace{\begin{pmatrix} 0 & 0 \\ 0 & 1 \end{pmatrix} \otimes \hat{H'}_{\mathrm{Q}}(-\Theta)}_{\text{Quadrupole interaction left well}} \tag{4.14}$$

with the quadrupole Hamiltonian

$$\hat{H'}_{\mathrm{Q}}(\Theta) = \frac{e^2 qQ}{4I(2I-1)} \left[3 \left(\hat{I}_{\tilde{z}} \cos(\Theta) + \hat{I}_{\tilde{x}} \sin(\Theta) \right)^2 - I(I+1) \right]. \tag{4.15}$$

The only parameter that need to be determined for this Hamiltonian are the quadrupole coupling constant C_{Q} and the tunneling angle Θ. The first parameter is measured by nuclear quadrupole resonance (compare table A.1). The second one is usually a free parameter when describing measured data with this model (compare section 4.4) and may allow insights into the nature of the tunneling systems [Bra04a, Baz08, Bar13]. A calculation of the energy states in dependence of Θ for a system with $I = 1$ and $\eta = 0$ via perturbation theory can be found in [Bra04a, Baz08].

Tunneling systems with several nuclear quadrupole moments

The case of a tunneling system with more than one quadrupole moment is shortly addressed in [Wür04, Par04] and more elaborate in [Bra04a]. The following overview is given based on those references. If the tunneling particle consists of several atoms which carry a nuclear moment the Hamiltonian given in equation 4.15 is extended by the additional nuclear moments. In case the tunneling particle contains S nuclear

quadrupole moments $Q1$ to QS, it holds

$$\begin{aligned}\hat{H}_{\mathrm{res}} = & \underbrace{\hat{H}_0 \otimes \hat{\mathbb{1}}_{Q1} \otimes \hat{\mathbb{1}}_{Q2} \otimes ...}_{\text{Tunneling system alone}} \\ & + \underbrace{\begin{pmatrix}1 & 0\\ 0 & 0\end{pmatrix} \otimes \hat{H}_{Q1}(\Theta_1) \otimes \hat{\mathbb{1}}_{Q2} \otimes .... + \begin{pmatrix}0 & 0\\ 0 & 1\end{pmatrix} \otimes \hat{H}_{Q1}(-\Theta_1) \otimes \hat{\mathbb{1}}_{Q2} \otimes ...}_{\text{Quadrupole moment } Q1} \\ & + \underbrace{\begin{pmatrix}1 & 0\\ 0 & 0\end{pmatrix} \otimes \hat{\mathbb{1}}_{Q1} \otimes \hat{H}_{Q2}(\Theta_2) \otimes ... + \begin{pmatrix}0 & 0\\ 0 & 1\end{pmatrix} \otimes \hat{\mathbb{1}}_{Q1} \otimes \hat{H}_{Q2}(-\Theta_2) \otimes ...}_{\text{Quadrupole moment } Q2} \\ & + \underbrace{...}_{\text{Quadrupole moment } Q3 \text{ to } QS} \\ & + \underbrace{\sum_{i,j} \begin{pmatrix}1 & 0\\ 0 & 1\end{pmatrix} \otimes \hat{I}_{Qi,Qj}.}_{\text{Interactions between nuclear spins}}\end{aligned} \tag{4.16}$$

In this general Hamiltonian it is assumed, analogous to before, that the electric field gradient at the two positions of the respective atoms, carrying nuclear quadrupole moments, only differ in orientation and enclose an angle $\Theta_{\mathrm{T}} = 2\Theta$. Depending on how exactly the tunneling motion looks like, it is possible that every nuclear quadrupole moment experiences a different tunneling angle $\Theta_{1,2,..}$. At present this information cannot be obtained such that a common resulting tunneling angle is assumed. The operator $\hat{I}_{\mathrm{Qi,Qj}}$ describes a possible interaction between the nuclear moments. Usually this operator is neglected [Wür04, Bra04a]. However, with a high concentration of nuclear quadrupole carrying atoms in a glass this assumption may no longer be valid. In such a case the formulation of the operators $\hat{I}_{\mathrm{Qi,Qj}}$ and of the whole Hamiltonian $\hat{H}_{\mathrm{res}}$ is challenging since usually the nature of the tunneling systems as well as the exact structural properties of the amorphous solid,

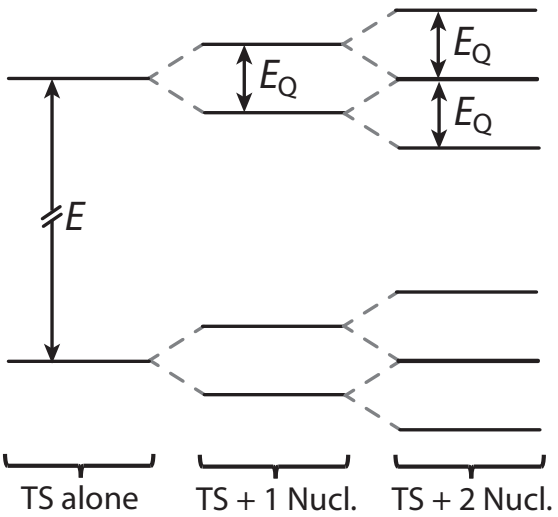

Figure 4.10: Schematic drawing of the level schema of a tunneling system (TS) alone, of a tunneling system coupled to one nuclear moment of $I = 1$, $\eta = 0$ and of one coupled to two nuclear moments of the same kind. For $I = 1$ and $\eta = 0$ the levels $m = \pm 1$ are degenerate. Illustration created according to [Bra04a].

in particular of multicomponent glasses, are unknown. In general, organic materials with well known constituents are more eligible for a theoretical description (compare for example [Bra04a, Baz07, Baz08, Bar13]).
The energy states of the coupled system, which are needed to calculate the echo amplitude in section 4.3.3, are again obtained by a diagonalization of $\hat{H}_{\mathrm{res}}$.
The level schema for a tunneling system exhibiting two nuclear moments of $I = 1$ and $\eta = 0$ with identical tunneling angles Θ and neglected interaction between the spins is shown in figure 4.10. For tunneling systems with different nuclear spins, asymmetry factors and interactions this schema becomes very complicated.

4.3.2 Coupling of nuclear quadrupole moments and tunneling systems with additional magnetic field

If an additional static magnetic field is applied, it couples to the magnetic dipole moment of the tunneling particle leading to an additional Zeeman splitting of the nuclear states, see section 4.2.1.
In the following the influence of a magnetic field on the resulting Hamiltonian is outlined, mainly based on [Bra04a, Wür04, Par04]. The tunneling systems in an amorphous solid are randomly oriented. Thus the magnetic field is pointing in arbitrary directions with respect to the nuclear spin quantization axis, as illustrated in figure 4.11. In the $(\tilde{x}, \tilde{y}, \tilde{z})$ frame of reference the Zeeman Hamiltonian from equation 4.11 can be rewritten to [Bra04a]

$$\hat{H}_{\mathrm{Zee}} = -\gamma_{\mathrm{gy}} \hbar B \left[\hat{I}_{\tilde{\mathrm{z}}} \cos(\delta) + \hat{I}_{\tilde{\mathrm{x}}} \sin(\delta) \cos(\varphi) + \hat{I}_{\tilde{\mathrm{y}}} \sin(\delta) \sin(\varphi) \right]. \tag{4.17}$$

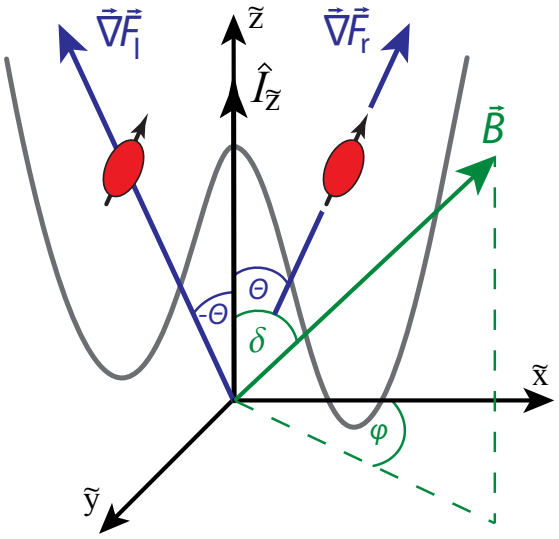

Figure 4.11: Illustration of a tunneling particle carrying a nuclear quadrupole moment in a double well potential. The orientation ofthe electric field gradients and the magnetic field are in the reference frame $(\tilde{x}, \tilde{y}, \tilde{z})$. Illustration based on [Bra04a, Baz08].

Based on equation 4.14, a tunneling system with an atom carrying a nuclear quadrupole moment in an external static magnetic field is described by

$$\hat{H}_{\mathrm{res}} = \underbrace{\hat{H}_0 \otimes \hat{\mathbb{1}}_{\mathrm{Q}} + \begin{pmatrix} 1 & 0 \\ 0 & 0 \end{pmatrix} \otimes \hat{H'}_{\mathrm{Q}}(\Theta) + \begin{pmatrix} 0 & 0 \\ 0 & 1 \end{pmatrix} \otimes \hat{H'}_{\mathrm{Q}}(-\Theta)}_{\text{Tunneling system with one nuclear quadrupole moment}} + \underbrace{\begin{pmatrix} 1 & 0 \\ 0 & 1 \end{pmatrix} \otimes \hat{H}_{\mathrm{Zee}}}_{\text{Add. mag. field}}. \tag{4.18}$$

To get the energy levels of this system, the Hamiltonian is diagonalized as mentioned previously.
The development from a pure two-level system to a multi-level system, caused by the interaction of the tunneling system with a nuclear spin of $I = 3/2$, to a multi-level system with additional Zeeman splittings is shown in figure 4.12.

Up to this point it was assumed, that the Zeeman interaction is small compared to the quadrupole splitting $E_{\mathrm{Zee}} \ll E_{\mathrm{Q}}$. In a sufficiently large magnetic field, the orientation of the nuclear spin quantization axis is predominantly given by the direction of the external magnetic field and the quadrupole interaction becomes a small perturbation. This has a significant influence on the echo amplitude and is discussed in the next section.

4.3.3 Two-pulse echo in a multi-level system

Previously it was shown that by adding one nuclear quadrupole moment to a tunneling systems its two energy levels transform into a multitude. Thereby every energy state of the two-level system splits up according to the nuclear spin states of the quadrupole carrying atom. The resulting level schema of the coupled system consists of two multiplets of $2I + 1$ states that are shifted with respect to each other by the energy splitting E of the tunneling system (compare figure 4.12). Due to the larger number of energy levels compared to an ordinary two-level system, more transitions and thus phase evolutions are possible during an echo sequence. Before the general expression for the polarization in a multi-level system is introduced, the possible effects caused by the additional energy levels are shortly motivated.

A helpful tool to illustrate the different phase evolutions of a tunneling system during

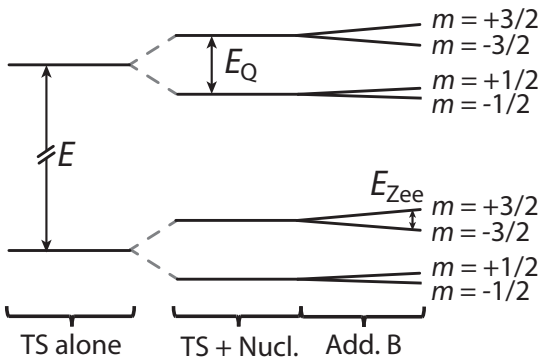

Figure 4.12: Illustration of the level schema of a tunneling system (TS) alone, the same tunneling system coupled to a nuclear spin with $I = 3/2$ and the effect of an additional magnetic field B.

an echo sequence are the path diagrams introduced in section 3.3.2. As an example, a tunneling system with one atom carrying a spin of $I = 1$ or $I = 3/2$ and $\eta = 0$ without an additional static magnetic field is selected. Thus each of the two levels of the tunneling system splits up into two levels with an energy splitting of $E_\mathrm{Q} = h\nu_{I=1,3/2}$, such that finally a four-level system is obtained. In dependence of the spin those levels are degenerate. In figure 4.13 four relevant path pairs of the possible phase evolutions of the tunneling system during an echo sequence are shown. As a reminder, every horizontal line in a path diagram represents a phase factor of $\mathrm{e}^{-iE_i t/\hbar}$ with the energy of the evolved path E_i and every vertical line illustrates a mixing of energy levels caused by the high frequency electric field pulses during the echo sequence. The area below a path can be interpreted as the collected phase during the free evolution. The resulting polarization of the considered tunneling system is given by the sum over all pairs of paths. In the multi-level system, there are additional possible transitions between different nuclear states due to the coupling between the nuclear state and the tunneling motion. In a two-level system only path pairs that collected the same phase during the time $t = 2\tau_{12}$, independent of the precession frequency ω_d, contribute to the polarization of the tunneling system. In figure 4.13 it can be seen that in a multi-level system also path pairs with finite phase differences exist (depicted in green), which are independent of the tunneling system's energy splitting E and thus ω_d. They only depend on the quadrupole splitting E_Q and the pulse separation time τ_{12}. In an echo measurement the path pairs with $\Delta\Phi = 0$ always contribute to the polarization of the tunneling system. The pairs with $\Delta\Phi \neq 0$

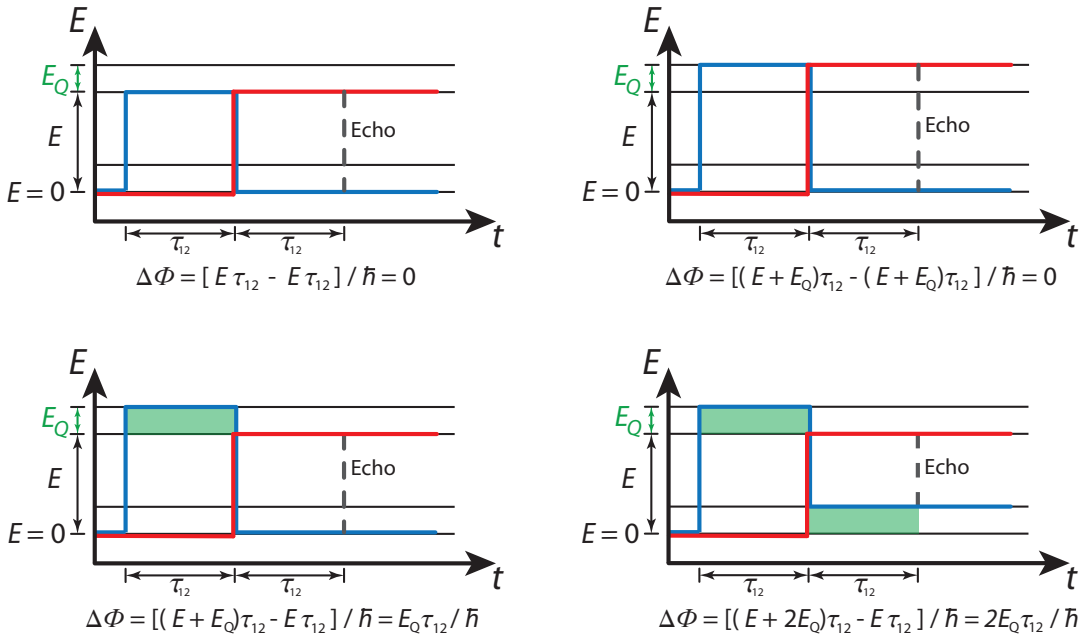

Figure 4.13: Illustration of four path pairs, relevant for the formation of the echo in a four-level system. The phase difference between the two paths $\Delta\Phi$ accumulated during the phase evolution is depicted in green. Illustration adapted from [Sch16a].

contribute only if their phase difference is a multiple of 2π. Consequently, the echo amplitude of such an ensemble of tunneling systems oscillates with the frequencies ${}^{E_Q}/_{\hbar} = \omega_Q$ and ${}^{2E_Q}/_{\hbar} = 2\omega_Q$ in dependence of the pulse separation time. This effect is called 'quantum beating' and the explanation for the observations in figure 4.4.

A general formula for the polarization of a multi-level tunneling system was developed in [Par04]. Analogous to this publication the derivation can be motivated by using a general multi-level system, as illustrated in figure 4.14, and the path diagram rules introduced in section 3.3.2. Applying those rules to the shown path pair gives the following contribution to the polarization of the tunneling system. The polarization operator $\hat{P}$ is thereby expanded by the nuclear spin.

$$\langle P\rangle_{\text{PathPair}}(t > \tau_{12}) = \langle \pi_{|j,1\rangle,|j,2\rangle} | \hat{P} | \pi_{|j,1\rangle,|k,1\rangle} \rangle \tag{4.19}$$

$$\propto \underbrace{\frac{1}{\sqrt{N}}(-iF_{0,(1)})\alpha_{ij}^{21} \cdot \mathrm{e}^{-i\frac{E_{i2}}{\hbar}\tau_{12}} \cdot (-iF_{0,(2)})\alpha_{ki}^{12} \cdot \mathrm{e}^{-i\frac{E_{k1}}{\hbar}(t-\tau_{12})}}_{\text{Red (solid line) path}}$$

$$\times \underbrace{\frac{1}{\sqrt{N}}\left[\mathrm{e}^{-i\frac{E_{j1}}{\hbar}\tau_{12}} \cdot (-iF_{0,(2)})\alpha_{jj}^{21} \cdot \mathrm{e}^{-i\frac{E_{j2}}{\hbar}(t-\tau_{12})}\right]^*}_{\text{Blue (dashed line) path}} \cdot \underbrace{\alpha_{kj}^{12}}_{\text{Echo}}$$

$$= \underbrace{-\frac{i}{N}F_{0,(1)}F_{0,(2)}^2\alpha_{ij}^{21}\alpha_{ki}^{12}\left(\alpha_{jj}^{21}\right)^*\alpha_{kj}^{12}}_{\propto \text{ Amplitude}}$$

$$\times \underbrace{\mathrm{e}^{i\frac{(E_{j2}-E_{k1})}{\hbar}(t-\tau_{12})-i\frac{(E_{i2}-E_{j1})}{\hbar}\tau_{12}}}_{\propto \text{ Phase}}$$

The factor ${}^1/\sqrt{N}$, with the number of sub-levels $N = 2I + 1$, corresponds to the case where the levels in the lower multiplet are equally populated and the higher multiplet is empty before the start of the echo sequence. Using that the two multiplets are shifted with respect to each other by E, the energies can be rewritten to $E_{j2} = E + E_{j1}$ and $E_{i2} = E + E_{i1}$ and equation 4.20 transforms to

$$\langle P\rangle_{\text{PathPair}}(t > \tau_{12}) \propto \underbrace{-\frac{i}{N}F_{0,(1)}F_{0,(2)}^2\alpha_{ij}^{21}\alpha_{ki}^{12}\alpha_{jj}^{*21}\alpha_{kj}^{12}}_{\propto \text{ Amplitude}} \tag{4.20}$$

$$\times \underbrace{\mathrm{e}^{i\frac{E}{\hbar}(t-2\tau_{12})+i\frac{(E_{j1}-E_{k1})}{\hbar}(t-\tau_{12})-i\frac{(E_{i1}-E_{j1})}{\hbar}\tau_{12}}}_{\propto \text{ Phase}}.$$

The phase factor consists of three terms. The first one depends on the energy splitting of the tunneling system and is always zero at $t = 2\tau_{12}$, similar to a common two-level system. Factor two and three depend on the quadrupole splitting of the sub-levels $(E_{j1} - E_{k1})$ and $(E_{i1} - E_{j1})$, but not on the tunneling system's energy splitting. These

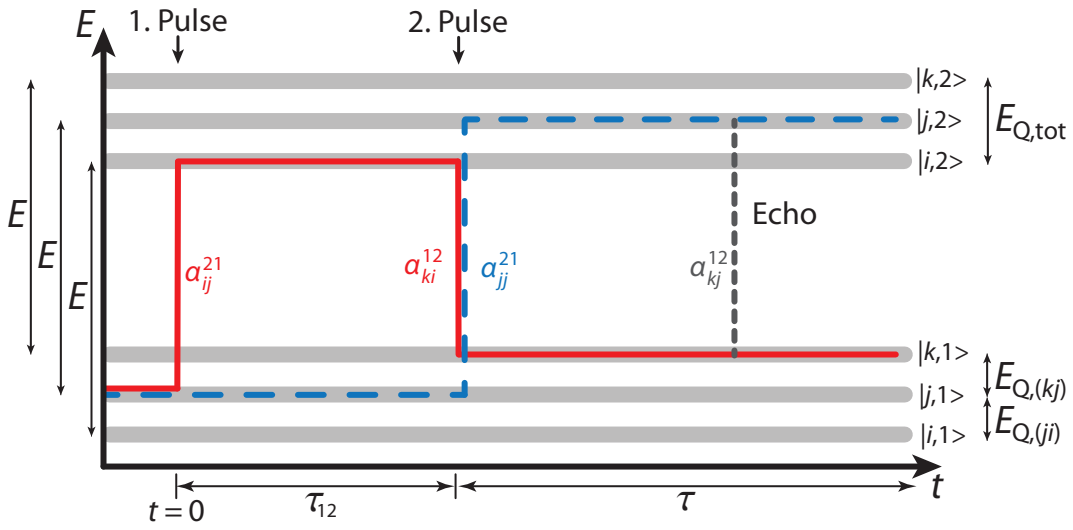

Figure 4.14: One of the path pairs with a nonzero phase difference, which contributes to the polarization of the tunneling system. Each energy level is specified by $|m,n\rangle$ with m representing the nuclear state and n the corresponding multiplet. The two multiplets are shifted by the energy splitting E of the tunneling system with respect to each other. Illustration created according to [Par04].

factors are responsible for the phase differences $\Delta\Phi \neq 0$ mentioned in the framework of figure 4.13. Summing over all possible path pairs gives the contribution of one tunneling system to the echo signal as

$$\langle P\rangle(2\tau_{12}) \propto -\frac{i}{N} F_{0,(1)} F_{0,(2)}^2 \sum_{i,k} \mathrm{e}^{i(E_i - E_k)\tau_{12}} \left| \sum_j \alpha_{ij}^{12} \alpha_{kj}^{*12} \mathrm{e}^{iE_j\tau_{12}} \right|^2 \tag{4.21}$$

[Par04]. Due to the nonzero phase factors at $t = 2\tau_{12}$, the polarization of the tunneling system oscillates as a function of the pulse separation time with a frequency given by the interference of the different oscillating phase factors. The indices i, j, k range from 1 to the number of sub-levels N. Analogous to the echo in a two-level system, the echo in a multi-level system also shows a F_0^3 behavior when it is measured in dependence of the electric field strength (assuming both pulses have the same field strength $F_{0,(1)} = F_{0,(2)} = F_0$). The $(\Delta_0/E)^4$ dependence of the echo amplitude, see equation 3.50 for the two-level system, follows from the $|\alpha\alpha|^2$ factor and can also be seen in equation 4.22 for the multi-level system.

The obtained equation 4.21 for the echo amplitude only applies if the following requirements are fulfilled [Par04]:

- To satisfy the condition of an equally populated lower multiplet (origin of the $1/N$ factor) the temperature of the sample must be smaller than the energy splitting E of the tunneling system ($T \ll E$) and larger than the energy splitting of the lower multiplet ($T \gg E_{\mathrm{Q,tot}}$). If $E_{\mathrm{Q,tot}} \ll E$, these conditions are

usually fulfilled during an echo measurement. If the condition $T \ll E$ is not met thermal occupation numbers need to be introduced.

- In the calculation it is assumed that the nuclear states of the two multiplets mix equally well during the application of a high frequency electric field pulse. This is usually the case when all transition factors for the different states are similar. If the spectral width ($\hbar/t_{\mathrm{pulse}}$) of the pulse is much broader than the quadrupole splitting of the multiplet this condition is fulfilled. If not, the transition amplitudes α have to be adjusted. To ensure that this condition is met, the pulses of the echo sequence must be sufficiently short $E_{\mathrm{Q,tot}} t_{\mathrm{pulse}}/\hbar \ll 1$ (compare also the end of section 3.3.2). This issue is illustrated in figure 4.15. The excitation pulse with frequency $\omega_{\mathrm{ef}} = E/\hbar$ and duration t_{pulse} has a spectral width smaller than the quadrupole splitting in the multiplet $E_{\mathrm{Q,tot}}/\hbar$. Thus no complete mixing of nuclear states occurs, illustrated by the fading of the blue path. In a measurement this circumstance would lead to no or a modified quantum beating of the echo amplitude and the calculated formula cannot be applied. This issue was observed in [Bra04a] in a measurement on meta-fluoroaniline.

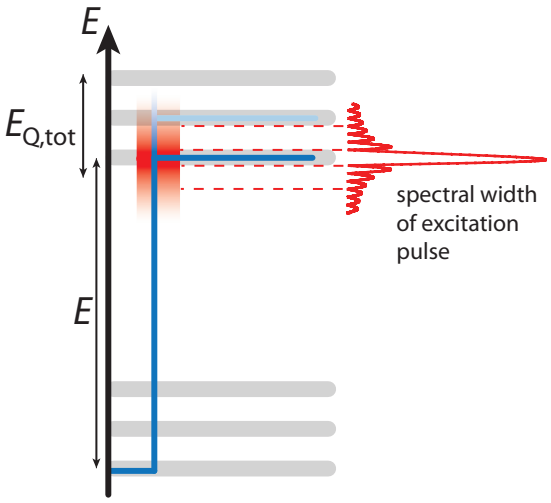

Figure 4.15: Illustration of possible paths according to the spectral width of the excitation pulse in a multi-level system. The excitation pulse with frequency $\omega_{\mathrm{ef}} = E/\hbar$ and duration t_{pulse} has a spectral width which is smaller than the quadrupole splitting $E_{\mathrm{Q,tot}}/\hbar$. This results in an incomplete mixing of the nuclear states.

To calculate the polarization of a single tunneling system, the corresponding Hamiltonian (e.g. equation 4.14) has to be diagonalized. This gives the energy eigenstates and eigenvalues of the multi-level system. Afterwards the transition matrix elements α are calculated by applying the Hamiltonian of the high frequency electric field pulse (equation 3.27) to the new eigenstates. For more details concerning the calculation of the transition matrix elements [Par04] (for a general consideration) and [Bra04a, Baz08] (for the case of $I = 1$) are recommended.

For a single multi-level system, created by the interaction of one nuclear quadrupole

moment with a tunneling system with defined Δ_0 and Δ, a polarization of

$$\langle P\rangle(2\tau_{12}) \propto \left(\frac{\Delta_0}{E}\right)^4 \underbrace{\left[1 - \frac{64}{N}\sum_{n,m>n} b_{nm}^2 \sin^4\left(\frac{E_{\mathrm{Q}(nm)}\tau_{12}}{2\hbar}\right)\right]}_{=:A_{\mathrm{mod}}(2\tau_{12})} \tag{4.22}$$

is expected [Par04]. $E_{\mathrm{Q}(nm)}$ is thereby the quadrupole splitting between level n and m and

$$b_{nm} \propto \alpha_{nm}^{(12)} \propto \frac{\Delta}{E}\frac{1}{E_{\mathrm{Q}(nm)}}. \tag{4.23}$$

The term A_{mod} describes the modulation of the tunneling system's polarization as a function of the pulse separation time τ_{12}. The modulation frequencies are determined by the splittings of the tunneling system's nuclear states $E_{\mathrm{Q}(nm)}$. The Δ^2 proportionality of equation 4.22, which arises from b_{nm}^2, shows that just multi-level systems with a finite asymmetry energy contribute to the quantum beating as mentioned at the beginning of section 4.3.1. The total polarization depends on $(\Delta_0/E)^4$ equivalent to an ordinary two-level system. Thus in an echo measurement, the more symmetric tunneling systems contribute more. Consequently, the observed modulation in a measurement is not caused by the tunneling systems with a very large asymmetry energy, but by those which have besides a finite asymmetry energy also a sizable tunnel splitting Δ_0. To get the echo amplitude of an ensemble of tunneling systems the individual amplitudes, given in equation 4.22, have to be integrated over all Δ_0 according to the distribution function given in section 3.2.3.

The previous considerations suggest that in an amorphous solid with nuclear quadrupole moments a beating of the echo amplitude is visible until the asymmetric tunneling systems are decayed. Asymmetric tunneling systems are strongly influenced by spectral diffusion (compare section 3.4) which is more effective as the one-phonon process at short pulse separation times (compare figure 3.17). Thus, an echo measurement on a sample containing nuclear quadrupole moments shows a modulation of the echo amplitude at small pulse separation times. With increasing pulse separation time, the amount of asymmetric tunneling systems decreases and the modulation of the echo amplitude becomes smaller. At large pulse separation times just the symmetric tunneling systems remain and no beating is visible. Since this simple picture is not completely correct its limits will be discussed in the following.
It was already pointed out that most samples containing atoms with nuclear quadrupole moments also exhibit tunneling systems without nuclear quadrupole moments. Therefore, an echo measurement on a glass containing nuclear quadrupole moments shows always a superposition of an ordinary echo decay and one which is modulated by quantum beating.
As an example, an amorphous solid which contains just one kind of atoms carrying a nuclear quadrupole moment and every tunneling system contains maximal one of these atoms is considered. In contrast to a crystalline material the electric field gradients experienced by the different nuclei in an amorphous solid vary due to the

disordered structure in a large range, leading to different coupling constants C_Q and consequently to a certain broadening of the quadrupole splitting in the whole sample. During an echo measurement in dependence of the pulse separation time the tunneling systems with nuclear quadrupole moment show a quantum beating according to their nuclear splitting. When measuring the polarization of the whole sample the individual beating frequencies interfere and a resulting quantum beating is observed. At small pulse separation times, the constructive interfering parts of the quantum beating dominate. With increasing pulse separation time the individual quantum beatings diverge more and more. Consequently, the macroscopic polarization of the sample shows no quantum beating at large pulse separation times. But the echo amplitude of the sample experiences a overall reduction due to the destructive interfering quantum beatings. How fast the tunneling systems diverge depends on the width of the quadrupole splitting. Often this is in the range of 10 % of the resonance frequency (compare for example [Rub74] for ^{75}As).
The two processes leading to the disappearance of the quantum beating, namely the decay of asymmetric tunneling systems and the broadening of the quadrupole splitting, cause two different behaviors of the echo amplitude. The decay of the asymmetric tunneling systems by relaxation processes (especially spectral diffusion) causes a reduction of the modulation depth of the quantum beating relative to the total echo amplitude. The broadening of the quadrupole splitting causes a smearing of the beating frequency, a reduction of the modulation depth as well as an overall reduction of the echo amplitude. These effects are illustrated in figure 4.16 and were observed and discussed in [Bra04a] and more elaborate in [Baz08]. To take the broadening of the quadrupole splitting into account a certain distribution of the transition frequencies is assumed (e.g. Gaussian) and included in the calculation of the echo amplitude. This possibility is discussed in [Wür04] and used in [Bra04a] and [Baz08]. Another way to take the distribution of the quadrupole splittings into

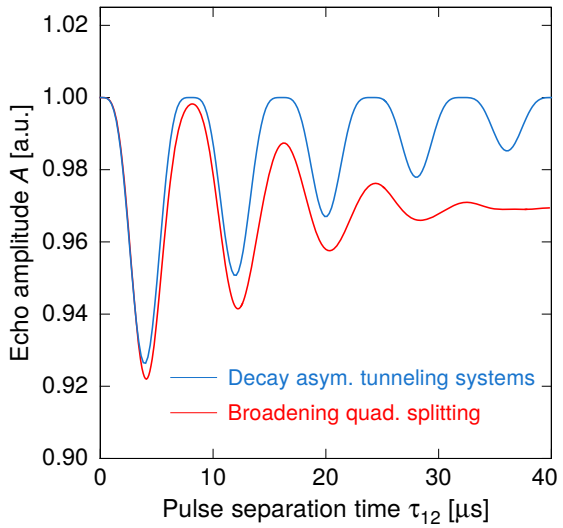

Figure 4.16: Influence of a distributed quadrupole splitting and a fast decay of the asymmetric tunneling system on the quantum beating. The influence of the broadening was calculated with the simulation discussed in section 4.4, assuming the parameters for glycerol-d5 (given in section 4.4) and a broadening of the transition frequency of 10 %. For the decay of asymmetric tunneling systems the second term of the formula for the echo modulation (equation 4.24) is for simplicity multiplied by a factor $e^{-\tau_{12}/T_1}$. Plot created according to [Baz08].

account is via a simulation based on Monte Carlo methods, which is addressed in section 4.4. In a measurement usually both processes are present. In dependence of temperature and sample composition one of them can dominate.

Special case $I = 1$ and $\eta = 0$

For the special case of a single tunneling system containing one atom with nuclear spin $I = 1$ and $\eta = 0$, the polarization can be derived analytically via perturbation theory [Bra04a, Baz08]. A two-level system with just one of these nuclear spins splits, due to the degeneracy of the states $m = \pm 1$, up in a four-level system. The lower and the upper doublet has a quadrupole splitting E_Q. Possible evolutions of the wave function of a tunneling system with such a level schema are depicted in figure 4.13. Two different modulation frequencies are observed considering the phase differences $\Delta\Phi$ in this illustration.
The analytic calculation of the modulation of the polarization for such a tunneling system with defined Δ results in

$$A_{\mathrm{mod},I=1}\left(2\tau_{12}\right) = 1 - \frac{16}{3}\left(\frac{\Delta}{E}\sin(2\Theta)\right)^2 \sin^4\left(\frac{E_\mathrm{Q}\tau_{12}}{2\hbar}\right). \tag{4.24}$$

The subtrahend is proportional to Δ^2 and depends on the rotation angle during the tunneling motion Θ, as expected from equation 4.22. For $\Theta = 0$, the modulation of the echo amplitude vanishes. Rewriting the $\sin^4\left(\frac{E_\mathrm{Q}\tau_{12}}{2\hbar}\right)$ factor to $1/8(3 - 4\cos(E_\mathrm{Q}\tau_{12}/\hbar) + \cos(2E_\mathrm{Q}\tau_{12}/\hbar))$ the two frequencies $E_\mathrm{Q}/\hbar$ and $2E_\mathrm{Q}/\hbar$ can be seen.

Polarization of a tunneling system containing several nuclear moments

For determining the polarization of a tunneling system containing several nuclear quadruple moments the Hamiltonian, given in equation 3.16, has to be diagonalized. The obtained results can be used to calculate the polarization with equation 4.21.

If the tunneling system contains S non-interacting atoms carrying a nuclear quadrupole moment with uncorrelated quadrupole potentials the resulting modulation of the polarization factorizes and is given by [Wür04, Bra04a, Baz08]

$$A_{\mathrm{mod,res}}\left(2\tau_{12}\right) = \prod_{i=1}^{S} A_{\mathrm{mod,i}}\left(2\tau_{12}\right). \tag{4.25}$$

If the tunneling system contains S identical non-interacting atoms carrying a nuclear quadrupole moment and each nuclear moment experiences the same electric field gradient as well as the same rotation angle Θ during the tunneling motion, it holds

$$A_{\mathrm{mod,res}}\left(2\tau_{12}\right) \propto \left(A_{\mathrm{mod}}\left(2\tau_{12}\right)\right)^S. \tag{4.26}$$

Applying these results to a multicomponent glass which contains several isotopes carrying nuclear quadrupole moments, the following behavior of the echo is expected.

First, the nature of the tunneling systems in the glass most likely differs from system to system and each may contain several atoms carrying nuclear quadrupole moments. Thus the individual polarizations of these tunneling systems are the result of different interfering modulation frequencies. Second, the quadrupole splittings of the different isotopes exhibit a certain broadening, as already mentioned above, leading to an even larger amount of possible beating frequencies. During a measurement of the echo amplitude in dependence of the pulse separation time the individual polarizations of the tunneling systems are 'summed up'. Due to the variety of beating frequencies caused by the multitude of quadrupole carrying atoms as well as the broadening of their transitions frequencies, the different quantum beatings are expected to interfere destructively already at small pulse separation times. Thus, the echo amplitude measured in dependence of the pulse separation time shows most likely no beating but the overall echo amplitude is reduced by the destructively interfering parts of the different quantum beatings.

Echo in multi-level system with additional magnetic field

To calculate the magnetic field dependence of the echo amplitude, the Hamiltonian of equation 4.18 is diagonalized and the obtained results are inserted in equation 4.21. Usually two different kind of measurements are performed with additional magnetic fields. First, the echo is measured in dependence of the pulse separation time to see if the additional field influences the decay behavior of the echo amplitude. Second, the echo is measured at fixed pulse separation time and the magnetic field strength is varied as shown in figure 4.2 and 4.3.
In general, two different regimes can be distinguished when measuring with additional magnetic field [Par04, Bra04a]. However, before continuing with the discussion, it is advantageous to recap the 'composition' of the quadrupole splitting when an additional magnetic field is applied

$$\underbrace{E_{\mathrm{Q}(nm)}\left(\vec{B}\right)}_{\text{Total quadrupole splitting}} = \underbrace{E_{\mathrm{Zee}}\left(\vec{B}\right)}_{\text{Zeeman splitting}} + \underbrace{E^{0}_{\mathrm{Q}(nm)}}_{\text{Quadrupole splitting caused by el. field gradient}}. \tag{4.27}$$

The quadrupole splitting relevant for the time evolution of the tunneling system is given by $E_{\mathrm{Q}(nm)}$ and depends on the Zeeman splitting E_{Zee} as well as the quadrupole splitting $E^{0}_{\mathrm{Q}(nm)}$ caused by the interaction of the corresponding nucleus with the electric field gradient. The total quadrupole splitting depends through the Zeeman splitting on the strength of the magnetic field and its orientation relative to the magnetic dipole moment of the nucleus.
At small field strengths, at which the Zeeman splitting is just a small correction to the quadrupole splitting $E^{0}_{\mathrm{Q}(nm)}$, the quantization axis of the nuclear moment is mainly defined by the electric field gradient. The shifting of the energy levels of the multi-level system by the Zeeman interaction as well as the lifting of possible degeneracies increases the amount of possible time evolutions (paths) and changes

the phase differences $\Delta\Phi$ of the path pairs. This leads to different constructive and destructive interferences and thus to a modified quantum beating for every tunneling system. When the echo is measured in dependence of the pulse separation time on a multicomponent glass with various isotopes carrying nuclear quadrupole moments, the variation of the quantum beating is most likely not visible since it averages out like without magnetic field (compare explanations from the previous subsection). If the same measurement is performed on a glass with defined quadrupole splitting, such that without magnetic field a quantum beating is visible, the beating frequency will change since the quadrupole splittings $E_{\mathrm{Q}(nm)}$ are different (compare for example the measurement on deuterated glycerol [Bra04a]). In addition, the quantum beatings of the tunneling systems are altered similar to the case of a broad distribution of quadrupole splittings. The magnetic moments of the tunneling systems are oriented arbitrarily with respect to the magnetic field, causing a slightly different Zeeman splitting for every system. In total the different Zeeman splittings look like a broadened quadrupole splitting. If the echo amplitude is measured at fixed pulse separation time in dependence of the magnetic field, the variations in the phase differences $\Delta\Phi$ cause the oscillations visible in figure 4.2 and 4.3.
At large magnetic fields, where the Zeeman splitting is much larger than the quadrupole splitting $E^0_{\mathrm{Q}(nm)}$, the latter can be treated as a perturbation and the total quadrupole splitting $E_{\mathrm{Q}(nm)}$ becomes a linear function of the magnetic field. Since the parameter b_{nm} in equation 4.22 is proportional to $1/E_{\mathrm{Q}(nm)}$, b_{nm} reduces with increasing magnetic field strength. This leads to a vanishing modulation of the polarization of a tunneling system $A_{\mathrm{mod}} \propto 1/B^2$. Thus, for $B \to \infty$ the polarization of a tunneling system without nuclear quadrupole moment is obtained [Par04]. In this case the quantization axis of the nuclear moment is mainly determined by the magnetic field. Therefore, the interaction of the nucleus and the magnetic field is the same in both wells of the double well potential and the mixing of the different nuclear states m vanishes during the tunneling motion (compare also $b_{nm} \propto \alpha^{(12)}_{nm}$).

4.4 Simulating the influence of nuclear quadrupole moments on the echo amplitude

In the previous sections the necessary Hamiltonians and formulas needed for the calculation of the polarization of individual tunneling systems were introduced. Based on those equations the impact of nuclear quadrupole moments on the echo amplitude can be simulated. Since an analytical derivation, as for a system with $I = 1$ and $\eta = 0$, is for systems with large nuclear spins or additional magnetic fields very cumbersome a numerical approach is used. A numerical ansatz was used in [Baz08], based on an effective tunneling system, to calculate the polarization of a tunneling system with $I = 1$, $\eta = 0$ and fixed quadrupole splitting. In the framework of this thesis a new approach was implemented based on Monte Carlo methods, written in

Python[2].
By Monte Carlo an ensemble of tunneling systems is created based on the distribution function introduced in section 3.2.3. Each tunneling system of the ensemble has an energy splitting within $E \pm \sigma_E$. The parameter σ_E takes into account that not only tunneling systems with $E = \hbar\omega_{\mathrm{ef}}$ are excited during the electric field pulses but also some within a certain range around E. Here $E = 1\,\mathrm{GHz}$ in all calculations. An additional Δ_0^{min} takes care of the divergence of the distribution function. The creation of the tunneling systems is based on a module developed in [Fre21]. In addition to E, Δ, Δ_0, nuclear properties are assigned to every tunneling system. Those properties are:

- The nuclear spin of the isotope present in the tunneling system. Values between $I = 1$ and $I = 7/2$ are possible.
- The nuclear quadrupole splitting of the isotope. The value of the splitting can be Gaussian distributed with a broadening of σ_{Q}
- A tunneling angle Θ_{T} in a predefined range of $\Theta_{\mathrm{T}} \pm \Delta_\Theta$.
- The gyromagnetic ratio of the isotope.
- An angle δ, between 0° and 180°, and φ, between 0° and 360°, describing the orientation of the magnetic field with respect to the magnetic moment.

In the simulation, either a fixed magnetic field is supplied and the dependence of the echo amplitude on the pulse separation time is calculated or a fixed pulse separation time is given and the magnetic field dependence of the echo amplitude is calculated. For every single tunneling system the Hamiltonian given in equation 4.18 is created and numerically diagonalized. The obtained results are used to calculate the transition matrix elements via

$$T = \langle \mathrm{Eigenvectors} | \left(\hat{H}_{\mathrm{pert}} \otimes \hat{\mathbb{1}}_{\mathrm{Q}} \right) | \mathrm{Eigenvectors} \rangle = \begin{pmatrix} T^{11} & T^{21} \\ T^{12} & T^{22} \end{pmatrix} \tag{4.28}$$

with $\hat{H}_{\mathrm{pert}}$ from equation 3.21 (and 3.26) being the Hamiltonian of the high frequency electric field pulse. For simplicity the values δp and F are set to one. The matrices T^{ij} are the transition matrices between the levels of the multi-level system. To calculate the polarization of a tunneling system only the off-diagonal elements are relevant which are given by $T^{21} = T^{12}$. This calculation of the transition matrix elements is equivalent to the one in [Bra04a] with the exception that no perturbation approach is used.
The obtained energy values and transition matrix elements are then used to calculate the polarization of every single tunneling system with equation 4.21. The polarization of the ensemble is obtained by the sum of the individual polarizations. Finally,

[2] www.python.org

the resulting echo amplitude is received relative to the maximal amplitude obtained in the current simulation. When the echo is simulated in dependence of the pulse separation time no decay processes are considered and just the quantum beating is calculated.

The current simulation allows no asymmetry parameter η and just one nuclear moment per tunneling system. An extension to $\eta \neq 0$ and multiple nuclear moments per tunneling system (equation 3.16) is possible due to the modular implementation. However, in multicomponent glasses, the implementation of many isotopes is still unknown as well as the nature of the tunneling systems. Most likely there is a huge amount of different tunneling systems. Thus simulations of such complex materials are challenging, especially because the increased number of free parameters maybe cause a good agreement with the data by chance. Organic glasses consisting of well defined molecules are better candidates to simulate the influence of nuclear quadrupole moments. It is conceivable that in these materials the nature of the different tunneling systems is similar. In deuterated glycerol it was, for example, possible to determine the nature of the tunneling systems by detailed simulations [Baz08, Bar13].

For all simulations it has to be taken into account that the spectral width of the excitation pulses $^1/_{(2\pi t_{\mathrm{pulse}})}$ ($t_{\mathrm{pulse}} = 230\,\mathrm{ns} \rightarrow \Delta f \approx 0.7\,\mathrm{MHz}$, $t_{\mathrm{pulse}} = 80\,\mathrm{ns} \rightarrow \Delta f \approx 2\,\mathrm{MHz}$) used during the measurement has to be much broader than the quadrupole splitting of the multiplet of the tunneling system. Only this way, the pulse leads to a

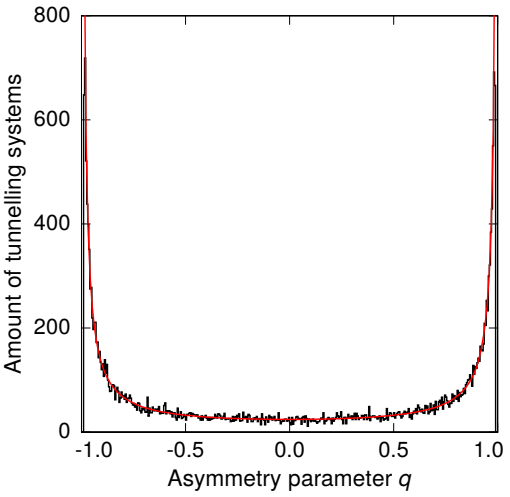

Figure 4.17: Distribution of the 25000 tunneling systems as used for the simulations shown in figure 4.18 and A.1. The parameter for the simulated tunneling systems are $E = 1\,\mathrm{GHz}$, $\sigma_E = 10\,\mathrm{MHz}$ and $\Delta_0^{\mathrm{min}} = 0.15\,\mathrm{GHz}$. A fit of the distribution function (equation 3.19), shown in red, provides good agreement.

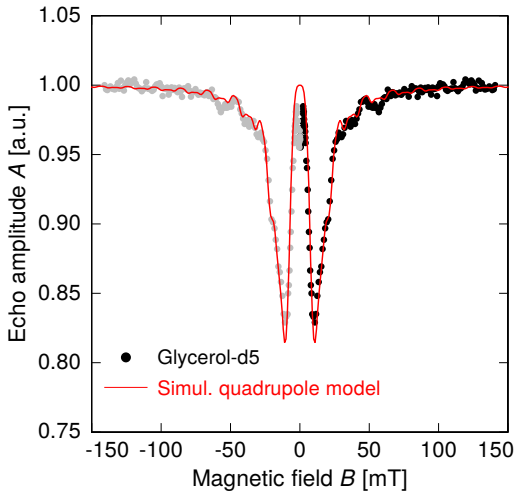

Figure 4.18: Measured magnetic field dependence of glycerol-d5 at $\tau_{12} = 8\,\mu\mathrm{s}$ and $T = 12\,\mathrm{mK}$ in black [Baz08]. The grey data points are obtained by reflecting the black ones at $x = 0$. In red the result of the simulation is shown.

mixing of all nuclear states as it is assumed in the simulation (compare explanations in the context of equation 4.21). The isotopes present in the glasses which were measured in the framework of this thesis have larger quadrupole splittings (compare table A.1). Therefore, for the nominal pulse duration of $t_1 = 230\,\mathrm{ns}$ the simulation cannot be used to describe the data. Nevertheless, the simulation can be employed to assign observed effects to nuclear properties.

For samples, where the simulation is valid, the data can be described well. As an example, the magnetic field dependence of glycerol-d5 as measured in [Baz08] and the result of the simulation is shown in figure 4.18. Besides a deviation around 0 mT, caused by the dipole effect which is not considered in the simulation, the simulation describes the data very well. The simulated distribution of the tunneling systems is shown in figure 4.17 and agrees well with the distribution function introduced in section 3.2.3. In the simulation, the minimal tunnel splitting Δ_0^{min} is set to 0.15 GHz at an energy splitting of $E = 1\,\mathrm{GHz}$. Given that the contribution of one tunneling system scales as $(\Delta_0/E)^4$ (compare for example equation 4.22) tunneling systems with a small tunnel splitting can be neglected in the simulation. The quadrupole splitting used for the simulation is 124.5 kHz without any broadening and the tunnel angle is $\Theta_{\mathrm{T}} = 16°$, as obtained in [Baz08]. Since the simulation considers only one nuclear moment per tunneling system the obtained result for the polarization is taken to the power of five, according to equation 4.26. The magnetic field dependence of the upper multiplet of a tunneling system containing one atom with $I = 1$ and in which the magnetic field is aligned parallel to the nuclear spin is shown in figure A.2. In addition, the simulated quantum beating for glycerol-d5 is shown in figure A.1.

4.4.1 Interacting dipole moments

Besides the interaction of the quadrupole moments of a tunneling system with the electric field gradient there is another mechanism that leads to a fine splitting of the tunneling system's energy levels. This mechanism is based on the anisotropy of the nuclear dipole-dipole interaction and was introduced in [Baz07, Baz08]. This coupling mechanism is illustrated in figure 4.19. If a tunneling motion contains a

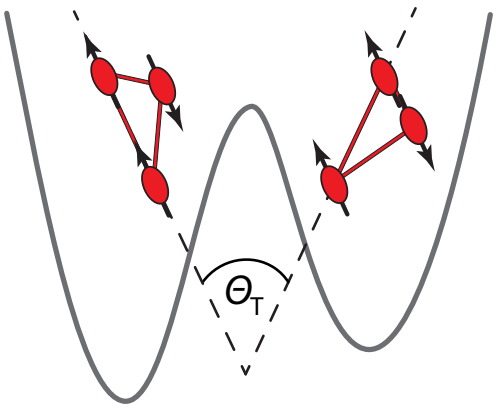

Figure 4.19: Illustration of three nuclear magnetic dipole moments in a double well potential. The dipole moments maintain there orientation during the tunneling motion. However, the vectors connecting the three nuclei change. Illustration created according to [Baz08].

rotary component, the vectors connecting the different nuclei rotate. In contrast, the orientation of the spins is maintained due to the long nuclear spin relaxation time at low temperatures [Sze75]. Since the dipole-dipole interaction depends on the distance and orientation of the dipoles with respect to each other, the tunneling motion leads to a change of the dipole-dipole energy and thus to a coupling of the tunneling motion and the dipole-dipole interaction. This coupling causes an additional mixing of the nuclear states during the tunneling motion. Not only the dipole moments of the tunneling particles are relevant for this coupling mechanism. Also nearby dipole moments are important because the tunneling motion affects their interaction with the tunneling ones.
The additional levels of the tunneling systems cause a modified quantum beating and magnetic field dependence. Since an atom with a magnetic dipole moment does not necessarily have a quadrupole moment (e.g. ^{1}H) this effect cannot only modify the quantum beating and magnetic field dependence of tunneling systems carrying quadrupole moments but it can cause a quantum beating and magnetic field dependences of non-magnetic glasses without nuclear quadrupole moments. As example, the magnetic field dependence of ordinary glycerol is shown in figure 4.3. The Hamiltonian describing the interaction of n dipoles is given by [Baz07]

$$\hat{H}_\mathrm{d} = \frac{1}{2}\sum_{j=1}^{n}\sum_{k=1}^{n}\left[\frac{\vec{\mu}_j\cdot\vec{\mu}_k}{r_{jk}^3} - \frac{3\left(\vec{\mu}_j\cdot\vec{r}_{jk}\right)\left(\vec{\mu}_k\cdot\vec{r}_{jk}\right)}{r_{jk}^5}\right] \tag{4.29}$$

with the distance r_{jk} between two dipoles and the magnetic moment $\vec{\mu}_j$. In table A.2 the nuclear magnetic moments of the isotopes relevant for this thesis are listed. In contrast to the quadrupole coupling, where usually individual quadrupole moments are considered, the dipole effect is based on several interacting magnetic dipoles (regardless of whether they are part of the tunneling system or not). The interaction between two dipoles depends on their distance as well as their orientation relative to each other and decreases rapidly with the distance. Therefore, depending on the strength of the magnetic moment only the nearest neighbours are relevant and dipole moments far apart can be neglected.
The equations introduced in the framework of the quadrupole coupling can be transferred to the dipole model. However, it has to be considered that results based on non-interacting quadrupole moments cannot be used for interacting dipole moments. For a detailed description of the nuclear dipole-dipole interaction the positions and orientations of the magnetic moments with respect to each other are important. This information is often not available. For organic glasses with well known molecular structure a modelling is possible under certain assumptions like the nature of the tunneling systems. For example, the data of deuterated and ordinary glycerol could be successfully described [Baz07, Baz08, Fic09]. Without detailed knowledge of the structure of multicomponent glasses a modeling would purely be based on assumptions.

If an additional magnetic field is applied the Zeeman splitting shifts the energy levels and lifts possible degeneracies. This affects the interference of possible time

evolutions (or path paris) and consequently the quantum beating of the tunneling system's polarization. Depending on the number of interacting dipole moments a sufficiently large magnetic field can completely suppress a mixing of nuclear states as in the quadrupole model or lead to a constant but not maximal echo amplitude. Simulations with two and three interacting dipoles can be found in [Baz08].
The strength of the dipole-dipole interaction depends on the size of the magnetic moments and their distance to each other. Therefore the quadrupole interaction is usually stronger. In deuterated glycerol-d5 the influence of the quadrupole and dipole-dipole interaction on the echo amplitude can be seen, compare figure 4.18. Whereas the quadrupole effect can be observed up to a magnetic field of rougly 60 mT, the dipole-dipole coupling (mainly caused by the hydrogen atoms in the molecule and their about six times larger magnetic moment compared to the deuteron) vanishes at about 5 mT. The temperature dependence of the dipole-dipole coupling is investigated in [Fic09].

4.5 Relaxation between tunneling systems and nuclear moments

Nuclear moments, embedded in a solid, are in a dynamic interaction with their surroundings. These interaction processes cause transversal and longitudinal relaxation processes. A classical way to motivate these relaxation times can be done, analogous to section 3.4, via the Bloch equations [Blo46]. The introduced longitudinal or spin-lattice relaxation, characterized by the relaxation time T_1, leads to a thermal equilibrium between the nuclear moments and the environment by the exchange of energy. The term lattice thereby comprises all degrees of freedom, with the exception of the spin orientation of the respective material (solid, fluid or gas) [Lös57]. The transversal relaxation, given by the time T_2, depicts processes which do not lead to an energy exchange between the spin system and the environment. They rather change the component of the polarization that is perpendicular to the external field defining the quantization axis. Given the coupling between nuclear moments and tunneling systems, visible as quantum beating, energy can also be exchanged between them. That this coupling contributes to the relaxation rate is visible in nuclear magnetic and quadrupole resonance measurements, where an increased relaxation rate is observed in the vitreous state compared to the crystalline state of the same material. This is discussed in more detail in section 4.5.2.
The so far introduced models do not consider such a relaxation mechanism. They are all based on the assumption of long spin lattice relaxation times, which is also supported by several measurements. For example, in [Sze75], the spin-lattice relaxation time of ^{11}B in amorphous B_2O_3 and ^{23}Na in vitreous $(Na_2O)_{0.3}(SiO_2)_{0.7}$ was measured at a temperature of about 1 K to be in the order of several minutes. This is much larger than the duration of an echo sequence, which is most of the times shorter than 200 µs. Thus, the models of the nuclear quadrupole and magnetic dipole-dipole

coupling together with the relaxation processes, introduced in section 3.4, should be able to describe the data measured of miscellaneous glasses containing nuclear quadrupole moments. However, different measurements showed an unexpected behavior indicating the need of additional mechanisms. The observations made on different glasses containing nuclear quadrupole moments are presented in the following. They finally led to the discovery of an additional relaxation process relevant in amorphous solids at low temperatures. This relaxation mechanism is introduced in section 4.5.3.

4.5.1 Observations in glasses containing nuclear moments

The introduced quadrupole and dipole model and the associated quantum beatings are based on the assumption that the relaxation times of nuclear spins at low temperatures are very long so that the orientation of the nuclear moment is maintained during an echo sequence. Under this assumption, the decay of the echo amplitude of an amorphous solid can in principle show three different behaviors. These three possibilities are shown in simplified form in figure 4.20. In this plot, it is assumed that the materials of all curves are the same, just the broadening of the nuclear quadrupole splitting is varied. Therefore, the overall decay behavior is the same vor all curves and determined by the processes introduced in section 3.4. The black line corresponds to the case of a decay with a quantum beating. For simplicity only the upper envelope, which is received when all points of maximal echo amplitude are connected, is shown. The red line represents a decay which shows only a quantum beating at small pulse separation times. In this case the beating de-phases quickly due to a broad distribution of quadrupole splittings and thus different beating frequencies of the individual tunneling systems leading to a overall reduced echo amplitude. The blue curve illustrates the case, where already at smallest pulse sep-

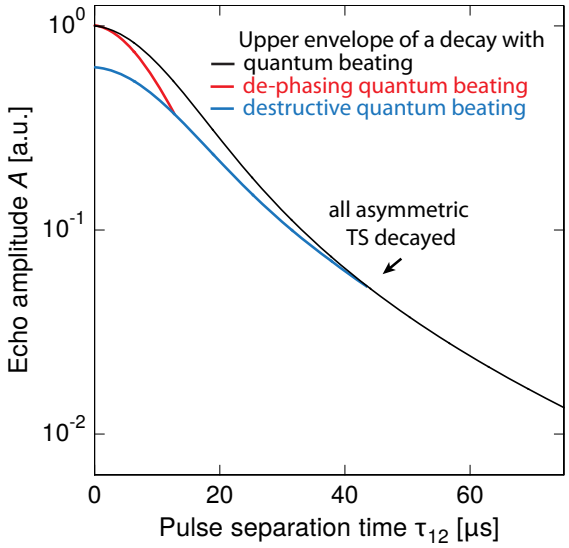

Figure 4.20: Possible decay behaviors of the echo amplitude for samples containing nuclear quadrupole moments. The black line shows the upper envelope of a decay with quantum beating. The red line shows the case of a quantum beating at the beginning but it de-phases due to a distribution of quadrupole splittings. The blue line shows the situation of destrucive interferring quantum beating of the single tunneling systems already at the beginning of the measurement.

aration times a purely destructive interference of the different quantum beatings is present. Thus this curve shows an overall reduced echo amplitude right from the beginning of the measurement. At some point in the decay curve (marked by the arrow), all asymmetric tunneling systems decayed by relaxation processes (mainly spectral diffusion) and just the symmetric ones remain. Therefore, no mixing of nuclear states and thus quantum beating is present anymore and all three curves show the same decay behavior. In addition, a large enough magnetic field which prevents the mixing of nuclear states during the tunneling leads to the same decay behavior for all three samples. The curve describing this scenario is equivalent to the black one. A measurement, in agreement with the black curve, is shown in figure 4.4. In this plot a measurement of the same material with applied magnetic field can be seen as well.
However, in reality it is not possible to prepare a sample in three different ways such that the three curves of figure 4.20 can be measured. If a sample contains nuclear moments and shows a quantum beating, it is not trivial to determine whether the red or black situation is present (compare for example [Baz08] for an investigation on deuterated glycerol). If the sample contains quadrupole moments such that a beating is expectable, but no beating is visible most likely the case of the blue curve is measured. If this curve is plotted relative to the maximal echo amplitude, it looks like a less fast decay compared to a curve measured on a similar sample showing a beating.

Turning to actual measurements, the decay of the echo amplitude in deuterated glycerol could, with the exception of very small pulse separation times, be described qualitatively well by spectral diffusion theory using the exponential decay of the intermediate time range, regardless of whether the mixing of different nuclear states was prevented by an additional magnetic field or not [Bra04a, Baz08]. This observation supports the assumption regarding the fixed nuclear spin orientation during echo measurements. In contrast to that, the decay of the two-pulse echo amplitude of the multicomponent glass Albasi (BaO-Al_2O_3-SiO_2), which contains several isotopes with nuclear quadrupole moments, showed no quantum beating and a decay behavior which is neither exponential nor Gaussian and much faster as expected from spectral diffusion theory (compare figure 4.21) [Ens02a]. This decay behavior points towards an additional relaxation mechanism at low temperatures, besides the spectral diffusion and the one-phonon process. Collective excitations can only partially describe the data [Ens02a]. The missing quantum beating is most likely caused by the variety of the atoms carrying nuclear moments in this sample and their broad distribution of quadrupole splittings. In [Lud02] the same material was investigated at a temperature of 10 mK with and without a constant magnetic field of 230 mT. According to the discussion of figure 4.20 an additional magnetic field prevents a mixing of nuclear states and thus modifies the decay behavior at short pulse separation times (the decay behavior changes from the blue to the red curve). However, in Albasi the applied magnetic field showed no or just a minor influence on the decay behavior of the two-pulse echo. According to figure 4.2 a magnetic field of 230 mT is

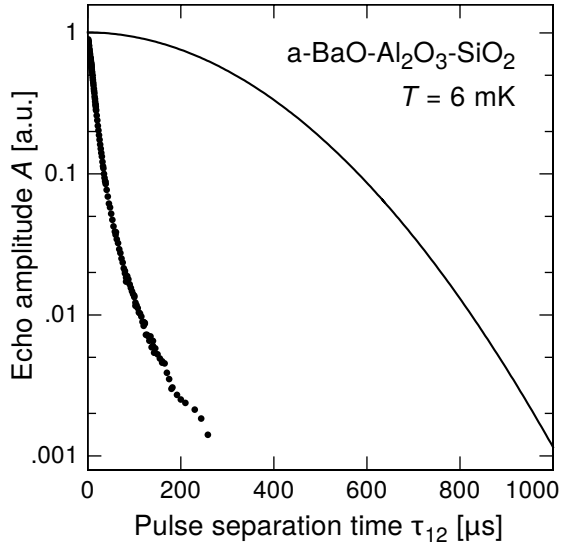

Figure 4.21: Decay of the two-pulse echo of Albasi ($BaO\text{-}Al_2O_3\text{-}SiO_2$) as function of the pulse separation time, measured at a frequency of $f_{ef} = 1\,GHz$ and a temperature of 6 mK. The solid line shows the theoretical prediction according to spectral diffusion theory. Plot taken from [Ens02a].

smaller than the saturation field of Albasi where the maximal echo amplitude is recovered. Thus the applied magnetic field was probably too small to prevent a mixing of nuclear states and to influence an additional relaxation mechanism, maybe based on the nuclear moments of the material.
In addition, a faster decay behavior than expected was observed in studies on several multicomponent glasses [Lud03]. Also here an hitherto unconsidered relaxation mechanism, based on the nuclear quadrupole moments could be the reason.

The influence of nuclear quadrupole moments on the dielectric properties of glasses cannot only be observed in polarization echoes. As shown in section 4.1, the first observation of a magnetic field dependence of non-magnetic glasses was in measurements of the dielectric constant. Thus, a possible additional relaxation mechanism, caused by nuclear moments, should also be observable in measurements of the dielectric constant. Indeed, a relaxation mechanism between tunneling systems and the nuclear quadrupole moments was observed in two glasses containing large nuclear quadrupole moments [Luc16]. This relaxation mechanism manifests itself in a constant temperature of the minimum T_{min} in the real part of a measurement of the dielectric function in dependence of the temperature. According to the standard tunneling model, the minimum temperature between the relaxational and the resonant flank of the dielectric function is defined by the temperature dependence of the dominant relaxation. If only phonons are considered the minimum temperature shifts proportional to the third root of the measurement frequency $T_{min} \propto \nu^{1/3}$ (compare figure A.5). The deviation from this behavior is explained by an additional relaxation process. The minimum temperature as a function of frequency for various samples is shown in figure 4.22. The samples HY-1, N-KZFS11 and N-BK7 are multicomponent glasses. The two first mentioned contain isotopes with large nuclear quadrupole moments and most likely large quadrupole coupling. N-BK7 contains also isotopes with nuclear moments, but they have a comparably small quadrupole

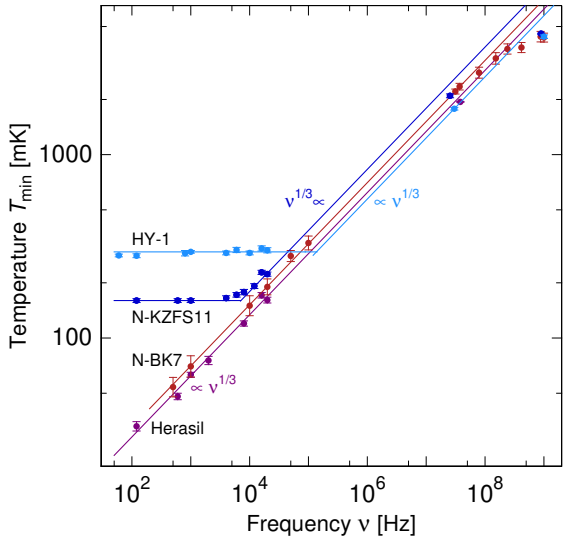

Figure 4.22: Minimum temperature T_{min} of the real part the dielectric function of Herasil (dark red), N-BK7 (red), N-KZFS11 (blue) and HY-1 (light blue) in dependence of the frequency. The expected $\nu^{1/3}$ behavior as well as the constant value indicating the relaxation between the nuclear quadrupole moments and the tunneling systems are indicated by solid lines. Plot taken from [Luc16].

coupling constant. Herasil is a standard quartz glass containing just a negligible amount of nuclear moments. The exact composition of those glasses can be found in section 5.4. For the samples with large quadrupole moments (and most likely large quadrupole coupling), there is a clear indication for an additional relaxation mechanism. This observation shows, that nuclear quadrupole moments actually affect the relaxation behavior.

It took 14 years from the discovery of the influence of nuclear quadrupole moments on the dielectric properties to the direct proof that nuclear moments influence the relaxation behavior of tunneling systems at low temperatures. To further investigate the influence of nuclear moments on the relaxation of tunneling systems this thesis studies various glasses containing atoms with small to large quadrupole moments and quadrupole couplings. The relaxation between nuclear moments and tunneling systems is also visible in the relaxation behavior of nuclear moments in amorphous solids. In the following corresponding observations and the underlying models are addressed. Afterwards the relaxation of tunneling systems due to an interaction with nuclear moments is introduced. In this section the phenomenological model which was developed in [Luc16] is described in more detail.

4.5.2 Relaxation of nuclear moments in amorphous solids

When the nuclear spin-lattice relaxation time of an isotope, for example measured with nuclear magnetic resonance (NMR) or nuclear quadrupole resonance (NQR) techniques, is discussed, it has to be considered that the obtained relaxation time is an average over the whole sample. If for example a reduced relaxation time is measured in an amorphous solid and the supposed cause is a modulation of the quadrupole coupling caused by tunneling systems, it is obvious that in general not every isotope carrying the respective nuclear moment is participating in a tunneling

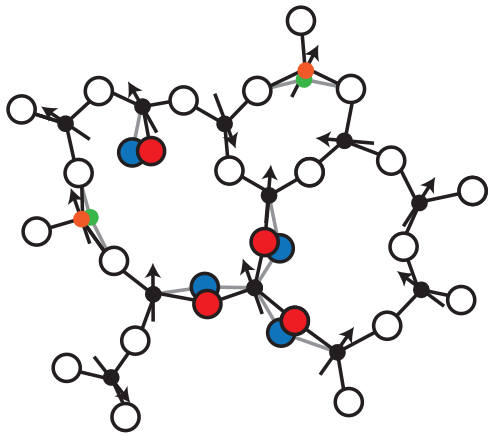

Figure 4.23: Illustration of an amorphous solid of stoichiometry XY_2 or X_2Y_3 in which the X is carrying a nuclear spin, indicated by the small arrow. In solids of this stoichiometry every tunneling system either contains or is connected to a nuclear moment, but not every nuclear moment is 'seeing' a tunneling system.

system (compare figure 4.23). Just as not every tunneling system usually contains a nuclei of the respective isotope[3]. Thus it is conceivable that the relaxation time of a nuclear moment being actually part of a tunneling system is even lower than the value obtained by the measurement. The excitation or de-excitation of a nuclear moment being part of a tunneling system is then transmitted throughout the glass by spin-spin diffusion. In dependence of the dipole-dipole interaction and concentration of the respective nuclei this process can either be very fast or take a comparably long time [San87, BJ88]. There are two processes that lead together with the tunneling systems to a significantly reduced relaxation time of nuclear moments at low temperatures (in many glasses these processes dominate below about 100 K [BJ88]). These are the quadrupole coupling and the magnetic dipole-dipole interaction. In the following, the influence of quadruple coupling is discussed before the dipole-dipole interaction is addressed.

The observation that the quadrupole coupling can be the dominant relaxation channel for the respective nuclei was already made in 1948 by Bloembergen. He reported a reduced longitudinal relaxation of the deuterons ($I = 1$) compared to the protons ($I = 1/2$) in partly deuterated water although the magnetic moment of the deuteron is smaller [Blo48]. In [Pou50] similar observations were made on crystalline solids. There are many theories dealing with various aspects of the influence of quadrupole moments on the relaxation of nuclear spins. For example, in [Kra54] the relaxation of nuclei due to quadrupole coupling in ionic crystals is discussed and in [Bay51] a model considering the influence of quadrupole moments on the nuclear relaxation in molecular crystals is developed. A list of various models can be found in [Woe63]. The basic idea behind these relaxation processes is that the considered nucleus, which has a nuclear quadrupole moment, experiences variations of the electric field gradient around its transition frequency stimulating a relaxation process. The cause of the

[3] An exception are solids consisting of just one material with a stoichiometry of XY_2 or X_2Y_3 where at least one of the isotopes carries a nuclear quadrupole moment. In those solids every tunneling system will be connected to at least one atom with an nuclear moment. But not every nuclear moment will most likely be part of a tunneling system.

variation can amongst others be a phonon, a reorientation of a molecular side-group or a tunneling system.

Since the number of phonons as well as possible rotational degrees of freedom within the solid are reduced with decreasing temperature it is expectable that amorphous solids, which have tunneling systems as additional degree of freedom, show a reduced relaxation time at low temperatures. Indeed, as already mentioned at the beginning of section 4.5, measurements on amorphous materials show a reduced nuclear spin-lattice relaxation time in the investigated temperature range compared to their crystalline counterpart. This was for example observed in NQR measurements on vitreous and crystalline As_2S_3 [Rub74] and, as already introduced, in NMR measurements on the isotopes ^{11}B in amorphous and crystalline B_2O_3 and ^{23}Na in vitreous and crystalline $(Na_2O)_{0.3}(SiO_2)_{0.7}$ [Sze75]. The results of those NMR measurements are shown in figure 4.24. It was determined that at low temperatures ($\approx 1\,K$ to $100\,K$) the nuclear spin-lattice relaxation time scales with temperature as $T_1 \propto T^{-1.3}$. For comparison, in crystalline solids T_1 varies with temperature as T^{-n} with n between 5 and 9 depending on the type of nucleus-phonon interaction [BJ88]. The nuclear spin-lattice relaxation time of ^{29}Si in amorphous $(Na_2O)_{0.3}(SiO_2)_{0.7}$ was measured in [Sze75]. However, this isotope shows no drastic reduction of its relaxation time. Since ^{11}B as well as ^{23}Na are carrying nuclear quadrupole moments in contrast to ^{29}Si, which has a nuclear spin of $I = 1/2$, it can be concluded that the relaxation mechanism is based on a modulation of the quadrupole coupling, which is just present in the amorphous state and might be caused by the influence of tunneling systems [Sze75]. If the relaxation was based on magnetic interactions, for example by paramagnetic impurities in the material, which are known to be a dominant relaxation channel in crystalline solids, the difference between the ^{29}Si and ^{23}Na relaxation time could not be explained by the different gyromagnetic ratios and spin factors [Sze75]. In addition, an extensive study of the influence of different paramagnetic

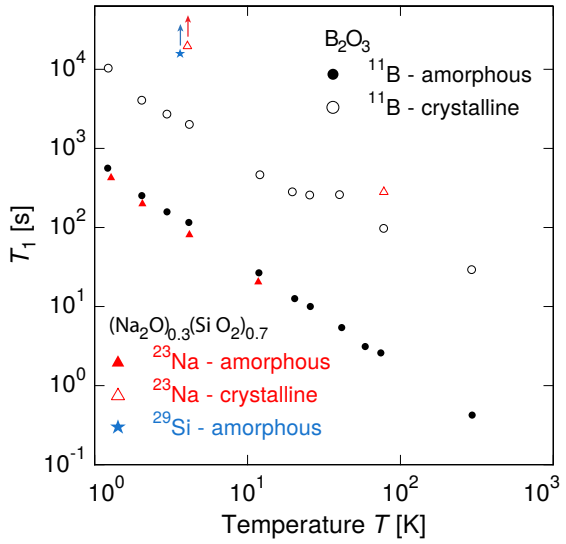

Figure 4.24: Relaxation time in dependence of the temperature for ^{11}B ($I = 3/2$) in amorphous and crystalline B_2O_3 and ^{23}Na ($I = 3/2$) as well as ^{29}Si ($I = 1/2$) in vitreous and crystalline $(Na_2O)_{0.3}(SiO_2)_{0.7}$. For ^{23}Na in the crystalline state and ^{29}Si in the amorphous state only lower limits are given. Data from [Sze75].

impurity concentrations and absorbed water content on the spin relaxation in amorphous B_2O_3 showed no correlations [Rub75]. Experiments with various amounts of different paramagnetic impurities on the glass $(B_2O_3)_x(CaF_2)_{1-x}$ showed also only small changes in the T_1 time of ^{11}B compared to an undoped sample [San87].

The mentioned measurement of the spin-lattice relaxation time of ^{29}Si in amorphous $(Na_2O)_{0.3}(SiO_2)_{0.7}$ in [Sze75] might suggest that the quadrupole coupling is the only interaction which can lead to a significant reduced relaxation time in glasses. However, a magnetic dipole-dipole coupling can also influence the relaxation behavior. For example, glasses containing fluorine experience a reduced relaxation time of the ^{19}F isotope ($I = 1/2$), which shows a similar temperature dependence as the isotopes with quadrupole moment at low temperatures (about 1 K to 100 K) [San87, BJ88, Est91]. An investigation of the influence of paramagnetic impurities on the relaxation of ^{19}F in vitreous $(B_2O_3)_x(CaF_2)_{1-x}$ revealed only a small influence, similar to the quadrupole case [San87]. A study of the ^1H ($I = 1/2$) and ^2H ($I = 1$) relaxation in the glasses $LiCl \cdot 7H_2O$ and $LiCl \cdot 7D_2O$ showed similar temperature dependencies ($T_1 \approx T^{-1.3}$) for both isotopes [BJ88].
The observed reduced relaxation time of isotopes with a nuclear spin of $I = 1/2$ is induced by a variation of the dipolar field experienced by the respective nuclei. This variation can be caused by neighboring nuclei with magnetic moments that are part of tunneling systems. Their tunneling motion create varying dipolar fields at the positions of the considered nuclei [San87]. The process should also work if the considered nuclei are part of tunneling systems and nearby nuclei with magnetic moment rest. Comparing the obtained results on the glasses containing ^{19}F and ^1H, where the isotopes have a large magnetic moment and occur with high natural abundance, to ^{29}Si, which has only a small magnetic moment and occurs with low natural abundance, it seems to be essential that the magnetic moment as well as the density of the respective nuclei are large enough. The natural abundances and nuclear magnetic moments of the isotopes relevant for this thesis are listen in table A.2.
The above described observations on the glasses containing isotopes with large magnetic moments indicate that the dipolar coupling can influence the relaxation behavior of nuclei in glasses as much as the quadrupole coupling. The relaxation rates of isotopes with and without nuclear quadrupole moment are shown in figure 4.25. It can be seen that the low temperature dependence of all curves is similar and it holds

$$T_1^{-1} \propto T^{1+\alpha} \qquad \text{with} \qquad 0 \lesssim \alpha \lesssim 1 \tag{4.30}$$

[Est91]. A model describing the low temperature behavior of the relaxation of a nuclear spin with a quadrupole moment was developed in [Rub75]. In the model, the dominant mechanism at low temperature leading to relaxations of the nuclear spins are Raman processes involving two tunneling systems. The decay into one single tunneling system or phonon is neglected since it gives only a minor contribution to the nuclear relaxation time T_1. The two relevant tunneling systems for the relaxation

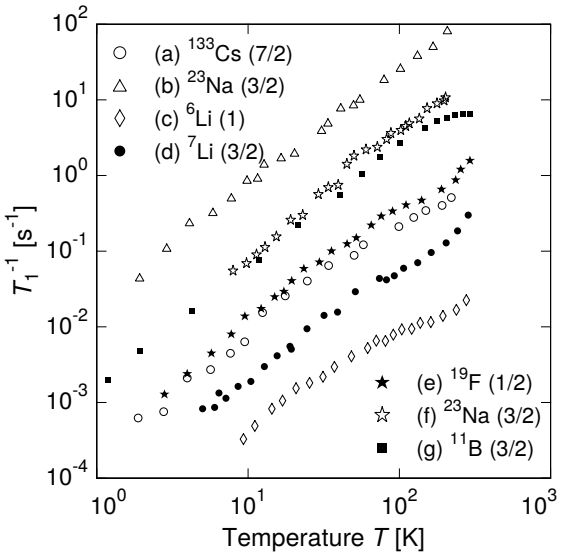

Figure 4.25: Nuclear spin-lattice relaxation rates in dependence of temperature. The nuclear spin of the respective nuclei is given in brackets. The samples, nuclear probes and corresponding Larmor frequencies are: **(a)** [$Cs_2O \cdot 3SiO_2$] ^{133}Cs - 23.6 MHz; **(b)** [$Na_2O \cdot 3SiO_2$] ^{23}Na - 47.6 MHz; **(c)** [$Li_2O \cdot 3B_2O_3$] ^{6}Li - 26.3 MHz; **(d)** [$Li_2O \cdot 3B_2O_3$] ^{7}Li - 104 MHz; **(e)** [$0.1Li_2F_2$ $0.9Li_2O \cdot 3B_2O_3$] ^{19}F - 94 MHz; **(f)** [$Na_2O \cdot GeO_2$] ^{23}Na - 47.6 MHz; **(g)** [B_2O_3] ^{11}B - 18.4 MHz;. Data from [BJ88].

overlap and the nucleus experiences the electric field gradient variation caused by both tunneling motions. The relaxation of the nuclear spin by a combination of a single tunneling system and a phonon or two phonons is also considered. However, their contribution to T_1 is weak at low temperatures ($T < 100\,\mathrm{K}$) for the studied materials with a temperature dependence of $T_1 \propto T^{-4}$ and T^{-7} in contrast to $T_1 \propto T^{-1}$ for the two tunneling system process [Rub75]. This model was extended by [BJ88] and [Est91] to describe their NMR measurements and to consider also the dipolar interaction. According to [Est91], the relaxation rate is given by

$$T_1^{-1} = \xi \int_0^{\Delta_{\max}} \int_0^{V_{\max}} \mathrm{d}\Delta \mathrm{d}V \frac{P(\Delta, V)}{\cosh^2\left(\frac{\Delta}{2k_\mathrm{B}T}\right)} \frac{\tau}{1+\omega_\mathrm{L}^2\tau^2} \tag{4.31}$$

with the distribution function of the tunneling systems $P(\Delta, V)$ in dependence of the asymmetry energy Δ and the barrier height V, the Larmor frequency ω_L, the maximum asymmetry energy $\Delta_{\max}$ and barrier height $V_{\max}$, the correlation time τ and the strength of the tunneling system nucleus coupling ξ. Depending on the coupling mechanism it holds:

$$\text{Quadrupolar coupling}: \quad \xi \propto Q^2 \, \langle [\Delta(\vec{\nabla}\vec{F})]^2 \rangle \qquad \text{[Rub75]} \tag{4.32}$$

$$\text{Dipolar coupling}: \quad \xi \propto \frac{\gamma_{\mathrm{gy},1}^2 \gamma_{\mathrm{gy},2}^2}{r^6} I(I+1) \qquad \text{[San87, Kim77]} \tag{4.33}$$

with the quadrupole moment Q, the averaged variation of the electric field gradient $\langle [\Delta(\vec{\nabla}\vec{F})]^2 \rangle$, the gyromagnetic ratio $\gamma_{\mathrm{gy},i}$ of the interacting nuclei and the mean distance between them r. When equation 4.31 is fitted to data, the coupling strength ξ is usually a free parameter. The correlation rate τ^{-1} is at low temperatures given by the one-phonon processes of the tunneling system (compare equation 3.58) and by thermally activated processes at higher temperatures [Est91]. The multi-phonon

processes are not considered in these publications. The $\tau/(1+\omega_L^2\tau^2)$ dependence of equation 4.31 shows that the relaxation mechanism is most effective for tunneling systems which fulfill $\omega_L\tau = 1$. For temperatures smaller than V_{max}/k_B and Δ_{max}/k_B, equation 4.31 can be rewritten to $T_1^{-1} \propto T^{1+\alpha}\omega_L^{-\beta}$ so that the power law from equation 4.30 is obtained [BJ88, Est91]. The $\omega_L^{-\beta}$ dependence with $0.6 \lesssim \beta \lesssim 1$ shows that the relaxation rate observed in NMR measurements usually decreases for a higher Larmor frequency. This can for example be seen in measurements in [BJ88] and [Est91].

According to equation 4.32 the ratio of the relaxation rates of two different nuclei with a quadrupole moment should roughly be given by the ratio of their quadrupole moments squared, if they experience similar variations of the electric field gradients. This behavior was observed in [Est91] for ^{7}Li and ^{23}Na in fluorozirconate glasses validating the theory.

Since a nucleus with a nuclear quadrupole moment has also a nuclear magnetic moment a relaxation process can happen via quadrupolar and dipolar coupling. In general both processes occur simultaneously. However, depending on the implementation of the respective nucleus in the glass and the experienced electric field gradient one of them usually dominate. For a covalently bound nucleus the quadrupole coupling dominates. For example, in [Woe63], the quadrupole interaction energy of ^{35}Cl, covalently bound to carbon, is estimated to be 10^4 to 10^5 times that of of the nuclear magnetic dipole-dipole interaction. Since their contributions to T_1 are proportional to the squares of their interaction energies (compare equations 4.32 and 4.33) the quadrupole coupling is in this case 10^8 to 10^{10} times more important than the magnetic interaction.

The model introduced in equation 4.31 describes the case of a NMR measurement. Of course, both relaxation mechanisms are also present without magnetic field. In this case the nuclear spin of a nucleus with a quadrupole moment precesses around the direction of the maximal electric field gradient and thus ω_L is replaced by the respective quadrupole frequency ω_Q.

4.5.3 Relaxation of tunneling systems due to nuclear quadrupole moments

The previous section showed that tunneling systems influence the relaxation behavior of nuclear moments at low temperatures significantly. The opposite side, namely the influence of nuclear quadrupole moments on the relaxation behavior of tunneling systems was directly observed in measurements of the complex dielectric function of HY-1 and N-KZFS11 [Luc16]. Both glasses contain atoms with large nuclear quadrupole moments (compare section 5.4) and show an additional non-phononic relaxation mechanism at low temperatures. This relaxation leads to a fixed minimum temperature T_{min} of the dielectric function's real part as a function of frequency (compare figure 4.22). The relaxation becomes dominant at low temperatures when

the phononic relaxation is less effective due to the decreasing number of phonons ($\propto T^3$). Since the observed effect is in the same order of magnitude as the relaxation via phonons and shows the same behavior in dielectric and acoustic measurements on the glass HY-1, it is attributed to the interaction of the tunneling systems and the quadrupole carrying nuclei.
To describe the measured data a phenomenological model for the nuclear quadrupole relaxation was developed with the relaxation rate

$$T_{\mathrm{NQR}}^{-1} = T_{\mathrm{c},0}^{-1} \left(\frac{\Delta_0}{E}\right)^2 \coth\left(\frac{E}{2k_{\mathrm{B}}T}\right) \left(1 - \mathrm{e}^{\left(-\frac{T}{2\delta T}\right)^a}\right) \tag{4.34}$$

[Luc16]. This rate dies out towards very low temperatures. Since the exact temperature dependence is not known a modified exponential decay is used which is for example purely exponential for $a = 1$ or Gaussian for $a = 2$. The $\coth\left({}^{E}/_{(2k_{\mathrm{B}}T)}\right)$ factor takes the population of the tunneling system's energy levels into account and the factor $\left({}^{\Delta_0}/_{E}\right)^2$ considers that the relaxation occurs in the temperature regime of coherent tunneling. The rate $T_{\mathrm{c},0}^{-1}$ is given by the frequency at which the $\nu^{1/3}$ dependence is crossing the regime of constant minimum temperature in figure 4.22 ($T_{\mathrm{c},0}^{-1} = 2\pi \cdot 138\,\mathrm{kHz}$ for HY-1). In the dielectric measurements performed on HY-1, the relaxation rate decreases significantly at about 15 mK. It is expected that this temperature corresponds to the quadrupole splitting of the holmium atoms in this glass. To model this dying out, δT was set to 10 mK and a to 3.5.
Since the strength of the tunneling system nuclear quadrupole moment coupling depends amongst others on the quadrupole splitting, possible paramagnetic impurities, the implementation of the respective nuclei in the glass or the concentration of the quadrupole carrying nuclei, the point at which the nuclear relaxation is the dominant relaxation process for the tunneling systems is strongly sample dependent. In measurements with large magnetic fields, where the nuclear moments align along the magnetic field and become less sensitive to variations of the electric field gradient caused by tunneling processes, a recovery of the classical phonon dominated behavior is expected.
In figure 4.26 the relaxation rate T_{NQR}^{-1} for a tunneling system with fixed energy splitting E is shown as a function of temperature for four different cases. In the blue curves $T_{\mathrm{c},0}^{-1}$ is set to $2\pi \cdot 138\,\mathrm{kHz}$ and δT to 15 mK. In the red ones $T_{\mathrm{c},0}^{-1}$ is set to $2\pi \cdot 1.38\,\mathrm{kHz}$ and δT to 2 mK. For the blue and the red case, ${}^{\Delta_0}/_{k_{\mathrm{B}}} = 15\,\mathrm{mK}$ and to 35 mK is considered. It can be seen that in dependence of δT the dying out of the relaxation starts at a different temperature. The absolute value of the plateau region, before the dying out begins, depends on the rate $T_{\mathrm{c},0}^{-1}$ and on the tunneling system's tunnel splitting. Due to the $\left({}^{\Delta_0}/_{E}\right)^2$ dependence of T_{NQR}^{-1} the relaxation process is most effective for symmetric tunneling systems ($\Delta \to 0 \;\Rightarrow\; {}^{\Delta_0}/_{E} \to 1$). The rising relaxation rate towards higher temperatures is caused by the $\coth\left({}^{E}/_{2k_{\mathrm{B}}T}\right)$. For $E < k_{\mathrm{B}}T$, the $\coth({}^{E}/_{2k_{\mathrm{B}}T})$ factor can be approximated by T.
It is worth mentioning, that the relaxation of tunneling systems due to nuclear quadrupole moments is, according to equation 4.34, most effective for symmetric

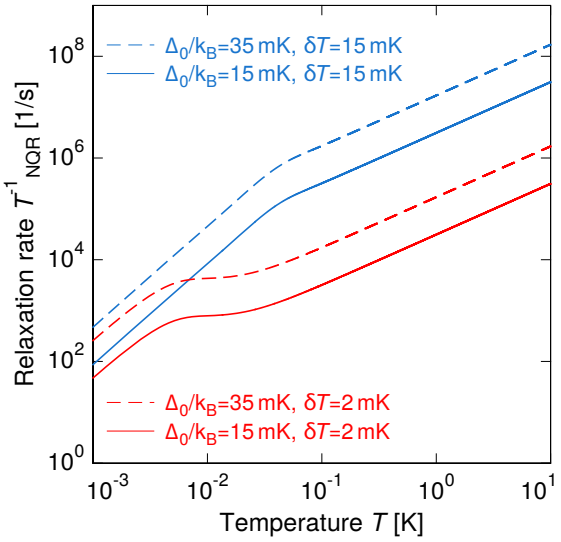

Figure 4.26: Temperature dependence of the relaxation rate T_{NQR}^{-1} according to equation 4.34 for a tunneling system with fixed energy splitting $E/k_{\mathrm{B}} = 50\,\mathrm{mK}$ and different tunnel splitting Δ_0/k_{B}. For the blue curves $T_{\mathrm{c},0}^{-1}$ is $2\pi\cdot 138\,\mathrm{kHz}$ and for the red curves $2\pi \cdot 1.38\,\mathrm{kHz}$. The parameter a is set to 2.

tunneling systems, although it was shown in section 4.3.1 that the effective field gradient seen by the nuclear quadrupole moment is changing only for tunneling systems with a finite asymmetry energy Δ.

In addition to the measurements in [Luc16], the model describes also qualitatively the course of acoustic measurements on the polymer glass FR-122P (see section 5.4 for details of the sample) [Sch18c]. This sample contains bromine in a Br-C bond with an quadrupole splitting of about $250\,\mathrm{MHz} \approx 12\,\mathrm{mK}$. However, the resonant flank in these and additional dielectric measurements are only weakly pronounced. Thus, the non-shifting of the maximum (elastic measurements) and minimum (dielectric measurements) temperature in dependence of the measurement frequency cannot be clearly seen.

Assuming an exponential decay of the echo amplitude due to the additional relaxation based on nuclear quadrupole moments, the contribution of this relaxation mechanism to the decay of the echo amplitude is given by

$$W_{\mathrm{NQR}}(2\tau_{12}) = \mathrm{e}^{-2\tau_{12}T_{\mathrm{NQR}}^{-1}(E,q)}. \tag{4.35}$$

Thereby the relation $\Delta_0/E = \sqrt{1-q^2}$ is used. The expected decay of the echo amplitude, as given by equation 4.35, is shown in red in figure 4.27. For comparison, the blue curve represents the case of spectral diffusion and one-phonon process with the same parameters as for figure 3.17. The black curve shows the combination of all three relaxation mechanisms. It can be seen that the Gaussian like leveling-off of the echo amplitude towards small pulse separation times, as predicted by spectral diffusion theory, is noticeably suppressed by the influence of the quadrupole relaxation.

In [Ler88] phonon echoes in the frequency range 10 to 500 MHz were measured on aluminosilicate glasses ($(SiO_2)_x(Al_2O_3)_y$) doped with different amounts of magnetic Ho^{3+} ions ($I = 7/2$) at temperatures down to 10 mK. The investigated atomic con-

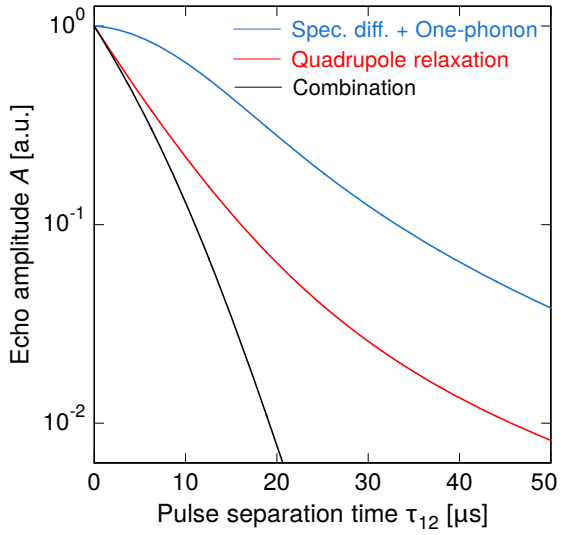

Figure 4.27: Numerical calculation of the echo amplitude A in dependence of the pulse separation time τ_{12} for an ensemble of tunneling systems at a temperature of 10 mK. For better comparability the curves are plotted relative to the maximal echo amplitude. The parameters for the one-phonon relaxation and spectral diffusion are the same as for figure 3.17. For the nuclear quadrupole relaxation the parameters $T_{c,0}^{-1} = 2\pi \cdot 138\,\mathrm{kHz}$, $a = 3$ and $\delta T = 0.01\,\mathrm{K}$ are used based on [Luc16].

centrations are in between 1.5 % and 10.1 %. The sample with a holmium concentration of 10.1 % exhibits a spin glass behavior below about 0.5 K. In the samples with reduced holmium concentration the holmium ions were partly replaced by non-magnetic La^{3+} ions ($I = 7/2$) to obtain good glass forming properties. A measurement of the echo amplitude at fixed pulse separation time in dependence of the magnetic field strength for the 1.5 % sample showed that the amplitude increases with increasing magnetic field strength and saturates at about 3 T. The investigations of the relaxation times T_1 and T_2 revealed the following. The longitudinal relaxation time T_1 is much shorter compared to a common SiO_2 glass and independent of the holmium concentration. With applied static magnetic field the relaxation time increases up to circa 3 T and saturates afterwards, but stays smaller as the one measured in SiO_2. The deformation potential γ and the density of states of the tunneling systems remain constant. The transversal relaxation time T_2 is also much shorter than in SiO_2 and independent of the holmium concentration. Furthermore, T_2 is independent of an applied static magnetic field at short pulse separation times. However, a kink in the decay curve, indicating the overlap of at least two different decay processes, is shifting with the applied magnetic field strength. In addition, the Gaussian shape like leveling-off towards small pulse separation time, as predicted by spectral diffusion theory, is not observed. An investigation of the temperature dependence of T_1 and T_2 of the sample containing 1.5 % holmium reveals for both parameters a T^{-1} dependence independent of the applied magnetic field strength. According to spectral diffusion theory a T^{-2} dependence is expected for T_2 (compare equation 3.69). At the time of this publication, the relaxation due to nuclear quadrupole moments was not yet known. Therefore just the tunneling system phonon coupling and magneto-elastic coupling are considered to interpret the data. Since the observations cannot be described within these mechanisms it is speculated that there are some magnetic excitations at very low temperatures which can relax tunneling systems directly.

Knowing about the properties of the relaxation between tunneling systems and nuclear quadrupole moments introduced in this section, the data can to a large extend be understood qualitatively without an additional magnetic excitation. Under consideration of the relaxation channel via the quadrupole moment of the rare earth ions (and the aluminium of the aluminosilicate glass), the independence of T_1 and T_2 on the concentration of the holmium ions in the glass is probably caused by the replacement of holmium with lanthanum which carries a large quadrupole moment, too. The increased relaxation time T_1 with additional magnetic field is expected in the quadrupole model as well since the nuclear moments tend to orient along the magnetic field and the quadrupole coupling becomes less and less important. Since the transversal relaxation time T_2 shows almost no magnetic field dependence there has to exist an additional mechanism, maybe also connected to the quadrupole moment, leading to a very short phase memory time T_Φ because the T_1 relaxation becomes long with rising magnetic field (compare equation 3.62). The missing Gaussian shape like leveling-off towards small pulse separation times can also be caused by an additional relaxation process, as shown in figure 4.27. For $E < k_\mathrm{B}T$, the $\coth(E/2k_\mathrm{B}T)$ factor from equation 4.34 can be approximated by T. Thus a linear temperature dependence is obtained at temperatures $T > E/k_\mathrm{B}$.

Also in [Fic13] indications for a quadrupole moment relaxation are observed. Here three-pulse echo measurements with a magnetic field of 200 mT on the multicomponent glass N-BK7, containing atoms carrying quadrupole moments, showed a slightly smaller relaxation rate at large pulse separation times compared to a measurement without magnetic field. A measurement of the two-pulse echo showed no influence in the scope of the measurement accuarcy. Since three-pulse echoes are sensitive to T_1 processes, this observation is in accordance with [Ler88].

An additional relaxation mechanism for multi-level systems is introduced in [Pol05]. There the model of collective excitations, introduced for two-level systems in section 3.4.3, is extended to multi-level systems. The obtained relaxation rates T_1^{-1} and T_2^{-1} show a linear temperature dependence. This behavior is observed in the measurements of [Ler88] and also expected in the model of [Luc16]. Since section 4.5.2 showed that there is a relaxation mechanism based on the direct interaction of tunneling systems and nuclear moments, the relaxation due to the coupling of resonant pairs is expected to play only a minor role and is not discussed further.

5. Experimental methods

This chapter provides an introduction to the experimental methods and setups used in the framework of this thesis. At first, the arrangements made to achieve conditions which allow the measurement of coherent properties like the echo are introduced. Afterwards, the experimental setup, consisting of the resonator and the needed electronics to excite the tunneling systems and measure the echo signal is explained. This is followed by a discussion of the limits and the accuracy of the experiment. Finally, the samples studied in the framework of this thesis are characterized. The experimental setup used for the echo measurements was, amongst others, already used in [Bra04a, Baz08, Fic13, Wol14, Sch16a]. Therefore, the following chapter partially builds upon their theses.

5.1 Creating the conditions for echo measurements

As mentioned in section 3.3, two main requirements must be fulfilled for the measurement of coherent effects in amorphous solids. First, the occupation difference of the tunneling systems must be sufficiently large. Second, the relaxation processes of the tunneling systems must be prevented as much as possible such that they do not destroy the coherence too fast.
In all measurements, the alternating electric field to excite the tunneling systems during an echo sequence had a frequency of about 1 GHz. Thus tunneling systems in the spectral width of the pulse around 1 GHz are resonantly excited, which corresponds to an energy splitting E of approximately $k_\mathrm{B} \cdot 50\,\mathrm{mK}$. Consequently, the samples must be placed in an environment of very low temperatures to obtain a significant occupation difference. The temperature mostly used in the framework of this thesis was about 10 mK, leading to a sizable occupation difference of the studied tunneling systems. In addition, there are only few thermal phonons that cause relaxation processes. These low temperatures are achieved by a ^{3}He/^{4}He-dilution refrigerator. The working principle of these cryostats is not discussed in this thesis, since it is well-known and subject to many literature [Ens10, Pob07].

In figure 5.1 a schematic drawing of the low temperature parts of the used ^{3}He/^{4}He-dilution cryostat as well as the built-in components of the echo experiment are shown. The vacuum pot is situated within a super insulated dewar filled with liquid ^{4}He, thus having a temperature of about 4.2 K. The temperature of the 1 K pot is about 1.3 K and the still reaches approximately 0.7 K. The minimal temperature is achieved at the mixing chamber and is in the used cryostat about 6 mK. The experiment itself consists of a reentrant cavity resonator (compare section 5.2.1) mounted onto the experimental platform, which is in turn connected to the mixing chamber. All parts

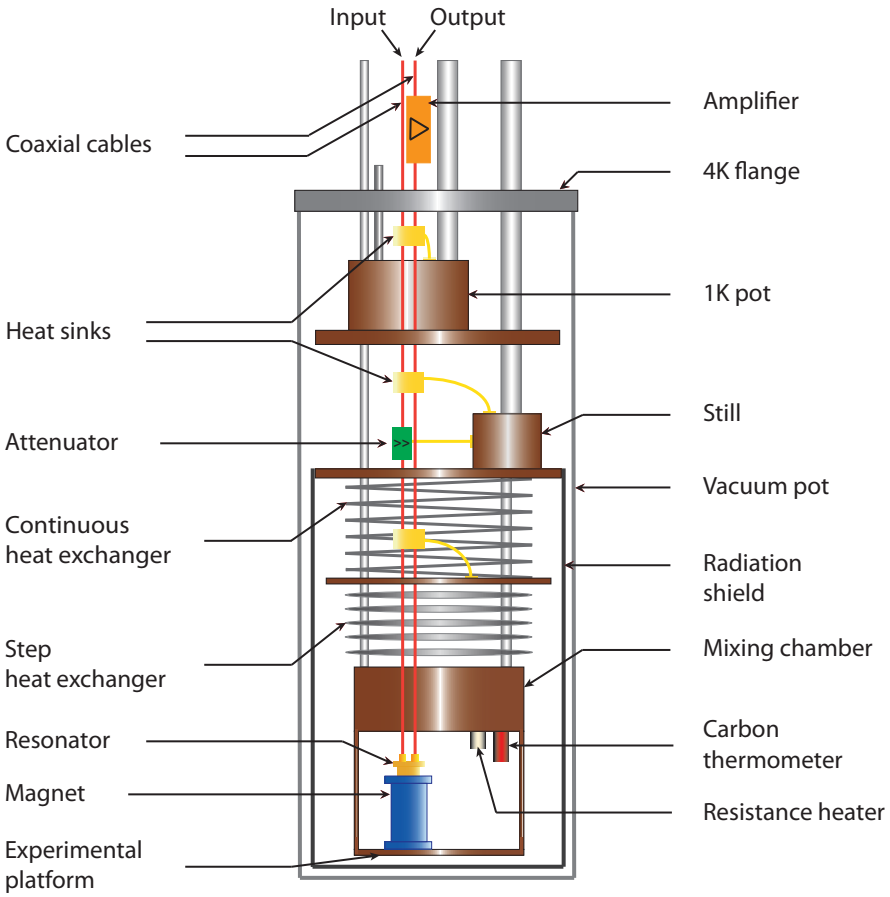

Figure 5.1: Illustration of the ^{3}He/^{4}He-dilution refrigerator and the components of the echo experiment built into the cryostat. Adapted from [Wol14, Sch16a].

of the cryostat which are essential for a good cooling performance and successful experiments, like the 1 K pot, the still, the mixing chamber and the resonator itself consist of gold-plated copper. The copper has even at low temperatures a comparably high thermal conductance. The gold plating prevents oxidation and ensures a good thermal coupling. The radiation shield, which surrounds the heat exchanger, the mixing chamber and the experimental platform consists of two layers and has two functions. The inner layer is made of copper which guarantees a good thermal contact to the still. Thus the experiments situated at the experimental platform do not experience the 4.2 K 'warm' thermal radiation of the vacuum pot but only the 0.7 K from the still which reduces the parasitic heat input. The outer layer of the radiation shield is made of lead. Lead becomes superconducting at low temperatures. This protects the components within the shield from external magnetic fields that can influence the measurement or heat the cryostat by eddy currents.
The electronics creating the two-pulse sequence and recording the echo are situated at room temperature and discussed in section 5.2.2. In order to guide the high frequency signals from those components to the resonator, located on the experimental platform in the cryostat, several arrangements must be taken to ensure good exper-

imental conditions. The main focus is thereby a as much as possible undisturbed transmission of the two-pulse sequence and the echo signal and the prevention of heating of the experimental setup, which perturbs the measurement. Therefore, the cables and the other components are matched to an impedance of 50 Ω. The room temperature electronics is connected to the components in the cryostat by flexible high frequency suitable coaxial cables. At the lid of the dewar they are changed to semi-rigid coaxial cables. On their way down to the resonator the cables pass the liquid ^{4}He reservoir of the cryostat. Thereby the cables are cooled to liquid helium temperature before being fed into the vacuum pot. Since the 4.2 K cold cables are still to warm for a direct connection to the experimental setup at millikelvin temperatures, the heat flow in the input and output cable is reduced further. For this purpose so-called heat sinks are used at several cooling steps within the cryostat. They gradually reduce the heat carried by the cables in accordance with the cooling power of the different cooling steps of the cryostat. These heat sinks are indicated by the yellow rectangles in figure 5.1 and located at the 1 K pot, the still and between the two heat exchangers. They consist of a gold-plated copper box that contains a sapphire substrate with sputtered niobium lines on top. The microstrips are matched to an impedance of 50 Ω to ensure a good transmission of the signals. When a coaxial cable is connected via the SMA connector to a heat sink, the outer conductor is connected directly to the copper box, whereas the inner conductor of the SMA connector is soldered to the niobium microstrip. The sapphire substrate insulates the inner from the outer conductor and transfers, due to its good thermal conductivity at low temperatures, the heat carried by the inner conductor to the copper box. Since the heat sink is mounted at a position in the cryostat where enough cooling power is available, the heat load carried by the outer and inner conductor is reduced. To further reduce the thermal conduction between different temperature levels of the cryostat, the cables below the 1 K pot are made from superconducting materials [Fic13]. They have a low loss transmission and a low thermal conductivity in the superconducting state. However, during measurements with superconducting micro-fabricated resonators, where the inner conductor is directly connected to the sample, it turned out that the heat carried by the cables is despite the already taken arrangements still to large to measure at lowest temperatures [Pol17]. Therefore the last 20 cm of the cables before the resonator were exchanged by very thin superconducting semi-rigid coaxial cables made of niobium-titanium, which become superconducting below about 9 K. The reentrant cavity resonator, used up to this point, is not as sensitive to a residual heat flow in the cables since the cables are not directly connected to the sample (compare 5.2.1).

On the input line an additional 20 dB attenuator is located at the level of the still (green box in figure 5.1). This attenuator damps the incoming signal, but more importantly the noise of the room temperature components, which have a higher noise temperature than the attenuator. By this means disturbances of the measurement are reduced. The damping of the two-pulse sequence by the attenuator can be compensated by a higher input power. To ensure that the attenuator stays cold it

is connected with a copper rod to the still. The output cable is equipped with an additional low temperature low-noise amplifier (orange box in figure 5.1). Through the amplification even very small echo signals can be detected. Furthermore, the thermal noise on the output line, which can disturb the measurement, is given by the cold amplifier and not by the room temperature components.
To measure the echo amplitude with an additional magnetic field, the resonator is situated inside a superconducting coil made of a niobium-titanium wire wound around a stainless steel cylinder (illustrated in blue in figure 5.1). This coil enables magnetic fields up to 230 mT.
To ensure the measurements take place at defined and constant temperatures, the cryostat has a very sensitive temperature regulation consisting of three parts. The thermometer, which is introduced in more detail in section 5.1.1, a resistance heater and a PID-controller. The thermometer and the heater are mounted to the mixing chamber (shown in red and beige in figure 5.1). Since the mixing chamber as well as the experimental platform are made of gold-plated copper, the thermal connection between these two components and the experiments located on the experimental platform is very good. Thus it is assumed that the temperature measured by the thermometer is equivalent to the temperature of the sample. The PID-controller in the control software of the cryostat gets the measured temperature and regulates the current applied to the resistance heater to achieve a stable temperature. All cables needed for the readout of the thermometer and the regulation of the heater power and the magnetic field are passing several heat sinks on their way from the room temperature electronics to the mixing chamber. This prevents a parasitic heat input, which can influence the temperature determination and limit the minimal reachable temperature of the cryostat.

5.1.1 Thermometry

In general, there are two classes of thermometers, so-called primary and secondary thermometers. Primary thermometers are based on well understood physical systems and allow for a direct determination of the temperature. Known representatives of this class are fix point and noise thermometers. However, these thermometers often provide only a few discrete temperature points or they are not easy to use. To measure the temperature over a wide range secondary thermometers are employed. They are based on the temperature dependence of various physical properties like the resistance or the susceptibility of a material. Since the exact temperature dependence of the respective property is device dependent, they need to be calibrated against primary thermometers before they can be used for temperature determination.
The thermometer used in the framework of this thesis is a carbon resistor and belongs to the secondary thermometers. This thermometer can be used for temperatures below about 1 K. It is based on the temperature dependence of the resistance, which grows monotonically with falling temperature. To avoid an overheating of the thermometer, which leads to a wrong temperature determination, the readout voltage is

adapted with decreasing temperature. The device used for the determination of the resistance is the AC resistance bridge AVS-47[0].

5.2 Experimental setup

This section introduces the experimental setup used for the measurement of polarization echoes. At first, the resonator is introduced. Afterwards, the electronics are discussed.

5.2.1 Resonator

The samples studied in the framework of this thesis are macroscopic. Thus special resonator designs are needed to measure at frequencies of about 1 GHz. The resonance frequency of a LC resonator is given by $\omega_{\mathrm{res}} = 1/\sqrt{LC}$. In order to measure at about 1 GHz very small inductances L and capacitances C are necessary. In principle two classes of resonators fulfill these requirements, each of which has its advantages and disadvantages. The first kind, the so-called reentrant cavity resonator are introduced in the following. This resonator was used for the measurements shown in section 6. However, made observations induced additional demands and a new technique based on planar micro-fabricated superconducting resonators was developed, which is introduced in section 7.

A schematic drawing of the used reentrant cavity resonator is shown in figure 5.2. The resonator consists of a hollow cylinder that is closed at the bottom. On top the cylinder is closed by a lid with a rod in its center. Thus a cavity is created where standing waves can develop. In the closed state there is a gap with variable height between the end of the rod and the bottom of the cylinder in which the sample to be studied is placed. With the column below the cavity, the resonator is attached to the experimental platform via one singe screw. The column's height is given by the requirement that the sample is positioned in the center of the solenoid, needed for measurements in magnetic fields (compare figure 5.1), since there the magnetic field is strongest and most homogeneous. The diameter of the column is as thick as possible to guarantee a good thermal contact between the resonator and the experimental platform, which acts as thermal bath. Simultaneously, it is as thin as possible to cause just small heating effects by eddy currents when the magnetic field is changed. The chosen diameter is thus 5 mm and the height 29 mm. The dimensions of the resonator are: height of the hollow cylinder circa 42.5 mm, inner diameter 18 mm and diameter of the rod: 8 mm. Since the height of the cavity is approximately $1/4$ of the basic resonance frequency's wave length λ, this resonator is also called $\lambda/4$ resonator. The whole resonator is made of oxygen free gold-plated copper (the gilding is not shown in figure 5.2). The copper ensures a good thermal

[0]AVS-47, RV-Elektroniikka Oy Picowatt, Veromiehentie 14, FI-01510 Vantaa, Finland

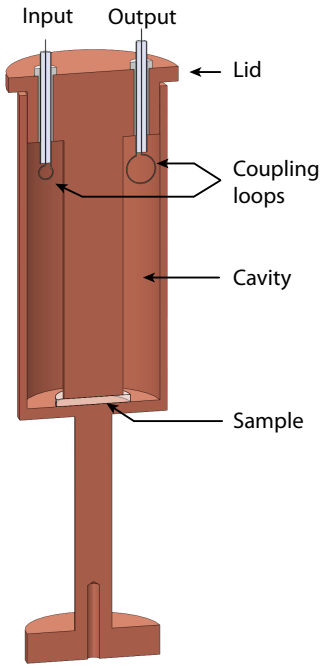

Figure 5.2: Cross section of the used reentrant cavity resonator. The gilding is not shown in this drawing.

conductivity at low temperatures. The gilding prevents the copper from oxidation which would lead to a bad electric conductivity and thus to a bad thermal contact to the thermal bath. Furthermore, it would cause additional heating between the lid and the hollow cylinder when the resonator oscillates.
The electromagnetic standing wave in the fundamental TM-mode [Hil] developing in the resonator has its maximum electric field strength in the gap between the rod and the bottom of the hollow cylinder. Therefore this gap can, in the picture of a *LC* resonator, be identified as the capacitance. The magnetic field runs parallel to the cylinder walls and is largest at the top of the cavity. Thus the rod and the hollow cylinder represent the inductance. Since the electric field is strongest and most homogenous within the gap the sample to be studied is positioned there. According to [Bra04a], the electric field is homogenous as long as the size of the gap is much smaller than the diameter of the rod. The thermal coupling between the sample and the resonator is realized by firmly pressing the lid and the cylinder together, while fixing the lid with six screws. In addition, a little bit of vacuum grease[1] is put between the bottom of the cavity and the sample. The filling factors of similar resonators are in the range from 0.45 [Ens91] to 0.7 [Wei95].
In the oscillating resonator the total field energy is continuously transferred from maximal electric and minimal magnetic field energy to minimal electric and maximal magnetic field energy. The cases of maximal electric and maximal magnetic field are illustrated in figure 5.3. The density of the drawn field lines is proportional to the strength of the respective field. The excitation and readout of the resonator is done inductively via two loops. To ensure a good coupling, the loops are situated in the strongest magnetic field, at the top of the cavity. The loops are created by

[1] Baysilone paste - produced by GE Bayer Silicones

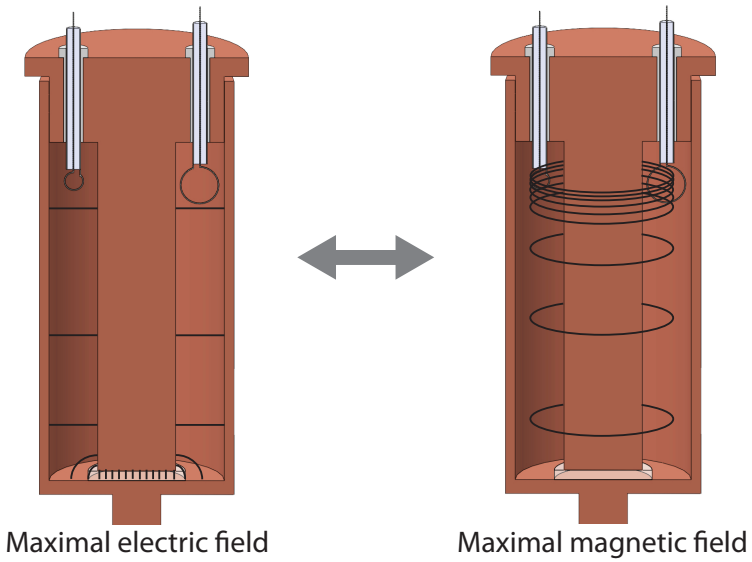

Figure 5.3: Schematic illustration of the oscillation of the field energy between maximum electric field (left) and maximum magnetic field (right). The strength of the respective field is indicated by the density of the drawn field lines. The field lines have no direction since they are oscillating.

connecting the inner and outer conductor of the semi-rigid cables, which enter the lid through two Teflon insulated holes, with a silver-coated copper wire. This way a coil with one single winding is created. The strength of the coupling can be varied either by changing the size of the coupling loop or by changing the orientation of the loop relative to the magnetic field lines. In the used resonator the loop on the output side is significantly larger than the one on the input side. In addition, the coupling out loop is oriented perpendicular to the magnetic field lines, whereas the coupling in loop has an angle of about 45° relative to the magnetic field lines. Both arrangements, the difference in size and orientation, ensure that as much signal as possible is coupled out and thus detected. Simultaneously, the noise from the input side is less effectively coupled into the resonator.
An important parameter of each resonator is the quality factor $\mathcal{Q}_{\text{res}}$,

$$\mathcal{Q}_{\text{res}} \propto \frac{\text{energy stored in resonator}}{\text{energy dissipated per oscillation cycle}}. \tag{5.1}$$

It describes how much of the stored energy in the resonator dissipates per oscillation cycle. The energy dissipation of a resonator depends on various processes, which vary in strength depending on the chosen design and materials (for example radiation losses, ohmic losses or dissipation in the dielectric material). In general, when the quality factor $\mathcal{Q}_{\text{res}}$ of a resonator is determined, the obtained value is the reciprocal sum of the actual resonator $\mathcal{Q}_{\text{res}}$ and an additional $\mathcal{Q}_{\text{ext}}$, caused by the coupling of the resonator to the readout electronics, such that $\mathcal{Q}^{-1} = \mathcal{Q}_{\text{res}}^{-1} + \mathcal{Q}_{\text{ext}}^{-1}$. For the measurements done in the framework of this thesis just the overall quality factor $\mathcal{Q}$ is relevant. The dominating energy dissipation of the used reentrant cavity is caused by

the ohmic losses of the resonator material. The $\mathcal{Q}$ value of the reentrant cavity can be changed by twisting the input loop relative to the magnetic field lines[14]. However, measurements performed in [Sch16a] at liquid nitrogen temperatures showed only a minor influence of the twisting angle on the quality factor of the resonator.
The resonance curve of the reentrant cavity resonator filled with Br-DGEBA at a temperature of 7.5 mK is shown in figure 5.4. The quality factor can be determined by the quotient of the resonance frequency f_{res} and the full width half maximum Δf, $\mathcal{Q} = f_{\mathrm{res}}/\Delta f$. Another way of obtaining the resonance frequency and the quality factor is fitting a Lorentzian to the resonance curve as it is done in figure 5.4. The fitted function in the figure is a Lorentzian with a quadratic background and given by

$$L(f) = A\frac{\mathcal{Q}}{\sqrt{\left(f^2 - f_{\mathrm{res}}^2\right)^2 \mathcal{Q}^2 + f^2 f_{\mathrm{res}}^2}} + \left(c_0 + c_1 f + c_2 f^2\right). \tag{5.2}$$

The resonance frequency obtained by the fit is about 1122 MHz and the quality factor 178. In all measurements performed in the framework of this thesis on various samples the resonance frequency was between about 800 MHz and 1.4 GHz. The $\mathcal{Q}$ factor was between 100 and 200. If a sample is measured across different measurement cycles, between which the cryostat is warmed up to room temperature, the resonance frequency and the quality factor can slightly shift. This can be caused, for example, by different degrees of pressing the lid onto the cylinder during the assembly of the resonator or by slightly different thermal stress during the cool down process.

Directly connected to the $\mathcal{Q}$ factor and the resonance frequency f_{res} is the so-called attack or rise/ ring-down or fall time t_{at} of the resonator. This time depends on the characteristic time constant τ_{res} of the resonator, which indicates how fast the stored

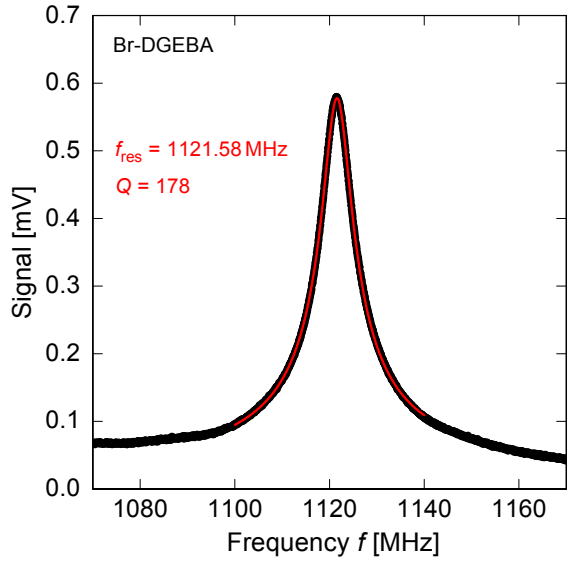

Figure 5.4: Resonance curve of the reentrant cavity resonator filled with Br-DGEBA measured at a temperature of 7.5 mK. The also shown Lorentz fit yields a resonance frequency of 1121.58 MHz and a quality factor of 178.

[14] The quality factor should decrease when the area of the loop projected to the magnetic field lines increases. Since then more energy should be coupled out of the resonator per cycle.

energy in the resonator decays to $1/e$ or rises to $(1 - 1/e)$ after a change in excitation. The time constant is given by [Hil]

$$\tau_{\mathrm{res}} = \frac{\mathcal{Q}}{2\pi f_{\mathrm{res}}}. \tag{5.3}$$

For the echo measurements presented in this thesis the excitation pulses had usually a length of 230 ns for the $\pi/2$ pulse and 460 ns for the π pulse. Thus the attack time of the resonator needs to be sufficiently short, such that the resonator can be excited quickly and enough energy is transferred into the resonator during the pulses. Furthermore, a short attack time is required to measure the echo signal. For a quality factor of 200 and a resonance frequency of 1 GHz the characteristic time constant τ_{res} is about 30 ns and therefore suitable for echo measurements.

5.2.2 Electronics

A sketch of the electronics used for the excitation and readout of two-pulse polarization echoes is shown in figure 5.5. Simply speaking, the whole circuitry consists of two sub circuits. In the black one the components used for the excitation and readout of the echo are shown. In the red part the devices needed for the determination of the resonator's resonance frequency are depicted. The components below the switches, connecting both circuitries, are used by both. In the following, the electronics used for the excitation of the tunneling systems and the readout of the polarization are introduced. Afterwards, the determination of the resonance frequency is shortly addressed.

The circuitry for the measurement of the echo can be divided into two branches, one responsible for the generation of the two-pulse sequence and one for recording the data. The left side of figure 5.5 shows the components used for the excitation of the tunneling systems and the right side those for the readout.
The different steps in the generation of the echo sequence and the recording of the data are:

- The **signal generator** (Rohde & Schwarz SMH and SMT06[2]) provides a high frequency signal. The frequency is set to the resonance frequency of the resonator and the amplitude to 13 dBm.
- The **3 dB power splitter** splits the signal from the signal generator into two parts. One is following the excitation branch. The other part is guided, via a **phase shifter** as a reference signal, to the **mixer** in the readout branch.
- The **pulse generator** (Stanford Research Systems INC, Model DG535[3]), in combination with a homemade pulse distributor (not drawn), simultaneously

[2]Rhode und Schwarz, Mühldorfstrasse 15, 81671 München, Germany
[3]Stanford Research Systems, 1290-D Reamwood Ave., Sunnyvale, CA 94089, USA

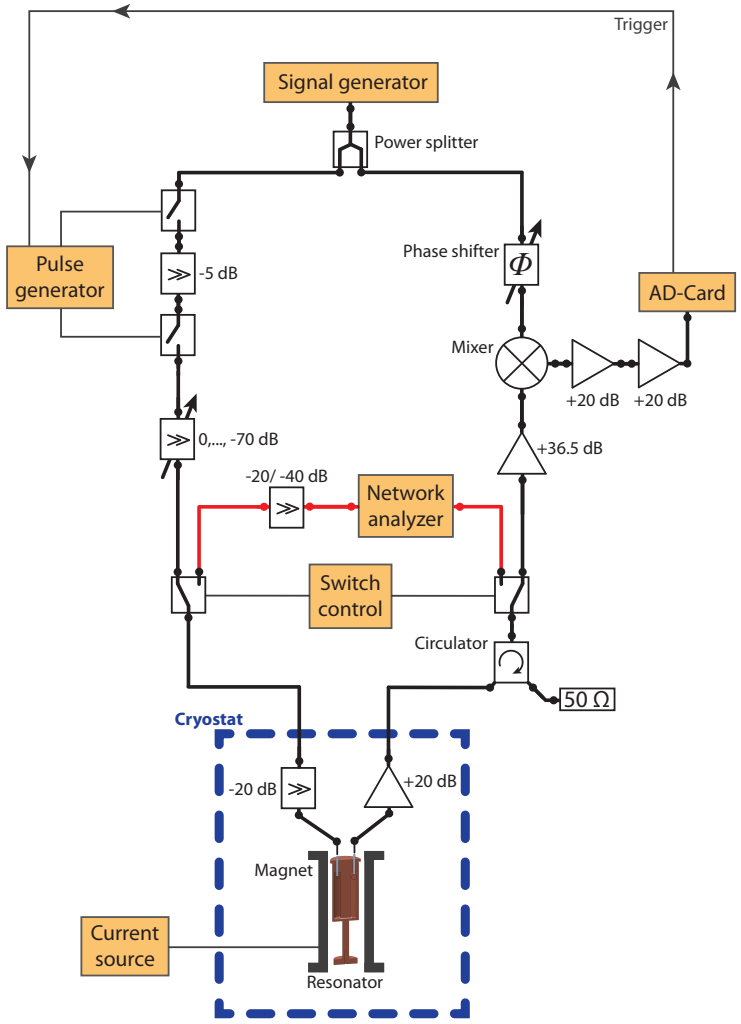

Figure 5.5: Illustration of the electronic setup used for the measurement of two-pulse echoes. The components inside the blue box are located inside the cryostat. All other parts are at room temperature. The devices drawn in orange are remote controlled by the measurement computer. The black circuitry is used for the excitation and readout of two-pulse echoes. In red, the part used for the determination of the resonance frequency of the resonator is shown.

controls the two **switches** (MITEQ S113BNU1[4]). Therefore a sequence of TTL pulses, corresponding to the two-pulse sequence, is sent to the switches. The **5 dB attenuator** between the two switches prevents an impedance miss-match and thereby an increased leak rate. The leak rate of both switches together is less than 80 dB [Fic13].

- The **adjustable attenuator**, located behind the switches, reduces the field strength of the generated high frequency two-pulse sequence. With this device the echo amplitude can be studied in dependence of the electric field strength, to find the predicted F_0^3 dependence from equation 3.50.

[4]L3Harris Narda-MITEQ, 435 Moreland Road, Hauppauge, NY 11788, USA

- The **20 dB attenuator** in the cryostat was already introduced in the framework of figure 5.1. It attenuates noise with a higher noise temperature than itself. This noise originates from the electronics at room temperature.

- Afterwards the two-pulse sequence is coupled into the **resonator**. The generated echo, as well as the two-pulse sequence, is coupled out of the resonator and following the readout branch.

- The low noise **20 dB HEMT amplifier** (Kuhne electronic GmbH, LNA 1020 A-Cool[5]) located in the helium bath of the cryostat amplifies the signal leaving the resonator in dependence of the supply voltage by 15 dB to 20 dB [Baz08, Fic13]. Simultaneously, it protects the resonator and thus the sample from noise of the readout electronics at room temperature.

- The **circulator** (Aertech Industries A4C-9011-M) protects the low noise amplifier from signals trying to enter the cryostat backwards by diverting them onto a 50 Ohm resistance.

- The **36.5 dB amplifier** (Kuhne electronics LS-Band Super Low Noise Broadband Amplifier[5]) is a high frequency suitable amplifier which increases the readout signal once more.

- By the **mixer** (MITEQ DM0052LA2[4]) the high frequency part of the measured signal is eliminated and just the envelope of the two-pulse sequence, the free induction decay and the echo remain. Therefore the reference signal from the **phase shifter** and the one coming from the cryostat are multiplied. This is similar to a transformation into the rotating frame of reference in the Bloch-sphere picture.

- The **phase shifter** (manufactured by ATM[6]) is used to adjust the phase of the reference signal to achieve suitable mixing conditions at the **mixer** such that the high frequency part of the measured signal is eliminated completely. In a measurement the phase is adjusted such that the measured echo amplitude is maximal.

- The two **20 dB amplifiers** (Comlinear Corporation CLC100 Video Amplifier[7]) amplify the envelopes obtained by the **mixer** before they are recorded by the **AD-Card**. It is possible to either use one or both amplifiers.

- The **AD-card** (GaGe CompuScope 14200[8]) digitizes the signal with 200 $^{\mathrm{MS}}/_{\mathrm{s}}$. The digitized data is then saved and pre-evaluated by the measurement computer.

[5]KUHNE electronic GmbH, Scheibenacker 3, 95180 Berg, Germany
[6]L3Harris Narda-ATM, 49 Rider Ave, Patchogue, NY 11772-3915, USA
[7]Comlinear Corporation, Fort Collins, Colorado 80525, USA - meanwhile part of Texas Instruments
[8]DynamicSignals LLC, 900 N. State Street, Lockport, IL 60441, USA

If the resonance frequency of the resonator is measured, the two **switches** (Agilent N1810UL[9]), controlled by a **switch control** (Arduino Uno micro-controller[10]), switch from the echo circuitry to the network analyzer circuitry. This part of the circuit includes also the **20 dB attenuator** and **HEMT amplifier** located inside the cryostat as well as the **circulator**. In addition, a **20 dB** or **40 dB attenuator** is placed at the output of the **network analyzer** (Hewlett Packard 8752A[11]) to prevent a heating of the sample by a too high measurement power. The transmitting power of the **network analyzer** is therefore reduced to the minimal value of -20 dBm as well. The used **network analyzer** allows for measurements up to 1.3 GHz. One sample, measured in the framework of this thesis, resulted in a resonance frequency of about 1.4 GHz. In this case the resonance frequency was determined by a lock-in amplifier instead of the network analyzer. The respective setup is shown in [Arn19] and similar to the one used in [Luc16] for the measurement of the dielectric function in the gigahertz range. The measurement of the resonator's resonance frequency is necessary after every cooldown of the cryostat. In addition, it can also be done after changing the temperature of the cryostat during one measurement cycle, since the resonance frequency of the resonator depends on the dielectric constant of the sample, which in turn depends on the temperature.

All parts mentioned so far are matched to an impedance of 50 Ω to ensure good transmission conditions. Besides the used attenuators, the cables cause an additional attenuation of several decibel. However, for the measurements performed within this thesis the knowledge of the absolute value of the applied electric field strength on the resonator is not essential.

For measurements with an additional magnetic field the **current source** (Keithley 2601 System SourceMeter[12]) is used to send a defined current I to the homemade coil, mentioned in section 5.1. The generated magnetic field is given by

$$B = k \cdot I \qquad \text{with} \qquad k = 0.229 \,\frac{\mathrm{mT}}{\mathrm{A}}. \tag{5.4}$$

The devices drawn in orange in figure 5.5 can be remote controlled via a GPIB or USB interface. The AD-Card is mounted directly to the mainboard of the measurement computer. For the actual measurement mainly a software bundle, developed in the framework of [Sch16a], was used. This is shortly introduced in section A.3.

5.3 Limitations and error sources of the experimental setup

Despite all arrangements, that are made to ensure stable and reproducible measurement conditions, every echo measurement is subject to various statistical and

[9] meanwhile Keysight, 1400 Fountaingrove Parkway, Santa Rosa, CA 95403-1738, USA

[10] www.arduino.cc

[11] Hewlett-Packard Company, 3000 Hanover Street, Palo Alto, CA 94304-1185, USA

[12] meanwhile Tektronix Inc., 14150 SW Karl Braun Drive, P.O. Box 500 Beaverton, OR 97077, USA

systematic error sources. However, by taking adequate countermeasures, their impact can be significantly reduced. In the following, the known error sources and used methods to reduce their influence on echo measurements are presented. For the discussion, the different error sources are divided into the three topics: temperature, mechanical disturbances and electric disturbances.

5.3.1 Temperature stability

The relaxation processes, determining the course of the decay of the echo amplitude, are sensitive to the temperature of the sample. Thus fluctuating temperatures of the cryostat cause wrong measurements. A general error source is the readout of the carbon thermometer that regulates the cryostat's temperature (compare section 5.1.1). At 10 mK the resistance of this thermometer is in the order of 150 kΩ. Thus the voltages applied to readout the resistance and to determine the temperature can lead to an unintended heating of the carbon resistance, such that the determined temperature is higher than the actual temperature of the cryostat. This effect is in particular relevant at very low temperatures, since there the specific heat and thermal conductance of the thermometer is small. Hence a small heat input can generate a comparatively large temperature change compared to the same heat input at a higher temperature. If the temperature dependence of the relaxation times of tunneling systems in glasses is measured under such circumstances, it can cause an incorrect proportionality. To prevent this parasitic heating, the readout voltages of the thermometer are as small as possible and the carbon resistance is very well thermally coupled to the mixing chamber and experimental platform. The small readout voltages cause a scattering of the measured resistance values and consequently of the calculated temperature. In order to counteract subsequent fluctuations of the heater current, the PID controller, used for the temperature control, is adjusted properly. With the used setting the spread of the measured temperature is at 10 mK usually less than 0.2 %. At higher temperatures the spread is a bit bigger, but well below 1 %.
To ensure that the echo measurements are stopped if the temperature of the cryostat fluctuates too much, the measured temperature is compared to the set temperature before every single two-pulse sequence. If the deviation is more than a predefined value (e.g. 1 % at 10 mK) the measurement is paused and continued after the cryostat temperature is in the accepted range for several minutes.

However, the extensive monitoring of the cryostat's temperature cannot guarantee that the sample has the same temperature as the cryostat. A wide variety of processes can lead to a higher sample temperature which cannot be detected by the cryostat's thermometer. The most obvious are a heating by the high field strengths of the two-pulse sequence, a high repetition rate and not thermalized cables. If this heat input is small, it can be compensated by a gradual reduction of the cryostat's heater current. In this case the overheated sample takes a part of the heating necessary

to stabilize the cryostat's temperature. The spatial separation of the resonator and the thermometer promotes this effect since the introduced heat at the resonator has to heat up the whole experimental platform to be recognized by the thermometer. To prevent such an effect in decay measurements, it is important to adjust the attenuation and repetition rate accordingly in advance. The influence of warm cables can for example be checked by measuring the decay of a sample in two different experimental setups. If the same decay behavior is found, the used heat sinking is sufficient. In chapter 7 it can be seen, that the decay behavior of N-BK7 measured in the reentrant cavity resonator and the micro-fabricated setup are equal, proving the good thermalization of the cables. Both resonators were connected to the same cables, but in the micro-fabricated setup the cables are directly connected to the sample, whereas in the reentrant cavity resonator the cables are connected to the coupling loops of the resonator. A heat input via the cables should cause different temperature offsets and consequently different decay behaviors, as it was observed in measurements on micro-fabricated resonators before parts of the cables were replaced [Pol17].
Further possible heating effects cause no deviation of the sample temperature over the whole measurement, but only during a short time and are caused, for example, by the energy deposition of a muon [Fic13] or radioactive decays nearby. This manifests itself in a reduced echo amplitudes over these periods of time.

5.3.2 Mechanical vibrations

As shown in section 3.2.4, a tunneling system couples not only to electric but also to elastic fields. Consequently, mechanical deformations of the sample lead to a change of the tunneling system's asymmetry energy and thus energy splitting E (compare equation 3.22). Since the phase collection during the free evolution of a tunneling system in an echo sequence is governed by its energy splitting, a variation of E leads to a loss of phase coherence of the respective tunneling system, similar to spectral diffusion. In [Fic07] it was shown that an absolute deformation of the sample by 10^{-3} Å is sufficient to reduce the echo amplitude for two-pulse echoes with a pulse-separation time of 5 µs. Considering the reentrant cavity resonator, mechanical vibrations are most likely transferred via the rod in the center of the cavity to the sample. There are various causes of mechanical disturbances in the cryostat. Some can be reduced by an adaption of the measurement routine, some have to be considered in the design of the cryostat.
The most dominant source of vibrations in the used setup is the refilling of liquid ^{4}He into the dewar and the refilling of the cryostat's 1K-pot. Both processes happen in a regular term and generate vibrations in the cryostat which are visible in the echo measurements. The dewar has to be refilled at least every 48 hours. The 1K-pot is filled for 30 minutes and then closed until the liquid helium reserve in the pot is empty again. In dependence of the measurement cycle the closing lasted from about 20 minutes to several hours. In figure 5.6 stability measurements performed on

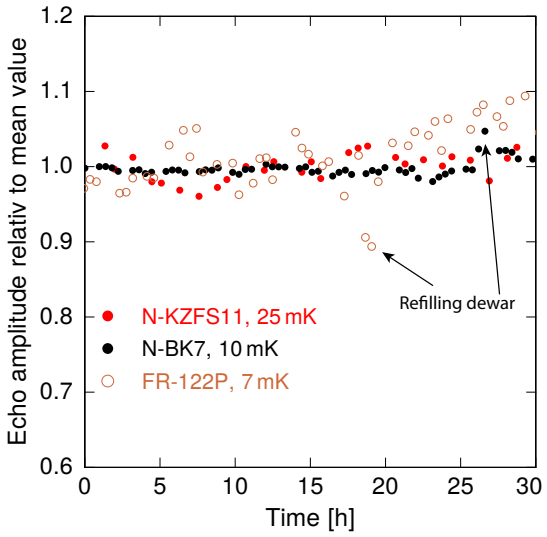

Figure 5.6: Deviation of the echo amplitude from the mean value over time. All data was measured with a pulse duration of $t_1 = 230\,\text{ns}$. The pulse separation time τ_{12} was for N-KZFS11 and N-BK7 5 µs and for FR-122P 2 µs. The attenuation was chosen such that the small angle approximation was fulfilled. The temperature of the cryostat is given in the caption. Every data point is an average over 15000 measurements for N-KZFS11 and 10000 for N-BK7 and FR-122P.

various samples can be seen. In these measurements the echo amplitude was recorded with constant settings over a large period of time to detect possible disturbances. It can be seen that FR-122P shows a small drift of the echo amplitude towards larger values. This is discussed in section 5.3.3. The influence of the helium refilling into the dewar can be seen on the samples FR-122P and N-BK7. Although the temperature of the cryostat was almost the same, the refilling process has a stronger influence on the sample FR-122P. A possible reason is that FR-122P is a polymer and thus softer than the multicomponent glass N-BK7. In addition, the echo amplitude is not reduced for N-BK7, but increased during the filling process. The same behavior was observed in [Sch16a] on the same sample. The exact cause for this behavior is not yet known, but there is a plausible explanation. Right after refilling of the dewar all cables in the dewar are located in liquid helium. The cold temperature maybe causes a reduced attenuation of the signals and thus the echo amplitude is increased. If the mechanical vibrations during the filling process couple less good to a hard multicomponent glass compared to a polymer, the reduced attenuation can maybe overcompensate the reduction by phase coherence destroying processes. To ensure that the refilling of the dewar does not disturb the measurement of the echo decay, the measurement is paused during the refilling process and additional 3 hours. After this time the helium level in the dewar is usually about 75 % and stable measuring conditions are achieved. The influence of the 1K-pot refilling cannot be seen in figure 5.6. In [Sch16a] an investigation of the 1K-pot's influence onto the measurement showed that at helium levels in the dewar lower than 20 % the refilling of the 1K-pot is visible in the data. Thus, in all measurements the dewar is refilled before the level drops below 20 % and the measurement is paused during the filling process of the 1K-pot (30 minutes) and additional 5 minutes.

Another source of vibrations, present during the whole measurement, origins from the pumps that circulate the ^{3}He/^{4}He mix and pump the 1K-pot. These pumps

can generate mechanical vibrations and sound waves in the pipes and the gas. To reduce their influence on the measurement, the pumps are located in the basement under the laboratory. To prevent disturbances via the helium reserve in the dewar, an exhaust silencer is mounted between the dewar's exhaust pipe line and the helium recovery.
In addition, sound waves or vibrations generated in the laboratory can couple to the cryostat and can be transferred to the sample. A measurement with a microfabricated resonator and a speaker on top of the cryostat showed that especially low-frequency waves (about 100 Hz to 250 Hz) couple to the sample and cause a reduced echo amplitude. Higher frequencies up to 15 kHz showed no influence. This measurement shows that a silent environment is important for stable measurement conditions.

Finally, during a measurement with applied magnetic field a vibration of the resonator leads to eddy currents and thus to a heating effect near the sample. For a sample containing nuclear quadrupole moments this effect would hardly be detectable since the echo amplitude changes with the magnetic field, too. Since the resonator is always mounted at the same position in the cryostat, such a possible heating effect should also exist in measurements on samples containing no nuclear quadrupole moments. In measurements on corresponding samples no heating effect is observed, indicating that this effect is negligible.

5.3.3 Stability and noise of the electronic setup

The electronic components, in particular their noise, used to excite the tunneling systems and readout the echo can influence the echo measurement in various ways. Besides a direct impact on the tunneling systems, the noise and stability of the devices also influence the measured signal and limit the measurement range and accuracy.
In general, noise from the room temperature electronics can enter the resonator via the coupling loops and lead to a variation of the electric field in the resonator's capacity, where the sample is located. This additional electric bias shifts the asymmetry energy of the tunneling systems in dependence of the orientation of their dipole moments relative to the electric field (compare equation 3.22 and 3.26). Thereby the tunneling systems can lose their phase coherence similar to spectral diffusion theory. On the output side of the resonator, noise is caused by the low temperature amplifier. On the input side the noise from the room temperature electronics is reduced by the cold attenuator, located in the cryostat. An explicit investigation of the influence of noise on the echo measurements was done in [Fic13]. Therefore the noise of a 50 Ω resistor was amplified by two high frequency amplifiers and then coupled into the excitation branch without being pulsed. The recorded echo became more noisy, but the decay behavior was unaffected. Thus the precautions regarding the noise reduction are sufficient. In addition, the resonator itself acts as some kind of frequency

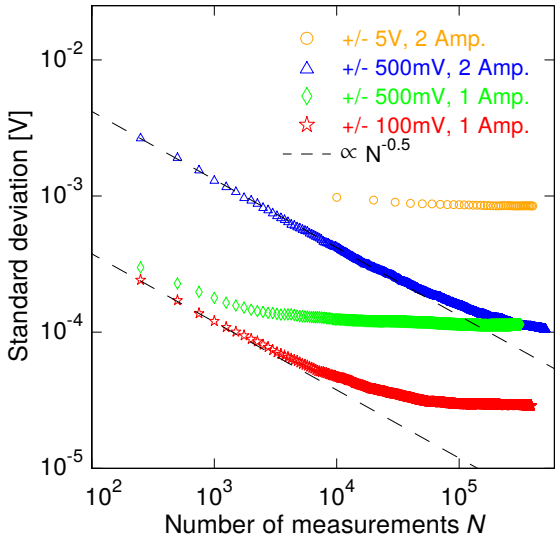

Figure 5.7: Standard deviation of the noise measured beside the echo signal in dependence of the number of averaged measurements. In the caption the first value refers to the used sensitivity of the AD-card and the second refers to the number of amplifiers after the mixer. Plot taken from [Sch16a].

filter by suppressing noise contributions far from the resonance frequency.
Every single recorded echo is subject to noise. Towards large pulse separation times or at high temperatures the echo becomes very small and can thus become indistinguishable from the noise. If the noise is purely statistical, it can be minimized by averaging many measurements. In this case the standard deviation is proportional to $1/\sqrt{N}$ with N being the number of measurements. Due to systematic noise contributions, the noise cannot be reduced to an arbitrarily small level. A detailed investigation of the noise reduction by averaging different amounts of measurements was done in [Sch16a] for the current setup. The standard deviation in dependence of the averaged number of measurements is shown in figure 5.7. For all shown cases the uncertainty follows the $1/\sqrt{N}$ behavior up to a certain number of averaged measurements. For large N, the systematic uncertainty prevails. The limiting systematic contribution depends on the chosen sensitivity of the AD-Card. In most measurements, shown in this thesis, both amplifiers and a sensitivity of $\pm 500\,\mathrm{mV}$ was used. Consequently, an averaging of measurements improves the data quality up to several hundred thousand measurements.
Besides limiting the measurement range, the noise adds an uncertainty to the determined echo amplitude. The error depends on the number of averaged measurements. An estimation of the error relative to the signal size is given by the signal to noise ratio, which is calculated during the measurements (compare section A.3 and figure A.4). The minimal accepted signal to noise ratio is usually around 5. The signal to noise ratio is calculated by the ratio of the maximal signal in the time window of the echo and the standard deviation of the noise in a 5 µs window far apart from the echo. For a signal to noise ratio of 5, the noise contributes with an error of about 20 %. However, this value is only reached at the largest measured pulse separation times of the respective samples.

A further issue is the long time stability of the electronic components. To check,

amongst others, their influence onto decay measurements so-called reference echoes are measured in fixed time intervals during decay measurements. A reference echo is a regular echo, measured at a short pulse separation time (usually $\tau_{12} = 2\,\mu s$ or $5\,\mu s$) so that a small number of measurements is sufficient to reach a good signal to noise ratio. In figure 5.8, a selection of the, in the framework of this thesis, measured reference echoes of the samples N-KZFS11, N-BK7 and As_2S_3 are shown. The reference echoes show in general a small tendency towards larger echo amplitudes with increasing measuring time. For all measurements the largest overall drift was about 2.5 % per 10 hours. This behavior was also observed in previous studies on molecular and multicomponent glasses e.g. [Rüd08, Baz08, Fic13, Wol14, Sch16a]. The largest drift reported in [Fic13] is about 7 % in 10 hours. The reason for these drifts is not fully clarified. Since reference echoes do not allow to distinguish between effects of the sample and electric artifacts, different causes are possible.
An obvious cause is that the respective sample is not well thermalized and the rising echo amplitude is caused by the further cooling of the sample. Since this argument can at this point not easily ruled out, it is discussed in more detail in section 6.2.1. Another possibility is the long time stability of the electric components in the circuitry. In measurements done in [Baz08] an additional reference pulse was sent through the circuitry after every echo. This reference pulse is independent of the sample and cryostat temperature and thus suitable to investigate drifts in the electronic setup. A measurement of the reference pulse over time showed a drift towards larger values as well. Extrapolated to a measurement window of 10 hours the amplitude of the reference pulse increases by about 2.8 %. For the echo amplitude a similar increase was observed in this study. A possible reason for the observed drift is a variation of the gain of the amplifiers in the readout branch over time. This can either be caused by processes in the amplifiers or in the power supplies of these devices. A further reason could be varying environmental conditions. For example a change in the room temperature of the laboratory or the varying helium level in the

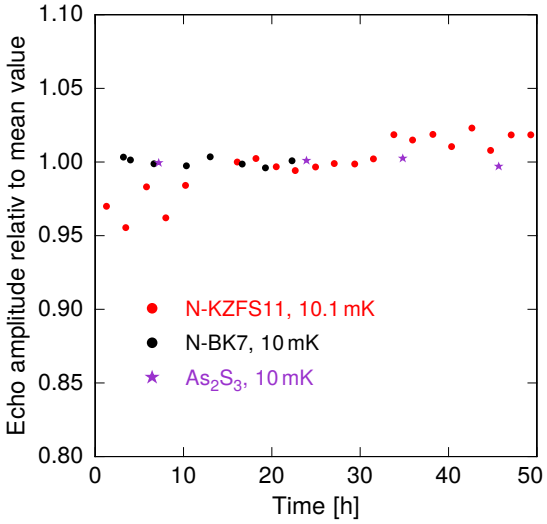

Figure 5.8: Deviation of the echo amplitude from the mean value over time for the reference echoes measured on the samples N-KZFS11, N-BK7 and As_2S_3 at a cryostat temperature of 10 mK and 10.1 mK. The pulse separation time was $2\,\mu s$ for As_2S_3 and $5\,\mu s$ for N-KZFS11 and N-BK7. The number of measurements averaged per data point are 750 for N-KZFS11 and N-BK7 and 50000 for As_2S_3.

dewar, which directly influences the cables going through the liquid helium reservoir and the low temperature amplifier. However, the last mentioned possibility should rather lead to some kind of oscillating behavior.
The drift rate observed in [Baz08] for the electric components is in accordance with the one observed in the measurements performed in the framework of this thesis. If the drift would be purely caused by electric artifacts, the echo amplitude could be corrected. With the known drift rate from the reference echoes and the time stamps of the measured echo amplitudes, the amplitude can be shifted accordingly. If also some thermalization effects, like long time heat releases, are present, a correction is not trivial since the relaxation behavior would slightly change with time. Given that the origin of the drifts is not completely clarified, the echo amplitudes, shown in the framework of this thesis, are not corrected and the drift enters as an additional error on the echo amplitude. Since the echo amplitude changes by several orders of magnitude during a decay measurement, this error affects the decay behavior only marginally. For future measurements it would be beneficial to use an additional reference pulse as well, to discriminate between drifts of the electronic setup and the sample.

A last point, which can influence the measured echo amplitude are high frequency signals that couple into the electric circuitry. These signals are caused, for example, by mobile phones as shown in figure 5.9. If these disturbed echo sequences are incorporated into the averaging, they modify the echo amplitude. To prevent this, a fast Fourier transformation is performed for every single echo sequence by the measurement software. Thereby disturbances of this kind are detected and the corresponding echo sequence is deleted. Since the Fourier transformation slows down the measurement, it can be turned off after a certain amount of measurements is averaged (e.g. 20000). In this case the error caused by a disturbed signal is negligible.

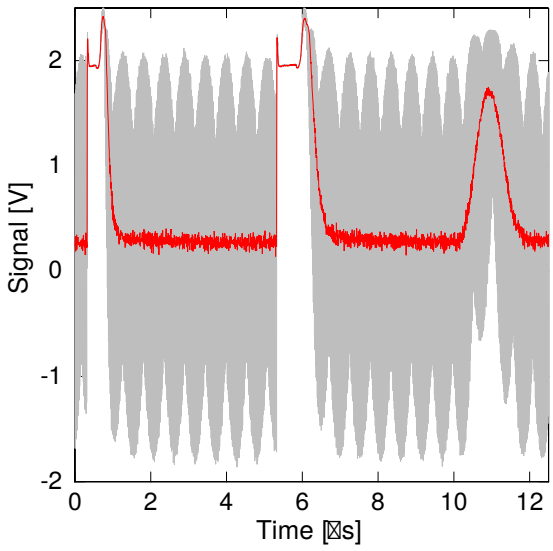

Figure 5.9: Comparison of a measurement which is disturbed by a high frequency signal coupled into the circuitry (shown in gray) and a regular echo sequence (shown in red). Plot taken from [Sch16a].

5.4 Samples

In the framework of this thesis the influence of nuclear quadrupole moments on the decay behavior of tunneling systems is investigated. Therefore various glasses containing atoms carrying nuclear quadrupole moments are examined and data, obtained in previous measurements on further glasses, are collected. All samples are dielectric glasses and can be roughly classified as shown in figure 5.10. The multitude of examined glasses contains samples, without atoms carrying nuclear quadrupole moments up to samples which carry large nuclear quadrupole moments. Thus this selection is well suited to investigate the influence of nuclear quadrupole moments on the decay behavior of tunneling systems at low temperatures. In the following, at first the samples measured in the framework of this thesis are introduced. Several of those glasses were studied in collaboration with bachelor and master students. Afterwards the glasses investigated in other publications are shortly addressed.

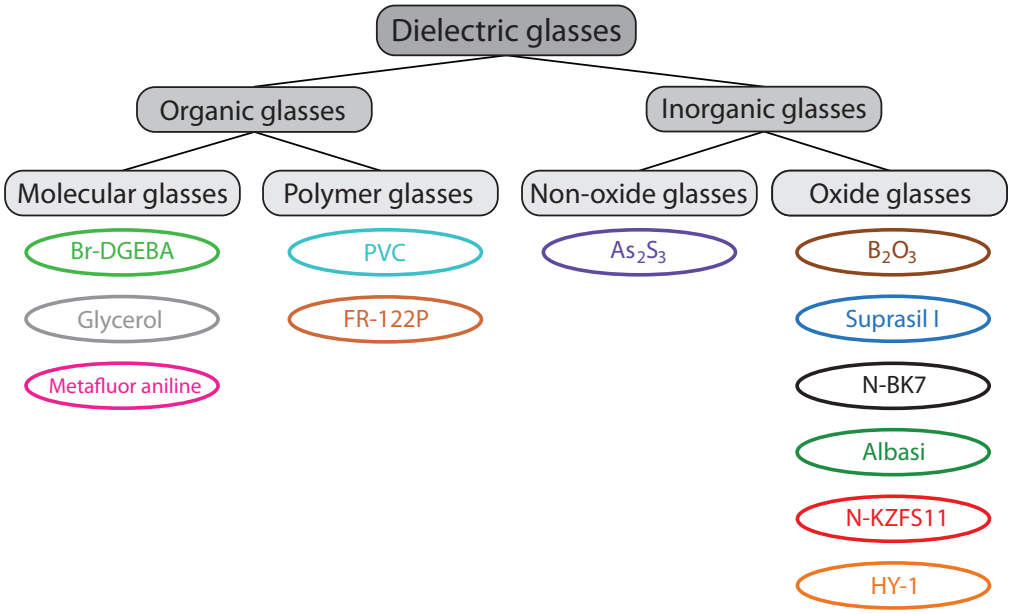

Figure 5.10: Classification of the glasses studied in the framework of this thesis.

5.4.1 Measured samples

N-BK7

The multicomponent glass N-BK7 is a standard optical glass, manufactured by the company Schott[1], which is widely used in various low temperature measurements, e.g. [Arn75, Woh01a, Luc16, Fre16, Aue19, Kör19]. Since also various echo measurements were already performed on this material [Lud03, Fic13, Bur13, Wol14, Sch16a],

[1]Schott AG, Hattenbergstr. 10, 55122 Mainz, Germany

it is also a suitable reference sample for the microfabricated resonators presented in chapter 7. The sample used in the reentrant cavity resonator was a disc with a diameter of 10 mm and a thickness of 0.5 mm. The samples used in the microfabricated resonators were rectangular with thicknesses between 1 mm and 0.2 mm. The measurements on N-BK7, shown in this thesis, were partially performed within [Sch16a]. In the reentrant cavity resonator, the resonance frequency at a temperature of 10 mK was about 950 MHz and the quality factor approximately 150. The composition of the glass is given in table 5.1. The bold written atoms have isotopes with a significant natural abundance that carry nuclear quadrupole moments (compare table A.1). According to section 2.2.1, the glass network is most likely build by the silicon, boron, aluminum and oxygen atoms whereas the sodium, potassium and barium have the function of network modifiers.

N-BK7							
	SiO_2	Na_2O	B_2O_3	K_2O	BaO	Al_2O_3	
Molar percent	74.8	10.1	9.6	4.7	0.76	0.03	
	Si	**Na**	**B**	**K**	**Ba**	**Al**	O
Atomic percent	24.9	6.8	3.8	3.1	0.38	0.01	60.9

Table 5.1: Chemical composition of BK7 according to [Lud03]. The bold written atoms have isotopes with a significant natural abundance that carry nuclear quadrupole moments (compare table A.1).

N-KZFS11

The glass N-KZFS11 is a multicomponent glass and manufactured by Schott[1]. Measurements of the dielectric properties of the glass from room temperature to very low temperatures were conducted amongst other in [Däh10, Wes15, Sch16b, Luc16, Aue19]. The low frequency dielectric measurements in [Luc16] showed that large nuclear quadrupole moments influence the relaxation behavior of tunneling systems at low temperatures. The composition of N-KZFS11 is shown in table 5.2. Besides various isotopes with nuclear quadrupole moments, N-KZFS11 contains about 1.5 at.% tantalum, which carries a very large nuclear quadrupole moment of 3.14 barn. In the entirety of all studied samples N-KZFS11 is, together with HY-1, one of the representatives with large nuclear quadrupole moments. The sample used in the reentrant cavity resonator was a square with an edge length of 11.5 mm and a thickness of 0.5 mm. At a temperature of 10 mK the resonance frequency of the resonator was about 871 MHz and the quality factor 208. Some of the measurements on N-KZFS11 shown in this thesis were performed in collaboration with [Tsu17].
The glass matrix of N-KZFS11 is most likely also build by the classical network formers silicon, boron and the corresponding oxygen. Sodium is a classical network modifier. The other elements are intermediate oxides. Thus their position is not easy

to determine. Different studies showed that niobium and tantalum form a negatively charged $[(Nb/Ta)O_6]^-$ octahedra and act as network former in a glass, if additional network modifiers with a valence of 1 (like sodium) are present to compensate for the charge [Ver94].

N-KZFS11								
	SiO_2	Na_2O	B_2O_3	ZrO_2	Ta_2O_5	Nb_2O_5	ZnO	
Molar percent	40	16	25	12.6	5.1	0.3	0.8	
	Si	**Na**	**B**	**Zr**	**Ta**	**Nb**	**Zn**	O
Atomic percent	13	11	9.8	4.2	1.5	0.1	0.4	60

Table 5.2: Chemical composition of N-KZFS11 according to [Luc16]. The given values have an accuracy of ±10 %. The bold written atoms have isotopes with a significant natural abundance that carry nuclear quadrupole moments (compare table A.1).

HY-1

The multicomponent glass HY-1 is manufactured by Hoya Optics[2]. Its dielectric properties were studied amongst others in [Hau15, Bol15, Zei15, Luc16]. First dielectric polarization echoes were measured in [Wol14]. The composition of HY-1 is shown in table 5.3. It contains about 0.5 at.% holmium which carries a nuclear quadrupole moment of 3.58 barn. In the low frequency dielectric measurements of [Luc16], HY-1 showed besides N-KZFS11, the crucial role of nuclear quadrupole moments on the relaxation behavior of tunneling systems at low temperatures. Aside the large nuclear quadrupole moment, holmium has also a strong magnetic moment and spin orbit coupling. HY-1 even sticks to strong magnets [Rei]. The sample used in the reentrant cavity resonator was a square with an edge length of 12 mm and a thickness of 0.5 mm. The resonance frequency of the resonator at a temperature of 10 mK was about 952 MHz and the quality factor 224. All measurements of HY-1, shown in the framework of this thesis, were conducted in collaboration with [Sin16b, Tsu17].
Concerning the role of the holmium atoms in the glass matrix, it is assumed that it has the role of a network modifier and is embedded loosely in the glass matrix. This assumption is supported by measurements of the absorption spectrum of holmium oxide glass which differs only slightly from Ho_2O_3 in solution [Wei85, All07]. Measurements in [Nei15, Del15] showed also an increased ion conductivity of HY-1 compared to N-BK7 in the temperature range of 80 K to 350 K. Since their composition is similar, except for holmium, it can be assumed that holmium ions are responsible for the increased conductivity. This also supports the assumption that holmium acts as network modifier in HY-1.

[2]HOYA Candeo optronics corporation, 3-5-24 Hikawa-cho, Toda-shi, Saitama 335-0027, Japan

HY-1							
	SiO_2	Na_2O	B_2O_3	BaO	Ho_2O_3	Sb_2O_3	
Molar percent	74	18	3.8	3.4	1.2	0.1	
	Si	**Na**	**Ba**	**Ho**	**B**	**Sb**	O
Atomic percent	25	12	1.7	0.5	1.5	0.03	60

Table 5.3: Chemical composition of HY-1 according to [Luc16]. The given values have an accuracy of ±2 %. The bold written atoms have isotopes with a significant natural abundance that carry nuclear quadrupole moments (compare table A.1).

As_2S_3

The chalcogenide glass As_2S_3 is produced by the company Schott[1]. Usually this material is used in infrared applications due to its good transmission properties in this wavelength range. Its glass transition temperature is at 197 °C [Sch18b] and thus clearly lower compared to the oxide glasses N-BK7, N-KZFS11 and HY-1 which have transition temperatures above 500 °C [Sch07, Sch14, Hoy16]. Dielectric and acoustic investigations were performed in [Jac92, Mün19, Mül19, Bli20].
For studying the influence of nuclear moments on the relaxation behavior in glasses this sample is well suited. Due to its stoichiometry it contains 40 at.% of the quadrupole carrying arsenic (compare table 5.4) and every thinkable tunneling system either contains at least one arsenic atom or is connected to it. The quadrupole splitting of arsenic in As_2S_3 is also well known (compare table A.1).
The used sample was a disc with an diameter of 10 mm and a thickness of 3 mm. The resonance frequency of the resonator at a temperature of 10 mK was about 1403 MHz and the quality factor 212. The measurements presented in this thesis were performed together with [Arn19].
The structural properties of As_2S_3 are addressed in section 2.2.1.

As_2S_3		
	S	**As**
Atomic percent	60	40

Table 5.4: Composition of As_2S_3. The bold written atoms have isotopes with a significant natural abundance that carry nuclear quadrupole moments (compare table A.1).

Poly(vinyl chloride) - PVC

The thermoplastic amorphous polymer poly(vinyl chloride) belongs to the group of organic glasses. The structural formula of the repetitive unit of PVC is illustrated in figure 5.11. It consists of a carbon backbone with a chlorine atom at every second carbon atom. Thus 1/6 of the atoms in the material are quadrupole carrying isotopes

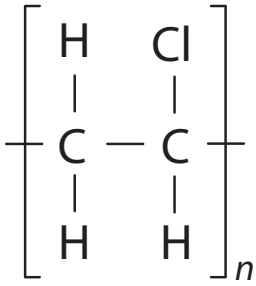

Figure 5.11: Structural formula of the repetitive unit of PVC.

of chlorine (compare table 5.5). The material, used in the framework of this thesis, was produced by the company Goodfellow[3].
Dielectric investigations were performed in [Sin16a, Sch17, Aue19, Säu21] and the thermalization behavior was studied in detail in [Str18]. The used sample was a disc with a diameter of 10 mm and a thickness of 0.38 mm. At 10 mK the resonance frequency of the resonator was about 1160 MHz and the quality factor 80. The structural properties are discussed in section 2.2.2.

PVC			
	H	C	**Cl**
Atomic percent	50	33.33	16.67

Table 5.5: Composition of PVC. The bold written atoms have isotopes with a significant natural abundance that carry nuclear quadrupole moments (compare table A.1).

FR-122P

The polymer with the trade name FR-122P is distributed by the company ICL[4] and usually used as insulating flame retardant. Its structural formula is shown in figure 5.12. The high content of the quadrupole carrying bromine isotopes, which is often present in such materials, makes it a suitable material for studying the influence of nuclear moments on the low temperature behavior of tunneling systems. For FR-122P the bromine content by weight is minimal 62.5 % [Icl]. This corresponds to about 11 at.%. The complete composition is given in table 5.6. The exact quadrupole splitting of this material is unknown, but it can be assumed that it is similar to other materials in which bromine is covalently bound to a carbon atom. For organic glasses this assumption is possible since the intramolecular forces are usually significantly stronger than the intermolecular ones. The isotopes of other elements present in the material, that carry a nuclear quadrupole moment, have only a negligible natural abundance (compare table A.1).
The material, obtained from the company ICL, was a powder from which a disc with

[3]Goodfellow Cambridge Ltd, Ermine Business Park, Huntingdon, England
[4]ICL Industrial Products, Kroitzer St. 12, Beer Sheva 84101, Israel

FR-122P			
	H	C	**Br**
Atomic percent	50	39.1	10.9

Table 5.6: Composition of FR-122P based on the assumption that $x = 2$ and $y = z = 5$ in figure 5.12. The bold written atoms have isotopes with a significant natural abundance that carry nuclear quadrupole moments (compare table A.1).

a diameter of 10 mm and a thickness of 0.65 mm was produced under the influence of pressure and temperature. A detailed description of the sample fabrication is given in [Sch18c]. The resonance frequency of the reentrant cavity resonator at 10 mK was circa 1266 MHz and the quality factor about 130.
Dielectric and acoustic measurements were performed in [Her17, Sch18c] and showed the glassy behavior of the material.

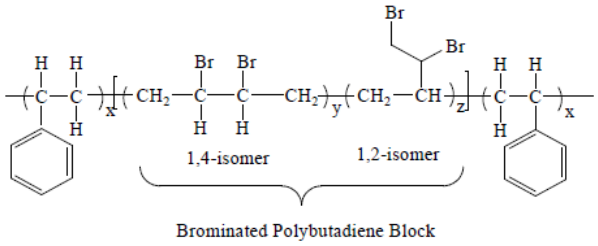

Figure 5.12: Structural formula of the polymer FR-122P. Picture taken from [Icl].

Br-DGEBA

The monomer Br-DGEBA (Bisphenol A diglycidyl ether, brominated) is a brominated epoxy resin used as an insulating flame retardant for example in electronic printed circuit boards. The structural formula of the material is shown in figure 5.13. Equivalent to FR-122P, only the bromine atoms are relevant to discuss the influence of nuclear quadrupole moments on the relaxation behavior of tunneling systems. The isotopes of the other elements carrying a nuclear quadrupole moment present in the monomer have only a very small natural abundance. The bromine content by weight is 48 % [Sig], which corresponds to about 11 at.%. The complete composition is given in table 5.7. The exact quadrupole splitting of this material is not known, but should be similar to the one of other materials with a Br-C bond.

Br-DGEBA				
	H	C	**Br**	O
Atomic percent	37.8	42.8	11.2	8.2

Table 5.7: Composition of Br-DGEBA based on the molecular formula $C_{42}H_{37}Br_{11}O_8$ [Sig]. The bold written atoms have isotopes with a significant natural abundance that carry nuclear quadrupole moments (compare table A.1).

The available material was a powder obtained from Sigma Aldrich[5]. The powder was carefully molten (melting temperature 55 - 56 °C [Sig]) and then put into the reentrant cavity resonator which was heated as well. This type of sample preparation ensured a very good thermal coupling between the resonator and the sample. The exact thickness of the sample could not be determined, but it should be about 0.5 mm. The resonance frequency at a temperature of 7.5 mK was about 1122 Mhz and the quality factor 176. The measurements on Br-DGEBA were performed in collaboration with [Haa18b].
Dielectric measurements on this material showed the glassy behavior and were performed in [Aß18, Wer18, Sch18c]. A detailed study of the thermalization behavior was done in [Low19].

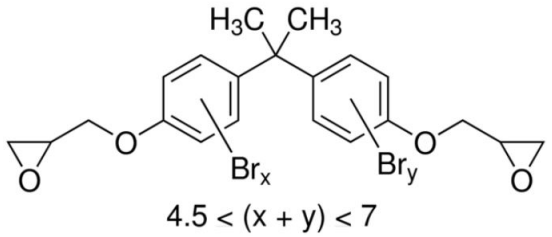

Figure 5.13: Structural formula of the polymer Br-DGEBA. Picture taken from [Sig].

5.4.2 Further discussed samples

B_2O_3

Due to its stoichiometry, the inorganic glass B_2O_3 contains 40 at.% of the quadrupole carrying boron (compare table 5.8). Equivalent to As_2S_3, every tunneling system present in the sample either contains or is connected to a boron atom.
The data shown in the framework of this thesis is taken from [Lud00].

$\mathbf{B_2O_3}$		
	O	**B**
Atomic percent	60	40

Table 5.8: Composition of B_2O_3. The bold written atoms have isotopes with a significant natural abundance that carry nuclear quadrupole moments (compare table A.1).

Suprasil I

The quartz glass Suprasil I contains about 1200 ppm OH^- ions. Neglecting the 1200pm OH^- ions, its composition is given in table 5.9. Apart from the isotope

[5]Sigma-Aldrich Chemie GmbH, Eschenstrasse 5, 82024 Taufkirchen, Germany

^{17}O, which has a negligible natural abundance, no elements with nuclear quadrupole moments are present in the material. Thus it is a well suited reference sample. The data shown in the next chapter is taken from [Ens96a, Lud03]. The structural properties of vitreous SiO_2 are similar to the one shown in figure 2.4.

Suprasil		
	Si	O
Atomic percent	33.33	66.67

Table 5.9: Composition of the sample Suprasil.

Albasi

The multicomponent glass Albasi or BAS (a-BaO-Al_2O_3-SiO_2) contains several isotopes carrying nuclear quadrupole moments (compare table 5.10). The glass network is most likely build by the silicon, boron and aluminum atoms together with the oxygen. The other isotopes act as network modifiers.
The data shown in chapter 6 is taken from [Lud02, Arc13]. Further two- and three-pulse echo measurements were performed in [Ahr13].

Albasi							
	SiO_2	Na_2O	B_2O_3	K_2O	BaO	Al_2O_3	
Molar percent	72.7	0.28	0.72	0.064	17	8.8	
	Si	**Na**	**B**	**K**	**Ba**	**Al**	O
Atomic percent	24.2	0.19	0.29	0.04	8.05	3.52	62.79

Table 5.10: Chemical composition of Albasi according to [Lud03]. The bold written atoms have isotopes with a significant natural abundance that carry nuclear quadrupole moments (compare table A.1).

Glycerol

Glycerol allows a defined deuteration and thus a systematic study of the influence of nuclear quadrupole moments on the decay behavior of tunneling systems via the isotope effect. The structural formulas of ordinary glycerol up to glycerol-d7 are shown in figure 5.14. In dependence of the degree of deuteration the sample contains up to 57 % of atoms which carry a nuclear quadrupole moment (glycerol-d8). The molecules are connected by hydrogen bonds [Baz08] and build thus a molecular glass. The data shown in section 6 was measured on glycerol-d0 which has the composition given in table 5.11. The corresponding data is taken from [Bra04a, Nag04]. Further echo measurements were performed amongst others in [Baz07, Baz08, Fic07, Fic09].

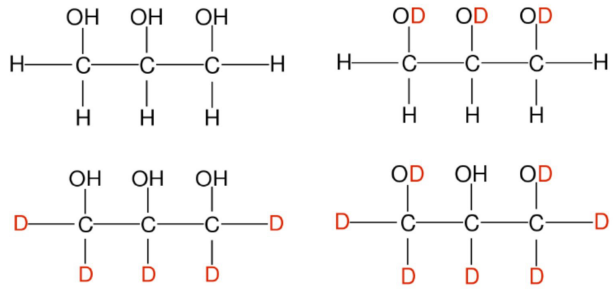

Figure 5.14: Structural formula of glycerol, glycerol-d3, -d5 and glycerol-d7. Picture taken from [Baz08].

Glycerol-d0			
	H	C	O
Atomic percent	21.4	57.2	21.4

Table 5.11: Composition of Glycerol-d0

Meta-fluoroaniline

The molecule m-fluoroaniline forms a molecular glass below a temperature of about 173 K [Bra04a]. It contains one nitrogen atom per molecule which carries a nuclear quadrupole moment. This corresponds to about 7 at.%. The complete composition of metaflour aniline is given in table 5.12. The data shown in section 6 is taken from [Bra04a]. More information regarding the sample can be found in the same publication.

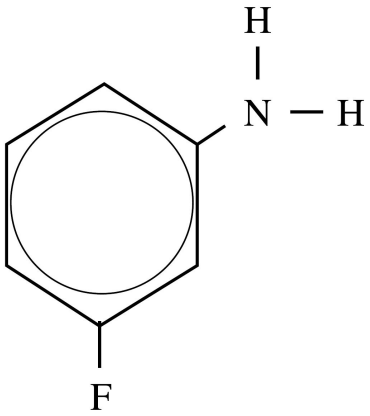

Figure 5.15: Structural formula of m-fluoroaniline. Picture taken from [Bra04a].

m-fluoroaniline				
	H	C	**N**	F
Atomic percent	42.9	42.9	7.1	7.1

Table 5.12: Composition of m-fluoroaniline based on the molecular formula $FC_5H_4NH_2$. The bold written atoms have isotopes with a significant natural abundance that carry nuclear quadrupole moments (compare table A.1).

6. Experimental results

In this chapter the experimental results obtained in the framework of this thesis are presented. First, the analysis of the data is introduced. After that, the preparatory measurements, which are performed before the actual decay measurements, are discussed. These include the thermalization, the measuring rate and the electric field dependence of the echo amplitude. Subsequently, the decay measurements, performed on the samples introduced in section 5.4, are shown with a focus on the influence of nuclear moments on the decay behavior. Thereafter, the magnetic field dependence of the echo amplitude is discussed.

6.1 Data evaluation

The quantity of interest in all measurements shown in the following is the echo amplitude. Before the echo amplitude can be determined from the measured echo sequence, the underlying background has to be subtracted. In figure 6.1 an echo sequence measured on the sample PVC is shown in black. The small echo after the second pulse is on top of a nonconstant background which is amongst others caused by the ring-down of the resonator. The subtraction of this background is in dependence of the pulse separation time done in two different ways. For pulse separation times larger or equal 20 µs, the ring-down of the second pulse of the echo sequence is completely over and the echo lies on a flat baseline. Thus for measurements with $\tau_{12} \geq 20\,\mu s$ an offset correction is sufficient. For pulse separation times smaller than 20 µs, the background is subtracted more elaborately and done in three steps. In the following all steps needed for the analysis of measurements at small pulse separation times are introduced.

For every echo measurement a background measurement is performed at a pulse separation time of $\tau_{12}^{\mathrm{Echo}} + \Delta\tau$. Usually $\Delta\tau$ is set to 50 µs or 300 µs. This large pulse separation time ensures that the echo appears far away from the second pulse. During the measurements for this thesis, the value of $\Delta\tau$ changed from 300 µs to 50 µs, since it turned out that 50 µs are sufficient for a good background correction and the size of the saved data is be reduced. The measured background is afterwards shifted in time by $-\Delta\tau$, such that the left sides of the second pulses of the echo and the background sequence align (compare figure 6.1). Then the background sequence is subtracted pointwise from the echo sequence. Thereby it is assumed that the shape of the signal after the second pulse is independent of the pulse separation time. In a second step an offset correction is performed. Therefore the signal in an area far away from the two pulses and the echo is averaged in a 5 µs window and the obtained

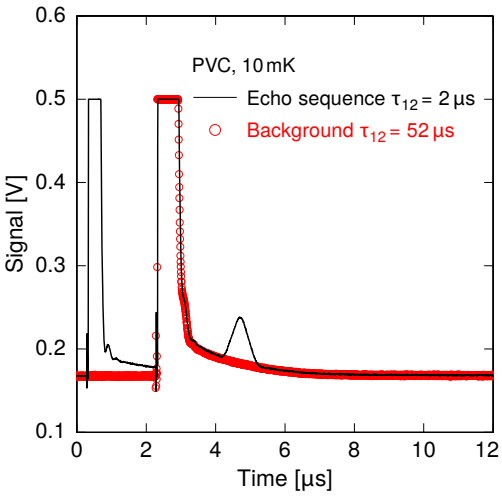

Figure 6.1: Echo sequence measured on PVC with a pulse separation time of 2 µs (black) and corresponding background sequence with a pulse separation time of 52 µs (red). Both sequences are averages of 5000 single measurements. It can be seen that the echo lies on a nonconstant background.

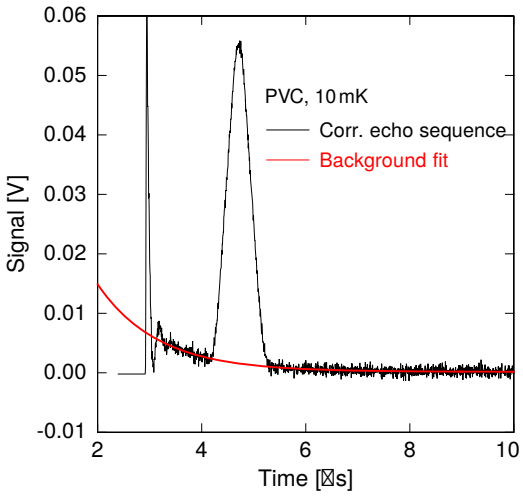

Figure 6.2: Echo sequence after the first background correction (black) and the fit used for the subtraction of the remaining background (red). The first background correction includes a subtraction of the background sequence and an offset correction.

value is subtracted from every point of the echo sequence (for the two-pulse sequence shown in figure 6.1 an appropriate time window would be 20 µs to 25 µs). This offset correction ensures that the echo sequence has a baseline of $y = 0$. The result of the two introduced background correction steps, applied to the echo sequence shown in figure 6.1, is depicted in black in figure 6.2. It can be seen that the baseline is flat and equal to $y = 0$ at large times, but shortly after the second pulse the background exhibits still a slope. This slope shows that the assumption of equally shaped pulses of the echo and the background sequence is not completely correct. Different effects can cause this discrepancy. One possibility is that the shape of the second pulse is influenced by the tunneling systems which are already decayed at the time $\tau_{12}^{\mathrm{Echo}} + \Delta\tau$. Furthermore, the amplifiers in the readout electronics, which are saturated during the pulses, have more time to recover in the background sequence compared to the echo sequence. This can influence their performance.
The remaining background is removed in a third correction step. In dependence of the shape of the signal, either an exponential function of the form

$$f_{\mathrm{exp}}(t) = a\mathrm{e}^{-b((t-t_0))} + c \tag{6.1}$$

with the free parameters a, b, c and t_0 or a straight line

$$f_{\mathrm{line}}(t) = a \cdot t + b \tag{6.2}$$

with the free parameters a and b is fitted to the signal. For the fit only the time intervals left and right of the echo signal are considered. The fitted exponential

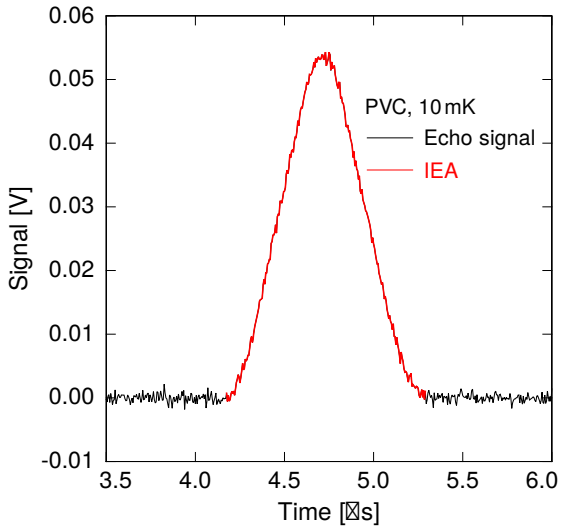

Figure 6.3: Background corrected echo signal (black) and window used for the calculation of the integrated echo amplitude (IEA) (red).

function can be seen in figure 6.2. The subtraction results in an echo on a flat baseline as shown in figure 6.3. Since the background component, present after the subtraction of the background sequence, exists only directly after the second pulse, the third step of the background correction is not necessary up to a pulse separation time of 20 µs. In dependence of the sample and the measurement settings, the third step of the background correction is only necessary for pulse separation times smaller than 5 µs to 10 µs.

After the background subtraction the echo amplitude is determined. In the framework of this thesis the integrated echo amplitude is used which is proportional to the actual echo amplitude. For the determination of this quantity, the start and end point of the echo signal is determined by eye. The respective time window is shown in red in figure 6.3. Then every data point in this time window is multiplied by the time distance between two points. This time distance is the same for all data points and given by the sampling rate of the AD-card. The used sampling rate was 200 $^{\mathrm{MS}}/_{\mathrm{s}}$ which corresponds to a point distance of 0.005 µs. This calculation of the integrated echo amplitude has the advantage that the noise, superimposed the echo, is automatically averaged. In principle the integrated echo amplitude is the integrated step function of the echo.

The pointwise subtraction of the background from the echo sequence as well as the offset correction is performed by the measurement software. In the framework of this thesis, the further steps are performed by hand to simultaneously check the data quality, decide whether a background fit is needed and define the time window for the the calculation of the integrated echo amplitude. In addition, the software is also capable to determine the integrated echo amplitude on the basis of the pointwise and offset corrected data. These values are amongst others used for the signal to noise determination. On the basis of this value is decided how many measurements are averaged at a respective pulse separation time (compare section A.3). Furthermore,

the automatically calculated echo amplitudes are sensitive to drifts in the background or the echo itself and are thus sufficient to check the stability of the measurement.

In the following the integrated echo amplitude is for simplicity just called echo amplitude. All data which was obtained together with the bachelor and master students [Tsu17, Sin16b, Arn19, Haa18b] (compare section 5.4.1) or in the framework of [Sch16a] were re-analyzed since the background correction improved.

6.2 Preparatory measurements

Before the decay behavior of the echo amplitude can be measured, the experimental setup has to be adjusted accordingly. The procedure is shortly introduced in section A.3. In the following, the results of the different steps are discussed. At first, the thermalization behavior is addressed. Next, the influence of the measuring rate is shortly mentioned. Finally, the pulse duration and electric field dependence of the echo amplitude are discussed.

6.2.1 Thermalization

Since the relaxation processes, causing the decay of the echo amplitude, are sensitive to temperature a defined and stable temperature is essential. As experimental setups used in low temperature experiments usually do not allow to determine the sample temperature directly, thermalization measurements are performed. Thereby usually the to be investigated quantity, here the echo amplitude, is measured in dependence of the temperature. For lower temperatures a larger echo amplitude is expected, since relaxation processes are less effective and the occupation difference increases. In figures 6.4 and 6.5 the thermalization measurements on As_2S_3 and PVC are shown as examples. In both measurements the temperature steps and the steps in the echo amplitude coincide very well, showing that the samples follow the temperature of the cryostat. However, these measurements usually need a lot of measurement time since the sample needs time to adapted to the new temperature. In addition, for most of the samples investigated in the framework of this thesis the echo amplitude is very small such that many measurements need to be averaged (compare section 6.4.1). For example, the measurement of As_2S_3 needed 80000 single measurements per data point for the echo and the background sequence each. Due to limited overall measurement time it was hence not always possible to measure the thermalization behavior in such detail.
For the samples studied within this thesis, it was sometimes possible to investigate the thermalization behavior during temperature ramps of another experiment, measuring the temperature dependence of the dielectric constant, located in the same cryostat.
This was for example the case for PVC, shown in figure 6.5, and is the reason for the high amount of different temperature steps in this measurement. However, this is

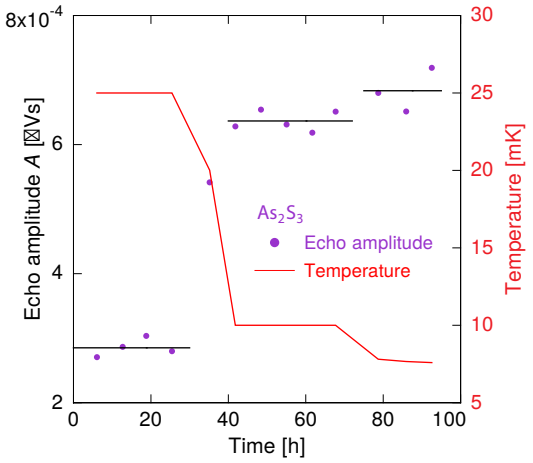

Figure 6.4: Thermalization measurement of the sample As_2S_3 between 25 mK and about 7.5 mK. The echo amplitude is depicted on the left y-axis and the temperature on the right. The black lines are a guide to the eye. It can be seen that the echo amplitude follows the temperature well. Due to the very samll echo amplitude there is a comparably large scattering of the data points.

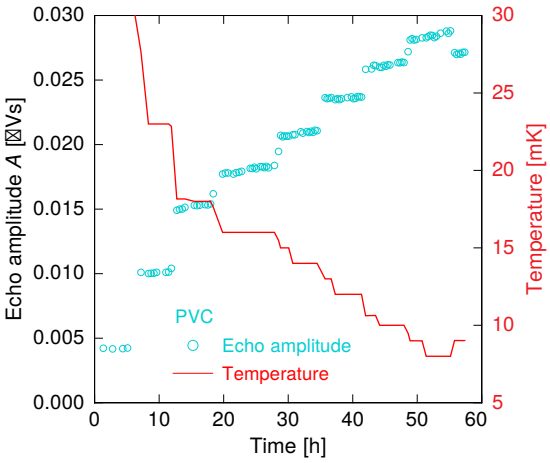

Figure 6.5: Thermalization measurement of the sample PVC between 30 mK and about 8 mK. The echo amplitude is depicted on the left y-axis and the temperature on the right. The course of the echo amplitude is in accordance with the variation of the temperature.

only possible if the sample thermalizes comparatively fast. Especially samples containing isotopes with a large nuclear spin or a quadrupole splitting in the high MHz range, such that it becomes comparable with the measuring temperature, have long thermalization times at low temperatures. These are HY-1, N-KZFS11, Br-DGEBA and FR-122P. For the two last mentioned the quadrupole splitting of the contained bromine is most likely about 250 MHz, which corresponds to about 12 mK. In figure 6.7 two temperature steps measured on FR-122P are shown. It can be seen that the sample thermalizes fast at a temperature of 20 mK. But after the temperature is lowered to 10 mK, a drift in the data can be seen which only flattens after about 80 hours.

The long thermalization times are caused by the nuclear properties of the atoms contained in these samples. In [Pob07] this behavior is explained for the case of nuclear moments in a magnetic field. The additional degrees of freedom introduced by a nuclear moment I, which can orient itself in $2I + 1$ ways with respect to the magnetic field, lead to a significant contribution to the specific heat of the sample, called Schottky anomaly. Thereby the maximal contribution to the specific heat is the larger, the larger the nuclear spin I. The temperature of the maximum of the additional specific heat is determined by the nuclear splitting ΔE of the respective isotope. In dependence of I the maximum occurs at a temperature between about

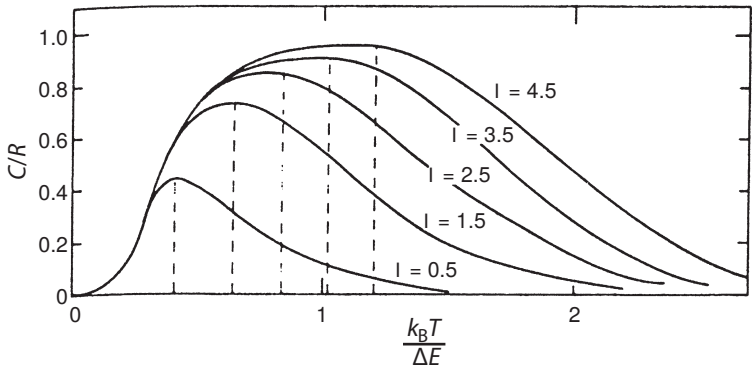

Figure 6.6: Molar heat capacity C in units of the gas constant R as function of $^{k_B T}/_{\Delta E}$ for different nuclear spins I. ΔE represents the energy splitting between the sublevels of the respective isotope. In case of magnetic interaction, the energy splitting is given by the Zeeman splitting and in case of quadrupole interaction by the quadrupole splitting E_Q. Picture taken from [Pob07].

$0.4\,^{\Delta E}/_{k_B}$ and $1.2\,^{\Delta E}/_{k_B}$. The shape of the Schottky anomaly and the position of the maximum is shown in figure 6.6 for different nuclear spins I.
Without magnetic field the isotopes with $I = {}^1/_2$ show no additional heat capacity. Atoms with a nuclear quadrupole moment ($I \geq 1$) which are located in a electric field gradient exhibit a nuclear splitting. Thus their contribution to the specific heat is described by same theory as nuclear moments in a magnetic field. In the case of quadrupole coupling, an additional magnetic field modifies the energy splitting ΔE by the Zeeman interaction. Thereby the temperature where the additional heat capacity occurs is shifted to higher temperatures. This was observed in [Woh01a] on N-BK7.

The bromine atoms contained in Br-DGEBA and FR-122P (about 11 at.%) have a nuclear spin of ${}^3/_2$. This leads together with the nuclear splitting of about 12 mK to a significant contribution to the specific heat of the sample at 10 mK causing long thermalization times. The holmium and tantalum atoms contained in HY-1 and N-KZFS11 have a nuclear spin of ${}^7/_2$. Their nuclear splitting is not known exactly, but a detailed investigation of their thermalization times in [Luc16] showed a strong increase at about 15 mK which is attributed to the nuclear moments. The other samples, investigated in the framework of the present thesis, showed no large additional heat capacity in the investigated temperature range. The atoms carrying nuclear moments contained in those samples have usually nuclear spins smaller or equal ${}^3/_2$ and their nuclear splitting is distinctly smaller than 10 mK.
To ensure a good thermalization of the samples containing atoms with large nuclear spin or splitting, they were kept at the desired measurement temperature for several days, up to a week, until the maximal drift in the data was not larger than the expected one from the electronics (compare section 5.3). Only afterwards the decay of the echo amplitude was measured. In the meantime some of the prepara-

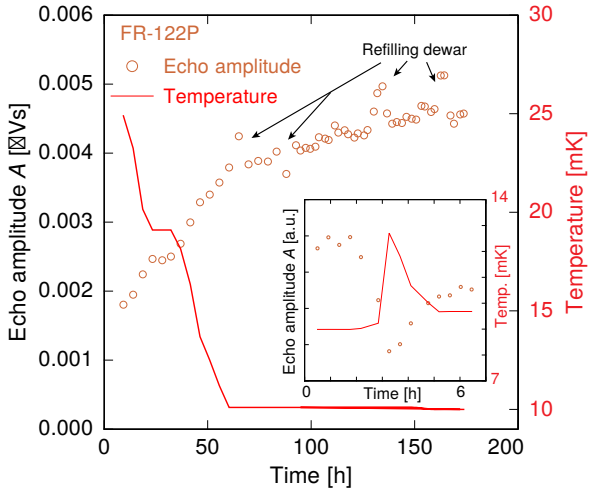

Figure 6.7: Thermalization measurement of the sample FR-122P. The echo amplitude is depicted on the left y-axis and the temperature on the right. The inlay shows the echo amplitude during a small temperature step, which shows that the sample is actually thermalized.

tory measurements were performed, for example the measurement of the electric field dependence. A large drift of the echo amplitude during these measurements would cause a deviation from the expected behavior. Given that no anomalies were observed, the samples' thermalization was sufficient (compare section 6.2.4). Measurements of the dielectric function of HY-1, N-KZFS11, Br-DGEBA and FR-122P in a reentrant cavity resonator or in a MHz-resonator with similar thermal coupling resulted at low temperatures in thermalization times usually smaller than 50 hours [Hau15, Wes15, Zei15, Sch16b, Wer18].

A detailed investigation of the thermalization behavior is, depending on the sample, very time-consuming. However, whether a sample has reached the desired temperature can also be checked more quickly by a small change of the temperature. An example of such a test is shown in the inlay of figure 6.7. The sample follows the temperature as expected and is thus thermalized.

Despite a careful investigation of the thermalization it can never be excluded that the sample exhibits a certain offset with respect to the cryostat temperature. Thus, the temperatures mentioned in the framework of this thesis always refer to the cryostat temperature.
To investigate the actual thermalization behavior of a sample, which means to monitor its actual temperature in comparison to the cryostat temperature, a separate experiment was developed and implemented in collaboration with [Str18] and [Low19]. In this experiment an additional thermometer, which was calibrated against the cryostat thermometer beforehand, was placed in-between two pieces of the sample to be studied (compare figure 6.8). The rest of the experimental setup is designed to be similar to the other resonators used for echo and other dielectric measurements, such that the thermal properties are similar. By monitoring the thermometer of the cryostat and the one between the samples it can be checked if the sample reaches the cryostat temperature. Since it was ensured by suitable cables for the thermometer readout that the thermometer between the samples can only thermalize through the

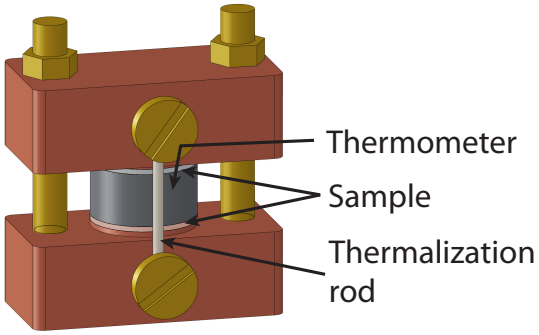

Figure 6.8: Setup to determine the actual thermalization behavior of a sample. The two copper blocks are pressed to each other by two threaded rods made from brass. The thermalization rod, made from silver coated copper, ensures a good thermalization of the copper block above and below the sample.

samples, a thermalization of the thermometer is synonymous with a phononic thermalization of the sample.
Up to now three samples were investigated in detail. Thereby it could be shown that the sample poly(vinyl acetate) does not thermalize completely, which explains the unexpected behavior observed in [Pol17, Sch17]. The samples PVC as well as Br-DGEBA follow the cryostat temperature well.

6.2.2 Influence of the repetition rate

A possible source of unintended heating of the sample is the repetition rate of the echo sequence. Every application of a high frequency electric field pulse leads to dissipative effects in the sample and the resonator. Therefore, there must be enough time in between two single measurements that the sample and the resonator can re-thermalize. If the repetition rate is too high, the tiny heat inputs accumulate and lead to a significant higher temperature of the sample, influencing the relaxation processes of the tunneling systems and thus the decay behavior.

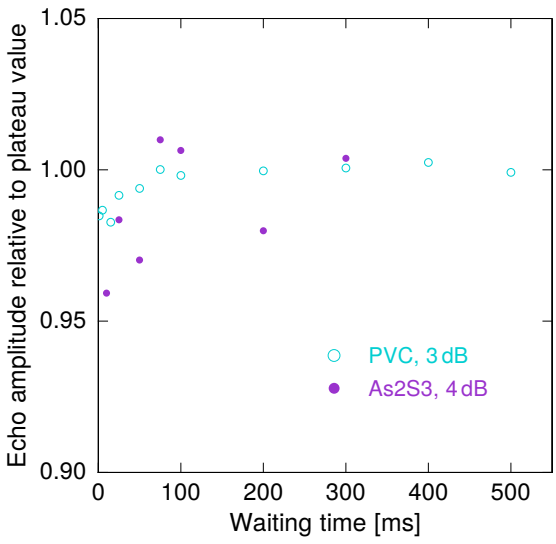

Figure 6.9: Measurement of the echo amplitude in dependence of the waiting time between two single measurements. The echo amplitude is plotted relative to the average value of the amplitudes at large waiting times. Both measurements were performed at a temperature of 10 mK, a pulse duration of $t_1 = 230$ ns and a pulse separation time of 2 µs.

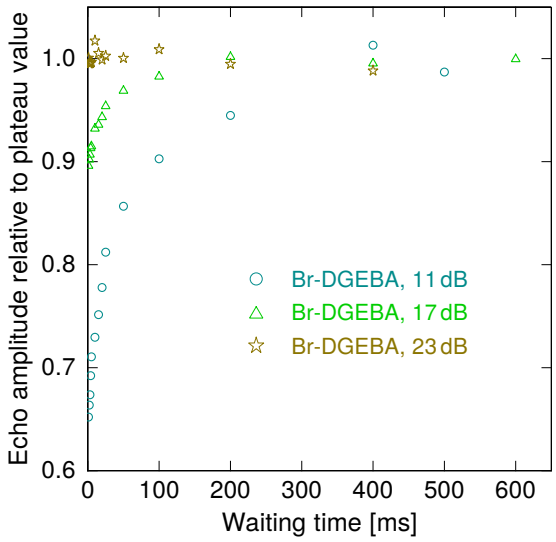

Figure 6.10: Measurement of the echo amplitude in dependence of the waiting time between two single measurements. The echo amplitude is plotted relative to the average value of the amplitudes at large waiting times. The smaller the attenuation, the larger the heating effect. The measurements were performed at a temperature of 7.2 mK, a pulse duration of $t_1 = 230$ ns and a pulse separation time of 5 µs.

To prevent this heating effect in decay measurements, the echo amplitude is measured in dependence of the repetition rate at the lowest temperature used in the respective measurement cycle. In the current measurement setup it is not possible to define an exact measuring rate, but the waiting time between two single two-pulse sequences can be adjusted. Since the measurement itself needs some time as well as the processing of the data in the measurement computer, the waiting time cannot be directly translated into a measuring rate. To investigate the echo amplitude in dependence of the waiting time, the waiting time is varied from long to short, to avoid disturbances by heating effects that are likely to occur at short waiting times. In figure 6.9 the results obtained for the measurements on PVC and As_2S_3 are shown. In this plot the echo amplitude is depicted relative to the average value of the plateau region at large waiting times, where the echo amplitude is independent of the measuring rate. Since the echo amplitude of As_2S_3 is very small and only 5000 measurements were averaged, the spread of the data is comparatively high. A heating might occur for waiting times smaller than 75 ms. For PVC the spread of the data is considerably smaller and a weak heating effect is visible for waiting times below 50 ms. Whether and when a heating effect occurs depends on the dissipation of the sample and on the electric field strength of the excitation pulses. Therefore it is important that this measurement is performed with the same or less attenuation than the decay measurement. In figure 6.10 the influence of the attenuation on the heating effect can be seen for Br-DGEBA. With the highest attenuation (23 dB) no heating effect is visible, even for the smallest waiting times. An reduction of the applied attenuation to 17 dB causes a reduction of the echo amplitude by about 10 % for short waiting times. If only 11 dB are applied the echo amplitude is reduced by up to 35 % and a heating is already present at waiting times smaller than 400 ms.

In all measurements carried out within this thesis, the applied attenuation allowed a waiting time of at least 100 ms. This corresponds to an upper limit of the measuring

rate of 10 Hz. The actual repetition rate was due to the data processing usually in the range of 7 to 8 Hz.

6.2.3 Pulse duration dependence of the echo amplitude

According to the small angle approximation, the echo amplitude is proportional to the pulse duration t_1^3 (compare equation 3.50). To check this prediction, the echo amplitude of N-BK7 was measured in dependence of the pulse duration by keeping all other parameters fixed. The function

$$A_{\mathrm{Echo}}(t_1) = a t_1^b \quad \rightarrow \quad \log(A_{\mathrm{Echo}}(t_1)) = b \log(t_1) + \log(a) \tag{6.3}$$

with the free parameters a and b is afterwards fitted to the linear regime in a double logarithmic plot. In figure 6.11 the obtained echo amplitudes and fit results can be seen. In dependence of the temperature and the pulse separation time the prediction of the small angle approximation is either fulfilled or not. This behavior is caused by the assumption of delta like pulses in the derivation of the echo amplitude in section 3.3.2 and by the definition of the two-pulse sequence (compare figure 3.9).
In a real measurement the pulses have a finite length. Thus during the pulses the tunneling systems do already precess and relax. Due to the definition of the echo sequence in figure 3.9, an increasing pulse duration leads to an overall prolonged two-pulse sequence. This is caused by choosing the end of the first excitation pulse as the reference point for the pulse separation time τ_{12} (compare also the discussion at the end of section 3.3.2 concerning the actual pulse separation time). Since the relaxation processes also act in this overall increased time, more tunneling systems undergo relaxation processes in measurements at large pulse durations. Consequently, the echo amplitude becomes smaller. This changes the dependence of the echo amplitude on the pulse duration and leads to a reduced pulse duration dependency. The dominant

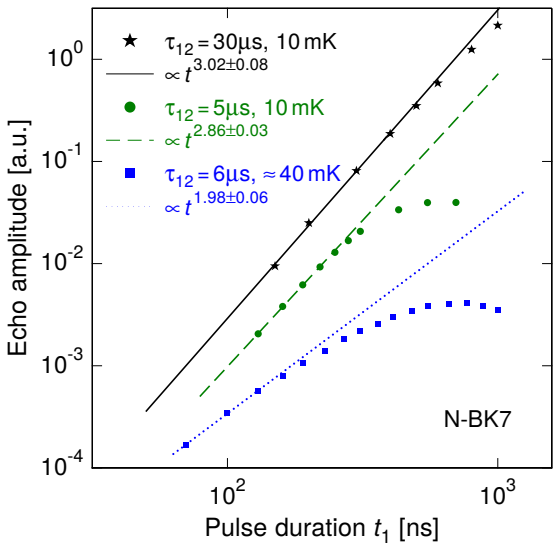

Figure 6.11: Echo amplitude in dependence of the pulse duration measured on N-BK7 at different pulse separation times and temperatures. The data at 40 mK was measured with the microfabricated resonator D [Haa18a] (see section 7.2).

relaxation mechanism at short pulse separation times in N-BK7 is spectral diffusion[1]. Since spectral diffusion is due to its strong temperature dependence more effective at higher temperatures, the measurement at 40 mK shows the strongest deviation from the expected t_1^3 dependence. At a temperature of 10 mK, the influence of spectral diffusion is significant lower. For larger pulse separation times, like 30 µs, the impact of spectral diffusion is even further reduced since the tunneling systems with large asymmetry energy, which are especially sensitive to this relaxation mechanism, already decayed. Thus the expected t_1^3 dependence can be observed.
Another possibility to observe the t_1^3 dependence should be a redefinition of the two-pulse sequence such that the overall extension of the two-pulse sequence, due to the increasing pulse duration, is compensated by a reduced pulse separation time. This would, for example, be possible by defining the two-pulse sequence from the start of the first excitation pulse to the middle of the second one.

In figure 6.12 the influence of the pulse duration on the shape of the echo signal is shown. With increasing pulse duration the echo becomes larger and broader. The shift of the maximal echo amplitude to larger times is caused by the overall extension of the two-pulse sequence with larger pulse duration, as discussed above.
The broadening of the echo signal is caused by the changing frequency composition of the excitation pulses. The frequency composition of the excitation pulses is broader, the shorter the pulse duration (compare figure 3.14). The de-phasing of the tunneling systems after the first pulse, as well as the re- and de-phasing at the time of the echo depend on the tunneling systems' energy splittings. A broad energy spectrum results thus in a broad distribution of the energy splittings E of the excited tunneling

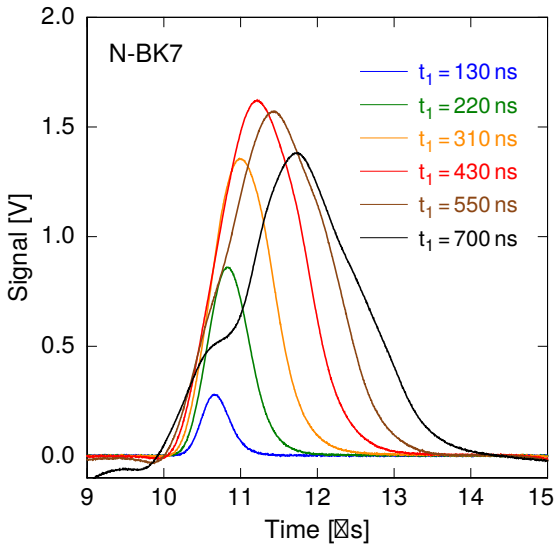

Figure 6.12: Echo signal in dependence of the pulse duration. The data was obtained at a temperature of 10 mK and a pulse separation time of 5 µs. The corresponding echo amplitudes are shown in figure 6.11.

[1]Besides spectral diffusion there is another relaxation mechanism, probably based on nuclear quadrupole moments, effective at low temperatures in N-BK7 (compare further course of this chapter and section 7.3.2). However, for the discussion regarding the deviation from the expected t_1^3 dependence this is not relevant.

systems, leading to a fast de- and re-phasing, corresponding to a narrow echo. Considering the Bloch sphere picture, the increased echo amplitude can be understood qualitatively. Since all measurements were performed on the same sample with the same pulse separation time (neglecting the prolongation by the increased pulse duration) and the same field strength, the mean value of the ensemble's Rabi frequency should be similar for all measurements (compare also the discussion in the framework of figure 6.16). Thus, during a longer pulse the contribution of the excited state to the total wave function of the resonant tunneling systems increases more compared to a short pulse. In the Bloch sphere this corresponds to a larger rotation of the pseudo spin vectors around the x-axis and thus to an increased expectation value in y-direction, which corresponds to the polarization. If the pulse becomes too large, the tunneling systems become 'overexcited' leading to the characteristic shoulders of the echo signal and a reduction of the maximum height.

6.2.4 Electric field strength dependence of the echo amplitude

Besides the t_1^3 dependence, the echo amplitude is also expected to show a F_0^3 proportionality, with F_0 being the field strength of the excitation pulses (compare equation 3.50 and 4.21). The measurement of the electric field dependence has the advantage over the pulse dependency that the overall echo sequence is not elongated by a variation of the electric field strength. Thus neither the relaxation processes present in the different samples, nor their temperature dependence distort this measurement. The electric field dependency of the echo amplitude was checked for every sample measured in the framework of this thesis to determine the regime in which the small angle approximation is fulfilled. Therefore the echo amplitude is measured in dependence of the applied field strength, which can be varied by the adjustable attenuator in the circuitry. To prevent an influence by heating effects, which can be caused by high field strengths, the measurement is performed from small electric field strengths (high attenuation) to high electric field strengths (small attenuation). All other parameters are kept constant. A pulse duration of $t_1 = 230\,\mathrm{ns}$ was used, like in the decay measurements. The pulse separation time was set to $2\,\mu\mathrm{s}$ such that a small number of measurements is sufficient for a good data quality.

The results of the measured electric field dependence are depicted in figure 6.13. Some samples show a scattering of the data at the smallest electric field strengths. This is caused by the very small echo amplitude at those field strengths and the limited number of averaged echo sequences. The data in the plot is shifted in y-direction for better visualization. All measurements were performed in the reentrant cavity resonator with a similar coupling to the excitation and readout electronics. Neglecting the differences in the resonance frequencies, the quality factors and the dielectric constants of the materials, it can be assumed that the energy stored in the resonator was the same for each attenuation. Since the samples had different

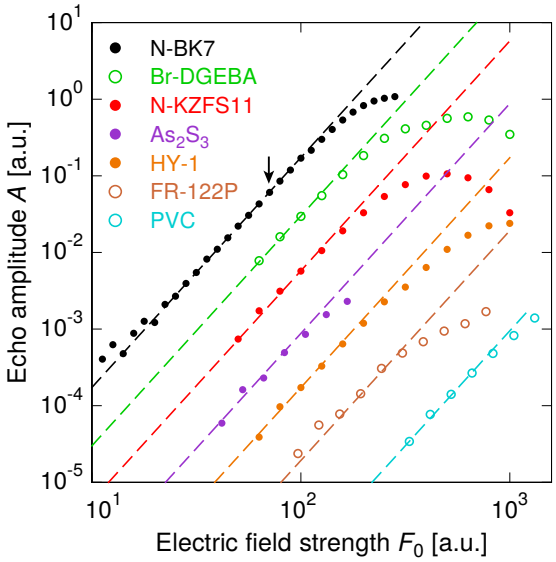

Figure 6.13: Echo amplitude in dependence of the electric field strength for the samples measured in this thesis. The settings are: $t_1 = 230\,\mathrm{ns}$, $\tau_{12} = 2\,\mu\mathrm{s}$, $7\,\mathrm{mK} \leq T \leq 10.1\,\mathrm{mK}$. The data is corrected for the different sample thicknesses and shifted in y-direction for better visualization. The lines indicate the expected F_0^3 dependence. The arrow indicates an attenuation of 23 dB.

thicknesses, the actual electric field in the sample was different for the same attenuation. However, the known sample thicknesses allow a rough correction for the field strength and thus a shift of the data in x-direction to a common reference point. Thereby it is assumed, similar to a classical plate capacitor, that the field in the gap of the resonator is homogeneous and inverse proportional to the distance between the end of the rod and the bottom of the cavity. This distance is given by the sample thickness.

The absolute field strength, present in the resonator, is difficult to determine since the attenuation of the cables is not known. In addition, the coupling quality factor of the resonator is unknown. A rough approximation, with an attenuation of 23 dB at the adjustable attenuator, leads to a field strength in the order of $100\,\mathrm{V/m}$. In figure 6.13 the data point of N-BK7 measured with an attenuation of 23 dB at the adjustable attenuator is marked by an arrow.

To check the validity of the small angle approximation the function

$$A_{\mathrm{Echo}}(F_0) = aF_0^3 \quad \rightarrow \quad \log(A_{\mathrm{Echo}}(F_0)) = 3\log(F_0) + \log(a) \tag{6.4}$$

with the free parameter a is fitted to the linear regime of the data in figure 6.13. It can be seen that the small angle approximation is fulfilled for every sample at small electric field strengths. This good agreement shows also that the samples were well thermalized. Since the echo amplitude becomes very small at small field strengths, the whole electric field dependence measurement usually takes at least one day, and up to several days for samples containing atoms with large quadrupole coupling constants. A significant drift in the data, caused by a non-adequate thermalization, would therefore cause a deviation from the expected electric field dependence.

The point from which the small angle approximation is valid depends on $\Omega_{\mathrm{R}} t_1 \propto {}^{\delta \vec{p} \vec{F}_0 \Delta_0 t_1}/_{E}$ (compare equation 3.49 and 3.50). Thus it is in principle possible to extract information on the ensemble of tunneling systems contributing to the echo from

a measurement of the electric field dependence. Since for the measurements shown in figure 6.13 the exact field strengths in the resonator and the dipole moments of the tunneling systems are unknown, it is not possible to extract information on the ensemble's averaged Δ_0/E. However, if the electric field dependence is measured for the same sample in the same measurement cycle at different pulse separation times all parameters except for the ensemble's averaged Δ_0/E are constant[2]. Therefore Δ_0/E can be studied in dependence of the pulse separation time and the temperature. This in turn can provide information on the relaxation mechanism present in the sample. Due to relaxation processes the ensemble of tunneling systems contributing to the echo signal changes with increasing pulse separation time. Symmetric tunneling systems relax via the one-phonon processes (see section 3.4.1). Asymmetric tunneling systems are predominantly relaxed by spectral diffusion, which is significantly stronger than the one-phonon process at short pulse separation times (see section 3.4.2). Therefore the ensemble of tunneling systems contributing to the echo at large pulse separation times is on average more symmetric and the ensemble's mean value of Δ_0/E is larger. Thus it is expected that the point from which the small angle approximation is valid shifts to smaller field strengths at larger pulse separation times.

To check this expectation, the electric field dependence of the echo amplitude of N-BK7 was measured at different pulse separation times in the same measurement cycle. Thus the coupling of the resonator to the excitation and readout electronics as well as the size of the gap where the sample is located were equal for all measurements. This ensures that the electric field strength at a certain attenuation of the signal was the same. In figure 6.14 the obtained data as well as a fit of equation 6.4 to the

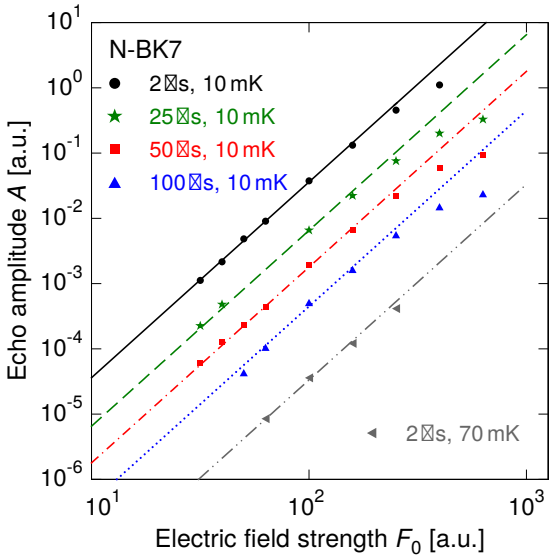

Figure 6.14: Echo amplitude as a function of the electric field strength measured on N-BK7 at different pulse separation times. The pulse duration was 230 ns and the temperature 10 mK and 70 mK. The lines indicate the expected F_0^3 dependence. All measurements were performed in one measurement cycle. Therefore data points on a vertical line were measured at the same electric field strengths in the resonator.

[2]It is assumed that the dipole moment $\delta\vec{p}$ is independent of the asymmetry energy of the tunneling system.

linear regime is shown. The small angle approximation is fulfilled independent of the pulse separation time. However, no significant difference in the point from which the small angle approximation is valid can be observed. Even at 70 mK, where spectral diffusion is significantly stronger, no change is observed.
Considering the distribution of tunneling systems contributing to the echo amplitude, at the respective pulse separation time, this behavior can be understood. In figure 6.15, the relative contribution of tunneling systems with asymmetry energy Δ to the echo amplitude is shown in dependence of the asymmetry parameter $q = \Delta/E$ for different pulse separation times τ_{12}. Therefore the argument of the integral given in equation 3.71 is calculated in dependence of q. The area below the curve is proportional to the echo amplitude at this pulse separation time. In the calculation the one-phonon process and the short time limit of spectral diffusion are considered[3]. At 10 mK the assumed minimal relaxation time is $T_{1,\min} = 220\,\mu s$ and $m = 10{\cdot}10^9\,{}^1/_{s^2}$. For the curve at 70 mK it is $T_{1,\min} = 60\,\mu s$ and $m = 2660{\cdot}10^9\,{}^1/_{s^2}$. The values of 70 mK were determined in [Fic13] and those for 10 mK are motivated by the relaxation times determined in the same publication at 7.5 mK and 15 mK[4]. In general, the tunneling systems with large asymmetry energy contribute only little to the echo amplitude even at low temperatures and small pule separation times. This is caused by the $(\Delta_0/E)^4$ dependence of the echo amplitude. With increasing pulse separation time the asymmetric tunneling systems (large q values) decay due to spectral diffusion. Thus their contribution to the echo amplitude reduces very fast. In figure 6.15 this can be seen by the shift of the curves towards small q values. The influence of the one-phonon process is visible by a reduction of the y-axis intercept with increasing pulse separation time. In figure A.7 the same plot is shown in a semi-logarithmic representation, pronouncing the influence of the relaxation processes even more. The

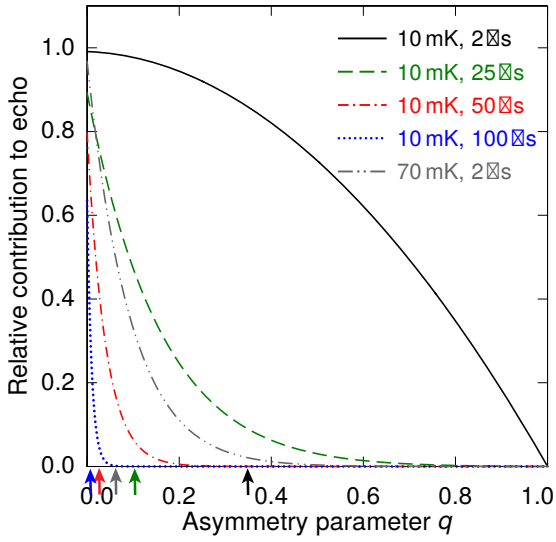

Figure 6.15: Relative contribution of tunneling systems with asymmetry parameter $q = \Delta/E$ to the echo amplitude at different pulse separation times and temperatures. The small arrows at the x-axis indicate the mean q values weighted with the relative contribution to the echo for the different ensembles of tunneling systems.

[3]The influence of a possible nuclear quadrupole moments bases relaxation is only weakly pronounced in N-BK7 (compare section 6.4.2) and thus neglected in this discussion.
[4]For the following discussion a rough estimation of the relaxation time is sufficient.

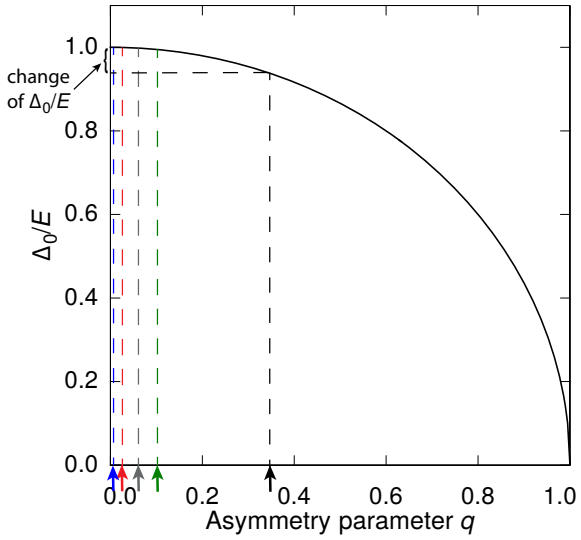

Figure 6.16: Δ_0/E as a function of the asymmetry parameter $q = \Delta/E$. It holds $\Delta_0/E = \sqrt{1-q^2}$. The arrows at the x-axis indicate the mean q values weighted with the relative contribution to the echo for the ensembles according to figure 6.15.

small arrows at the x-axis in figure 6.15 indicate the mean q values weighted by the relative contribution to the echo of the ensembles of tunneling systems at the different pulse separation times. Due to the cutting-off of the asymmetric tunneling systems by spectral diffusion, the average q value shifts towards smaller q. A small averaged q value corresponds to an ensemble with proportionally more symmetric tunneling systems. As mentioned above, the point from which the small angle approximation is valid depends on $\Omega_\mathrm{R} t_1$. In the measurements shown in figure 6.14 only the ensemble's mean value of Δ_0/E (which is part of Ω_R) changes. Therefore this is the relevant parameter for the onset of the small angle approximation. In figure 6.16, Δ_0/E is plotted in dependence of the asymmetry parameter q. It holds $\Delta_0/E = \sqrt{1-q^2}$. The arrows on the x-axis indicate the mean q value weighted by the relative contribution to the echo for the different ensembles of tunneling systems, see figure 6.15. In this plot it can be seen that the value of Δ_0/E changes only a little although the q value changes in total from about 0.35 to 0.0075. In numbers, the value of Δ_0/E changes from its smallest value 0.937 to about 1. Translated into the electric field strength dependence, this means that for the ensemble of tunneling systems probed at a pulse separation time of 100 µs the onset of the small angle approximation is at an electric field strength that is 93.7 % of the one at 2 µs.

This rough estimation shows, that this small change in the onset of the validity of the small angle approximation cannot be resolved with the data shown in figure 6.14. Even higher temperatures do not change the composition of the ensemble of tunneling systems in a way that it can be observed. Furthermore, the change in the onset is challenging to resolve with the current electronic setup. The adjustable attenuator which controls the electric field strength of the excitation pulses can be varied minimally in steps of 1 dB corresponding to changes in the electric field strength of about 12 %. Thus, to study the onset of the validity of the small angle approximation, a more precise control of the electric field strength is required. The rough electric field strength steps in the current electronic setup can also not be

compensated by very small pulse separation times. Since the echo is proportional to $(\Delta_0/E)^4$, even very small pulse separation times and low temperatures do not shift the ensembles weighted mean value of q significantly more to larger values than the 10 mK and 2 µs curve. If a precise control of the electric field strength is possible, the measurement of the electric field dependence at different pulse separation times enables a study of the change of the ensemble of tunneling systems contributing to the echo. This in turn enables conclusions about the relaxation processes present in the respective sample.

If the electric field dependence is measured on the same sample with different pulse durations t_1, the onset of the small angle approximation shifts due to its $\Omega_R t_1$ dependence to smaller field strengths with increasing pulse duration. This behavior was observed in [Sch16a] in measurements on N-BK7.

The change in the shape of the echo with increasing field strength (reduced attenuation) is depicted in figure 6.17. The echo signal has the same width for all measurements and only the size of the echo depends on the field strength. The right flank may exhibit a small additional broadening for very large echoes which is amongst others caused by the ring-down of the resonator. The echoes have the same width because the pulse duration stayed constant and thus the frequency spectrum of the excitation pulses. Only the Rabi frequency, which depends on the applied field strength, was varied during the measurement. In the measurements with high attenuation (small field strength) the echo seems more narrow. This observation is caused by the disappearing of the echo's flanks in the noise. If a small echo is scaled to the size of a large one, their widths are the same. In the Bloch sphere picture, the increase of the echo amplitude with reduced attenuation can be understood qualitatively. In the measurements shown in figure 6.17, the pulse duration t_1 and thus the time during which the pseudo spin vectors are rotated around the x-axis

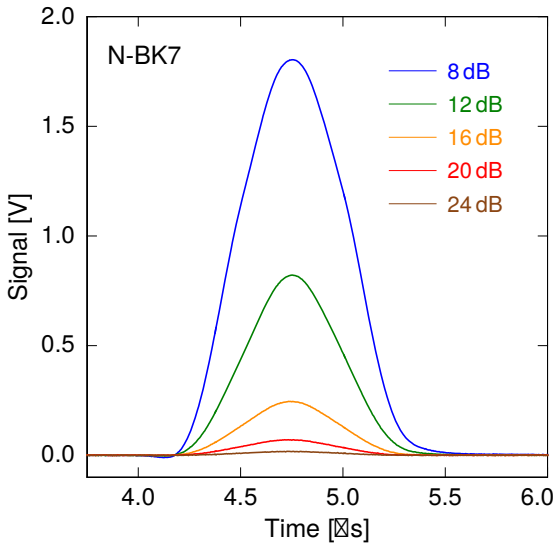

Figure 6.17: Echo signal measured on N-BK7 for different attenuations of the electric field. The data was obtained at a temperature of 10 mK, a pulse separation time of 2 µs and a pulse duration of 230 ns. The corresponding echo amplitudes are shown in figure 6.14.

stays constant. The reduced attenuation and thereby increased electric field strength causes an increase of the Rabi frequency and thus an increase of the rotation speed ($^{\text{degree}}/_{\text{time}}$) around the x-axis. Consequently, the expectation value in y-direction is larger after the same pulse duration and therefore the polarization. If the field strength is too large, the tunneling systems get 'overexcited' and the shape of the echo is distorted. This is visible in the measurement with an attenuation of 8 dB.

6.3 Reproducibility of the measurements

The data shown in this thesis was collected over several years. Thereby most sample were measured in various measurement cycles. The results obtained in the different cycles agree well. However, for most samples these measurement cycles were done one after the other such that the resonator was neither dismounted nor disassembled. For some samples the different measurement cycles were performed within several years. These data sets are suitable to verify the reproducibility of the measurements. In addition, these data sets can be used to check whether modifications in the electronic setup influence the decay behavior of the echo. During the time of this thesis the low temperature amplifier was removed and reinstalled (2017) and the cables between the last heat sink and the resonator were exchanged to superconducting niobium-

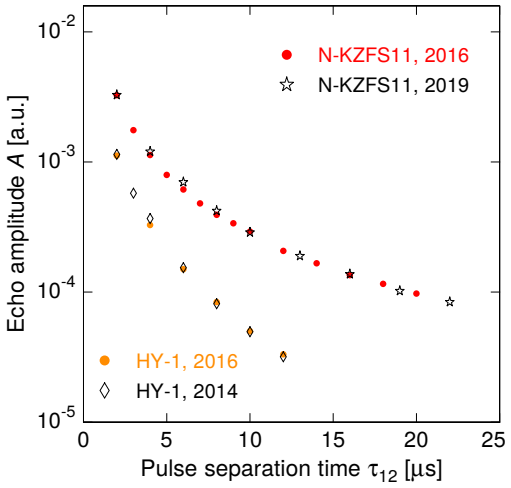

Figure 6.18: Measurement of the echo amplitude in dependence of the pulse separation time for the samples HY-1 (15 mK) and N-KZFS11 (2016: 10.1 mK, 2019: 10 mK) performed within an interval of several years. The respective data sets are scaled to each other. Within the measurement accuracy the decay behavior agrees well. The data from HY-1 2014 is taken from [Wol14].

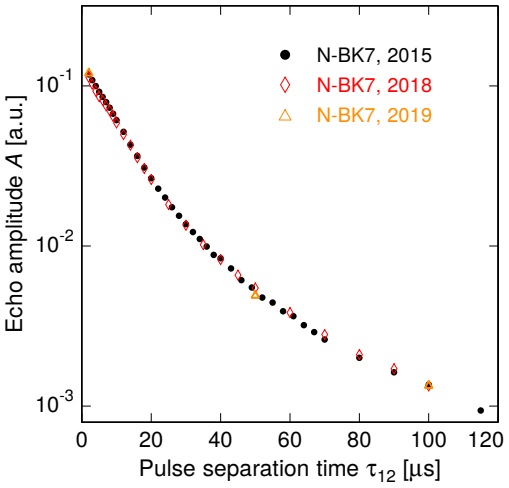

Figure 6.19: Measurement of the echo amplitude in dependence of the pulse separation time for N-BK7 at a temperature of 10 mK within an interval of several years. The different decays are scaled to each other. Within the measurement accutacy the decay curves align very well.

titanium semi-rigid coaxial cables (2016).
In figure 6.18 measurements on HY-1 and N-KZFS11 are shown. Between these measurements the sample was removed from the resonator, stored under normal ambient conditions and reinstalled into the resonator. In case of HY-1, the sample used in 2014 was not the same piece as the one used in 2016. Since the absolute value of the echo amplitude was not always the same (for example because a different attenuation was used for each of the measurements), the different data sets are scaled to each other. In the plot it can be seen that the decay behavior measured at the different times is equal. Thus it can be assumed that the overall electronic setup as well as the temperature control of the cryostat showed no large variation over these years and that the modifications of the cables do not influence the decay behavior. Figure 6.19 shows different measurements performed on N-BK7 over several years. The different data sets are scaled to each other as well. The good overlap of the data confirms that the modifications of the electronic setup do not influence the decay behavior of the samples measured in the reentrant cavity resonator.

6.4 Decay behavior

In the following section the decay behavior of the samples measured in the framework of this thesis is discussed in terms of an additional relaxation mechanism based on nuclear moments and compared to previously obtained data. Thereby the decay behavior is analyzed qualitatively and general properties of the relaxation based on nuclear quadrupole moments are deduced. Afterwards the decay curves of selected samples are compared to the existing theory. Before discussing the decay behavior, the size of the echo amplitude of the different samples is compared.

6.4.1 Size of the echo amplitude

All measurements within this thesis were performed in the regime where the small angle approximation is valid. To have still a large echo signal the field strength was chosen as large as possible within the linear regime, see figure 6.13. The echo signals of the samples measured in the framework of this thesis are shown in figure 6.20. All measurements were performed with a pulse separation time of 2 µs and a pulse duration of $t_1 = 230\,\mathrm{ns}$ (equal to the decay measurements). Although the temperature at the different measurements was similar (10 mK) the size of the different echo signals varies clearly. The signal of N-BK7 is scaled with a factor of 0.4 to fit into the plot. The signal of As_2S_3 is scaled by a factor of 2, such that the echo signal is visible at all in this figure. Several reasons are possible for the varying echo signal sizes. Since all measurements were performed at 10 mK (except for Br-DGEBA which was measured at 7.5 mK) the thermal occupation factor can be neglected and the echo

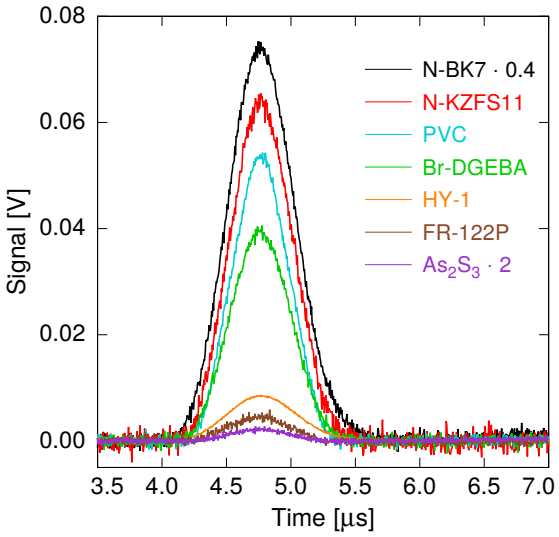

Figure 6.20: Echo signals measured at $\tau_{12} = 2\,\mu s$ and $t_1 = 230\,ns$. The electric field strength was chosen such that the small angle approximation was just fulfilled. The data of N-BK7 is scaled by a factor of 0.4 and the one of As_2S_3 by 2. The temperature was 7.5 mK for Br-DGEBA and 10 mK for all other samples.

amplitude at the pulse separation time τ_{12} is given by

$$A(\tau_{12}) \propto \int \underbrace{\sqrt{1-q^2}\sin(\Omega_R t_1)^3}_{A_{\mathrm{Echo,ts}},\ (\text{equation } 3.49)} \underbrace{\frac{P_0}{1-q^2}}_{P(E,q)} W_{1\mathrm{Phonon}} W_{\mathrm{specDiff}} W_{\mathrm{NQR}} \mathrm{d}q. \tag{6.5}$$

The electric field strength for every sample was chosen such that the small angle approximation was just fulfilled. Consequently, the argument $(\Omega_R t_1)$ of the sine function in equation 6.5 is similar for the different samples. Therefore only the density of states P_0 of the tunneling systems carrying permanent electric dipole moments in the different samples and relaxation processes remain as possible reasons for the different echo sizes. Considering N-BK7, N-KZFS11 and HY-1, these samples are all multicomponent glasses which have a similar basic composition such that the glass matrix is most likely build by the same atoms (compare section 5.4). Therefore it is expected that the coupling of the tunneling systems to the phonons and thereby the strength of the one-phonon relaxation, spectral diffusion and possible collective excitations is similar in these samples. However, N-KZFS11 and HY-1 contain, compared to N-BK7, also a small amount of atoms with a large nuclear quadrupole moment that have, as far as it is known, also a large nuclear quadrupole coupling constant. This may cause an additional fast relaxation (compare section 4.5.3) and thus a small echo amplitude already at a pulse separation time of 2 µs. The other samples showing small echo amplitudes contain atoms with comparatively large nuclear quadrupole coupling constants, too.
However, the measurement of the absolute echo size does not allow to distinguish between a small density of states and a fast relaxation process. For this differentiation the decay behavior of the echo amplitude of the different samples needs to be studied, which is presented in the next section. The performed measurements show that the glasses containing atoms with large nuclear quadrupole coupling indeed show a fast decay of the echo amplitude at small pulse separation times.

6.4.2 Decay of the echo amplitude - qualitative discussion

The previous section states that the echo amplitude of the samples containing atoms with large nuclear quadrupole coupling constants is small compared to N-BK7, which contains only atoms with a comparatively small nuclear quadrupole coupling. To study whether nuclear moments influence the relaxation of tunneling systems, decay measurements were performed. In figure 6.21 the decay of the echo amplitudes measured on the multicomponent glasses N-BK7, N-KZFS11 and HY-1 are shown semi-logarithmically. The temperature was 10 mK for N-BK7 and HY-1 and 10.1 mK for N-KZFS11. Since the relaxation processes in amorphous samples are temperature dependent, the following discussion considers only the case of about 10 mK. Given that the absolute values of the echo amplitude are sample dependent (compare section 6.4.1), the curves are aligned at a pulse separation time of 1.5 µs for better comparison[5]. This was the shortest measurable pulse separation time for all samples. In figure 6.21 it can be seen that the echo amplitudes of N-KZFS11 and HY-1 decay in the investigated time window very fast at short pulse separation times and cross over to a linear behavior between about 5 to 10 µs. The linear decay characteristic in this semi-logarithmic plot corresponds to an exponential decay of the echo amplitude. The characteristic of the fast decay at short pulse separation times seems to be linear as well, but this cannot be clearly verified in this narrow time window. In contrast to N-KZFS11 and HY-1, N-BK7 shows a linear behavior already at short pulse separation times. The cross over in the decay curves of N-KZFS11 and HY-1 at about 5 µs to 10 µs indicates a change in the dominant relaxation mechanism. At this point most of the tunneling systems sensitive to the process leading to the fast decay of the echo amplitude at short pulse separation times already decayed and

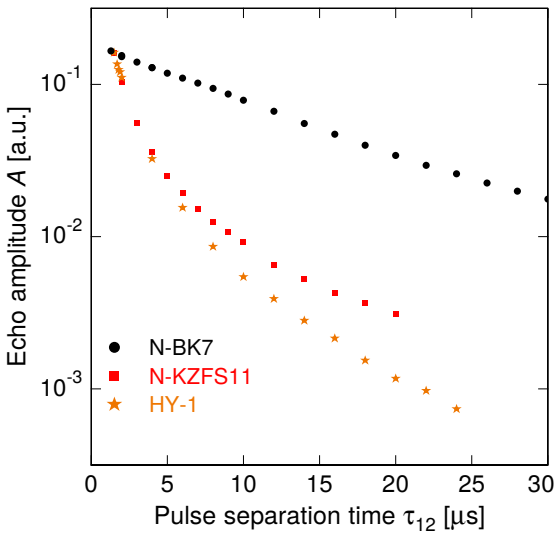

Figure 6.21: Echo amplitude as a function of the pulse separation time measured at a temperature of 10 mK (N-BK7, HY-1) and 10.1 mK (N-KZFS11). The data is aligned at $\tau_{12} = 1.5\,\mu s$. The curve of N-BK7 consist of two separate measurements which are aligned to each other. The field strength was such that the small angle approximation is fulfilled and $t_1 = 230\,ns$.

[5]For N-BK7 the echo amplitude was only measured at $\tau_{12} = 1.3\,\mu s$ and 2 µs. Here the data was interpolated for the alignment at 1.5 µs.

another relaxation mechanism dominates which relaxes the remaining tunneling systems. The decay of the echo amplitude and thus the relaxation rate of the tunneling systems of N-KZFS11 in the time window above about 10 µs is similar to N-BK7, indicating that at this time probably the same relaxation mechanism dominates. The relaxation rate of the tunneling systems of HY-1 in the same time window is still larger. The decay of the echo amplitude of N-BK7 at 10 mK and short pulse separation times is determined by spectral diffusion and probably collective excitations. In addition, a relaxation based on nuclear moments is possible [Fic13].
The basic composition of N-BK7 and HY-1 is similar, but the latter contains 0.5 at.% holmium (HY-1) which has a very large nuclear moment and most likely a large nuclear quadrupole coupling constant resulting in large nuclear splitting. The glass matrix of N-KZFS11 is most likely also similar to the one of N-BK7, but this material contains 1.5 at.% of tantalum and several other isotopes than N-BK7 which carry a nuclear quadrupole moment. Tantalum carries a very large nuclear quadrupole moment and exhibits most likey a large nuclear quadrupole coupling. Given the similar basic composition of HY-1 and N-BK7, it is expected that the coupling of the tunneling systems to the strain field is similar. Therefore the one-phonon process, spectral diffusion and collective excitations should be similarly pronounced in the samples N-BK7 and HY-1[6]. In dielectric measurements on N-KZFS11 and HY-1 an additional relaxation mechanism was observed which was attributed to the nuclear quadrupole moments present in these samples [Luc16] (compare section 4.5.3). Thus it is reasonable that the fast decay of the echo amplitude of N-KZFS11 and HY-1 at short pulse separation times is caused by the same relaxation mechanism. Since the main difference in the composition of N-KZFS11, HY-1 and N-BK7 are the elements tantalum (N-KZFS11) and holmium (HY-1), which have a large nuclear quadrupole moment and as far as known a sizable quadrupole coupling constant, it could be assumed that the fast relaxation is caused by the atoms with a large quadrupole moment or quadrupole coupling constant. However, further considerations show that it is neither the absolute value of the quadrupole moment, nor the one of the quadrupole coupling constant that is decisive for the strength of the relaxation mechanism. The most relevant parameter seems to be the variation of the quadrupole coupling constant during a tunneling motion. In the fast decay, visible on N-KZFS11 and HY-1 in figure 6.21, the tunneling systems, that are sensitive to the relaxation mechanism based on nuclear quadrupole moments, decay on short timescale. Therefore, after the crossover at around 5 µs to 10 µs only tunneling systems which contain atoms with a nuclear quadrupole moment being less sensitive to the quadrupole moment based relaxation or such without nuclear moment remain. These tunneling systems are then relaxed by a less strong relaxation mechanism based on nuclear quadrupole moments and the other known relaxation mechanisms (spectral diffusion, one-phonon). The

[6]Spectral diffusion and collective exciatations depend also on the density of tunneling systems in the material (compare for example the equations given in [Ens96b]). But it is unlikely that the difference in the density of tunneling systems is large enough to explain the observed deviations in the decay behavior.

observed fast decay at small pulse separation times is also in accordance with measurements in [Ler88] on holmium doped aluminosilicate glasses, mentioned in section 4.5.3.

In contrast to figure 4.4, in which the measurement of the echo amplitude in dependence of the pulse separation time of deuterated glycerol is shown, the decays of the echo amplitudes of the samples shown in figure 6.21 exhibit no quantum beating. There are various possible causes for the absence of the quantum beating. These are the spectral width of the excitation pulses, the level schema of the tunneling systems and the beating frequency. In section 4.3.3 these causes are shortly addressed. In the following, they are discussed in more detail with a focus on the investigated samples. All measurements shown in figure 6.21 were performed with a pulse duration of $t_1 = 230\,\mathrm{ns}$ for the $\pi/2$ pulse. According to equation 3.54, this corresponds to a spectral width of only about 0.7 MHz. The spectral width of the π pulse with a duration of $2t_1$ is even more narrow. Considering the composition of N-BK7, N-KZFS11 and HY-1 (section 5.4) and the nuclear quadrupole splittings from table A.1, it can be seen that the smallest quadrupole splittings of the isotopes in these materials are in the order of 1 MHz. Therefore the spectral width of the excitation pulses is significantly too small to cause a complete mixing of the nuclear states of the tunneling systems during the echo sequence. Thus, in dependence of the actual level schema of the tunneling systems no or only a modified quantum beating compared to the case of complete level mixing can arise.
The level schema of the tunneling systems present in these multicomponent glasses is not known since the nature of the tunneling systems and thus the number of atoms containing a nuclear quadrupole moment per tunneling systems is unknown. In addition, possible asymmetry factors η of the quadrupole coupling which would lead to even more nuclear levels are unknown as well. Together with the broadening of the quadrupole splittings due to the amorphous structure of the samples it is conceivable that every tunneling system has a different level schema. The excitation pulses, which have only a small spectral width, are potentially able to mix parts of the nuclear levels of the tunneling systems such that a modified quantum beating can arise. However, due to the different quantum beatings of the tunneling systems, caused by the different level schemata, there is destructive interference already at smallest pulse separation times. Thus no macroscopic quantum beating is visible. Even if the spectral width of the excitation pulses would be sufficient for a complete mixing of the nuclear states most likely no quantum beating would be observable. In this case the overall echo amplitude is reduced as long as the asymmetric tunneling systems are not completely decayed (compare figure 4.20).
The frequency or frequencies of the quantum beating(s) are given by the splittings of the nuclear states of the tunneling system. Due to the large quadrupole splittings present in N-BK7, N-KZFS11 and HY-1 the beating frequencies are potentially also high. Even supposing similar level schemata of the tunneling systems in these materials and that they exhibit only a broadening due to the amorphous structure, the arising modified quantum beating is most likely not observable at pulse separation

times larger 1.5 µs. The high beating frequency would together with the broadening due to the amorphous structure lead to a smearing of the macroscopic quantum beating already at short pulse separation times, such that after some oscillations only an overall reduced echo amplitude remains. The same also happens if the spectral width of the excitation pulses would be sufficient for a complete mixing of the nuclear states. This case is illustrated in figure 6.22, where the quantum beating of an ensemble of tunneling systems, in which each contains only one atom with a spin $I = 3/2$ and $\eta = 0$, is simulated (see section 4.4). The distribution of tunneling systems is similar in all plots, only the quadrupole splitting is varied from 100 kHz in the left plot, to 1 MHz in the center and 10 MHz in the right one. The used broadening of the quadrupole splitting is 10 %. The size of the broadening is motivated by nuclear quadrupole resonance measurements on amorphous materials, e.g. [Rub74]. Since every tunneling system contains only one atom with a nuclear quadrupole moment, the level schema is comparatively simple (compare figure 4.8) and every tunneling system exhibits only one beating frequency. But as can be seen in figure 6.22, the high beating frequency together with the broadening causes the quantum beating to disappear already at short pulse separation times. Thus in a multicomponent glass, in which several different isotopes carrying nuclear quadrupole moments are present and where the tunneling systems may carry several atoms with nuclear quadrupole moments, the variety of different beating frequencies cause the macroscopic quantum beating to disappear already at very short pulse separation times. Furthermore, a very fast quantum beating in the frequency range of about 1 MHz, if still present at pulse separation times larger than 1.5 µs, is difficult to detect with the temporal resolution of the data in figure 6.21.
The absence of any quantum beating in the measured decay curves is most likely

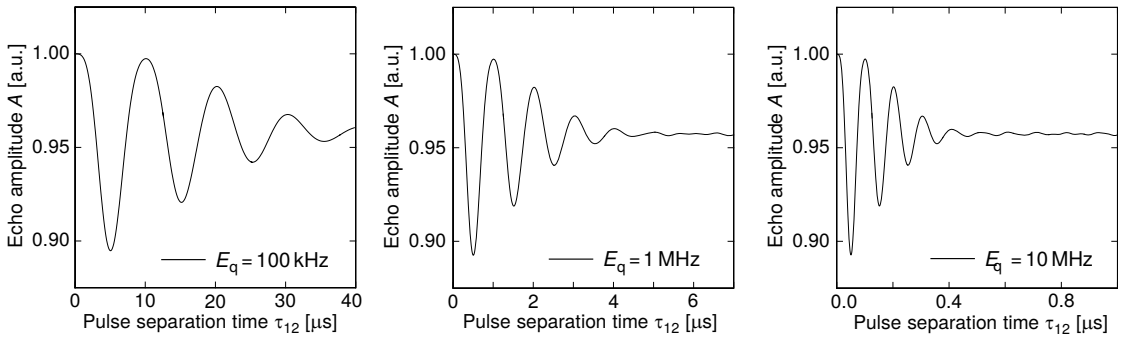

Figure 6.22: Simulated quantum beating for an ensemble of tunneling system with one atom carrying a spin of $I = 3/2$ each. The quadrupole splittings are varied from 100 kHz in the left plot, 1 MHz in the middle to 10 Mhz in the right one. The broadening of the quadrupole spitting due to the amorphous structure is set to 10 %. All other parameters ($E = 1$ GHz, $\sigma_E = 10$ Mhz, $\Delta_0^{\min} = 0.15$ GHz, $\Theta_T = 18°$) are kept constant. The higher beating frequencies lead to a faster disappearing of the observable quantum beating (compare the x-axes of the different plots).

caused by a mixture of all these reasons. Due to limits in the experimental setup, which are discussed in section 7.1, it was not possible to measure reliable data at pulse separation times much smaller than 1.5 µs to test if a quantum beating is observable at shorter times. In addition, a lot of the tunneling systems containing nuclear quadrupole moments, which can contribute to a quantum beating, already decay at short pulse separation times in N-KZFS11 and HY-1 by the fast relaxation based on the nuclear quadrupole moments.
Another observation which can be made in figure 6.21 is the missing Gaussian shape like leveling-off of the echo amplitude towards small pulse separation times, as predicted by spectral diffusion theory. The numerical calculation of the influence of the different relaxation processes on the decay behavior of the echo amplitude in figure 4.27 shows that an additional relaxation mechanism, based on nuclear quadrupole moments, can suppress the Gaussian shape. In N-KZFS11 and HY-1 the strong relaxation, visible in figure 6.21, may suppress the Gaussian shape very effectively such that it is only observable at very short pulse separation times. For N-BK7 a relaxation based on nuclear moments is less pronounced. Thus the Gaussian shape can be observed at shorter pulse separation times. The case of N-BK7 is discussed more elaborate in section 7.3.2.

In summary, figure 6.21 shows a fast decay for samples containing atoms with a large nuclear quadrupole moment and most likey a large quadrupole coupling constant. In addition, no quantum beating and Gaussian shape like leveling-off of the echo amplitude is observed.

To verify these observations and the conclusions, like an additional relaxation mechanism based on nuclear quadrupole moments, more samples containing atoms with large nuclear quadrupole coupling constants were investigated. In figure 6.23 the corresponding decay curves are shown.
All measurements were performed with a pulse duration of $t_1 = 230\,\text{ns}$ and a field

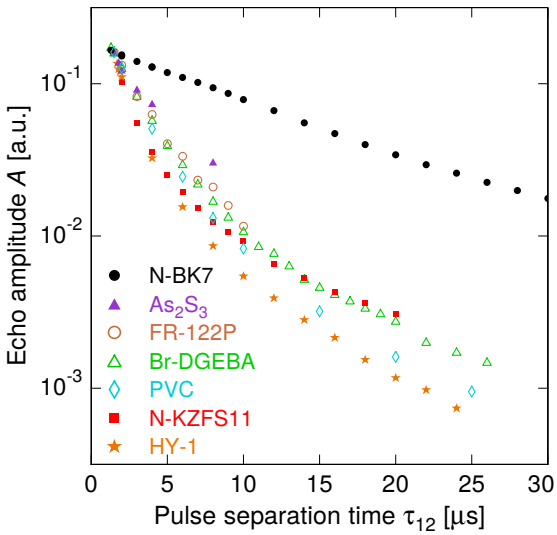

Figure 6.23: Echo amplitude in dependence of the pulse separation time measured at a temperature of 10 mK except for N-KZFS11 (10.1 mK) and Br-DGEBA (7.5 mK). The data is aligned at $\tau_{12} = 1.5\,\mu\text{s}$. The curve of N-BK7 consists of two separate measurements which are algined to each other. The field strength was such that the small angle approximation is fulfilled and t_1 =230 ns.

strength fulfilling the small angle approximation. The temperature was 7.5 mK for Br-DGEBA, 10.1 mK for N-KZFS11 and 10 mK for the remaining samples. All decay curves are aligned at a pulse separation time of 1.5 µs. The small difference in the temperature of Br-DGEBA to the other samples should not influence the decay behavior significantly. But if it has a significant influence it should rather lead to a less fast decay since the number of phonons is reduced. In the plot it can be seen that all decay curves show a very fast decay of the echo amplitude compared to N-BK7 above a pulse separation time of 1.5 µs. This behavior is independent of whether the sample is an inorganic oxide or non-oxide glass (shown with full symbols) or an organic molecular or polymer glass (depicted with open symbols). All the samples showing the fast decay have in common that they contain at least one kind of atom with a large nuclear quadrupole coupling constant (compare section 5.4 and table A.1). In contrast to the multicomponent glasses N-KZFS11 and HY-1 the other samples (As_2S_3, FR-122P, Br-DGEBA and PVC) contain only one kind of atom carrying a nuclear quadrupole moment (compare section 5.4). Thus the relaxation based on nuclear quadrupole moments can be attributed to one specific kind of atom. In addition, the properties of the nuclear quadrupole coupling in these materials are often well known (compare table A.1) which allows a closer examination of the properties of the relaxation mechanism in the further course of this section. As already anticipated, the variation of the quadrupole coupling constant seems to be more important than its absolute value. Thus it is in principle possible that the fast decay at short times, observable in N-KZFS11 and HY-1, is not caused by the obvious isotopes tantalum and holmium, but by another isotope with a quadrupole moment present in these glasses. However, these additional isotopes are to a large extent also present in N-BK7. In N-BK7 they cause no fast decay of the echo amplitude at short times. Since the basic composition of N-KZFS11, HY-1 and N-BK7 is similar these atoms are expected to be at similar positions in all three glasses. Thus the fast decay of the echo amplitude for N-KZFS11 and HY-1 is indeed caused by tantalum and holmium. Nevertheless, due to missing nuclear quadrupole studies on these materials, it cannot be completely ruled out that the local environment of the quadrupole carrying atoms and probably their coupling to the tunneling motion is different in these glasses.

The absence of the quantum beating and the Gaussian shape like leveling-off at small pulse separation times for these samples is caused by the same effects as discussed in the framework of figure 6.21. However, for the organic molecular samples it is due to the strong intramolecular forces, compared to the intermolecular ones, more likely that the level schemata of the different tunneling systems look similar. Thus for the organic molecular samples the absence of the quantum beating is most likely caused by the broadening of the quadrupole splittings due to the amorphous structure and the large beating frequencies leading to a fast smearing of the quantum beating (compare figure 6.22).

The observed fast decay at short pulse separation times of the samples with a large quadrupole coupling in figure 6.23 explains to a large extent the small echo ampli-

tudes, shown in figure 6.20. Besides a fast decay of the echo amplitude, a small density of states P_0 reduces the observed echo signal. For As_2S_3 this is suggested by dielectric measurements [Mün19]. The fast decay together with a small density of states can explain the very tiny echo of this sample in figure 6.20. The fast relaxation of the glasses containing atoms with large nuclear quadrupole coupling is also the reason why it was not possible to investigate the decay behavior of these samples at pulse separation times larger than about 30 µs. For the samples with very small echo amplitudes, like As_2S_3 and FR-122P, a measurement was only possible up to about 10 µs.

Based on the decay behavior at pulse separation times larger than 1.5 µs, only basic properties of the nuclear quadrupole based relaxation can be extracted. Definite conclusions on the actual strength of the relaxation process and a correlation to the properties of the contained nuclear moments in the samples are not possible, since the amount of tunneling systems that already decayed until $\tau_{12} = 1.5\,\mu s$ is unknown. Thus, indications for potential correlations between the nuclear properties and the relaxation rate need to be crosschecked with data at smaller pulse separation times. With the measurement setup used for the measurements in figure 6.23 it is not possible to measure reliable data below a pulse separation time of about 1.5 µs (compare section 7.1). The issue of the missing data at very small pulse separation times is illustrated in figure 6.24 by four numerically calculated decay curves. In the left plot four complete curves are shown, starting at a pulse separation time of 0 µs. In the right plot the same decay curves are shown, but without the data at pulse separation times smaller than 1.5 µs to imitate an actual measurement. The curves are aligned at a pulse separation time of 1.5 µs to compare their decay behavior. Without the data at pulse separation times smaller than 1.5 µs, the 'fast decay' (red) and the 'intermediate decay 1' (green) show a similar decay behavior, because they

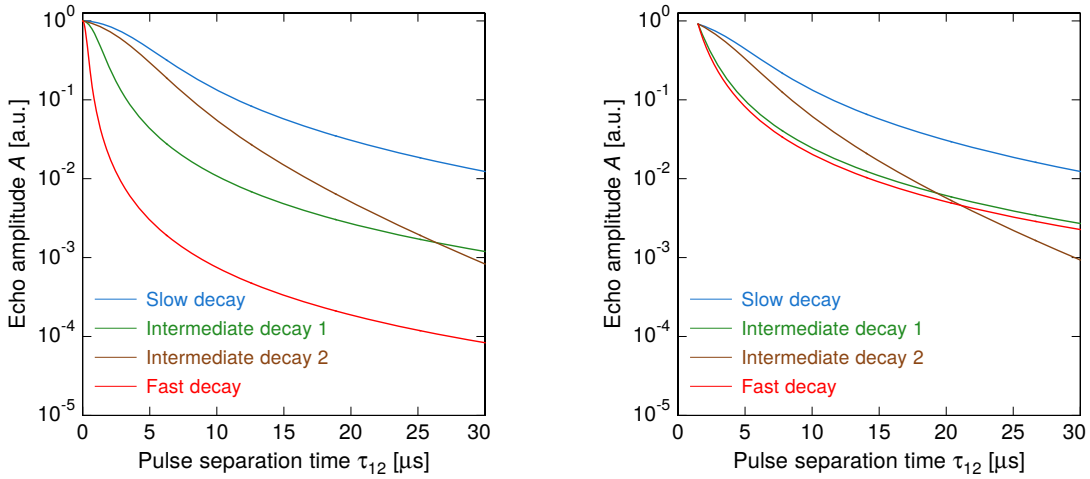

Figure 6.24: Left: Numerical calculation of four arbitrary decay curves. **Right:** The decay curves of the left plot are aligned at a pulse separation time of 1.5 µs.

have a similar relaxation rate in this time window. However, up to a pulse separation time of 1.5 µs, the tunneling systems in the 'fast decay' case relax significantly faster (see figure 6.24 left). This comparison underlines, that with data at pulse separation times larger than 1.5 µs only conclusions on the relaxation mechanism in this time regime can be drawn. Whether they are also true for smaller pulse separation times needs to be verified by additional measurements.

Transferring the problem to the decay curves shown in figure 6.23, the only definite conclusion is that the echo amplitudes of all samples containing atoms with a large nuclear quadrupole coupling constant decay, at pulse separation times larger than 1.5 µs, fast compared to N-BK7. In the group of the samples showing a fast relaxation at short time, the crossover from the fast decay to the linear regime and the slope of the decay curve at short times could indicate the strength of the relaxation based on nuclear quadrupole moments. Considering this case, a crossover at smaller pulse separation times corresponds to a stronger nuclear quadrupole moment based relaxation mechanism since the tunneling systems sensitive to this relaxation process decay faster and other relaxation mechanism dominate earlier. In addition, a steep slope indicates a high relaxation rate of the tunneling systems and thus probably a large influence of the nuclear quadrupole moments. If this relation is correct, the decay curves of N-KZFS11, HY-1 and PVC show the strongest relaxation. However, it is also thinkable, even if it is very unlikely, that the relaxation in As_2S_3 is such strong that the crossover region is already at pulse separation times smaller than 1.5 µs and the decay curve only seems to be not so influenced by the nuclear quadrupole moments in the sample. After all, As_2S_3 contains 40 at.% arsenic with a comparatively large quadrupole coupling constant resulting in a nuclear splitting of about 70 MHz. In addition, the stoichiometry of As_2S_3 causes that every tunneling system either contains a nuclear quadrupole moment or is connected to one which could potentially cause a very fast decay. Nevertheless, it is unlikely that As_2S_3 exhibits a very fast decay and a strong leveling-off of its echo amplitude, all below a pulse separation time of 1.5 µs.

Considering the knowledge about the relaxation of nuclear moments in amorphous solids (section 4.5.2, in particular equation 4.31 and 4.32), the relaxation rate of the nuclear quadrupole moment depends not on the absolute value of the quadrupole coupling constant, but on its variation. In the calculation of the nuclear quadrupole moment relaxation rate, the variation of the quadrupole coupling constant enters quadratically and is given by the quadrupole moment and the variation of the electric field gradient, caused by the tunneling motion. If the same relation holds for a relaxation of the tunneling systems due to interactions with nuclear quadrupole moments, the variation of the electric field gradient is, besides the magnitude of the quadrupole moment, a very important parameter. This may also explain to some extent why the relaxation of HY-1 and N-KZFS11 is so strong. The quadrupole moment of holmium and tantalum is about one order of magnitude larger than the one of all other atoms contained in the other samples shown in figure 6.23. Thus

Estimation of electric field gradient				
	As_2S_3	FR-122P	Br-DGEBA	PVC
Electric field gradient $\vec{\nabla}\vec{F}$ [a.u.]	366	1750 - 2000	1750 - 2000	795

Table 6.1: Estimation of the electric field gradient seen by the nuclear quadrupole moments present in the respective samples. For the calculation $\vec{\nabla}\vec{F} \propto {}^{C_Q}/_{Q}$ was used (compare equation 4.6). The values for the coupling constants and the quadrupole moments are taken from table A.1.

the variation in the electric field gradient caused by the tunneling motion can be about one order of magnitude smaller to cause a similar relaxation strength. If these assumptions are correct and the relaxation in PVC is indeed stronger than the one in As_2S_3, the electric field gradient variations present in PVC have to be significantly larger than those in As_2S_3, since the quadrupole moment of chlorine is distinctly smaller than the one of arsenic. An estimation of the electric field gradient, seen by the different nuclei of the organic samples, is given in table 6.1. The values are obtained using equation equation 4.6 and the quadrupole coupling constants and quadrupole moments from table A.1. For the multicomponent glasses this estimation is not possible, since there are no measurements of the quadrupole coupling constants in these materials available. The table shows, that the electric field gradient experienced by the chlorine atoms is about twice as large as the one experienced by the arsenic atoms. Thus, it is possible that there is also a large variation of the electric field gradient by a tunneling motion which overcompensates the small quadrupole moment. If the nuclear splitting of the bromine in Br-DGEBA and FR-122P is as expected in the range of 250 MHz (there is no exact value for these materials) this would imply that the electric field gradient experienced by the bromine atoms in these materials is even larger than the one seen by chlorine in PVC. If the strength of the nuclear relaxation in Br-DGEBA and FR-122P is indeed between the one in PVC and As_2S_3, as it seems to be in figure 6.23, this would mean that the electric field variation by the tunneling motion is comparatively small although the absolute electric field gradient is very large.
It should be mentioned again, that the above discussion on figure 6.23 is based on the decay at 10 mK and at pulse separation times larger than 1.5 µs. To verify and check the actual strength of the nuclear moments based relaxation mechanism, measurements below a pulse separation time of 1.5 µs are necessary.

A comparison of the decay behavior with further data, published in previous theses and different papers, is shown in figure 6.25. Since here also decay curves of samples containing atoms with a comparatively small nuclear quadrupole coupling constant are shown, the assumption of the variation of the nuclear quadrupole coupling constant as the relevant parameter for the nuclear quadrupole moment based relaxation can be tested.
The decay curves were measured at temperatures between 7.5 mK and 15 mK. The exact temperatures are given in the caption of the plot. The small temperature

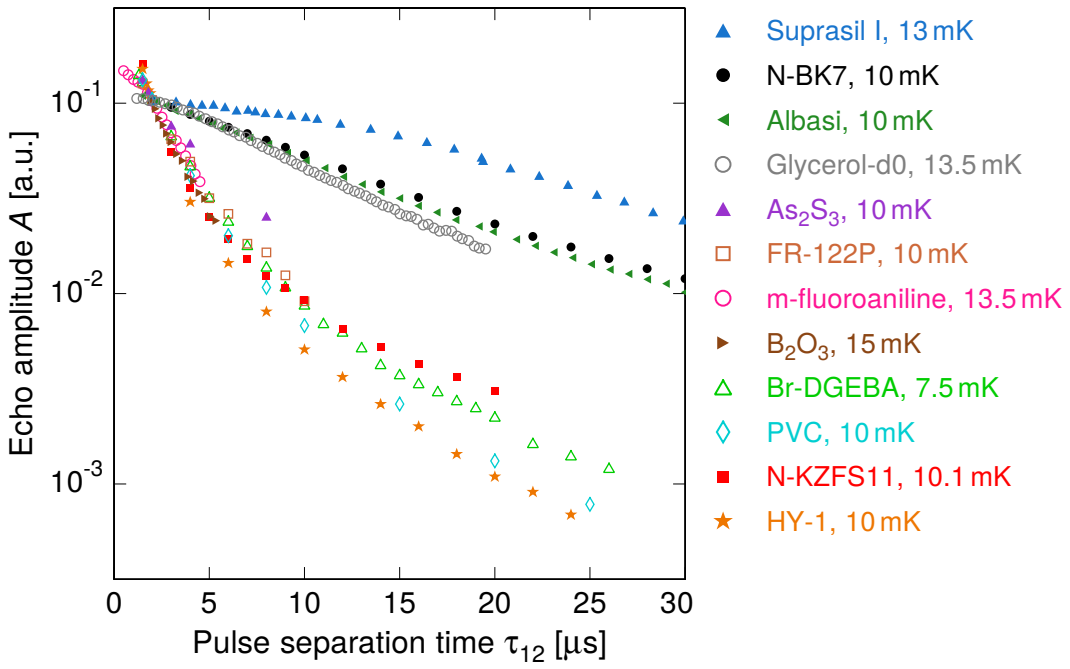

Figure 6.25: Echo amplitude as a function of the pulse separation time for various samples. The curves were measured at temperatures between 7.5 mK and 15 mK. For better comparison they are aligned at a pulse separation time of 2 µs. The data of Suprasil I is taken from [Ens96b], Albasi from [Lud02], glycerol-d0 and m-fluoroaniline from [Bra04a] and B_2O_3 from [Lud00].

differences should not influence the decay behavior significantly. Since the smallest pulse separation time measured for all samples is 2 µs, the decay curves are aligned at this pulse separation time. At pulse separation time larger 2 µs the decay behavior and thus the relaxation rates of the tunneling systems of the different samples cluster roughly in three groups.

The sample showing the smallest relaxation rate is Suprasil I. This sample also shows a very broad Gaussian shape like leveling-off of the echo amplitude at short pulse separation times. Suprasil I is, except for very rare isotopes, completely free of quadrupole moments (compare section 5.4) and consequently no influence of a nuclear quadrupole moment based relaxation is expected.

The second group contains the decay curves of N-BK7, Albasi and glycerol-d0. The first two mentioned contain atoms which have as far as known only a comparatively small nuclear quadrupole coupling constant. Glycerol-d0 contains apart from traces of rarely occurring isotopes, no atoms which carry nuclear quadrupole moments. In this plot the decay curve of glycerol-d0 (ordinary glycerol) is shown instead of deuterated glycerol, since the quantum beating of the deuterated samples makes the plot confusing. Furthermore, it was shown in [Bra04a, Baz08] that the overall decay behavior is similar for deuterated and ordinary glycerol. Thus the quadrupole moment of the deuteron atoms in deuterated glycerol do not influence the decay behavior

strongly in the investigated time window and at the investigated temperatures. The estimated electric field gradient seen by the deuteron atoms in deuterated glycerol is given in table 6.2. Compared to the electric field gradients of the samples showing a fast decay in figure 6.23 the absolute value is small. Since the strength of the nuclear quadrupole moment based relaxation of the tunneling systems is expected to be proportional to the quadrupole moment and the variation of the electric field gradient (compare equation 4.32) it is reasonable that the deuterons have only minor influence. The quadrupole moment of deuteron is very tiny such that a very large variation of the electric field gradient would be necessary to cause a strong contribution. This large variation is with this small absolute value of the electric field gradient probably not possible. For N-BK7 and Albasi no nuclear quadrupole data is available. Compared to N-BK7 and Albasi, the decay curve of glycerol-d0 is influenced by a quantum beating with a very small frequency, caused by the dipole effect (compare [Baz08]). Thus the decay curve looks a bit steeper. In N-BK7 and Albasi the quantum beating is smeared such that the overall echo amplitude is reduced. Considering the decay behavior, N-BK7 and Albasi show a faster decay than Suprasil I with a linear behavior. Glycerol-d0 shows a similar fast decay with a linear behavior, too. At very short pulse separation times a Gaussian shape like leveling-off of the echo amplitude can be guessed for glycerol-d0, but not for N-BK7 and Albasi. Whether the faster decay of the echo amplitude of N-BK7 and Albasi, compared to Suprasil I, is indeed caused by a comparatively weak influence of a nuclear quadrupole moment based relaxation or only by a different coupling to phonons cannot be determined from figure 6.25. The absence of the Gaussian shape like leveling-off of the echo amplitude towards small pulse separation times points towards an additional relaxation mechanism besides one-phonon relaxation and spectral diffusion. Later, it is shown that there is also substantive evidence for an additional relaxation process being dominant at low temperatures in these samples.

The third group consists of the samples As_2S_3, FR-122P, Br-DGEBA, PVC, N-KZFS11, HY-1, m-fluoroaniline and B_2O_3 and shows a very fast decay of the echo amplitude at short pulse separation times. All samples, except for m-fluoroaniline and B_2O_3, contain atoms with a comparatively large nuclear quadrupole coupling constant and were already discussed in the framework of figure 6.23. The nitrogen atoms in m-fluoroaniline have, as far as known, only a small quadrupole coupling constant. Since their quadrupole moment is very small, too, the electric field gradient experienced by the nitrogen atoms is comparatively large but still significantly smaller than the one experienced by the chlorine atoms in PVC or the bromine atoms in Br-DGEBA or FR-122P (compare table 6.2). Compared to deuteron, the quadrupole moment of the nitrogen atoms is about one order of magnitude larger. Thus a variation of the electric field gradient of the same size in deuterated glycerol and m-fluoroaniline causes an about 100 times[7] stronger contribution to the relaxation. In addition, the electric field gradient experienced by the nitrogen atoms in m-fluoroaniline is about 2.5 times stronger than the one seen by the deuterium atoms

[7]It is assumed, that equation 4.32 holds also for the case of tunneling systems

Estimation of electric field gradient - continuation of table 6.1			
	m-fluoroaniline	B_2O_3	Glycerol-d5
Electric field gradient $\vec{\nabla}\vec{F}$ [a.u.]	190	65	73

Table 6.2: Estimation of the electric field gradient seen by the nuclear quadrupole moments present in the respective samples. For the calculation $\vec{\nabla}\vec{F} \propto {}^{C_Q}/_{Q}$ was used (compare equation 4.6). The values for the coupling constants and the quadrupole moments are taken from table A.1.

in glycerol. In principle, it is also easier to create a larger variation of the electric field gradient if its absolute value is large as well. However, comparing the decay rate of the tunneling systems in m-fluoroaniline with the one of the tunneling systems in As_2S_3, it can be seen that neither the size of the quadrupole moment (the one of arsenic is more than one order of magnitude larger than the one of nitrogen) nor a high absolute value of the electric field gradient is a guarantee for a strong contribution of the quadrupole moment based relaxation. Hence, the variation of the electric field gradient by the tunneling motion seems to be the most relevant parameter. The kink in the data of m-fluoroaniline below a pulse separation time of 2 µs is caused by a quantum beating in this material at pulse separation times smaller than 2 µs [Bra04a].

The sample B_2O_3 contains 40 at.% of boron, which carries a comparatively small quadrupole moment. Since the boron atoms in B_2O_3 have only a small quadrupole coupling constant, the electric field gradient experienced by them is even smaller than the one seen by the nitrogen atoms in m-fluoroaniline (compare table 6.2). However, the modulation of the electric field gradient in B_2O_3 seems to be large enough to cause a fast relaxation of the tunneling systems. This observation is in accordance with NMR measurements of ^{11}B in glassy B_2O_3, discussed in the framework of figure 4.24, where a reduced relaxation time was observed, too. The value for the relaxation time at a temperature of about 1 K, measured in this investigation, is in the range of several minutes and thus much larger than the relaxation time observed in figure 6.25 for the tunneling systems in B_2O_3. As discussed in the framework of figure 4.23, the relaxation time measured in NMR experiments is determined by all boron nuclei in the respective solid. Since not every boron atom is part of a tunneling system the relaxation time of those which are actually part of a tunneling system could be significant lower. In addition, due to the stoichiometry of B_2O_3 every tunneling system in this material either contains at least one boron atom or is connected to one. Therefore it is possible that the averaged modulation of the quadrupole coupling by the tunneling motions of the tunneling systems and thus the relaxation time of the ensemble of tunneling systems is significantly smaller than the one measured for the boron atoms in NMR.

In [Lud00] the fast decay of the echo amplitude of B_2O_3 compared to Suprasil I is described by an enhanced coupling to thermal phonons, which leads to shorter relaxation times T_1 and T_ϕ. Of course, an enhanced coupling to the phonon bath

is, for all samples showing a fast decay on short pulse separation times, a possible explanation. However, the comparison of the different samples in figure 6.25 and the observation of a nuclear quadrupole moment based relaxation in [Luc16] also point towards a significant contribution of a nuclear quadrupole moment based relaxation in B_2O_3.
It is noteworthy that B_2O_3 shows a rapid relaxation, whereas N-BK7, which also contains about 4 at.% boron, does not show any major influence in the relaxation behavior. The quadrupole coupling constant of boron in N-BK7 is not known exactly, but should be similar to B_2O_3 or Pyrex (compare table A.1). Since the structure of the multicomponent glass N-BK7 and of pure B_2O_3 is different, the boron atoms in B_2O_3 could experience a larger change in their electric field gradient by a tunneling motion compared to N-BK7. Besides the variation of the electric field gradient, the absolute fraction of boron in the composition of the sample could be a relevant parameter. But if the fast decay of N-KZFS11 and HY-1 is indeed mainly caused by the 1.5 at.% tantalum (N-KZFS11) and 0.5 at.% holmium (HY-1), the absolute fraction seems to be less important. The remaining possibility is thus the variation of the electric field gradient, which is directly connected to the nature of the tunneling systems in the respective materials.

Based on the observations in figure 6.25 at pulse separation times larger than 2 µs and at a temperature of about 10 mK, the relaxation mechanism based on the atoms carrying nuclear quadrupole moments is:

- Independent of the nuclear spin I of the atom (e.g. $I = 7/2$ for holmium and tantalum; $I = 3/2$ for chlorine, bromine, boron; $I = 1$ nitorgen).
- Independent of whether the sample is a pure material, a multicomponent glass, a molecular glass or a polymer glass.
- Independent of the size of the quadrupole coupling constant. Although most samples showing a fast decay have a comparatively large coupling constant, B_2O_3 and m-fluoroaniline show that this is not mandatory.
- Depending on the nature of the tunneling systems in the respective samples. This includes the different atoms which are actually part of a tunneling system and the variation of their quadrupole coupling constant, or rather of the electric field gradient, during the tunneling motion.

The discussion so far showed, that the relaxation based on nuclear quadrupole moments is neither depending on the size of the quadrupole coupling constant of the atoms nor on their fraction in the sample. The implementation of the respective atoms in the sample is more important. To validate this assumption, figure 6.26 shows the isotopes carrying nuclear quadrupole moments and their fraction in the composition of the samples depicted in figure 6.25. The isotopes contained in N-BK7 and Albasi are highlighted in gray for better discrimination since those isotopes

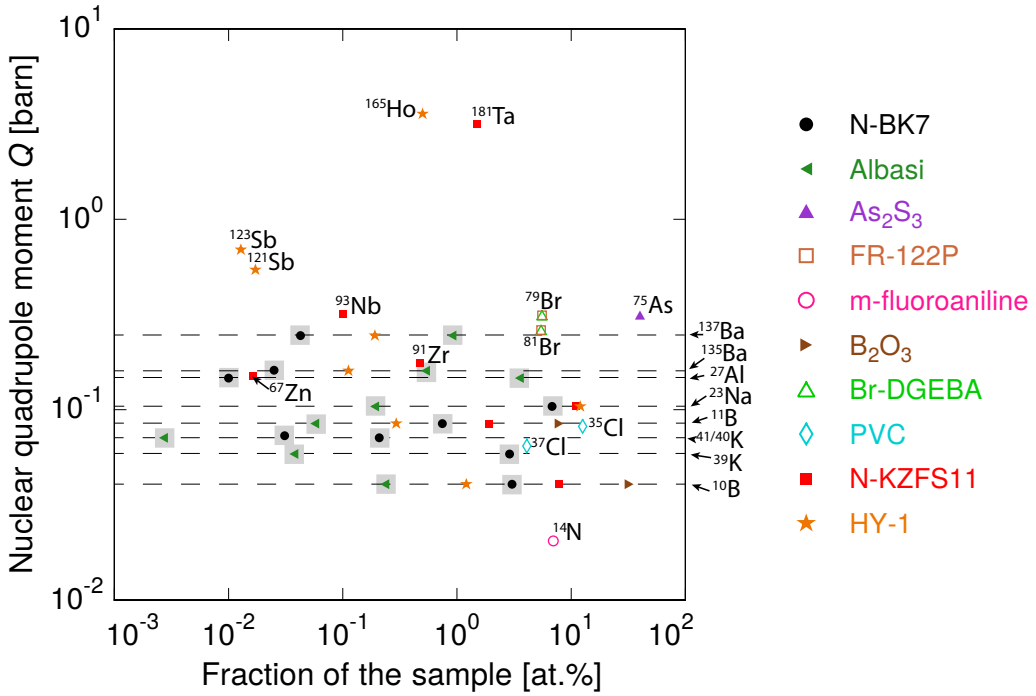

Figure 6.26: Fraction of the isotopes carrying a nuclear quadrupole moment of the samples shown in figure 6.25. The fraction was calculated by the composition of the sample (compare section 5.4) and the natural abundances of the respective isotopes (compare table A.1). The data points belonging to N-BK7 and Albasi are highlighted in gray since they do not show strong contribution to the relaxation processes of the tunneling systems in these materials at a temperature of 10 mK.

showed no or just little influence on the relaxation of the tunneling systems in these samples at a temperature of 10 mK. It is interesting that N-BK7 shows no large influence although it contains beside the boron atoms also a sizable amount of ^{23}Na and ^{39}K. Albasi, where also no large influence is observed, contains comparatively large amounts of $^{135/137}$Ba and ^{27}Al. The fraction of these atoms in N-BK7 and Albasi is comparable to the fraction of quadrupole carrying atoms in the other samples, which show a fast decay on short pulse separation times. Considering section 2.2.1, sodium, potassium and barium act as a network modifier in the multicomponent glasses. Thus the Na^+, K^+ and Ba^{2+} ions ly more or less loosely in the holes of the glass network and it is thinkable that they experience only a small or no electric field gradient and hence no or only a small change during a tunneling motion. Aluminum is an intermediate oxide. Since there are several ions with a valence of one in Albasi, it is possible, that aluminum acts as a network former. Therefore it should experience a large electric field gradient, but the nature of the tunneling systems in Albasi is probably such that the modulation of the quadrupole coupling constant of aluminum is small and no large contribution to the relaxation of the tunneling systems arises. In all non-multicomponent glasses the atoms carrying nu-

clear quadrupole moments are bound covalently and thus experience a large electric field gradient and possibly also a large variation. The tantalum atoms in N-KZFS11, which are supposed to be the main reason for the fast decay of the echo amplitude at short pulse separation times, are most likely part of the glass matrix and bound covalently such that they experience a large electric field gradient (compare section 5.4). The holmium atoms in HY-1 act most likely as a network modifier (compare section 5.4). Since the remaining composition of HY-1 is similar to N-BK7, the fast decay of the echo amplitude at short pulse separation times in HY-1 is attributed to the holmium atoms. The electric field gradient experienced by the holmium atoms in the holes of the glass network is unknown. It is possible that the electric field gradient is not very large, as mentioned in above discussion for the Na^+, K^+ and Ba^{2+} ions in N-BK7 and Albasi, but this information is not accessible without NQR studies on the glass HY-1. If the electric field gradient, experienced by the holmium atoms, is indeed very small, the quadrupole coupling constant cannot be large, as it was assumed so far. However, due to the large quadrupole moment of holmium compared to sodium, potassium or barium a small change of the electric field gradient could be sufficient for a fast decay of the echo amplitude at short pulse separation times.
This consideration confirms that the implementation of the quadrupole carrying atom in the respective solid and the nature of the tunneling systems is relevant for the contribution of these atoms to the nuclear quadrupole moment based relaxation of tunneling systems. In addition, in multicomponent glasses the atoms acting as network modifiers usually contribute less to the relaxation based on nuclear quadrupole moments. A possible so far not clarified exception could be holmium.
Finally, figure 6.26 also underlines the difficulty to attribute a fast relaxation, observed in the decay of the echo amplitude of a multicomponent glass, to a specific kind of atom in this material. Pure materials like As_2S_3 or B_2O_3 and organic compounds which contain only one kind of atom carrying a nuclear quadrupole moment are more suited for these investigations. Since the contribution of a nuclear quadrupole moment to the relaxation of the tunneling systems seems to be strongly dependent on the nature of the tunneling systems, the fast decay observed in N-KZFS11 and HY-1 could also be the result of the plurality of isotopes carrying nuclear quadrupole moments in these materials.

Until now only the contribution of a relaxation mechanism based on the nuclear quadrupole moments of the atoms contained in the different samples to the decay of the tunneling systems was considered. In section 4.5.2 it is shown that a fast relaxation of nuclear moments in an amorphous solid can also be caused by a magnetic dipole-dipole interaction. Thereby the tunneling motion of an atom with a magnetic moment causes a varying magnetic field at a nearby nucleus which stimulates a relaxation of this nucleus. The magnetic moment of an atom is given by the nuclear magnetic moment and the magnetic moment of its electron shell. A fully occupied orbital of an atom has no permanent magnetic moment. Thus the covalent bound atoms of the organic samples and those building the glass matrix in the inor-

ganic samples exhibit only a nuclear magnetic moment and no permanent magnetic moment of the electron shell. Only the network modifier ion Ho^{3+}, present in the multicomponent glass HY-1, has a not fully occupied orbital and hence also a permanent magnetic moment of the electron shell. From the observation of the dipole effect in glycerol, it is known that there is a coupling of the nuclear magnetic dipole moment and the tunneling systems. Hence it is obvious that the magnetic dipole moment of the atoms in the different samples, shown in figure 6.25, can also cause a relaxation of the tunneling systems. For atoms which also carry a nuclear quadrupole moment the nuclear dipole-dipole interaction is usually significantly smaller than the quadrupole interaction and thus negligible (compare section 4.5.2). However, if the electron shell has a magnetic moment, it is much larger than the nuclear magnetic moment, and this assumption may no longer be valid.

In the following the possible influence of the dipole-dipole interaction on the relaxation behavior of the samples shown in figure 6.25 is examined. The fraction of the atoms carrying nuclear magnetic moments of the different samples is summarized in table 6.3. In addition, the averaged magnetic moment, weighted by the fraction of the respective isotopes, and the most abundant isotopes are given for every sample. It is apparent that Suprasil I contains only a very small percentage of atoms which carry a nuclear magnetic moment, leading to a comparatively large distance between these atoms in the sample. The dipole-dipole interaction reduces strongly with the distance between the magnetic moments (compare equation 4.33). Therefore no influence of the magnetic moments in the decay behavior of Suprasil I is expected. This is in accordance with the small decay rate observable in figure 6.25. Furthermore, measurements of the ^{29}Si relaxation rate in amorphous $(Na_2O)_{0.2}(SiO_2)_{0.7}$ showed no reduced relaxation rate in the amorphous state (compare figure 4.24).
About a fifth of the atoms in glycerol-d0 carry a nuclear magnetic moment, almost exclusively hydrogen. In this sample and in deuterated glycerol, a quantum beating caused by the dipole effect is observed [Baz07, Baz08]. Besides the echo reduction by the quantum beating, the dipole-dipole interaction could also cause a small additional relaxation of the tunneling systems. Since the overall decay behavior of deuterated and ordinary glycerol is similar [Bra04a, Baz08], the contribution of the dipole moments to the decay could be similar to the contribution of the deuteron with its small nuclear quadrupole coupling (compare also the comment regarding hydrogen and deuteron in section 4.5.2). The other organic samples (FR-122P, m-fluoroaniline, Br-DGEBA, PVC), As_2S_3 and B_2O_3 contain a high percentage of atoms carrying a nuclear magnetic moment, too. Thus there is most likely a dipole-dipole interaction similar to glycerol. The influence on the relaxation behavior should therefore be of the same order of magnitude. In the decay of the echo amplitude of these samples no quantum beating caused by the dipole-dipole coupling is observed. This quantum beating is either smeared, as the one caused by the quadrupole interaction, or its frequency is too small to be observed in the time window of figure 6.25.
The multicomponent glasses N-BK7, Albasi and N-KZFS11 contain atoms which carry only a nuclear magnetic moment, since the network modifier ions (e.g. Na^+,

Nuclear magnetic moments in the samples			
Sample	Fraction of atoms carrying a magnetic moment. [at.%]	Averaged magnetic moment [μ_N]	Most abundant isotopes [at.%]
Suprasil I	1.59	0.577	^{29}Si - 1.6
Glycerol-d0	22.02	2.734	^{1}H - 21
N-BK7	14.97	1.794	^{23}Na - 6.8 ^{10}B - 3 ^{39}K - 2.9
Albasi	6.64	2.404	^{27}Al - 3.52
As_2S_3	40.46	1.43	^{75}As - 40
FR-122P	61.32	2.642	^{1}H - 39.8 ^{79}Br - 5.5 ^{81}Br - 5.4
m-fluoroaniline	57.53	2.462	^{1}H - 43 ^{14}N - 7 ^{19}F - 7
B_2O_3	40.02	2.512	^{10}B - 32 ^{11}B - 8
Br-DGEBA	51.46	2.642	^{1}H - 39.8 ^{79}Br - 5.7 ^{81}Br - 5.6
PVC	70	2.21	^{1}H - 50 ^{35}Cl - 12.6 ^{37}Cl - 4
N-KZFS11	22	2.3	^{23}Na - 11 ^{10}B - 7 ^{11}Br - 2
HY-1	15.53	2.159	^{23}Na - 12 ^{10}B - 1.2 ^{29}Si - 1.18

Table 6.3: Table of the fraction of atoms carrying a magnetic moment in the samples investigated in the framework of figure 6.25. The fraction is calculated based on the composition of the sample (section 5.4) and the natural abundances given in table A.2. The given averaged magnetic moment is weighted by the fraction of the respective isotopes in the samples and calculated by the values given in table A.2.

K^+, Ba^{2+}) in these glasses have fully occupied orbitals. Thus the dipole-dipole interaction between these atoms should not influence the decay behavior more than the dipole-dipole coupling present in glycerol. Since the absolute fraction of the atoms carrying nuclear magnetic moments is distinctly smaller than in the organic samples, the impact could be also even less pronounced. In contrast to these multicomponent

glasses, HY-1 contains 0.5 at.% holmium which is supposedly a network modifier. Its ion, Ho^{3+}, has due to its not fully occupied 4f orbital a permanent magnetic moment of the electron shell. The magnetic moment of the electron shell is much larger than the one from the nucleus[8]. This large magnetic moment causes large varying magnetic fields at other nearby nuclear spins and may induce relaxation processes. If the relaxed nuclear moments are part of tunneling systems, the relaxation behavior of the tunneling systems is influenced as well. If holmium influences the relaxation of the tunneling systems via such a magnetic dipole-dipole coupling, it is independent of whether the holmium atom tunnels or the nearby nuclear spins. Furthermore, it is independent of the size of the electric field gradient experienced by the holmium atoms in HY-1. Thus, if the fast decay of the echo amplitude of HY-1 at short pulse separation times is caused by the holmium atoms, this coupling mechanism could also explain why holmium influences the relaxation behavior of the tunneling systems significantly more compared to the other network modifiers, which are also present in N-BK7 and Albasi. To classify the influence of holmium on the relaxation of tunneling systems, more information concerning the implementation of holmium in HY-1 and its NQR properties are needed. The large thermalization time of HY-1 at low temperatures (compare section 6.2.1), which is most likely caused by the holmium atoms, does not allow to draw conclusions concerning the implementation of holmium. Due to the permanent magnetic moment of the electron shell, the nuclear spin exhibits a nuclear splitting independent of an electric field gradient. Thus holmium always contributes to the specific heat of the sample.

Temperature dependence

In the previous section it was shown that several samples show a very fast decay of their echo amplitude at 10 mK at short pulse separation times. This fast decay is attributed to tunneling systems which carry a nuclear quadrupole moment. According to the model, developed in [Luc16], the nuclear quadrupole moment based relaxation dies out towards low temperatures, when the temperature becomes comparable to the nuclear quadrupole splitting of the respective isotope. After all nuclear quadrupole moment based relaxation processes died out, the decay of the echo amplitude should, under the assumption that only the one-phonon process and spectral diffusion remain, be similar for all samples independent of the amount of atoms carrying quadrupole moments. The remaining differences of the decay curves are then caused by the different couplings to the phonon bath and the strength of spectral diffusion. This prediction could not be tested, since the needed temperatures cannot be reached with a ^{3}He/^{4}He-dilution refrigerator for most samples investigated within this thesis.
However, if the echo decay is measured at higher temperatures the course of the decay curve of the different samples should also become more similar at short pulse

[8] For comparison: The nuclear magnetic moment is usually given in units of $\mu_N \approx 5.05 \cdot 10^{-27}$ J/T, the magnetic moment of the electron shell in units of $\mu_B \approx 9.27 \cdot 10^{-24}$ J/T

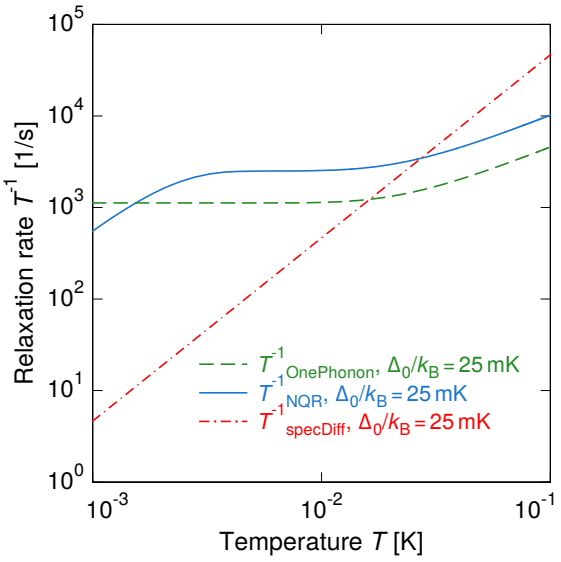

Figure 6.27: Relaxation rate as a function of temperature for tunneling systems with $E/k_B = 50\,\text{mK}$ and $\Delta_0/k_B = 25\,\text{mK}$. The parameters for the calculation of the relaxation rate of the one-phonon process and spectral diffusion are the same as in figure 3.17. For the quadrupole based relaxation $T_{c,0}^{-1} = 10\,\text{kHz}$, $\delta T = 1\,\text{mK}$ and $a = 2$ is assumed.

separation times. The origin for this assumption is exemplary illustrated in figure 6.27. The plot shows the temperature dependence of the relaxation rates caused by the one-phonon process (equation 3.58), the relaxation based on nuclear quadrupole moments (equation 4.34) and spectral diffusion (equation 3.67 and 3.68) for tunneling systems with an energy splitting $E/k_B = 50\,\text{mK}$ and a tunnel splitting of $\Delta_0/k_B = 25\,\text{mK}$. The parameters used for the calculation of the relaxation rate of the one-phonon process and spectral diffusion are the same as in figure 3.17. For the relaxation rate based on the nuclear quadrupole moments arbitrary values are used. These are $T_{c,0}^{-1} = 10\,\text{kHz}$, $\delta T = 1\,\text{mK}$ and $a = 2$. Figure 6.27 shows that the relaxation rate caused by spectral diffusion increases fast with rising temperature due to its T^2 dependence. At a certain temperature it becomes the dominant relaxation mechanism and determines the relaxation of the tunneling systems at short pulse separation times. The temperature from which spectral diffusion determines the course of the decay curve at short pulse separation times depends on the strength of spectral diffusion and the strength $T_{c,0}^{-1}$ of the quadrupole based relaxation rate, since this value determines the heigth of the plateau visible in figure 6.27.
The dominant relaxation is especially visible at short pulse separation times, because a strong spectral diffusion causes a fast decay of the asymmetric tunneling systems at short times. At a certain pulse separation time most of the tunneling systems with a large asymmetry decayed and the more symmetric remain. These decay afterwards via the one-phonon and the nuclear quadrupole based relaxation. Small variations in the strength of the one-phonon relaxation and the quadrupole based relaxation cause noticeable difference of the decay curves at large pulse separation times. This is visible in figure 6.28. In this plot decay curves at a temperature of 25 mK are shown. The samples are a selection of those shown in figure 6.25, since not for every sample a decay curve at a temperature of 25 mK is available. The different decay curves are aligned at a pulse separation time of 1.5 µs. Comparing the overall course

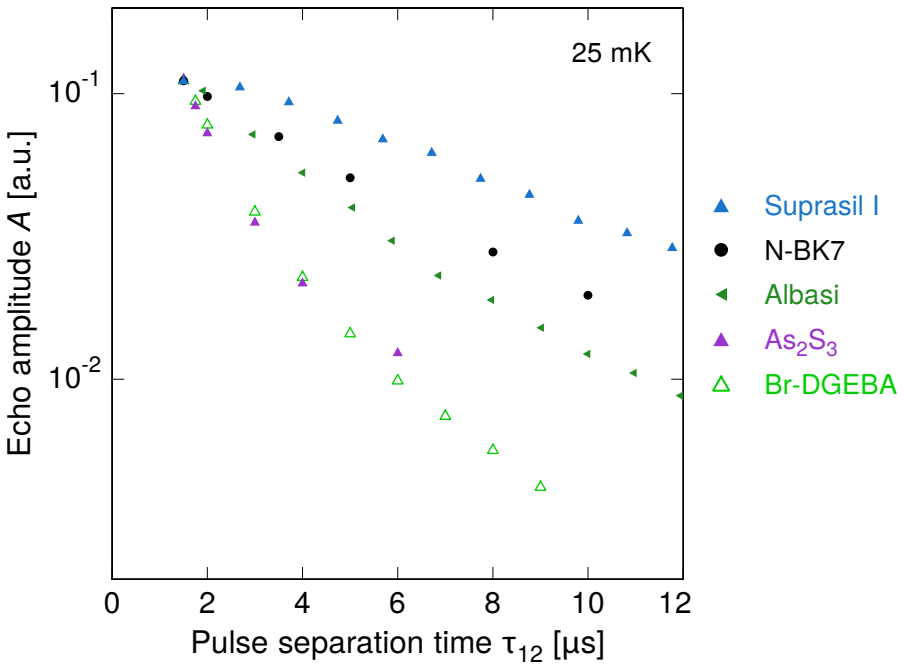

Figure 6.28: Echo amplitude as a function of the pulse separation time for various samples. The curves were measured at temperature of 25 mK. For better comparison they are aligned at a pulse separation time of 1.5 µs. The data of Suprasil I is taken from [Ens96b] and the one of Albasi from [Arc13].

of the decays shown in figure 6.28 and 6.25, the curves look more similar in figure 6.28. In addition, the clustering in three groups, visible in figure 6.25, is less pronounced in figure 6.28. The width of the different decay curves measured at 25 mK, which is given by the difference of the highest and lowest echo amplitude at a fixed pulse separation time, is also smaller. This can, as expected, be seen very good at short pulse separation times. The smaller width shows, that the relaxation rates are more similar at a temperature of 25 mK than at 10 mK. A more detailed comparison regarding the strength of the quadrupole moment based relaxation is not meaningful. Indeed, the absolute relaxation rate experienced by the tunneling systems is higher for a stronger relaxation based on nuclear quadrupole moments and thus the echo amplitude experiences a faster decay. But as the number of phonons is much higher at 25 mK than at 10 mK, the tunneling system phonon coupling determines the course of the echo decay more at 25 mK than at 10 mK. In addition, the data at very small pulse separation times is missing, which makes a comparison difficult.

Since the temperature change from about 10 mK in figure 6.25 to 25 mK in figure 6.28 is comparatively small, there is still a large spread in the decay behavior of the different samples. Due to the small echo amplitudes of the samples showing a very fast decay of the echo amplitude, no decay curves at higher temperatures were measured given the limited measurement time. But for BK7[9], Suprasil I and Albasi,

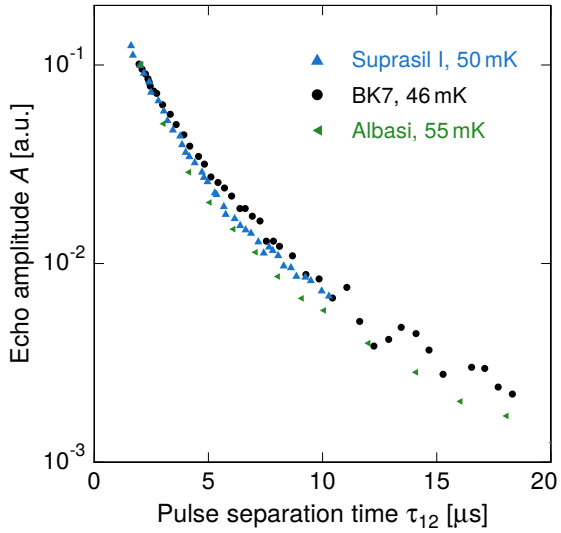

Figure 6.29: Echo amplitude as a function of the pulse separation time for Suprasil I , BK7 and Albasi. The curve of BK7 was measured at a temperature of 46 mK, the one of Suprasil I at 50 mK and the one of Albasi at 55 mK. For better comparison the decay curves are aligned to each other. Data of Suprasil I and BK7 taken from [Ens96b], of Albasi from [Arc13].

decay curves up to about 50 mK are available. At 10 mK (figure 6.25) the decay behavior of Albasi and N-BK7 differs significantly from Suprasil I. At 25 mK (figure 6.28) the difference between N-BK7 and Suprasil is already smaller and at about 50 mK the relaxation behavior of BK7, Albasi and Suprasil I is in the investigated time window very similar, as visible in figure 6.29. The small residual differences in the decay behavior are caused to a large extent by the difference in temperature (compare the caption). Since the relaxation rate of spectral diffusion, which is the dominant relaxation process at 50 mK, raises with T^2, the absolute temperature of the samples influence the decay of the echo amplitude significantly more than at about 10 mK. The data of Albasi was measured at a temperature of 55 mK, which corresponds to the highest temperature of the three shown curves. Thus it is expected that Albasi shows the fastest decay of its echo amplitude. Nevertheless, the high similarity of the decay behavior of BK7, Suprasil I and Albasi at about 50 mK shows that their coupling to the phonon bath and the strength of spectral diffusion is comparable. This is confirmed by measurements at 100 mK (see figure A.8), where the decay behavior of Suprasil I and BK7 is within the measurement accuracy equal. Thus the difference at low temperatures visible in figure 6.25 and 6.28 is not caused by a different coupling to phonons but by an additional relaxation mechanism.
The observations regarding the dominant relaxation mechanism are also in accordance with investigations of the temperature dependence of the phase memory time in N-BK7, Albasi and Suprasil. The temperature dependence of T_2^{-1} in N-BK7 [Fic13] and Albasi [Arc13] yielded a discrepancy from the expected T^2 dependence of the short time limit of spectral diffusion theory (equation 3.69) to a maybe linear temperature dependence at low temperatures. The exact temperature dependence in this temperature regime could in the framework of these publications not be de-

[9] The composition of BK7 and N-BK7 is except for probably some impurities similar. According to Schott AG the 'N' in N-BK7 stands for lead and arsenic free glasses. These elements were used for refining the molten glass.

termined. However, the change in the temperature dependence shows that there is another relaxation mechanism dominant at low temperatures. For N-BK7 and Albasi the change in the temperature dependency is between 30 mK and 40 mK. Possible mechanisms are the relaxation based on the nuclear quadrupole moments contained in the respective samples or collective excitations. The temperature dependence of the phase memory time T_2 of Suprasil I shows a T^{-2} dependence in the whole investigated temperature range (about 100 mK to 10 mK) [Ens96a]. Since Suprasil I is compared to N-BK7 and Albasi free of atoms carrying nuclear quadrupole moments, the discrepancy from the expected temperature dependence observed in N-BK7 and Albasi is probably caused by a relaxation based on nuclear moments.

The investigations of the temperature dependence of the relaxation based on nuclear quadrupole moments is in accordance with the model developed in [Luc16]. With rising temperature the coupling of the tunneling systems to the phonons becomes more important than the nuclear quadrupole moment based relaxation. But at low temperatures, when the number of phonons is small, the relaxation due to the nuclear quadrupole moments dominates the course of the echo decay.

6.4.3 Decay of the echo amplitude - comparison to theory

To test whether the observed fast decay at short pulse separation times coincides with the theoretical expectation, the data is compared to existing theory. According to these models, the echo amplitude in the limit of the small angle approximation is given by the integral

$$\begin{aligned} A(\tau_{12}) &= O_{\mathrm{cc}} \int A_{\mathrm{Echo,ts}} P(E,q)\, W_{\mathrm{1Phonon}} W_{\mathrm{specDiff,st}} W_{\mathrm{NQR}} \mathrm{d}q \\ &= A_0 O_{\mathrm{cc}} \int_0^1 \left(1-q^2\right) W_{\mathrm{1Phonon}} W_{\mathrm{specDiff}} W_{\mathrm{NQR}} \mathrm{d}q. \end{aligned} \tag{6.6}$$

To test whether the data can be described, the integral is fitted to the data. Thereby the relaxation times T_1 and T_2 are obtained. The factor A_0 in equation 6.6 represents the echo amplitude at the temperature $T = 0$ and a pulse separation time of $\tau_{12} = 0$. The factor O_{cc} gives the occupation difference of the tunneling system. For a two-level system it is given by equation 3.16. Since in the following only measurements at a fixed temperature are considered, this factor can be neglected.
To describe the measured data with equation 6.6 various issues need to be taken into account. The factor A_0 is not known. To describe echo decay curves at different temperatures, A_0 is usually determined based on data measured at the lowest temperature which was measured in the respective measurement cycle. For the description of the echo decay curves at the other temperatures, A_0 is kept constant, the occupation difference O_{cc} is adapted and the relaxation times are varied to get a good agreement of the data and the calculated curve. As shown in the context of figure 6.24, the missing data at short pulse separation times introduces a large uncertainty

in the determination of A_0. Furthermore, the reduction of the echo amplitude by destructive quantum beating influences A_0. Since A_0 is an important reference point, its correctness is crucial for a correct determination of the relaxation times and their temperature dependence. In addition, various combinations of $T_{1\text{Phonon}}$, T_{specDiff} and T_{NQR} can most likely describe the data well. Deciding whether the obtained values are reasonable for a sample, in which, for example, not much about the tunneling system phonon coupling is known, is not trivial.
Hence, the following examination considers the decay curves measured on N-KZFS11 and HY-1. These are multicomponent glasses with a similar composition as N-BK7. The consideration of the temperature dependence in the last section showed that the coupling to phonons is similar in the two oxide glasses N-BK7 and Suprasil I. Thus for the following rough estimation, it is assumed that the coupling of the phonons to the tunneling systems and hence the one-phonon relaxation and spectral diffusion is in N-KZFS11 and HY-1 similar to N-BK7 and Suprasil I[10]. This assumption is also supported by similar minimum temperatures[11] of the dielectric functions of these glasses at high frequencies, where the influence of the nuclear quadrupole moment based relaxation is very small (compare figure 4.22)[12]. Since Suprasil I is free from quadrupole moments and shows the temperature dependence of T_2 as predicted by spectral diffusion theory down to very low temperature [Ens96a], it is used to determine the relaxation times T_1 and T_2. These are $T_1 = T_{1\text{Phonon}} = 125\,\mu\text{s}$ and $T_2 = T_{\text{specDiff}} = 31.6\,\mu\text{s}$ (compare figure A.9). The data of Suprasil I, used for the determination of T_1 and T_2, was measured at a temperature of 13 mK, which is a bit higher than the 10 mK of N-KZFS11 and HY-1. However, the difference is negligible for the following estimation. The relaxation rate based on nuclear quadrupole moments for N-KZFS11 and HY-1 was determined in [Luc16] to be $T_{\text{c},0}^{-1} = 2\pi \cdot 5.4\,\text{kHz}$ for N-KZFS11 (no dying out of the rate was observed) and $T_{\text{c},0}^{-1} = 2\pi \cdot 138\,\text{kHz}$ for HY-1 (with $\delta T = 10\,\text{mK}$).
With the given relaxation times and rates the expected decay curves of the echo amplitude of N-KZFS11 and HY-1 can be calculated according to equation 6.6. The results are shown in figure 6.30 and 6.31. It is obvious, that the calculated curves do not describe the measured data. Furthermore, the curvature of the measured and calculated decay curve differs. This indicates that either equation 4.34 is not appropriate for describing echo measurements or that the decay, caused by the nuclear moments, cannot be described by an exponential decay behavior (compare equation 4.35). A third possibility is that there is another relaxation mechanism in these samples causing the fast decay at short pulse separation times. Especially the difference

[10]Spectral diffusion depends not only on the tunneling system phonon coupling but also on the density of states (compare for example the equations given in [Ens96b]). However, it is unlikely that the differences in the density of tunneling systems is large enough to explain the discrepancy observed in figure 6.30 and 6.31

[11]The minimum temperature is defined by the strength of the one-phonon or two-phonon process in the respective sample.

[12]The sample Herasil, shown in this figure, is a standard quartz glass and thus similar to Suprasil I, but with a lower amount of OH^- ions.

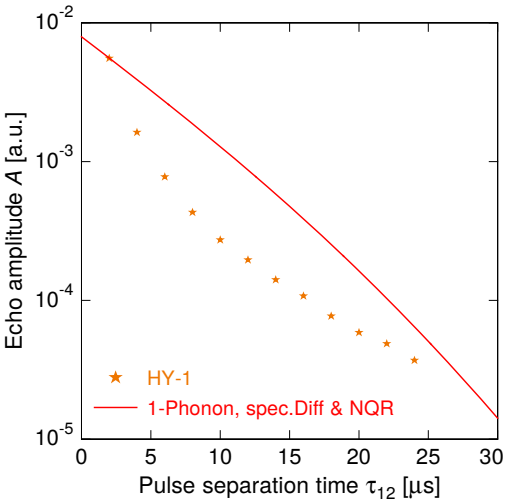

Figure 6.30: Echo amplitude of HY-1 in dependence of the pulse separation time, measured at a temperature of 10 mK. The curve is calculated according to equation 6.6 with the relaxation times given in the text.

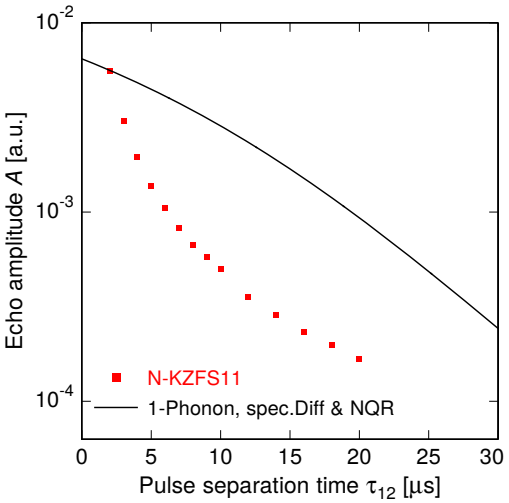

Figure 6.31: Echo amplitude of N-KZFS11 in dependence of the pulse separation time, measured at a temperature of 10.1 mK. The curve is calculated according to equation 6.6 with the relaxation times given in the text.

between the calculated and the measured decay curve in N-KZFS11, which is too large to be explainable by a larger influence of spectral diffusion or the one-phonon relaxation compared to N-BK7 or Suprasil I, points towards another relaxation mechanism.

In principle, every effect modifying the phase collection of the tunneling systems during the two-pulse sequence leads to an increased relaxation rate. For example, if a tunneling system contains atoms with a nuclear dipole moment that are in a dipole-dipole interaction with nearby atoms carrying nuclear dipole moments, a spin flip of one of the nearby atoms causes a change of the dipole-dipole interaction. Thereby the level schema of the tunneling system is slightly altered and the phase coherence lost. This effect is also present in glycerol-d0 and should therefore be weak in all samples shown in figure 6.25. An exception is HY-1, since the large magnetic moment of holmium potentially leads to an increase of this effect.

A more effective way to influence the phase collection of the tunneling systems should be a mechanism similar to spectral diffusion. But instead of transitions of nearby tunneling systems by interactions with phonons, the transitions are caused by the nuclear moments in the solid. The argumentation is similar to spectral diffusion theory (compare section 3.4.2). The resonantly excited tunneling system ($\mathcal{A}$-system) is surrounded by many $\mathcal{B}$-systems, which are not excited during the echo sequence. If one of the nearby $\mathcal{B}$-systems undergoes a transition due to an interaction with its nuclear quadrupole moment, the strain field in its proximity is altered. This change in the strain field shifts the asymmetry energy Δ of the $\mathcal{A}$-system and changes thereby

its energy splitting E, such that it loses phase coherence to the other resonantly excited $\mathcal{A}$-systems.
Properties of a possible spectral diffusion, based on nuclear quadrupole relaxation of the tunneling systems could be extracted from the temperature dependence of the longitudinal and transversal relaxation time of the samples that show a fast decay at small pulse separation times in figure 6.25. However, this information is not available. From the measurements performed within this thesis a determination of the temperature dependence of T_1 and T_2 is not possible, due to two reasons. First, the factor A_0 cannot be precisely determined without data at pulse separation times $\tau_{12} \to 0$. Second, the decay curves at the different temperatures were measured in various measurement cycles. However, if the faster decay of N-BK7 and Albasi compared to Suprasil I, shown in figure 6.25, is indeed caused by the influence of nuclear quadrupole moments, the mechanism causing the additional loss of phase coherence in figure 6.30 and 6.31 is also present in these samples, although less strong. As already mentioned at the end of the last section, the transversal relaxation time of the tunneling systems in Albasi and N-BK7 is proportional to T^{-2} at high temperatures, as predicted by the short time limit of spectral diffusion theory. At about 30 mK to 40 mK, the proportionality changes, probably to T^{-1} [Fic13, Arc13]. In phonon echoes on aluminosilicate glasses doped with holmium, a T^{-1} dependence of the transversal relaxation rate was observed over the whole investigated temperature range (about 10 mK to 50 mK) [Ler88] (compare also the discussion in section 4.5.3). If the reduced temperature dependence of the transversal relaxation time in N-BK7, Albasi and the aluminosilicate glasses doped with holmium is caused by an additional mechanism based on the relaxation due to nuclear quadrupole moments, it must fulfill two conditions. It is the dominant phase coherence destroying process at low temperatures. From a certain temperature on spectral diffusion dominates. The transition temperature depends on the strength of the quadrupole based relaxation in comparison to the strength of spectral diffusion. In N-BK7 and Albasi the transition temperature is reached at about 30 mK to 40 mK. In the measurements on aluminosilicate glasses doped with holmium the transition temperature could not be reached. If the cause for the reduced temperature dependence is indeed a mechanism similar to spectral diffusion, the underlying mechanism has to be a bit different compared to the ordinary spectral diffusion. Assuming that due to the quadrupole moments the relaxation time of the $\mathcal{B}$-systems becomes such short, that not the short time limit, but the intermediate time limit of spectral diffusion is valid in the investigated time window, a T^{-1} dependence of the transversal relaxation time is expected (compare discussion to equation 3.70). However, if this assumption is correct, the transition to the T^{-2} dependence at higher temperatures cannot be explained without a dying out of the nuclear quadrupole based relaxation at high temperatures, which is not expected and in contradiction to measurements (compare section 4.5.2).

To get an impression of the strength of the additional relaxation process, figure 6.32 shows the decay curves measured on N-KZFS11 and HY-1 at about 10 mK and one measured on N-BK7 at a temperature of 70 mK. The decay curves are aligned at

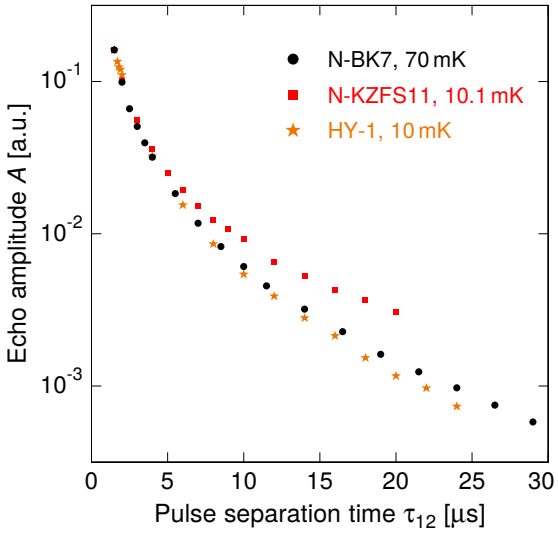

Figure 6.32: Echo amplitude as a function of the pulse separation time for N-KZFS11, HY-1 and N-BK7. The respective temperatures are given in the caption. For better comparability the decay curves are aligned at a pulse separation time of 1.5 µs. The data of N-BK7 is taken from [Fas10].

a pulse separation time of 1.5 µs. It can be seen that the decay rate is similar for these samples after a pulse separation time of 1.5 µs. Thus in this time window, the strength of the nuclear moments based relaxation in HY-1 and N-KZFS11 is similar to spectral diffusion in N-BK7 at 70 mK.

6.5 Magnetic field dependence

Section 6.4 shows that several glasses experience a fast decay of their echo amplitude at short pulse separation times. This fast decay behavior is attributed to a relaxation based on the nuclear moments in these glasses. The variety of different samples, which contain atoms with large and small nuclear quadrupole moments, show that the absolute size of the quadrupole moment is not crucial for the strength of the relaxation, but the modulation of the quadrupole coupling constant. To verify that the fast decay of the echo amplitude is indeed caused by a relaxation process based on the nuclear moments in the solid, measurements in magnetic fields are necessary. Due to the Zeeman interaction of the nuclear magnetic dipole moments with the magnetic field, the energy levels of the tunneling systems are shifted. This shift influences the echo amplitude and the decay behavior if the fast relaxation is caused by an interaction of tunneling systems and nuclear moments. Therefore the following sections investigate the magnetic field dependence of the echo amplitude (section 6.5.1) and of the decay behavior (section 6.5.2).

6.5.1 Magnetic field dependence of the echo amplitude

To verify that the tunneling systems in the samples are multi-level system, which means that they indeed contain atoms with a nuclear moment, the echo amplitude

was measured in dependence of the applied magnetic field strength for several of the samples shown in figure 6.25. The interaction of the magnetic field and the nuclear dipole moment causes a shift of the energy levels and lifts possible degeneracies (compare figure 4.12), independent of whether the multi-level system is caused by a quadrupole or dipole coupling. Due to the shift of the energy levels, the phase collected by the tunneling systems during the two-pulse sequence changes in dependence of the applied magnetic field strength. This in turn influences the echo amplitude (compare for example figure 4.2 or 4.18). In the following, the obtained results are shown. Thereby the samples showing a similar decay behavior in figure 6.25 are depicted in the same plot. Every figure shows also BK7 as reference.
The magnetic field dependence of the echo amplitude of Suprasil I is shown in figure 6.33. Since Suprasil I contains no quadrupole moments and shows no dipole effect, no influence of the magnetic field on the echo amplitude is expected, which is also observed. The small dip at around 150 mT originates most likely from drifts in the experiment.
In figure 6.34 the magnetic field dependencies of the glasses showing an increased relaxation rate compared to Suprasil I are depicted. Glycerol-d0 is free of quadrupole moments, but shows a strong dipole-dipole coupling. Thus there is a small influence of the magnetic field visible at very small field strengths. This influence can be seen more clearly in figure 4.3. From about 5 mT on the mixing of the nuclear levels of the tunneling systems in glycerol-d0 is prevented. Thus at larger magnetic fields the echo amplitude is independent of the applied magnetic field strength. The multi-

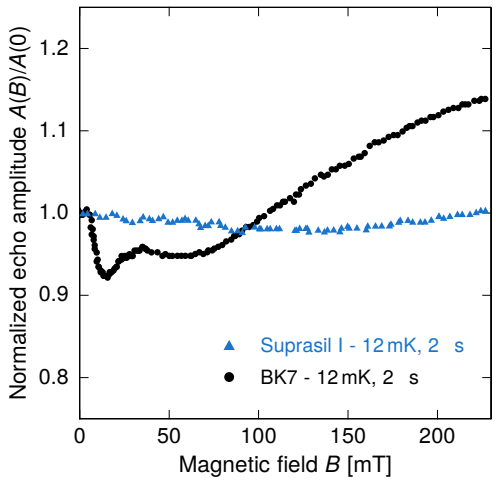

Figure 6.33: Echo amplitude of Suprasil I and BK7 in dependence of the applied magnetic field. The temperatures and pulse separation times are given in the caption. The data is taken from [Baz08].

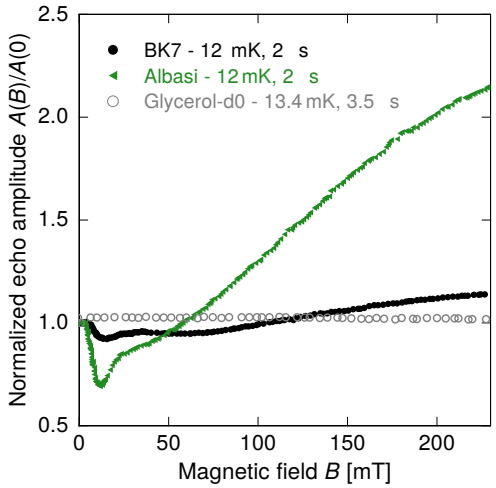

Figure 6.34: Echo amplitude of BK7, Albasi and glycerol-d0 in dependence of the applied magnetic field. The temperatures and pulse separation times are given in the caption. The data of BK7 and Albasi is taken from [Baz08]. The data of Glycerol-d0 from [Nag04].

component glasses BK7 and Albasi show a varying echo amplitude in dependence of the applied magnetic field strength. As expected from section 4.3.3, the echo amplitude becomes larger with increasing field strength, since the mixing of nuclear states is reduced. Considering the composition of BK7 and Albasi (compare section 5.4) and the nuclear properties of these isotopes (table A.1), it can be seen that the Zeeman splitting at a magnetic field of 230 mT is in in the low megahertz range. The quadrupole splittings due to the interactions with the electric field gradients in these samples are most likely of similar size. This explains the emerging leveling-off of the echo amplitudes of Albasi and BK7 at large magnetic fields. Furthermore, it is noteworthy that Albasi and BK7 consist of the same elements, but in different proportion. Although the decay behavior of both samples is similar (compare for example figure 6.25) the influence of an additional magnetic field causes a significant larger effect in Albasi. The reason for this different behavior is not known, but besides the number and kind of atoms carrying a nuclear quadrupole moment also the tunneling angle is relevant (see section 4.3.3).
The magnetic field dependence of several samples showing a fast decay in figure 6.25 is depicted in figure 6.35 and 6.36. The samples N-KZFS11, Br-DGEBA and FR-122P, shown in figure 6.35, experience only a small influence of the magnetic field on their echo amplitude compared to BK7. At small magnetic field strengths, the echo amplitude of these samples reduces by about 5 %. This behavior is similar to BK7. After that the echo amplitudes drift monotonically towards smaller values indepen-

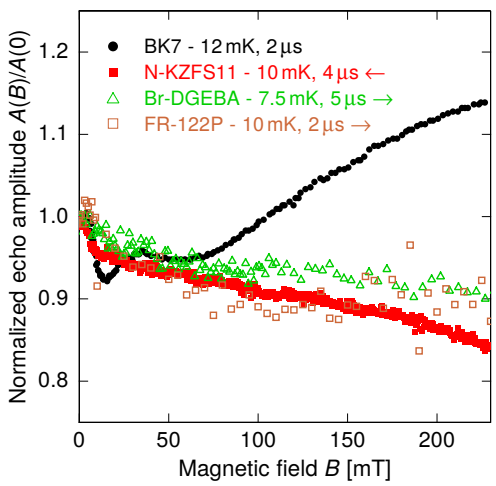

Figure 6.35: Echo amplitude of BK7, N-KZFS11, Br-DGEBA and FR-122P in dependence of the applied magnetic field. The temperatures and pulse separation times are given in the caption. The arrows indicate the direction of the magnetic field sweep. The data of BK7 is taken from [Baz08].

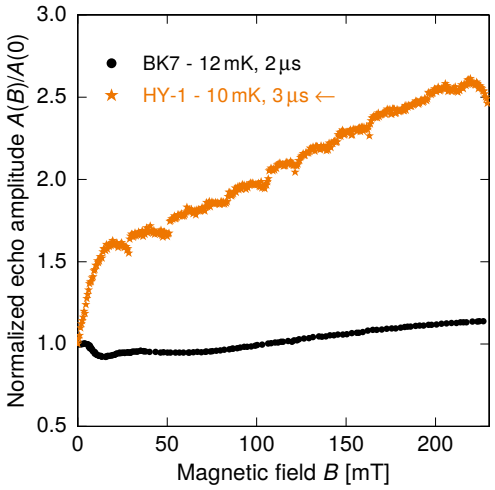

Figure 6.36: Echo amplitude of BK7 and HY-1 in dependence of the applied magnetic field. The temperatures and pulse separation times are given in the caption. The arrow indicates the direction of the magnetic field sweep. The data of BK7 is taken from [Baz08].

dent of the sweep direction of the magnetic field, which is given by the arrow in the figure caption. Thus the change of the echo amplitude with varying magnetic field is not caused by heating effects of the sample by eddy currents, but by the Zeeman effect. The increased scattering of the data measured on FR-122P with increasing magnetic field is caused by a reduced number of measurements per data point.
The gyromagnetic ratios of the isotopes present in N-KZFS11, Br-DGEBA and FR-122P are similar to those of BK7. However, the nuclear splittings, caused by the interactions of the quadruple moments with the electric field gradients, in these samples are much larger compared to BK7 (compare table A.1). Thus the additional shift of the energy levels due to the Zeeman splitting is only a small perturbation and consequently no large influence is expected. Another circumstance, which might influence the observable magnetic field dependence is the fast relaxation of these samples at short pulse separation times. Thereby a lot of the tunneling systems containing nuclear quadrupole moments in the respective samples already decayed and can no longer contribute to the echo amplitude. This probably reduces the visible magnetic field effect of the echo amplitude up to the point where the magnetic field is large enough to prevent the relaxation via the nuclear moments.
Figure 6.36 shows the magnetic field dependence of HY-1. In contrast to the samples depicted in figure 6.35, HY-1 shows a large influence of the magnetic field on its echo amplitude. The variation of the echo amplitude is of similar size than in Albasi. Like all other samples, HY-1 shows a strong magnetic field dependence at small magnetic field strengths which turns to an approximately linear behavior at about 20 mT. Compared to Albasi, HY-1 shows no oscillations of the echo amplitude. The small fluctuations are caused by the measurement procedure. As introduced in section 5.3, the dewar of the cryostat was refilled with liquid helium at least every 48 h. After the refilling process the measurement was paused for 3 h. Every step, visible in the magnetic field dependence of HY-1 corresponds to one filling process. Since the measurement was performed from large to small magnetic fields, the subsequent lowering of the magnetic field caused an additional magnetic cooling effect and thus an increasing or stable echo amplitude. During the 3 h waiting time after the filling process of the dewar, the sample thermalizes again such that afterwards the echo amplitude is reduced. This effect is only observed in HY-1. Thus it is most likely caused by the large magnetic moment of the holmium atoms. The overall course of the echo amplitude of HY-1 in dependence of the magnetic field corresponds to the one of aluminosilicate glasses doped with holmium [Ler88].

A description of the magnetic field dependencies of the echo amplitudes with the equations introduced in section 4.3.3 or the simulation discussed in section 4.4 is not possible. The electric field pulses for the measurements performed in the framework of this thesis had a duration of $t_1 = 230\,\mathrm{ns}$. Therefore the spectral width of the first excitation pulse is about 0.7 MHz. The nuclear splittings of the atoms carrying nuclear moments in the investigated samples are significantly larger. Thus no complete mixing of the nuclear states occurs during the application of an electric field pulse and consequently the formulas cannot be applied. To achieve a complete mixing

of the nuclear levels for all samples, very short pulse durations are required, which cannot be achieved with the current experimental setup (compare section 5.2.1). Nevertheless, the magnetic field dependence of the echo amplitude shows that the tunneling systems in the different samples actually contain nuclear moments and that there is a coupling of the tunneling motion and the nuclear moment.

6.5.2 Magnetic field dependence of the decay behavior

The application of a magnetic field leads to an additional splitting of the nuclear levels by the Zeeman interaction. If the magnetic filed strength is sufficiently large, the nuclear moments in the glass orient along the magnetic field and the quadrupole interaction is only a small correction. From this critical magnetic field on, a relaxation based on nuclear moments is prevented or at least significantly reduced.
Measurements of the decay of the echo amplitude with and without an additional magnetic field for the samples Br-DGEBA, N-KZFS11 and HY-1 are shown in figure 6.37. The measurements for each sample were performed at the same temperature and with the same pulse duration. For a better comparison the decay curves of the same sample are aligned at a pulse separation time of 1.5 µs. The data of the different samples is shifted with respect to each other for clarity. The measurements on N-KZFS11 show, in the investigated time window, no significant influence of the magnetic field on the decay behavior of the echo amplitude. For Br-DGEBA the decay behavior with applied magnetic field was measured only in a small time window. In this window no significant influence is observed. For these samples a negligible influence of a magnetic field with 230 mT is expected. As shown in section 6.5.1, the nuclear splitting caused by the Zeeman interaction is very small compared to the quadrupole splitting. Thus there should not be a large influence of the magnetic field.

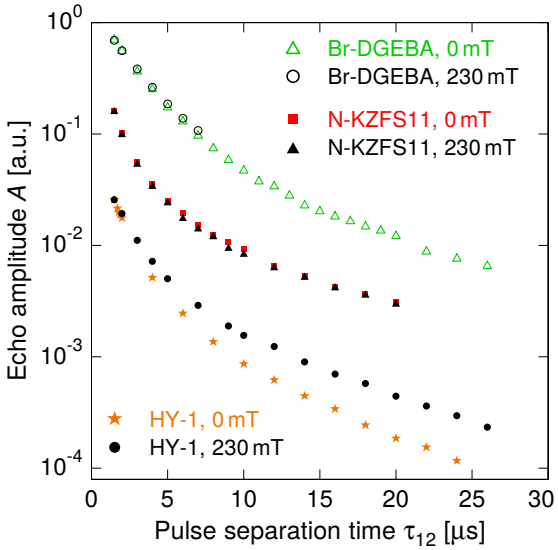

Figure 6.37: Decay of the echo amplitude of the samples Br-DGEBA, N-KZFS11 and HY-1 with and without a magnetic field. The temperatre was 7.5 mK for Br-DGEBA, 10.1 mK for N-KZFS11 and 10 mK for HY-1. The pulse duration was $t_1 = 230$ ns. The decay curves measured on the respective samples are aligned at a pulse separation time of 1.5 µs.

Also in the glass Albasi (not shown within figure 6.37) no significant difference in the decay behavior is observed with and without a magnetic field of 230 mT [Lud00]. In contrast to Br-DGEBA and N-KZFS11, the echo amplitude of Albasi changes notably as a function of the magnetic field strength (see figure 6.34). However, considering figure 6.34, the slope at 230 mT indicates that there is still a mixing of the nuclear levels during the tunneling motion. Thus the coupling of the tunneling motion and the nuclear quadrupole moments is not yet negligible and therefore also the relaxation based on nuclear moments. Since this kind of relaxation is only weakly pronounced in Albasi at 10 mK, as visible in figure 6.25, no strong difference in the decay behavior with and without magnetic field can be expected at all. Measurements of the echo amplitude on N-BK7 with and without a magnetic field of 200 mT also show no difference [Fic13]. The reason is the same as for Albasi.
For ordinary and deuterated glycerol the magnetic field strength necessary to prevent a mixing of the nuclear levels during the tunneling motion is well below 200 mT (compare for example figure 4.18). By a measurement with applied magnetic field of sufficient strength the quantum beating, caused by the quadrupole and the dipole moments, is suppressed (compare for example the measurement of glycerol-d8 in figure 4.4 or [Bra04a, Baz08]).
In contrast to Br-DGEBA, N-KZFS11, N-BK7 and Albasi, the sample HY-1 shows a large change of its decay behavior at a magnetic field of 230 mT, compare figure 6.37. This behavior is remarkable, since figure 6.36 showed, that a magnetic field of 230 mT is too small to cause a decoupling of the nuclear state from the tunneling motion and thus a leveling-off of the echo amplitude. The measurement also shows, that the increasing echo amplitude in figure 6.36 is not only caused by a shift of the nuclear levels and a varied mixing of nuclear states due to the tunneling motion, but also by a reduction of the relaxation rate of the tunneling systems. This behavior is probably caused by the large magnetic moment of the electron shell of holmium, which increases the effect of the applied magnetic field. Thus, in dependence of the actual quadrupole interaction of the holmium atoms in the glass, a magnetic field of 230 mT is for some of them already sufficient to cause a decoupling of the nuclear states from the tunneling motion. Another possibility for the reduced relaxation rate by an applied magnetic field could be that besides the quadrupole interaction, also the dipole coupling in HY-1 influences the relaxation behavior of the tunneling systems. A small magnetic field is probably already sufficient to align the magnetic moments with the magnetic field, which reduces the influence of the dipole-dipole interaction on the relaxation of the tunneling systems. This may also explain the strong increase of the echo amplitude at small magnetic fields, visible in figure 6.36.

Independent of the exact mechanism of the nuclear moment based relaxation, the reduced relaxation rate of HY-1 with applied magnetic field proves that the fast decay of the echo amplitude, seen in figure 6.25, is caused by the influence of the nuclear moments. To get further insights into the relaxation and to prove, that the fast decay of the other samples presented in figure 6.25 is caused by the nuclear moments as well, measurements in large enough magnetic fields are necessary to reach the

condition where the relaxation is suppressed by the magnetic field. Furthermore, additional three-pulse echo measurements, which are more sensitive to T_1 processes, can help to get more information on the properties of the nuclear quadrupole moment based relaxation. With this measurement technique it was for example possible to observe a small change of the relaxation rate in N-BK7 with applied magnetic field, although the decay of the two-pulse echo was not altered [Fic13].

6.6 Conclusion

In summary, a detailed consideration of the fast decay behavior of different glasses at a temperature of 10 mK with regard to their composition and the nuclear properties of their atoms reveals that the cause for the fast decay of the echo amplitude is neither the absolute size of the quadrupole moments of the atoms contained in the glasses nor the absolute size of the quadrupole coupling constant. The observations point towards the modulation of the quadrupole coupling constant during the tunneling motion, which is connected to the nature of the tunneling systems in the respective solid, as the most relevant parameter for a strong influence of a nuclear quadrupole moments based relaxation on the decay of the echo amplitude. With the exception for HY-1, the influence of the dipole-dipole coupling on the relaxation of tunneling systems is, if existing at all, only weakly pronounced. HY-1 contains holmium which has a large permanent magnetic moment of its electron shell. Thus for this sample the impact of the dipole-dipole coupling on the decay of the echo amplitude may be stronger. The observation of a modulation of the echo amplitude in dependence of the magnetic field proved that the tunneling systems in the respective samples indeed contain nuclear moments and that there is a coupling of the nuclear moment and the tunneling motion. This observation shows that the assumed connection between the nuclear moments in a sample and the fast decay of the echo amplitude at short pulse separation times is very likely. The proof for this assumption is provided for the sample HY-1 by a measurement of the decay behavior of the echo amplitude in a magnetic field where a reduced relaxation rate was observed. For the other samples showing a fast decay of the echo amplitude larger magnetic fields are necessary to validate that the nuclear moments influence the relaxation of tunneling systems. To further characterize this relaxation mechanism measurements at pulse separation times smaller 1.5 µs are necessary. For this purpose a novel resonator technique is presented in the following chapter.

7. Microfabricated superconducting resonator technique

To further investigate the influence of nuclear moments on the relaxation of tunneling systems, measurements at very short pulse separation times are required. To enable such measurements, a novel microfabricated resonator technique was developed in the framework of this thesis, which is introduced in this chapter. At first, the circumstances that prevent measurements at very short pulse separation times with the reentrant cavity resonator are demonstrated. Afterwards the microfabricated superconducting resonator technique is introduced. Finally, the first results obtained on the sample N-BK7 are presented.

7.1 Measuring at small pulse separation times

For the comparison of the echo amplitude's decay of various samples, data at very short pulse separation times is essential, as visualized in figure 6.24. This data is also substantial for a reliable description of the decay behavior with theory to limit the uncertainty on the parameter A_0 (see equation 6.6).
If the echo amplitude is measured with the reentrant cavity resonator at pulse separation times small than 1.5 µs, the echo signal and the second pulse overlap, as shown in figure 7.1. In principle, it is up to a certain degree of overlap still possible to determine a value for the echo amplitude with the methods introduced in section 6.1. However, these echo amplitudes are subject to large uncertainty and thus not suited for a discussion of the echo decay behavior. Considering the two-pulse sequence sent

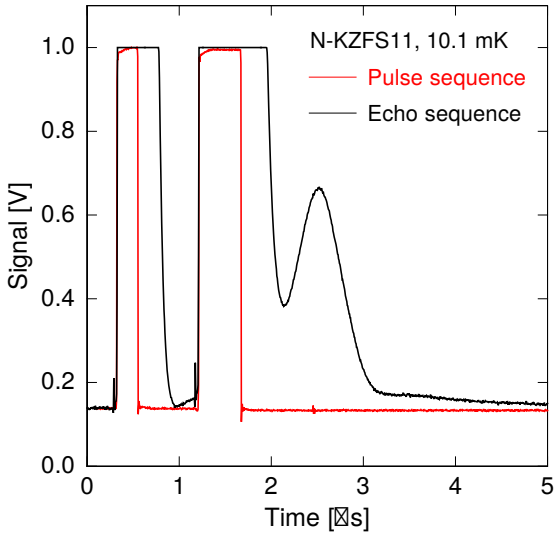

Figure 7.1: Echo sequence measured on N-KZFS11 (black) at a temperature of 10.1 mK, a pulse duration of $t_1 = 230$ ns and a pulse separation time of 1 µs. The right flank of the second pulse and the echo signal overlap. In red the actual two pulse sequence is shown.

into the cryostat (shown in red), it can be seen that the pulses of the measured echo sequence (shown in black) are distinctly broader. At a height of about 0.8 V the broadening of the second pulse is about 300 ns, which is much more than the characteristic time constant of the resonator $\tau_{\mathrm{res}} \approx 30\,\mathrm{ns}$ (compare section 5.2.1). This broadening is predominantly caused by two components in the experimental setup, namely the resonator and the low temperature amplifier in the cryostat (compare section 5.2.2). In addition, the free induction decays after the pulses lead to a certain broadening as well.
The influence of the low temperature amplifier on the pulse broadening was investigated by removing the amplifier in one measurement cycle. The measurements showed that without the low temperature amplifier the pulses are significantly narrower, but the echo signal is due to the missing amplification very tiny. However, the reduced width of the pulses is not linked to the recovery time of the low temperature amplifier after its saturation by the pulses. The reason for the broadening is the amplification of the resonator's ring-down. The signal size in the readout branch, caused by the ring-down after the excitation pulses, is still so large, that despite the short characteristic time constant of the reentrant cavity resonator, it is sufficient to cause a saturation of the low temperature amplifier.
Thus one possibility to measure echo signals at small pulse separation times with the reentrant cavity resonator is to remove the low temperature amplifier. However, with this possibility the echo signals measured at small pulse separation times are still sitting on the ring-down of the resonator. Therefore the echo signals have to be corrected for this non-linear background, which increases the uncertainty. In addition, it is possible that the ring-down causes a systematic deviation of the echo signals to larger values with reducing pulse separation time, since there is more and more energy of the excitation pulses left in the resonator. Furthermore, the echo signal of N-BK7 is without the low temperature amplifier about a factor of 33 smaller. Since N-BK7 is a sample having a large echo signal, it is questionable whether samples with small echo signal are measurable at all without the low temperature amplifier (compare section 6.4.1).
Another possibility to reach smaller pulse separation times are smaller field strengths of the excitation pulses. If the pulse sequence is attenuated more by the adjustable attenuator, the maximal energy in the resonator is reduced and consequently the ring-down of the resonator lasts less long. This effect can be observed in measurements of the electric field dependence of the echo amplitude as exemplarily shown for a measurement on N-KZFS11 in figure 7.2. However, the effect is limited since the echo signal becomes very small and can at some point no longer be evaluated. In addition, the slope after the second pulse decreases less fast than the echo signal, such that a possible error through a non-perfect background correction has a stronger influence on the echo amplitude.
Above considerations show that a new resonator for the measurement of dielectric polarization echoes at short pulse separation times has to fulfill two requirements. The resonator needs a very small characteristic time constant and work with small

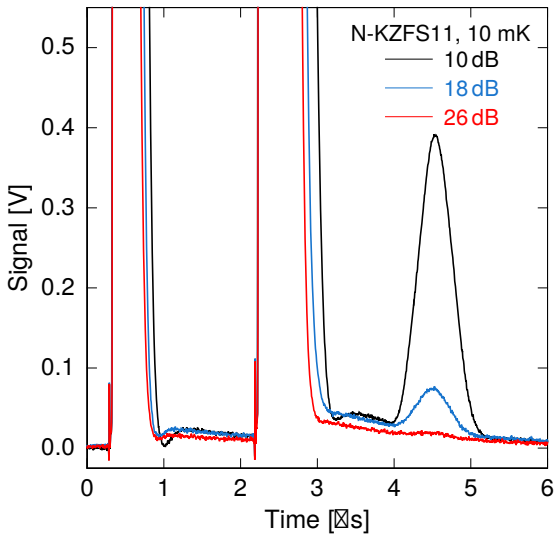

Figure 7.2: Echo sequence measured on N-KZFS11 at a temperature of 10 mK in dependence of the applied attenuation. The pulse duration was $t_1 = 230$ ns and the pulse separation time 2 µs. The data is shifted to a common reference point.

field strengths to prevent a saturation of the low temperature amplifier during the ring-down. The different resonators that have been developed to meet these requirements are introduced in the following section.

7.2 Resonator designs

To measure at smaller pulse separation times, the new resonator needs to have a reduced characteristic time constant. According to equation 5.3, this parameter can be reduced either by a higher resonance frequency or by a low quality factor. In the present case, the resonance frequency of about 1 GHz is maintained to ensure comparability to previous results and to be able to use the same electronics. Consequently, the quality factor of the resonator is adjusted.
Instead of a modified reentrant cavity resonator, the new measurement technique is based on planar microfabricated superconducting resonators. This has several advantages. Due to an in-house clean room the time from the design to the ready to run resonator is very short. In addition, the frequency response of the resonator and therewith its resonance frequency and quality factor can be simulated with confidence in advance by the software Sonnet[1]. The resonator design is transferred via a one-layer lift-off process directly to the sample and consists of sputter deposited niobium. Niobium becomes superconducting at temperatures below about 9 K, which prevents a heating of the sample by ohmic dissipation in the resonator. The required reduction of the resonator's quality factor is obtained by a strong coupling to the feed line.
Compared to the reentrant cavity resonator, where the sample is located in a homogeneous electric field, the electric field in the microfabricated setup is inhomogeneous. In addition, there is a magnetic probing of the sample caused by the magnetic field

[1]Sonnet Software Inc. 126 N Salina St., Syracuse, NY 13202

surrounding the striplines. This circumstance is illustrated in figure 7.3. However, measurements of polarization echoes in [Pol17, Haa18a] and those shown in section 7.3.2 as well as measurements of the dielectric function in [Fre16, Kör19, Fre21] show that the additional magnetic probing does not affect the measurement.
To find the optimal layout for the measurement of dielectric polarization echoes, different resonator designs were tested, which follow different ideas. In collaboration with [Pol17, Haa18a], the resonator designs shown in figure 7.4 were developed. Design A and B are $\lambda/2$ resonators with a capacitive coupling, design C is a hard coupled $\lambda/4$ resonator and design D is a $\lambda/2$ resonator with an inductive coupling. Based on the experience with those resonator designs, the lumped element resonator, which is shown in figure 7.5 was developed.
The designs shown in figure 7.4 were tested on N-BK7 due to the large amount of reference data available for this material. The ready resonator was placed on a specially developed sample holder and connected to the excitation and readout electronics via bond pads. This connection was realized by a copper wire which was glued with silver conducting glue[2] to the bond pad. For more information on the sample holder see [Pol17, Haa18a].
Concerning the further development of microfabricated resonators for dielectric polarization echoes, the measurements with the resonators, shown in figure 7.4, yielded the following two main results.

1. All contours of the design have to be rounded.
2. An inductive coupling is preferred to a direct coupling and both are preferred to a capacitive coupling.

In measurements with design A and B the small angle approximation could not be reached. Detailed simulations showed that the high electric field strengths in the coupling gap and at the corners of the design prevent a reaching of the small angle approximation (compare section 6.2.4). Design C and D take the experience from the measurements on A and B into account and test the direct and inductive coupling. In these measurements the small angle approximation could be reached. Furthermore, it turned out that the inductive coupling is better suited for echo measurements,

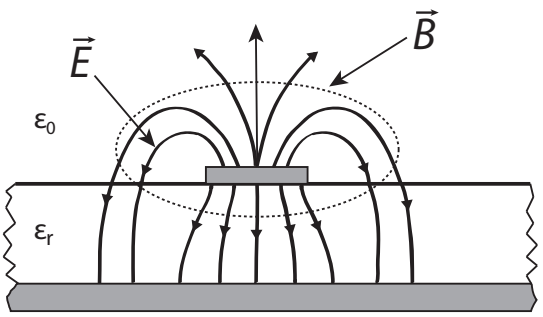

Figure 7.3: Cross section through a stripline with associated electric field $\vec{E}$ and magnetic field $\vec{B}$. Picture adapted from [Pol17].

[2]Leitsilber ACHESON 1415, Plano GmbH, Ernst-Befort Str. 12, D-35578 Wetzlar

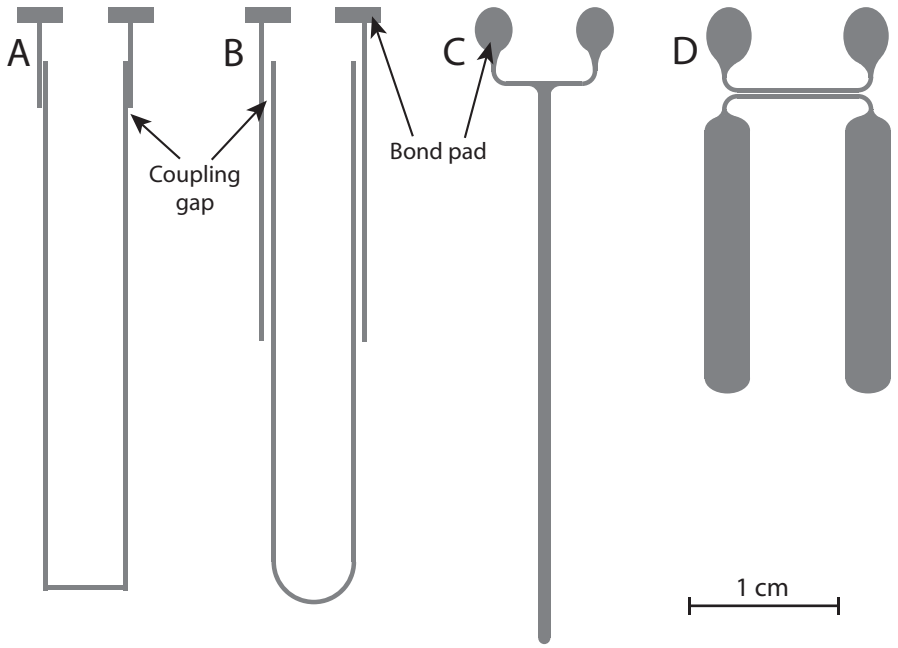

Figure 7.4: Resonator designs for the measurement of dielectric polarization echoes.

since it led in the tested resonators to less standing waves in the cable path and a larger echo signal compared to the direct coupling. With all four resonator designs it was possible to measure at pulse separation times smaller than 1.5 µs. Especially design C and D which have quality factors of about 10 allow for measurements at very small pulse separation times, yet the electric field strength of the excitation pulses, necessary for sizable echo signals, is comparably large.

The lumped element design, shown in figure 7.5, is based on these experiences. The actual resonator consists of an interdigital capacitor (IDC) with a 10 µm spacing between adjacent fingers and a single loop as inductor, which is also used to couple the resonator to the feed line (the width of the coupling gap is 10 µm). The feed line is matched to an impedance of 50 Ω to guarantee a good signal transmission and has a bond pad in the top left and right corner. All structures are made of 400 nm sputtered deposited niobium on a 200 µm thick sample of N-BK7. By choosing small structure sizes, the electric field strengths in the capacity of the resonator, needed for echo measurements, are achieved by smaller voltages. Thus the electric field strength of the excitation pulses can be reduced. Since the coupling to the feed line is realized in an inductive way, no spatially limited large electric field strengths, which prevent a reaching of the small angle approximation, occur. The resonator chip is mounted with GE 7031 varnish into a box made of OFHC copper. The inside of the box is covered with niobium to omit heating effects by eddy currents. The full-surface gluing on the sample backside creates a good thermal contact of the sample and the cryostat, leading to short thermalization times. The electric contact is realized by aluminum bonds, which makes it much more reliable than the silver conducting

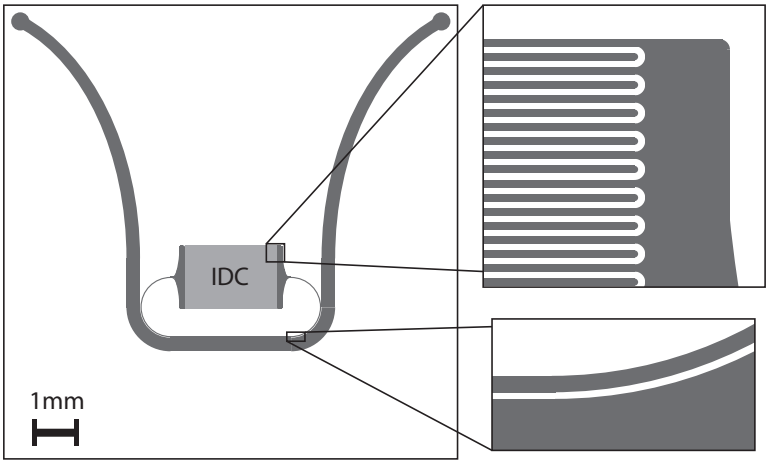

Figure 7.5: Design of the lumped element resonator chip. The resonator consists of an interdigital capacitor (IDC) with a spacing of 10 µm between the fingers and a single loop as inductor. The distance between the inductor and the feed line is 10 µm, too.

glue, used before. In addition, the aluminum bonds complete the superconducting shielding of the resonator.
For the measurement the resonator in the copper box is mounted to the experimental platform of the cryostat and connected to the same readout and excitation electronics as the reentrant cavity resonator (compare section 5.2.2).

7.3 Results of the lumped element resonator

This section presents the results obtained with the lumped element resonator. First, the general properties, like its resonance frequency, quality factor or electric field strength dependence are discussed. Afterwards, the decay behavior is compared to measurements performed with the reentrant cavity resonator.

7.3.1 General properties

Resonance frequency and quality factor

The simulation of the resonator's properties yields a resonance frequency of about 1065 MHz and a quality factor of about 40. At 10 mK the measured resonance frequency was 981 MHz and the quality factor about 40. The deviation of the measured resonance frequency from the simulation is most likely caused by a reduction of the spacing between adjacent fingers of the IDC during the production of the resonator. Thereby the capacity is increased and the resonance frequency is lowered. Simulations show that a reduction in the spacing from 10 µm to about 7 µm is sufficient to cause such a frequency shift.

Rate dependency

Investigations of the waiting time dependence of the echo amplitude with an attenuation of 44 dB at the adjustable attenuator showed no significant dependence. The measurement of the decay behavior, shown in section 7.3.2, was performed with an attenuation of 52 dB and a waiting time of 100 ms. Thus no influence of the repetition rate on the measurement is expected. The good performance of the lumped element resonator design in this field is caused by the small electric field strengths of the pulses, the superconducting shielding which prevents heating by eddy currents and the good thermal contact of the sample to the copper box.

Thermalization

The thermalization behavior of the lumped element resonator on the glass N-BK7 is shown in figure 7.6. It can be seen that the echo amplitude adapts very fast to an altered cryostat temperature, proving the excellent thermal contact of the sample. The scattering of the data points is caused by the small amount of averaged measurements.

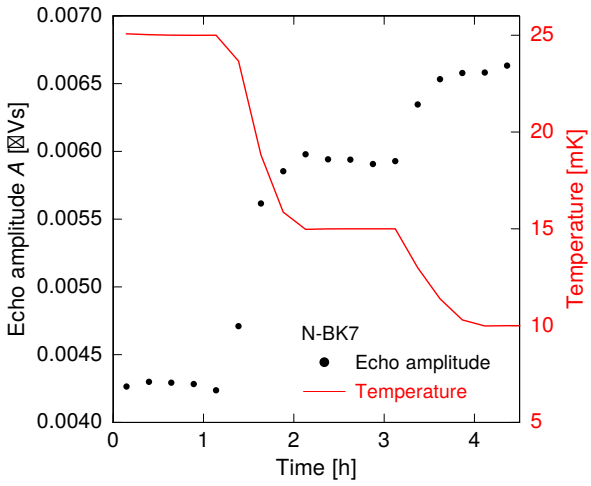

Figure 7.6: Thermalization measurement of the lumped element resonator on N-BK7 between 25 mK and 10 mK. The echo amplitude is depicted on the left y-axis and the temperature on the right.

Electric field strength dependence of the echo amplitude

To test whether the small structure sizes of the lumped element resonator prevent a reaching of the small angle approximation, the electric field strength dependence of the echo amplitude was studied. The procedure is analogous to the reentrant cavity resonator (compare section 6.2.4). The result of the measurement, which was performed at a temperature of 10 mK, a pulse separation time of 2 µs and a pulse duration of 230 ns, is shown in figure 7.7. To validate the small angle approximation, equation 6.4 is fit to the data. As can be seen, the small angle approximation is

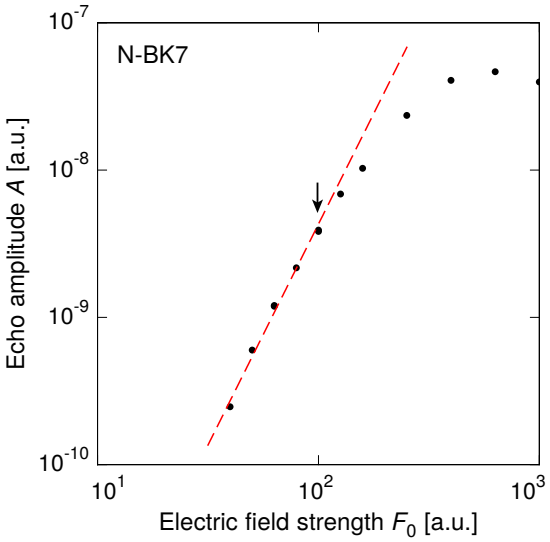

Figure 7.7: Electric field strength dependence of the echo amplitude, measured with the lumped element resonator at a temperature of 10 mK, a pulse separation time of 2 µs and a pulse duration of $t_1 = 230$ ns. The line shows the expected F_0^3 dependence. The arrow indicates the measurement with an attenuation of 52 dB.

fulfilled in a large range. The echo amplitude measured with an attenuation of 52 dB at the adjustable attenuator is marked by an arrow. This attenuation was used for the decay measurements presented in figure 7.9. Compared to the reentrant cavity resonator, where the commonly used attenuation is 23 dB for N-BK7 (with a sample thickness of 0.5 mm), the field strength of the excitation pulses is 29 dB smaller in the measurements with the lumped element.

Measuring at small pulse separation times

The characteristic time constant of the lumped element resonator is about 6.5 ns and thus distinctly smaller than the 30 ns of the reentrant cavity resonator. Together with the small amount of energy stored in the resonator during the pulses, this allows for measurements at very short pulse separation times. In figure 7.8 a pulse sequence measured with the same field strength of the excitation pulses as used for the decay curves is shown together with the pulse sequence. Due to the inductive coupling, the signals from the resonator have a phase difference of 180° compared to those just passing the feed line. Therefore the pulses of the echo sequence give a negative signal and the ring-down of the resonator as well as the echo a positive. In the plot it can be seen that the ring-down after the pulses is much shorter compared to the reentrant cavity resonator (see figure 7.1). The elongation of the second pulse at a signal height of 0.05 V is only 60 ns. Since the free induction decay, which is according to theory mainly present after the first pulse, leads to an elongation as well, there is always a certain broadening. In addition, the switches in the circuitry create no perfect rectangular pules (compare pulse sequence in figure 7.8), which can cause a broadening as well. The baseline of the echo sequence after the second pulse has no slope, such that the echoes are even at small pulse separation times not affected by the ring-down of the second pulse. The obtained echo signal is comparatively small,

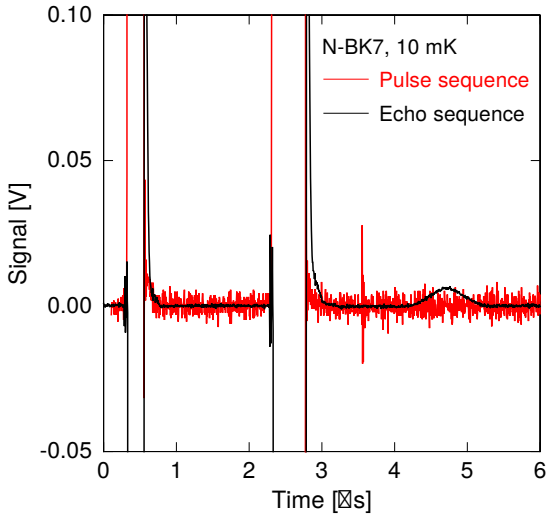

Figure 7.8: Echo sequence measured with the lumped element resonator at a temperature of 10 mK, a pulse duration of 230 ns and a pulse separation time of 2 µs. The pulse sequence is shown in red.

but still over a factor of 2 larger than the one measured under comparable conditions with the reentrant cavity resonator on N-BK7 without low temperature amplifier. Together with the flat baseline this setup is very suitable for measurements at short pulse separation times. The minimal achieved pulse separation time with the lumped element resonator was 0.4 µs at a pulse duration of 230 ns and 0.3 µs at 80 ns.
Given the small echo amplitude, only measurements at small pulse separation times are possible. Therefore decay studies are performed in two independent measurement cycles. The reentrant cavity resonator is used for measurements at large pulse separation times and the lumped element for those at small ones. To align both curves, certain pulse separation times are measured with both experimental setups (compare section 7.3.2).

7.3.2 Decay behavior

In the previous section it was shown that the lumped element resonator fulfills all requirements for the measurement at small pulse separation times. To validate, that the decay behavior of the echo amplitude is not altered by the microfabricated design, decay measurements were performed. A comparison of the obtained decay curves at different temperatures with decay curves measured with the reentrant cavity resonator is depicted in figure 7.9[3]. The decay curves measured with the lumped element resonator and those measured with the reentrant cavity resonator agree very well, showing the suitability of the lumped element resonator for the measurement of dielectric polarization echoes.

[3]The analysis of the decay curves presented in this section is analogous to section 6.1. However, for very small pulse separation times it was due to the position of the echo signal not possible to fit a background (step 3 of the background correction). In this case the background fit from a larger pulse separation time was shifted. This is possible since the background showed no dependency on the pulse separation time.

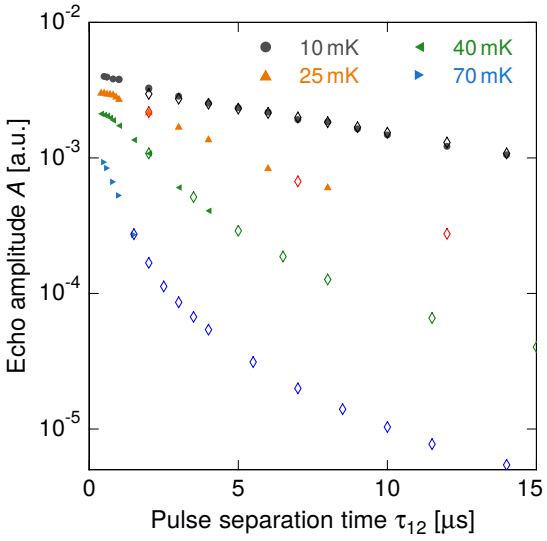

Figure 7.9: Decay of the echo amplitude of N-BK7 at temperatures of 10, 25, 40 and 70 mK. The filled symbols were measured with the lumped element resonator. The superimposed rhombuses were measured with the reentrant cavity resonator. The data at 25, 40 and 70 mK measured with the reentrant cavity resonator is taken from [Bur13].

Through the measurement at very short pulse separation times the Gaussian shape like leveling-off of the echo amplitude as predicted by spectral diffusion theory on the glass N-BK7 was observed for the first time this clearly (compare figure 3.17). At 25 mK and 40 mK the leveling-off can be seen unambiguously. At 40 mK it occurs at smaller pulse separation times compared to 25 mK since spectral diffusion is stronger at this temperature. For 70 mK the leveling-off appears most likely at even shorter pulse separation times such that it is not observable in the measurable time window. At 10 mK no Gaussian shape like leveling-off is observable at all. The linear behavior of the echo decay is visible down to the smallest accessible pulse separation time. This shows that at a temperature of 10 mK another relaxation mechanism and not spectral diffusion dominates the decay of the echo amplitude. This relaxation mechanism leads to an exponential decay of the echo amplitude instead of a Gaussian. Based on current knowledge, this relaxation is either caused by collective excitations (compare [Fic13]) or by nuclear quadrupole moments in the sample (compare this thesis).

Due to the shorter characteristic time constant the lumped element resonator is more suited for measurements with shorter excitation pulses compared to the reentrant cavity resonator. Thereby the spectral width of the pulses is broader, which causes a better mixing of the nuclear levels of the tunneling system during the tunneling motion. In a measurement on N-BK7 with a pulse duration of $t_1 = 80\,\mathrm{ns}$, corresponding to a spectral width of about 2 MHz (compare equation 3.54), an oscillating echo amplitude is observable at very small pulse separation times, see figure 7.10. The oscillation is significantly larger than the scattering of the data points at larger pulse separation times. Due to the limited amount of averaged measurements, the signal to noise ratio at the smallest pulse separation times was about 25, corresponding to a statistical error of approximately 4 %. The variation of the echo signal at small pulse separation is in the order of 10 % and thus significantly

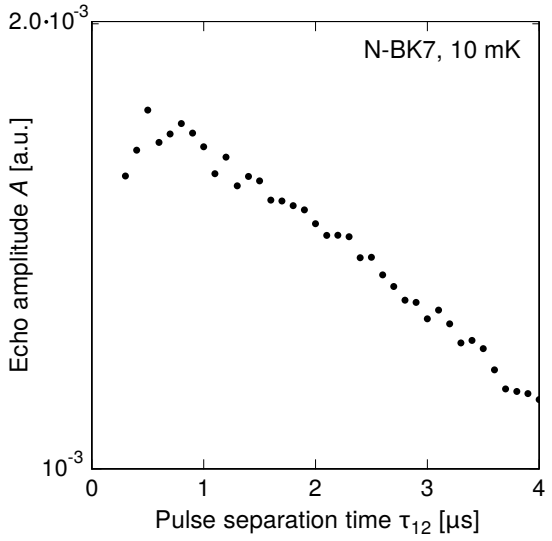

Figure 7.10: Decay of the echo amplitude of N-BK7 measured with the lumped element resonator at a temperature of 10 mK. The pulse duration was $t_1 = 80$ ns.

larger. The nuclear quadrupole splitting of the boron atoms in N-BK7 is expected to be about 1.3 MHz. Thus the broader spectral width of the excitation pulses can, depending on the actual nature of the tunneling system, cause a complete or at least larger mixing of the nuclear levels of the tunneling systems in N-BK7 such that a quantum beating is observable. The pattern in the echo amplitude at small pulse separation times, visible in figure 7.10, can be an indicator for a quantum beating in N-BK7. The disappearing of the oscillation at pulse separation time larger than 1 µs is in accordance with the expectation. Due to the broad distribution of the quadrupole splittings, caused by the amorphous structure and probably different natures of tunneling systems, an arising quantum beating smears very quickly and should therefore only be observable at very small pulse separation times (compare figure 6.22). To validate that the oscillating echo amplitude is indeed caused by a quantum beating, measurements with a higher time resolution and probably even reduced pulse duration are necessary.

In summary, the experimental results obtained with the lumped element resonator prove that this resonator technique is suited for the investigation of the decay of the echo amplitude at very small pulse separation times. In first measurements pulse separation times of 0.4 µs were achieved at a pulse duration of 230 ns, which is almost the theoretical limit with regard to the definition of the two-pulse sequence (compare figure 3.9). This enabled the observation of the Gaussian shape like leveling-off of the echo amplitude, as predicted by spectral diffusion theory for the first time. Compared to the other designs (figure 7.4) and the possibility of removing the low temperature amplifier, the lumped element resonator shows the best overall performance with minimal influence on the echo amplitude due to its very flat baseline. For the investigation of the fast decay of the echo amplitude of organic samples, which cannot be microstructured, a 'flip chip' technique is thinkable. Thereby the resonator design is transferred to a substrate which shows not much signal in dielectric measurements. The organic material is afterwards placed on top of the resonator

structure such that both materials, the substrate and the organic material, are measured simultaneously. Through a previously performed measurement of the echo decay of the substrate alone, the measured echo decay can be separated into the one caused by the organic material and the one of the substrate material.
The minimal accessible pulse separation time can be further reduced by a further reduction of the quality factor of the lumped element resonator. Therefore the coupling to the feed line has to be increased, either by a reduced coupling gap or by a modified design with a larger inductor and smaller capacity. Another way to reach shorter pulse separation times is a change of the pulse sequence from two pulses with equal field strength and $t_2 = 2t_1$, to a pulse sequence with equally long pulses $t_1 = t_2$ and different field strengths $F_{0,2} = 2F_{0,1}$. By this technique even the minimal pulse separation time accessible with the reentrant cavity resonator is significantly lowered. However, the suggested altered pulse sequence requires an adaption of the circuitry.

8. Summary and outlook

It is well known that the decay of dielectric polarization echoes is determined by the one-phonon process and spectral diffusion. In measurements of the dielectric function on glasses containing atoms carrying large nuclear quadrupole moments a further relaxation mechanism was observed that is dominant at low temperatures. This relaxation mechanism was attributed to the nuclear moments in the glass [Luc16]. Within this thesis, the influence of nuclear moments on the decay of dielectric two-pulse polarization echoes was studied to further characterize the nuclear moment based relaxation. Twelve glasses were investigated, from which seven were measured in the framework of this thesis. These samples cover a wide range of different glass types, from organic molecular and polymer glasses to inorganic oxide and non-oxide glasses. Furthermore, they contain a broad variety and different fractions of isotopes carrying nuclear quadrupole moments of different sizes and coupling constants, making them a suitable selection for the study of the nuclear moments based relaxation.

Several glasses exhibit, independent of the type of glass, an extraordinary fast decay of the echo amplitude at small pulse separation times and a temperature of about 10 mK. A detailed investigation of the composition of the glasses and the nuclear properties of the contained atoms with regard to the fast decay yields that all glasses containing atoms with large nuclear quadrupole moments and large quadrupole coupling constants show a fast decay on short timescales. However, also several samples with small quadrupole moments and comparably small coupling constants exhibit a fast decay. All observations together point towards the modulation of the quadrupole coupling constant during the tunneling motion as the most relevant parameter for the strong contribution of a nuclear moment to the relaxation of tunneling systems. This criterion is connected to the implementation of the respective isotope in the solid and the nature of the tunneling systems in the different glasses. Due to this material dependence, the relaxation based on nuclear moments eludes the so-called universality of glasses.
In addition, a python based code was developed to simulate the influence of nuclear quadrupole moments on the echo amplitude. By means of this simulation, the absence of a quantum beating in the measured decay curves can be understood.

The temperature dependence of the decay curves shows, as expected, that the nuclear moments based relaxation is most dominant at low temperatures. With increasing temperatures the decay rate of the investigated samples becomes more similar at small pulse separation times.

The measured decay of the echo amplitude cannot be described considering only the one-phonon process, spectral diffusion and the nuclear moments based relaxation introduced in [Luc16]. The echo amplitude decays much faster at short pulse separa-

tion times than expected from these models. A possible explanation is an additional phase coherence destroying process. A conceivable mechanism is an interaction of the non-resonantly excited tunneling systems with the nuclear moments, similar to spectral diffusion.

The observed magnetic field dependence of the echo amplitude proves that the tunneling systems in the respective samples are indeed multi-level systems. This confirms that nuclear moments are part of the tunneling systems and experience a change of the electric field gradient during the tunneling motion. Since a variation of the electric field gradient causes a modulation of the quadrupole coupling constant, a relaxation via nuclear moments is very probable. The maximal magnetic field strength, possible with the experimental setup, is for the investigated samples too small to allow the quadrupole interaction to become a small perturbation, such that the influence of the nuclear moments on the relaxation of tunneling systems is significantly reduced. Nevertheless, the multicomponent glass HY-1 shows already at a magnetic field of 230 mT a significantly reduced relaxation rate compared to the case without magnetic field. This proves that the fast decay of the echo amplitude in HY-1 at small pulse separation times is indeed caused by the nuclear moments.

For a more elaborate analysis of the fast decay of the echo amplitude at small pulse separation times, measurements at very small pulse separation times are required. The reentrant cavity resonator, used so far, is amongst others due to its characteristic time constant, limited to pulse separation times larger than about 1.5 µs. Therefore a novel resonator technique, based on planar microfabricated superconducting resonators, was developed in the framework of this thesis suitable for the measurement of dielectric polarization echoes at very small pulse separation times. Essential for the design are rounded contours. Otherwise the high electric field strengths at the corners of the design and the strong coupling of the tunneling systems in these areas disturb the measurement. This insight does not only improve the resonators for dielectric polarization echoes, but also other microfabricated designs, for example [Aue19, Kör19, Fre21]. In first measurements with the lumped element resonator, presented in this thesis, the pulse separation time was reduced to 0.4 µs at a pulse duration of 230 ns, which is close to the theoretical limit given the definition of the pulse sequence. Thereby it was possible to observe the Gaussian shape like leveling-off of the echo amplitude of N-BK7 glass, as predicted by spectral diffusion theory.

The novel resonator technique enables an extended characterization of the fast decay of the echo amplitude at short pulse separation times and a quantitative comparison between the different samples. Since the strength of the relaxation process is related to the modulation of the quadrupole coupling constant, this can also give insights into the nature of the tunneling systems. Especially, the multitude of available organic glass formers potentially allows a more detailed understanding of the relaxation process. For example, individual atoms can be replaced by others which carry a nuclear quadrupole moment (e.g. brominated and unbrominated variants of the same material).

Furthermore, for samples with quadrupole splittings in the low MHz-range a complete mixing of the nuclear levels is achievable with shorter pulse durations. In this case, the measurements can be described by the simulation, developed within this thesis (see section 4.4). Hence measurements of the magnetic field dependence of the echo amplitude at different pulse separation times along with detailed simulations allow to detect changes in the distribution of the tunneling systems. This in turn can give insights into the kind of tunneling systems (symmetric or asymmetric) most sensitive to a nuclear moments based relaxation. A suitable sample would be B_2O_3. This sample shows a fast decay at small pulse separation times and contains only one kind of quadrupole moment carrying atoms with a quadrupole splitting of about 1.3 MHz.
The lack of NQR data for most samples is encountered by an cross experiment developed in collaboration with [Aue19, Bli20, Säu21]. Thereby the dielectric function of the sample is measured while simultaneously a magnetic bias field with variable frequency is applied to the sample. If the frequency of the bias field and the nuclear splitting agree, energy is transferred to the nuclear moments. If a strong relaxation of the nuclear moments via the tunneling systems is present the energy input is visible in the dielectric function. This measurement technique does not only allow a determination of the nuclear quadrupole frequency, but also an identification of a strong relaxation. First measurements on N-KZFS11, As_2S_3 and PVC showed promising results.
Another possibility to further investigate the nuclear moments based relaxation are three-pulse echo measurements with and without magnetic field. In phonon echo experiments the longitudinal relaxation time T_1 was more sensitive to an applied magnetic field [Ler88]. For those measurements as well as for verifying that the fast decay observed in two-pulse echoes is indeed caused by nuclear moments, the maximal magnetic field of the experimental setup has to be increased, such that the quadrupole interaction becomes a small perturbation.

A. Appendix

A.1 Nuclear properties

Nuclear quadrupole properties

The nuclear quadrupole properties of the isotopes relevant for this thesis are listed in table A.1. The table is amongst others based on those given in [Luc16, Aue19]. Other fruitful sources are [Chi88a, Chi88b, Chi89].

Not in every publication the quadrupole coupling constant as well as the transition frequency are given. In those cases the missing parameter is calculated with equation 4.7 and 4.8 by assuming $\eta = 0$. If $I > 3/2$ only the highest and lowest possible transition frequency is given. For $\Delta m = 0, \pm 1$, all other transition frequencies are within these. For $\eta \neq 0$ transitions with $\Delta m = \pm 2$ become possible which have larger transition frequencies [Sui06]. In [Sui06] are some diagrams showing the possible transition frequencies in dependence of η for $I = 5/2,\ 7/2$ and $9/2$.

Since this table gives only a rough overview about the energy scale of the quadrupole coupling, the temperatures at which the listed coupling constants and transition frequencies were measured are not given. However, both values depend on the sample temperature. Usually the transition frequency increases with decreasing temperature. Staying in the simple picture of $\eta = 0$ this effect is caused by an increasing electric field gradient eq, leading to a larger quadrupole coupling constant C_Q and thus to higher transition frequency. In simplified terms, it can be understood by the thermal contraction of solids with decreasing temperature, whereby the atoms approach each other. By this movement the electric field gradient that an atom with a quadrupole moment experiences increases, since the electric field gradient is caused by the surrounding atoms and its binding. A theory treating the shift of the transition frequency with temperature for molecular crystals can be found in [Bay51]. However, this shift is usually not very large. In [Rub74] the shift of the ^{75}As resonance frequency in crystalline As_2S_3 is given. It changes from 69.8 MHz at 300 K to 70.38 at 4.2 K. This example shows, that those shifts should be negligible compared to the uncertainties with respect to the implementation of the respective atoms within a glass.
In addition, the broadening of the transition frequencies caused by the disordered structure is also not considered.

Nuclear properties of different isotopes

Isotope	Natural abund. [%]	Spin[a] I	Gyromag. ratio γ_{gy} [MHz/T]	Quadrup. moment[a] Q [barn]	Coupling constant C_Q [MHz]	η	Transition frequency/ies ν_Q [MHz]	Material
^{2}H	0.015[b]	1	6.54[b]	0.00286	0.210*	0.1[c]	0.158[c]	O-^{2}H in Glycerol (solid)
					0.165*	< 0.02[c]	0.124[c]	C-^{2}H in Glycerol (solid)
^{10}B	19.6[b]	3	4.58[b]	0.0845	2.594[f]	0.515[f]	0.55 - 1.37[f]	$CaO \cdot B_2O_3$ (polycryst.)
					5.51[e]	0.12[e]	0.21 - 1.38[e]	B_2O_3 glass
^{11}B	80.4[b]	3/2	13.66[b]	0.04059	0.300[d]	0[d]	0.15*	BO_4 in Pyrex (glass)
					2.2 - 2.65[d]	0.2 - 0.8[d]	1.1 - 1.33*	BO_3 in Pyrex (glass)
					2.64[e]	0.12[e]	1.32[e]	B_2O_3 glass
^{14}N	99.6[b]	1	3.08[b]	0.02044	3.89[g]	0.27[g]	0.54 - 3.26[g]	Metafluor aniline
^{17}O	0.048[b]	5/2	5.77[e]	-0.0256	2.35 - 5.0[h]	0.1 - 0.55[h]	0.35 - 1.5*	Alkali disilicate glasses
^{23}Na	100[b]	3/2	11.26[b]	0.104	1.79 - 3.3[i]	0.1 - 1[i]	0.9 - 1.65*	diff. crystallized glasses
^{27}Al	100[b]	5/2	11.09[b]	0.1466	3.5 - 4.5[d]	n/a	0.53 - 1.35*	Pyrex (glass)
^{33}S	0.75[e]	3/2	3.27[e]	-0.0678	-	-	-	-
^{35}Cl	75.5[b]	3/2	4.17[b]	-0.0817	65*	n/a	32.5[j]	powdery PVC
^{37}Cl	24.5[b]	3/2	3.47[b]	-0.0644	51.2*	n/a	25.6[j]	powdery PVC
^{39}K	93.26[e]	3/2	1.99[e]	0.0585	0.028 - 0.978[k]	0 - 1[k]	0.056 - 0.978[k]	diff. ^{39}K-salts (cryst.)
^{40}K	0.01[e]	4	2.47[e]	0.073	-	-	-	-
^{41}K	6.73[e]	3/2	1.09[e]	0.0711	1.84*	n/a	0.922[p]	salt
^{67}Zn	4.1[e]	5/2	2.66[e]	0.15	-	-	-	-
^{75}As	100[b]	3/2	7.29[b]	0.314	114 - 117[l,□]	0.15 - 0.42[l,□]	70.75[l]	amorphous As_2S_3
^{79}Br	50.5[b]	3/2	10.67[b]	0.313	508 - 604*	n/a	254 - 302[m]	diff. organic compounds
					617 - 641[n]	0.1 - 0.16[n]	309 - 322[n]	diff. C-Br$\cdots$N bindings

Nuclear properties of different isotopes - continued

Isotope	Natural abund. [%]	Spin[a] I	Gyromag. ratio γ_{gy} [MHz/T]	Quadrup. moment[a] Q [barn]	Coupling constant C_Q [MHz]	η	Transition frequency/ies ν [MHz]	Material
^{81}Br	49.5[b]	3/2	11.50[b]	0.262	515 - 535[n]	0.1 - 0.16[n]	258 - 269[n]	diff. C-Br$\cdots$N bindings
^{91}Zr	11.22[e]	5/2	3.97[e]	-0.176	20.47[r]	n/a	3.07 - 6.14*	$ZrSiO_4$ crystal
^{93}Nb	100[e]	9/2	10.41[e]	-0.32	$\approx$77.5[t]	$\approx$0.36[t]	5.7 - 12.8[t]	Niobium pentachloride
^{121}Sb	57.3[e]	5/2	10.19[e]	-0.543	-	-	-	-
^{123}Sb	42.7[e]	7/2	5.52[e]	-0.692	-	-	-	-
^{135}Ba	6.59[e]	3/2	4.23[e]	0.160	17.1*	n/a	8.55[q]	$BaCl_2O_6 \cdot H_2O$
^{137}Ba	11.23[e]	3/2	4.73[e]	0.245	7 - 25.4[o]	0 - 0.5[o]	3.5 - 12.7*	diff. crystals
^{165}Ho	100[e]	7/2	8.73[e]	3.58	736.4[q]	0[q]	52.6 - 157.8[q]	HoO_4V
^{181}Ta	99.99[e]	7/2	5.09[e]	3.17	266[s]	0.05[s]	19.2 - 56.9[s]	$LiTaO_3$

Table A.1: Table of the stable isotopes and their nuclear quadrupole properties relevant for this thesis. Data taken from *a* [Sto13], *b* [Sui06], *c* [Sch92], *d* [Pra06], *e* [Chi88a], *f* [Bra99], *g* [Bra04a], *h* [Mae96], *i* [Xue93], *j* [Kim77], *k* [Bas91], *l* [Rub74], *m* [Lud56], *n* [Vio18], *o* [Ham10], *p* [Chi88b], *q* [Chi89], *r* [Bas90], *s* [Zhu78], *t* [Oku84]. The properties marked with an additional □ are measured for the corresponding crystal. The coupling constants or transition frequencies marked with $*$ are calculated by assuming $\eta = 0$. If various transition frequencies are possible (e.g. $I > 3/2$) only the lowest and highest are given. For $\Delta m = 0, \pm 1$ all other transition frequencies are within these.

Nuclear magnetic moments of different isotopes							
Isotope	Natural abund. [%]	Spin I	Magnetic moment [μ_N]	Isotope	Natural abund. [%]	Spin I	Magnetic moment [μ_N]
^{1}H	99.99	1/2	2.793	^{39}K	93.26	3/2	0.391
^{2}H	0.01	1	0.857	^{40}K	0.01	4	1.298
^{10}B	80.1	3/2	2.689	^{41}K	6.73	3/2	1.458
^{11}B	19.9	3	1.801	^{67}Zn	4.1	5/2	0.875
^{13}C	1.07	1/2	0.702	^{75}As	100	3/2	1.439
^{14}N	99.63	1	0.404	^{79}Br	50.69	3/2	2.106
^{15}N	0.37	1/2	0.283	^{81}Br	49.31	3/2	2.271
^{17}O	0.04	5/2	1.894	^{91}Zr	11.22	5/2	1.304
^{19}F	100	1/2	2.629	^{93}Nb	100	9/2	6.171
^{23}Na	100	3/2	2.218	^{121}Sb	57.21	5/2	3.363
^{27}Al	100	5/2	3.642	^{123}Sb	42.79	7/2	2.55
^{29}Si	4.7	1/2	0.555	^{135}Ba	6.59	3/2	0.838
^{33}S	0.76	3/2	0.644	^{137}Ba	11.23	3/2	0.937
^{35}Cl	75.78	3/2	0.822	^{165}Ho	100	7/2	4.173
^{37}Cl	24.22	3/2	0.684	^{181}Ta	99.99	7/2	2.371

Table A.2: Table of the stable isotopes and their nuclear magnetic moments relevant for this thesis. All data is taken from [Web].

A.2 Supplementary plots for section 4.4

Figure A.1 shows the simulated quantum beating of glycerol-d5. The distribution of tunneling systems used for the simulation is shown in figure 4.17. The quadrupole splitting is 124.5 kHz and the tunneling angle $\Theta_T = 16°$ in accordance with the results obtained in [Baz08]. Since the simulation introduced in section 4.4 considers only one nuclear moment per tunneling system the result is taken to the power of five equivalent to the magnetic field dependence shown in figure 4.18.
Figure A.2 shows the magnetic field dependence of the energy levels of the upper multiplet of a tunneling system with $I = 1$. The other settings are equivalent to the simulation of the magnetic field dependence and the quantum beating. The nuclear spin of the shown tunneling system and the magnetic field are parallel to each.

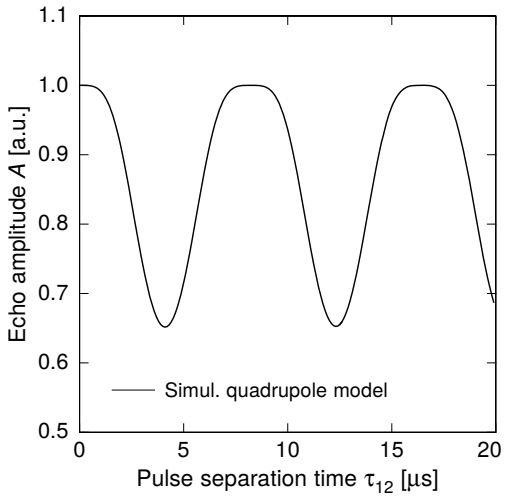

Figure A.1: Simulated beating of the echo amplitude for Glycerol-d5. The values used in the simulation are given in section 4.4. The obtained result is in accordance with measurements and simulations done in [Baz08].

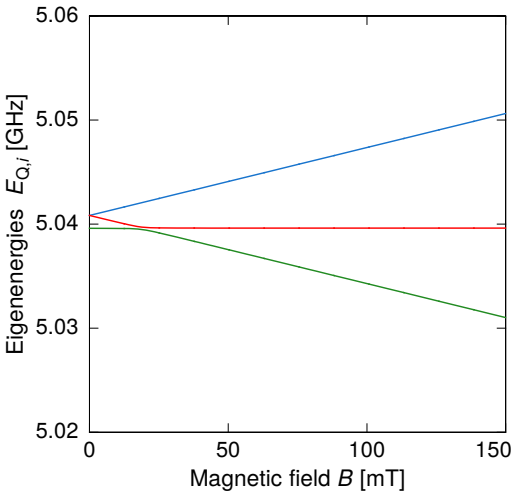

Figure A.2: Simulation of the magnetic field dependence of the energy levels of the upper multiplet of a tunneling system containing one nucear quadrupole moment with $I = 1$.

A.3 Software and measurement procedure

The software to control the different remote controllable devices is written in LabVIEW[13] and was developed in [Sch16a]. In the course of this thesis these routines were extended to meet the current needs.
Before an actual measurement of an echo sequence starts all devices are initialized. This means, that the signal generator is set to the resonance frequency of the resonator, which was determined by the network analyzer. The amplitude of the high frequency signal is set to 13 dBm. The pulse durations t_1 and t_2 as well as the pulse separation time τ_{12} are sent to the pulse generator. The magnetic field is ramped up to the desired value. Thereby the current sent to the coil is varied in small steps with small breaks in between to reduce the introduced heat by eddy currents and to give the resonator and the sample time to thermalize. Finally, the AD-card is initialized according to the needed time window for the measurement of the two-pulse sequence and the expected signal height of the echo.
Afterwards, the actual measurement is initiated by the AD-card. It starts the recording of the data and sends a trigger impulse to the pulse generator. The two switches are opened simultaneously in the predefined manner of the two-pulse sequence. Then the pulses pass the adjustable attenuator, where their field strength is reduced such that the small angle approximation is fulfilled. After passing the attenuator in the cryostat the two-pulse sequence is coupled into the resonator. Since the oscillating

[13]National Instruments, 11500 N. Mopac Expwy, Austin, TX 78759-3504, USA

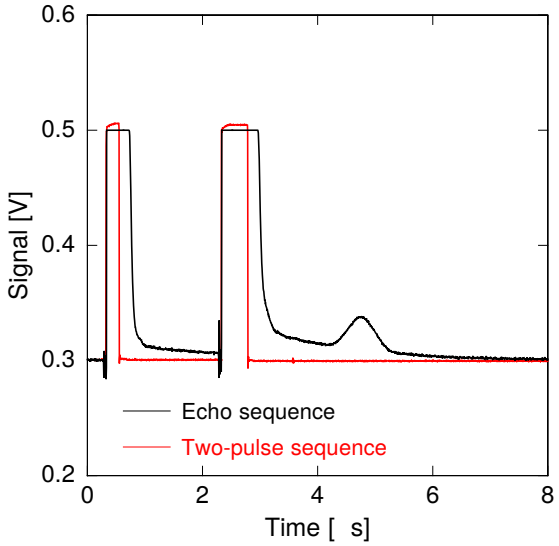

Figure A.3: Shape of a typcial echo sequence. The curves are an average over 5000 single measurements of the sample N-BK7 at a temperature of 10 mK. The used pulse durations are $t_1 = 230\,\mathrm{ns}$ and $t_2 = 460\,\mathrm{ns}$ at a pulse separation time of $\tau_{12} = 2\,\mathrm{s}$. The red line shows the actual two-pulse sequence as generated at the pulse generator.

magnetic field within the resonator is also coupled out during the pulses through the coupling-out loop, the signal in the readout branch consists of the two-pulse sequence and the corresponding echo. Subsequently the signal is amplified by the low and the room temperature amplifier before the high frequency part is eliminated by mixing with an appropriate adjusted reference signal. The envelopes are further amplified and finally recorded by the AD-card. Afterwards, the measuring software preliminary analyzes the data and triggers another two-pulse sequence. Thus the repetition rate of the echo sequence is defined by the the measuring computer.

An example of an echo sequence measured on the glass N-BK7 is shown in figure A.3. In addition, the two-pulse sequence, as generated by the pulse generator, is depicted in red. The offset, which can be seen in the echo sequence, of about 0.3 V is caused, amongst others, by the amplifiers in the readout branch. In the background correction of the analysis procedure this offset is considered and subtracted (see section 6.1). In figure A.3 the red curve is shifted by the same offset for clarity. The maximal signal height of the two pulses in the echo sequence is set by the AD-card. In the measurement, shown in figure A.3, the signal was limited to $\pm 0.5\,\mathrm{V}$. Actually, the voltage is considerably larger and leads usually to a saturation of the amplifiers in the readout branch at a voltage of about 2 V. In addition, figure A.3 shows that the recorded envelopes of the two pulses of the echo sequence are significantly broader than the generated two-pulse sequence. This broadening is mostly caused by the ring-down of the resonator but also by other components in the electronic setup and is discussed in section 7.1. The non-straight baseline after the pulses is caused by similar effects and considered in the background correction.

The preliminary analysis of the data by the measurement computer, mentioned above, is similar to the final analysis introduced in section 6.1. However, in the final analysis a more advanced background correction is applied. The analysis routine in the measurement software is used to determine how many measurements at

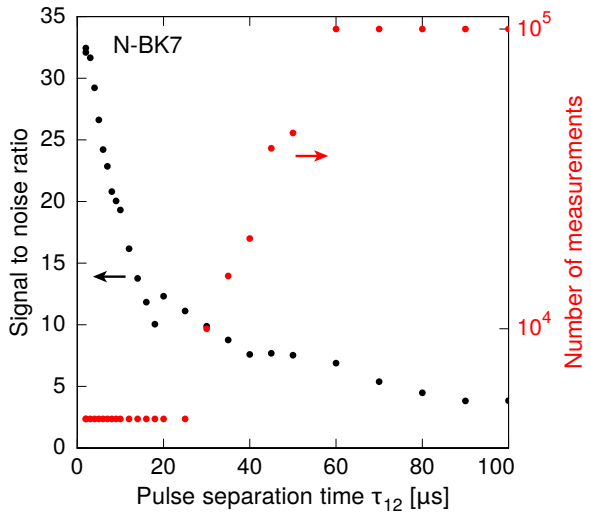

Figure A.4: Signal to noise ratio as calculated by the measurement software (shown in black, left y-axis) and the corresponding number of measurements (shown in red, right y-axis) as a function of the pulse separation time for a decay measurement on the sample N-BK7 at a temperature of 10 mK.

one pulse separation time and temperature have to be averaged to obtain a predefined signal to noise ratio for the echo signal. For this purpose the height of the echo signal is compared to the standard deviation of the signal far apart from the pulses and the echo (for the echo sequence, shown in figure A.3, a suitable window is for example between a measurement time of 15 µs and 20 µs). Until the predefined signal to noise ratio or a maximal number of measurements is reached more echo sequences are averaged. This procedure ensures that only the number of measurements needed for a suitable data quality is measured, which saves measurement time. With increasing pulse separation time the echo amplitude decreases due to relaxation processes and thus the needed number of measurements for a suitable signal to noise ratio increases. In figure A.4 this is exemplarily shown for an echo decay measurement on the glass N-BK7. In black the obtained signal to noise ratio is shown and in red the corresponding number of measurements. In this measurement the minimal number of measurements to be averaged is set to 5000, the maximal to 100000 and the minimal signal to noise ratio to 7. At small pulse separation times the minimal number of measurements is sufficient to reach a good signal to noise ratio. With increasing pulse separation time the signal to noise ratio drops while the number of measurements stays constant. At a pulse separation time of 30 µs the minimal number of measurements is too small to reach the defined signal to noise ratio of 7. Thus further 5000 measurements are averaged. Subsequently the number of measurements increases with larger pulse separation time to obtain the desired signal to noise ratio until the maximal number of measurements of 100000 is reached at $\tau_{12} = 60\,\mu s$. From this point on the signal to noise ratio drops. The maximal number of measurements is no arbitrary number, but motivated by the minimal reachable standard deviation of the measurement setup (compare section 5.3). The step in the signal to noise ratio in figure A.4 at a pulse separation time of 20 µs is caused by a change in the background correction (compare section 6.1).

After the procedure behind every measurement is introduced the different kind of

measurements usually done in a measurement cycle are shortly summarized.

1. **Determination of resonance frequency**
   After the cryostat is cooled to the desired temperature and the sample has thermalized for several hours, the resonance frequency of the resonator is measured with the network analyzer.

2. **Adjust phase shifter**
   The phase of the reference signal, used to remove the high frequency part of the echo sequence at the mixer, is adjusted by the phase shifter. This can either be done systematically by measuring the echo amplitude in dependence of the phase shift or by adjusting it by eye, such that the echo amplitude is maximal. For these measurements arbitrary values of the pulse duration and the field strength are used and the small angle approximation is neglected. However, the pulse duration and field strength should not be chosen too large to prevent heating effects, which can disturb the measurement. In addition, the repetition rate of the two-pulse sequence should not be too high since this can also cause heating effects. A rate of about $10\,{}^{1}/_{\mathrm{s}}$ is usually a good value. If the frequency applied to the resonator is changed during a measurement cycle, for example due to a temperature change, the phase of the reference signal has to be adjusted again.

3. **Adjust attenuation**
   With the used electronic setup the field strength of the ${}^{\pi}/_{2}$ and the π pulse is not adjustable independently. Thus to achieve the small angle approximation (equation 3.50) the field strength and the pulse duration are adjusted under the condition $t_2 = 2t_1$. Since the pulse duration defines also the frequency spectrum of the pulses usually a fixed pulse duration is chosen and the field strength is adapted accordingly. Therefore the echo amplitude is measured in dependence of the field strength of the excitation pulses to find the regime in which the amplitude is proportional to F_0^3.

4. **Repetition rate**
   After the desired measuring parameters (pulse duration and field strength) are found, it is checked whether the repetition rate used for the determination of these parameters was too high and led to unintended heating effects that influenced the measurement. Therefore the echo amplitude is measured in dependence of the repetition rate from small to large rates. A heating effect leads to a decrease of the echo amplitude. If a heating effect is detected at the same rate which was used to adjust the phase shifter and the attenuator, these measurements have to be repeated with a lower repetition rate.

5. **Thermalization**
   As last step, after all measurement parameters are defined it is checked whether

the sample is thermalized to the desired temperature. To check this circumstance, the echo amplitude is measured in dependence of the cryostat temperature at several temperatures. A reduction of the temperature thereby leads to an increased echo amplitude and vice versa. In addition, these measurements allow to determine the thermalization time needed by the sample to adapt after a change in temperature. However, these measurements do not allow to determine the absolute temperature of the sample. In principle it is possible that a constant offset to the cryostat's temperature exists. But if the thermalization measurement shows the expected behavior, it can be presumed that the sample has the same temperature as the cryostat. To determine the absolute temperature of the sample a thermometer has to be mounted directly on the sample, which is not possible in most experimental setups.
Another possibility to check the thermalization of the sample is via the resonance frequency of the resonator. A change in temperature leads to a change of the dielectric constant. Thus measuring the resonance frequency in dependence of the temperature gives the same information as measuring the echo amplitude in dependence of the temperature. However, in dependence of the sample, the resonance frequency and the temperature range, the change in resonance frequency is unsuited to determine the sample's thermalization. Considering the standard tunneling model, the dielectric constant is for a frequency of about 1 GHz and very low temperatures in a plateau region (compare figure A.5) such that there is no significant change of the resonance frequency with temperature. Thus in the framework of this thesis the echo amplitude is used as indicator for the thermalization.

6. **Measure decay and magnetic field dependence of the echo amplitude**
After all parameters are defined and the thermalization is checked, the decay of the echo amplitude in dependence of the pulse separation time at different temperatures as well as its magnetic field dependence can be measured.

A.4 Dielectric function in the standard tunneling model

In figure A.5 and A.6 the course of the real part of the dielectric function (which is proportional to $1/f_{\mathrm{res}}$) and the loss $\tan(\delta)$ (being proportional to $1/Q$) in dependence of temperature is shown for different frequencies. The curves are based on the standard tunneling model and calculated numerically. Regarding more details on the dielectric function and the numerical calculation see [Luc16]. For the topics discussed in the framework of this thesis the real part of the dielectric function at about 1 GHz is relevant. It can be seen that the curve exhibits a plateau region at very low temperatures. Thus a determination of the samples thermalization via the shift of the resonance frequency as mentioned in section A.3 is not possible in this temperature region. The loss $\tan(\delta)$ shows a plateau as well. The reentrant cavity resonator has a high intrinsic loss and is thus not suited to measure the sample's loss.

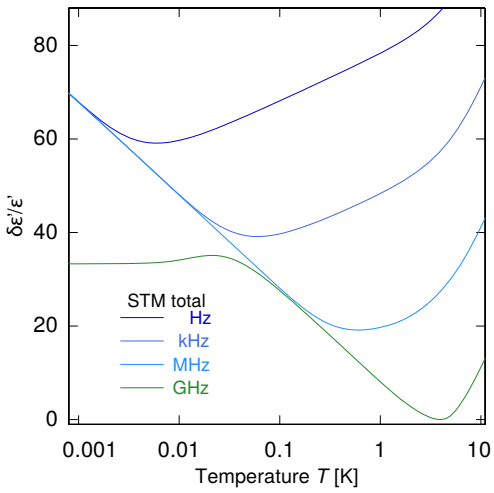

Figure A.5: Numerical calculation of the real part of the dielectric function in the standard tunneling model as a function of temperature for frequencies between 1 Hz and 1 GHz. Plot taken from [Luc16].

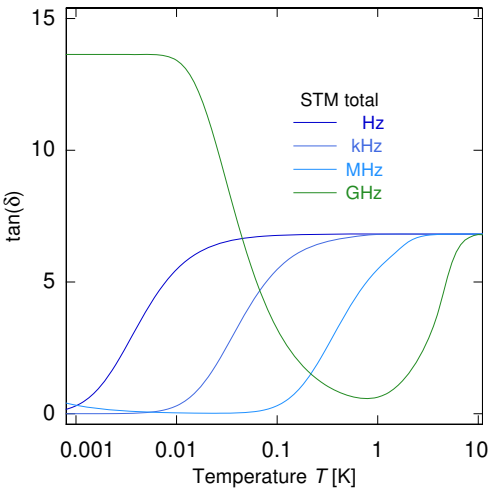

Figure A.6: Numerical calculation of $\tan(\delta)$ in the standard tunneling model as a function of temperature for frequencies between 1 Hz and 1 GHz. Plot taken from [Luc16].

A.5 Supplementary plots for chapter 6

Electric field dependence of the echo amplitude

In figure A.7 the relative contribution of tunneling systems with asymmetry energy Δ to the echo amplitude is shown in dependence of the asymmetry parameter $q = \Delta/E$ for different pulse separation times τ_{12}. For this illustration the argument of the integral given in equation 3.71 is calculated in dependence of q. The shown plot

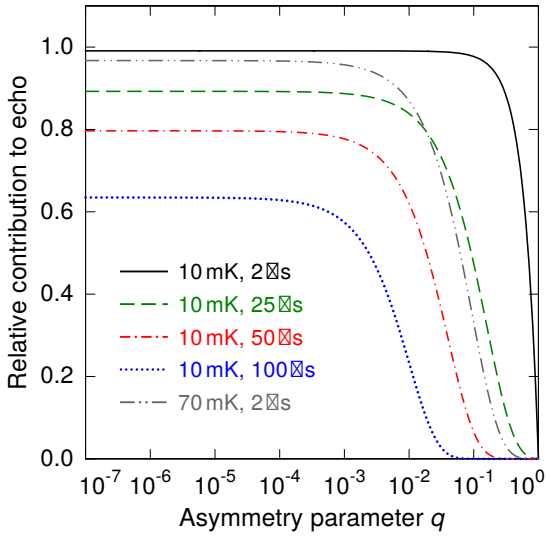

Figure A.7: Relative contribution of tunneling systems with asymmetry parameter $q = \Delta_0/E$ to the echo amplitude at different pulse separation times and temperatures.

is the semi-logarithmic version of figure 6.15. In this plot the influence of the one-phonon relaxation and spectral diffusion on the ensemble of tunneling systems can be seen better. Spectral diffusion leads to a shift of the curve towards smaller q since it is more effective for tunneling systems with a large asymmetry energy. The one-phonon process leads to a reduction of the plateau region.

Temperature dependence of the relaxation

In figure A.8 the echo amplitude of Suprasil I and BK7 is shown in dependence of the pulse separation time at a temperature of about 100 mK. It can be seen that the decay behavior is within the scope of the measurement accuracy equal. This indicates an equal strength of spectral diffusion and thereby a similar coupling of the tunneling systems present in these materials to phonons and the strain field.

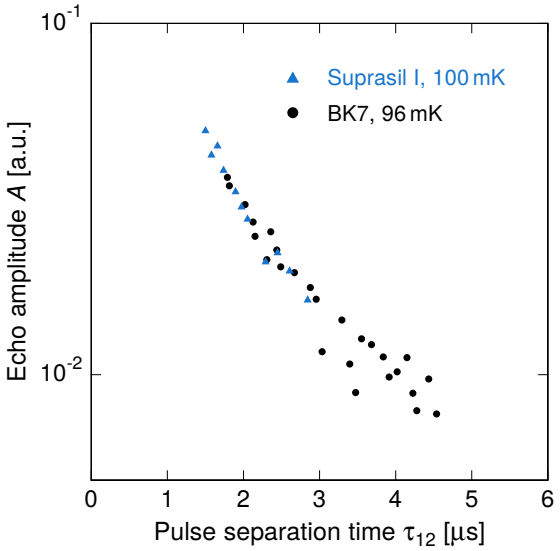

Figure A.8: Echo amplitude as a function of the pulse separation time for BK7 and Suprasil I. The curve of BK7 was measured at a temperature of 96 mK, the one of Suprasil I at 100 mK. For better comparison the decay curves are aligned to each other. Data taken from [Ens96b].

Determination of $T_{1\mathrm{Phonon}}$ and T_{specDiff} for Suprasil I

Figure A.9 shows the data measured on Suprasil I at a temperature of 13 mK and a curve based on the one-phonon relaxation and spectral diffusion in the short time limit (compare equation 3.71). The obtained relaxation times are: $T_1 = T_{1\mathrm{Phonon}} = 125\,\mu\mathrm{s}$ and $T_{\mathrm{specDiff}} = 31.6\,\mu\mathrm{s}$. The value for $T_2 \approx T_{\mathrm{specDiff}}$ is similar to the one obtained in [Ens96b].

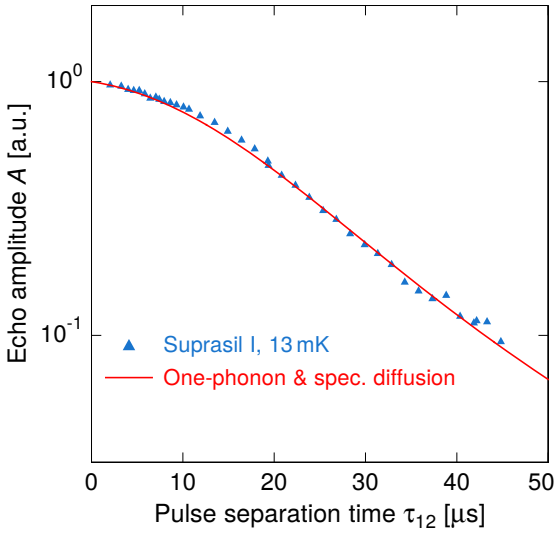

Figure A.9: Echo amplitude as a function of the pulse separation time for Suprasil I. The red curve is calculated based on equation 3.71. Data taken from [Ens96b].

Bibliography

[Aß18] N. Aßmann, Dielektrische Eigenschaften eines bromierten molekulaten Glases bei niedrigen Frequenzen und tiefen Temperaturen, Bachelor's thesis, Heidelberg University, 2018.

[Abe66] I. D. Abella, N. A. Kurnit, and S. R. Hartmann, Photon Echoes, *Phys. Rev.*, **141**(1), 141, 1966.

[Abr61] A. Abragam, The principles of nuclear magnetism, Oxford-Press, (Oxford), 1961.

[Ahr13] F. Ahrens, Dielektrische Dreipulsechomessungen am Bariumalumosilikatglas AlBaSi, Bachelor's thesis, Heidelberg University, 2013.

[All07] D. W. Allen, Holmium Oxide Glass Wavelength Standards, *J. Res. Natl. Inst. Stand. Technol.*, **112**(6), 303–306, 2007.

[And72] P. W. Anderson, B. I. Halperin, and C. M. Varma, Anomalous Low-temperature Thermal Properties of Glasses and Spin Glasses, *Philos. Mag.*, **25**(1), 1–9, 1972.

[And86] A. C. Anderson, Low-temperature thermal expansion of glassy solids, *Phys. Rev. B*, **34**(2), 1317–1318, 1986.

[Arc13] A. Archer, Two-pulse dielectric polarisation echo experiments on the aluminoborosilicate glass AlBaSi, Master's thesis, Heidelberg University, 2013.

[Arn75] W. Arnold and S. Hunklinger, Experimental evidence for the direct interaction between two-level systems in glasses at very low temperatures, *Solid State Commun.*, **17**(7), 883–886, 1975.

[Arn19] J. V. Arneth, Dielektrische Polarisationsechos an amorphem Arsentrisulfid bei tiefen Temperaturen, Bachelor's thesis, Heidelberg University, 2019.

[Aue19] A. Auer, Direct Probing of the Nuclear Quadrupole Impact onto Tunnelling Systems in Glasses at Low Temperatures, Master's thesis, Heidelberg University, 2019.

[Bar13] M. Bartkowiak, M. Bazrafshan, C. Fischer, A. Fleischmann, and C. Enss, Nuclear Quadrupole Moments as a Microscopic Probe to Study the Motion of Atomic Tunneling Systems in Amorphous Solids, *Phys. Rev. Lett.*, **110**(20), 205502, 2013.

[Bas90] T. J. Bastow, ^{91}Zr nuclear quadrupole coupling in zircon ($ZrSiO_4$), *J. Phys.: Condens. Matter*, **2**, 6327–6330, 1990.

[Bas91] T. J. Bastow, Powder Determination of ^{39}K Nuclear Quadrupole Coupling, *J. Chem. Soc. Faraday Trans.*, **87**(15), 2453–2455, 1991.

[Bay51] H. Bayer, Zur Theorie der Spin-Gitterrelaxation in Molekülkristallen, *Z. Physik*, **130**, 227–238, 1951.

[Baz07] M. Bazrafshan, G. Fickenscher, M. von Schickfus, A. Fleischmann, and C. Enss, Impact of nuclear dipoles on polarization echoes in glasses, *J. Phys.: Conf. Ser.*, **92**, 012135, 2007.

[Baz08] M. Bazrafshan, Investigation of the microscopic nature of tunnelling systems in amorphous glycerol by two-pulse polarisation echo experiments, Doctoral thesis, Heidelberg University, 2008.

[Ber79] L. Bernard, L. Piché, G. Schumacher, and J. Joffrin, Relaxation Times of Molecular Ions OH^- in Glasses at Very Low Temperatures, *J. Low Temp. Phys.*, **35**(3/4), 411–431, 1979.

[Ber88] J. Berret and M. Meißner, How Universal are the Low Temperature Acoustic Properties of Glasses?, *Z. Phys. B*, **70**(1), 65–72, 1988.

[BJ88] G. Balzer-Jöllenbeck, O. Kanert, and J. Steinert, Low-Temperature Properties of Nuclear Spin Relaxation in Inorganic Glasses, *Solid State Commun.*, **65**(5), 303–309, 1988.

[Bla77] J. L. Black and B. I. Halperin, Spectral diffusion, phonon echoes, and saturation recovery in glasses at low temperatures, *Phys. Rev. B*, **16**(6), 2879–2895, 1977.

[Bli20] J. Blickberndt, Einfluss von magnetischen Kernanregungen auf die dielektrische Funktion von amorphem Arsentrisulfid bei tiefen Temperaturen, Bachelor's thesis, Heidelberg University, 2020.

[Blo46] F. Bloch, Nuclear Induction, *Phys. Rev.*, **70**(7), 460–474, 1946.

[Blo48] N. Bloembergen, Nuclear Magnetic Relaxation, Doctoral thesis, Utrecht, 1948.

[Bol15] D. Boll, Dielektrische Permitivität von HY-1 Glas im MHz-Bereich zwischen 10 mK und 350 K, Bachelor's thesis, Heidelberg University, 2015.

[Bra91] C. J. Brabec, Structural model of amorphous arsenic sulfide, *Phys. Rev. B*, **44**(24), 13332–13342, 1991.

[Bra99] P. J. Bray, NMR and NQR studies of boron in vitreous and crystalline borates, *Inorganica Chimica Acta*, **289**, 158–173, 1999.

[Bra04a] M. Brandt, Einfluss von Kernquadrupolmomenten auf die Amplitude von Polarisationsechos in amorphen Festkörpern, Doctoral thesis, Heidelberg University, 2004.

[Bra04b] M. Brandt, P. Nagel, A. Fleischmann, C. Enss, and S. Hunklinger, Evidence for the crucial role of nuclear spins for the magnetic field effect in polarization echoes in glasses, *Phys. Stat. Sol. (C)*, **1**(11), 2875–2878, 2004.

[Bur98] A. L. Burin, Y. Kagan, L. A. Maksimov, and I. Y. Polishchuk, Dephasing Rate in Dielectric Glasses at Ultralow Temperatures, *Phys. Rev. Lett.*, **80**(13), 2945–2948, 1998.

[Bur13] A. L. Burin, J. M. Leveritt III, G. Ruyters, C. Schötz, M. Bazrafshan, P. Fassl, M. v. Schickfus, A. Fleischmann, and C. Enss, Low-temperature dipolar echoes in amorphous dielectrics: Significance of relaxation and decoherence free two-level systems, *EPL*, **104**, 57006, 2013.

[Chi88a] K. H. Chihara and N. Nakamura, Landolt-Börnstein - Group III Condensed Matter 20 A (Nuclei D - Cl), SpringerMaterials, (Heidelberg), 1988.

[Chi88b] K. H. Chihara and N. Nakamura, Landolt-Börnstein - Group III Condensed Matter 20 B (Nuclei Cl - Rb), SpringerMaterials, (Heidelberg), 1988.

[Chi89] K. H. Chihara and N. Nakamura, Landolt-Börnstein - Group III Condensed Matter 20 C (Nuclei Zr - Bi), SpringerMaterials, (Heidelberg), 1989.

[Däh10] D. Dähn, Messung der dielektrischen Funktion des Tantal-Oxid-Glases N-KZFS11 bei sehr tiefen Temperaturen, Diploma thesis, Heidelberg University, 2010.

[Deb12] P. Debye, Zur Theorie der spezifischen Wärmen, *Ann. Phys.*, **344**, 789–839, 1912.

[Del15] E. Delic, Breitbandmessung der dielektrischen Permittivität der Gläser N-BK7 und HY-1 zwischen 80 K und 360 K, Bachelor's thesis, Heidelberg University, 2015.

[Dra77] K. Dransfeld and S. Hunklinger, Acoustic and dielectric behaviour of glasses at low temperatures, in *Proc. 7th Int. Conf. on Amorphous and Liquid Semiconductors*, 155–163, Edinburgh, 1977.

[Dur89] A. V. Durrant, J. Manners, and P. M. Clark, Understanding optical echoes using Schrödinger's equation: I. Echoes excited by two optical pulses, *Eur. J. Phys.*, **10**, 291–297, 1989.

[Ens91] C. Enss, Untersuchung der Dynamik von Tunnelzuständen in Gläsern und kristallinen Defektsystemen, Doctoral thesis, Heidelberg University, 1991.

[Ens95] C. Enss, H. Schwoerer, D. Arndt, and M. v. Schickfus, Dielectric echo experiments on $(KBr)_{1-x}(KCN)_x$, *Phys. Rev. B*, **51**(2), 811–824, 1995.

[Ens96a] C. Enss, S. Ludwig, R. Weis, and S. Hunklinger, Decay of Spontaneous Echoes in Glasses, *Czech. J. Phys.*, **46**(Suppl. S4), 2247, 1996.

[Ens96b] C. Enss, R. Weis, S. Ludwig, and S. Hunklinger, Coherent Echoes in Glasses and Crystals with Point Defects, *Czech. J. Phys.*, **46**(Suppl. S4), 3287, 1996.

[Ens02a] C. Enss, Anomalous Behavior of Insulating Glasses at Ultra-low Temperatures, *Adv. in Solid State Phys.*, **42**, 335–346, 2002.

[Ens02b] C. Enss, Beyond the tunneling model: quantum phenomena in ultracold glasses, *Physica B*, **316-317**, 12–20, 2002.

[Ens10] C. Enss and S. Hunklinger, Low Temperature Physics, Springer, (Heidelberg), 2010.

[Esq98] P. Esquinazi (Ed.), Tunneling systems in amorphous and crystalline solids, Springer, (Heidelberg), 1998.

[Est91] S. Estalji, O. Kanert, J. Steinert, H. Jain, and K. L. Ngai, Uncommon nuclear-spin relaxation in fluorozirconate glasses at low temperatures, *Phys. Rev. B*, **43**(10), 7481–7486, 1991.

[Fas10] P. Fassl, Überprüfung des Modells der spektralen Diffusion mit Hilfe von Polarsiationsechomessungen am Borsilikat-Glas BK7, Bachelor's thesis, Heidelberg University, 2010.

[Fic07] G. Fickenscher, Einfluss der magnetischen Dipol-Dipol Wechselwirkung von Kernen auf atomare Tunnelsysteme, Diploma thesis, Heidelberg University, 2007.

[Fic09] G. Fickenscher, M. Bazrafshan, K. Reinhold, A. Fleischmann, and C. Enss, Influence of nuclear dipole-dipole interaction on atomic tunnelling systems in glycerol, *J. Phys. : Conf. Ser.*, **150**, 042032, 2009.

[Fic13] G. Fickenscher, Phasenkohärenz und Energierelaxation von Tunnelsystemen in Gläsern - Messung und Analyse von Polarisationsechos an BK7, Doctoral thesis, Heidelberg University, 2013.

[Fre16] B. Frey, Entwicklung mikrostrukturierter supraleitender Resonatoren zur breitbandigen Untersuchung dielektrischer Eigenschaften zwischen 37 MHz und 1 GHz bei tiefen Temperaturen, Master's thesis, Heidelberg University, 2016.

[Fre21] B. Frey, To be published, Doctoral thesis, Heidelberg University, 2021.

[Fuk81] E. Fukushima and S. B. W. Roeder, Experimental Pulse NMR - A Nuts and Bolts Approach, Addison-Wesley Publishing Company Inc., (London, Amsterdam, Don Mills, Ontario, Tokyo), 1. edition, 1981.

[Gol73] B. Golding, J. E. Graebner, B. I. Halperin, and R. J. Schutz, Nonlinear Phonon Propagation in Fused Silica below 1 K, *Phys. Rev. Lett.*, **30**(6), 223–226, 1973.

[Gol76] B. Golding and J. E. Graebner, Phonon Echo in Glass, *Phys. Rev. Lett*, **37**(13), 852, 1976.

[Gra79] J. E. Graebner and B. Golding, Phonon echoes in glass at low temperatures, *Phys. Rev. B*, **19**(2), 964, 1979.

[Gra12] G. J. Grabovskij, T. Peichl, J. Lisenfeld, G. Weiss, and A. V. Ustinov, Strain Tuning of Individual Atomic Tunneling Systems Detected by a Superconducting Qubit, *Science*, **338**, 232, 2012.

[Gro18] R. Gross and A. Marx, Festkörperphysik, de Gruyter, (Berlin), 2018.

[Gur90] V. Gurevich, M. Muradov, and D. Parshin, Electric dipole echo in glasses, *Sov. Phys. JETP*, **70**(5), 928–936, 1990.

[Haa18a] M. Haas, Development of planar superconducting microwave resonators for probing the short time regime of the dielectric polarization echo decay in glasses), Master's thesis, Heidelberg University, 2018.

[Haa18b] R. Haase, Dielektrische Polarisationsechos an Br-DGEBA Glas bei tiefen Temperaturen, Bachelor's thesis, Heidelberg University, 2018.

[Hah50] E. L. Hahn, Spin Echoes, *Phys. Rev.*, **80**(4), 580, 1950.

[Ham10] H. Hamaed, E. Ye, K. Udachin, and R. W. Schurko, Solid-State ^{137}Ba NMR Spectroscopy: An Experimental and Theoretical Investigation of ^{137}Ba Electric Field Gradient Tensors and Their Relation to Structure and Symmetry, *J. Phys. Chem. B*, **114**(18), 6014–6022, 2010.

[Hau15] N. V. Hauff, Dielektrische Permitivität von HY-1 Glas bei hohen Frequenzen und tiefen Temperaturen, Bachelor's thesis, Heidelberg University, 2015.

[Her17] T. J. Herbst, Dielectric Permittivity of the Glass FR-122P between 10 mK and 10 K at 36 MHz, Bachelor's thesis, Heidelberg University, 2017.

[Hil] W. Hillert, E106 hohlraumresonatoren/ cavities, `http://www-elsa.physik.uni-bonn.de/Lehrveranstaltungen/FP-E106/E106-Erlaeuterungen.pdf`, Accessed: February 2021.

[Hoy16] Hoya Corporation, Data sheet HY-1, 2016.

[Hu74] P. Hu and S. R. Hartmann, Theory of spectral diffusion decay using an uncorrelated-sudden jump model*, *Phys. Rev. B*, **9**(1), 1–13, 1974.

[Hu15] J. Hu, MIT 3.071 Amorphous Materials 14: Characterizing the Amorphous State, MIT OpenCourseWare, 2015.

[Hua12] P. Y. Huang, S. Kurasch, A. Srivastava, V. Skakalova, J. Kotakoski, A. V. Krasheninnikov, R. Hovden, Q. Mao, J. C. Meyer, J. Smet, D. A. Muller, and U. Kaiser, Direct Imaging of a Two-Dimensional Silica Glass on Graphene, *Nano Lett.*, **12**, 1081–1086, 2012.

[Hua13] P. Y. Huang, S. Kurasch, J. S. Alden, A. Shekhawat, A. A. Alemi, P. L. McEuen, J. P. Sethna, U. Kaiser, and D. A. Muller, Imaging Atomic Rearrangements in Two-Dimensional Silica Glass: Watching Silica's Dance, *Science*, **342**(6155), 224–227, 2013.

[Hun72] S. Hunklinger, W. Arnold, S. Stein, R. Nava, and K. Dransfeld, Saturation of the Ultrasonic Absorption in Vitreous Silica at low temperatures, *Phys. Lett.*, **42A**(3), 253–255, 1972.

[Hun73] S. Hunklinger, W. Arnold, and S. Stein, Anomalous ultrasonic attenuation in vitreous silica at low temperatures, *Phys. Lett.*, **45A**(4), 311–312, 1973.

[Hun76] S. Hunklinger and W. Arnold, Physical Acoustics, Vol. 12 - chapter 3, Academic Press, (New York, San Francisco, London), 1. edition, 1976.

[Hun87] S. Hunklinger, The universality of the density of states of low-energy excitations in glasses, *Philos. Mag.*, **56**(2), 199–211, 1987.

[Hun11] S. Hunklinger, Festkörperphysik, Oldenbourg Verlag, (München), 3. edition, 2011.

[Icl] ICL - Industrial Products, Application Data Sheet for Expanded Polystyrene foam (EPS).

[Jäc76] J. Jäckle, L. Piché, W. Arnold, and S. Hunklinger, Elastic effects of structural relaxation in glasses at low temperatures, *J. Non. Cryst. Solids*, **20**, 365–391, 1976.

[Jac92] H. Jacobsen, Strukturelle Relaxationen in amorphem Arsensulfid, Doctoral thesis, Heidelberg University, 1992.

[Kän94] W. Känzig, Kondensierte Materie, vdf Hochschulverlag AG at ETH Zurich, (Zurich), 1994.

[Kim77] R. Kimmich, Nuclear Magnetic Relaxation in the Presence of Quadrupole Nuclei, *Zeitschrift für Naturforschung A*, **32**(6), 544–554, 1977.

[Kla62] J. R. Klauder and P. W. Anderson, Spectral Diffusion Decay in Spin Resonance Experiments, *Phys. Rev.*, **125**(3), 912–932, 1962.

[Koh05] S. Kohara and K. Suzuya, Intermediate-range order in vitreous SiO_2 and GeO_2, *J. Phys. Condens. Matter*, **17**(5), S77–S86, 2005.

[Kör19] D. Körner, Nichtgleichgewichtsdynamik von Tunnelsystemen im Bor-Kronglas N-BK7 bei 1 GHz und tiefen Temperaturen, Bachelor's thesis, Heidelberg University, 2019.

[Kra54] J. v. Kranendonk, Theory of Quadrupolar Nuclear Spin-Lattice Relaxation, *Physica*, **XX**, 781–800, 1954.

[Kur64] N. A. Kurnit, I. D. Abella, and S. R. Hartmann, Observation of a Photon Echo, *Phys. Rev. Lett*, **13**(19), 567, 1964.

[Las75] J. C. Lasjaunias, A. Ravex, M. Vandorpe, and S. Hunklinger, The Density of Low Energy States in vitreous silica: Specific heat and thermal conductivity down to 25 mK, *Solid State Commun.*, **17**, 1045–1049, 1975.

[Leg91] A. J. Leggett, Amorphous materials at low temperatures: why are they so similar?, *Physica B*, **169**, 322–327, 1991.

[Ler88] F. Lerbert and G. Bellessa, Acoustical study of tunneling states in magnetic rare-earth glasses: wave propagation and phonon echoes, *J. Phys. France*, **49**, 1179–1193, 1988.

[Lic12] L. Lichtenstein, C. Büchner, B. Yang, S. Shaikhutdinov, M. Heyde, M. Sierka, R. Wlodarczyk, J. Sauer, and H.-J. Freund, The Atomic Structure of a Metal-Supported Vitreous Thin Silica Film, *Angew. Chem. Int. Ed.*, **51**, 404–407, 2012.

[Lis15] J. Lisenfeld, G. J. Grabovskij, C. Müller, J. H. Cole, G. Weiss, and A. V. Ustinov, Observation of directly interacting coherent two-level systems in an amorphous material, *Nat. Commun*, **6**(6182), 2015.

[Lis19] J. Lisenfeld, A. Bilmes, A. Megrant, R. Barends, K. J., P. Klimov, G. Weiss, J. M. Martinis, and A. V. Ustinov, Electric field spectroscopy of material defects in transmon qubits, *npj Quantum Inf.*, **5**(105), 2019.

[Lös57] A. Lösche, Kerninduktion, Deutscher Verlag der Wissenschaften, (Berlin), 1957.

[Low19] A. Lowack, Untersuchung des Thermalisationsverhaltens von bromiertem Bisphenol-A-Diglycidether bei tiefen Temperaturen, Bachelor's thesis, Heidelberg University, 2019.

[Luc16] A. Luck, Nuclear spin dominated relaxation of atomic tunneling systems in glasses, Doctoral thesis, Heidelberg University, 2016.

[Lud56] G. W. Ludwig, Some Bromine, Iodine, and Indium Nuclear Quadrupole Interaction Frequencies, *J. Chem. Phys.*, **25**(159), 159–171, 1956.

[Lud00] S. Ludwig, C. Enss, and S. Hunklinger, Decay of spontaneous echoes in amorphous B_2O_3 at very low temperatures, *Physica B*, **284-288**, 1139–1140, 2000.

[Lud02] S. Ludwig, C. Enss, P. Strehlow, and S. Hunklinger, Direct Coupling of Magnetic Fields to Tunneling Systems in Glasses, *Phys. Rev. Lett.*, **88**(7), 075501, 2002.

[Lud03] S. Ludwig, P. Nagel, S. Hunklinger, and C. Enss, Magnetic Field Dependent Coherent Polarization Echoes in Glasses, *J. Low Temp. Phys.*, **131**(1/2), 89–111, 2003.

[Mae96] H. Maekawa, P. Florian, D. Massiot, H. Kiyono, and M. Nakamura, Effect of Alkali Metal Oxide on ^{17}O NMR Parameters and Si-O-Si Angles of Alkali Metal Disilicate Glasses, *J. Phys. Chem.*, **100**(13), 5525–5532, 1996.

[Mar05] J. M. Martinis, K. B. Cooper, R. McDermott, M. Steffen, M. Ansmann, K. D. Osborn, K. Cicak, S. Oh, D. P. Pappas, R. W. Simmonds, and C. C. Yu, Decoherence in Josephson Qubits from Dielectric Loss, *Phys. Rev. Lett.*, **95**, 210503, 2005.

[Mül19] A. Müller, Dielektrische Messungen an amorphem Arsentrisulfid in einem supraleitenden Hochfrequenzresonator zwischen 10 mK und 8 K, Bachelor's thesis, Heidelberg University, 2019.

[Mün19] L. Münch, Dielektrische Messungen an amorphem Arsentrisulfid zwischen 10 mK und 10 K im MHz-Bereich, Bachelor's thesis, Heidelberg University, 2019.

[Nag04] P. Nagel, A. Fleischmann, S. Hunklinger, and C. Enss, Novel Isotope Effects Observed in Polarization Echo Experiments in Glasses, *Phys. Rev. Lett.*, **92**(24), 245511, 2004.

[Nei15] M. M. Neiczer, Dielektrische Permittivität und elektrische Leitfähigkeit von HY-1 Glas zwischen 80 K und 350 K, Bachelor's thesis, Heidelberg University, 2015.

[Oku84] N. Okubo and Y. Abe, ^{93}Nb and ^{35}Cl nuclear quadrupole resonance in the low temperature modification of niobium pentachloride, *Phys. Lett. A*, **106A**(9), 435–440, 1984.

[Par04] D. Parshin, Oscillations of the Electric-Dipole Echo in Glasses in a Magnetic Field, *J. Low Temp. Phys.*, **137**, 233–250, 2004.

[Pen95] F. C. Penning, M. M. Maior, P. Strehlow, S. A. J. Wiegers, H. v. Kempen, and J. C. Maan, Magnetic field independent capacitance thermometers at very low temperatures, *Physica B*, **211**, 363–365, 1995.

[Phi72] W. A. Phillips, Tunneling states in amorphous solids, *J. Low Temp. Phys.*, **7**(3-4), 351–360, 1972.

[Phi81] W. A. Phillips (Ed.), Amorphous Solids, Number 24 in Topics in Current Physics, Springer, (Heidelberg), 1981.

[Pic74] L. Piché, R. Maynard, S. Hunklinger, and J. Jäckle, Anomalous Sound Velocity in Vitreous Silica at Very Low Temperatures, *Phys. Rev. Lett.*, **32**(25), 1426–1429, 1974.

[Pob07] F. Pobell, Matter and Methods at Low Temperatures, Springer, (Berlin, Heidelberg), 3. edition, 2007.

[Poh02] R. O. Pohl, Low-temperature thermal conductivity and acoustic attenuation in amorphous solids, *Rev. Mod. Phys.*, **74**(October), 991–1013, 2002.

[Pol05] I. Y. Polishchuk, P. Fulde, A. L. Burin, Y. Sereda, and D. Balamurugan, Effect of Nuclear Quadrupole Interaction on the Relaxation in Amorphous Solids, *J. Low Temp. Phys.*, **140**(5/6), 355–376, 2005.

[Pol17] A. Pollithy, Development of a superconducting microstructured resonator for the measurement of dielectric polarization echoes and measurement of two-pulse polarization echoes on Poly(vinyl acetate), Master's thesis, Heidelberg University, 2017.

[Pou50] R. V. Pound, Nuclear Electric Quadrupole Interactions in Crystals, *Phys. Rev.*, **79**(4), 685–702, 1950.

[Pra06] S. Prasad, T. M. Clark, T. H. Sefzik, H. T. Kwak, Z. Gan, and P. J. Grandinetti, Solid-state multinuclear magnetic resonance investigation of Pyrex®, *J. Non-Cryst. Solids*, **352**, 2834–2840, 2006.

[Rei] A. Reiser, Heidelberg University, private communication.

[Rei86] P. J. Reijntjes, W. v. Rijswijk, G. A. Vermeulen, and G. Frossati, Comparison of a glass thermometer against a nuclear orientation thermometer in high magnetic fields, *Rev- Sci. Instrum.*, **57**(7), 1413, 1986.

[Roy15] C. P. Royall and S. R. Williams, The role of local structure in dynamical arrest, *Phys. Rep.*, **560**, 1–75, 2015.

[Rub74] M. Rubinstein and P. C. Taylor, Nuclear quadrupole resonance in amorphous and crystalline As_2S_3, *Phys. Rev. B.*, **9**(10), 4258–4276, 1974.

[Rub75] M. Rubinstein, H. A. Resing, T. L. Reinecke, and K. L. Ngai, Nuclear Spin-Lattice Relaxation in Amorphous Materials: B_2O_3, *Phys. Rev. Lett.*, **34**(23), 1444–1447, 1975.

[Rüd08] C. Rüdiger, Polarisationsechomessungen an amorphen Mischungen aus teildeuteriertem und natürlichem Glyzerin, Diploma thesis, Heidelberg University, 2008.

[San87] E. J. P. Santos and M. Engelsberg, Thermally induced two-level systems in glasses and nuclear spin-lattice relaxation, *Phys. Rev. B*, **36**(16), 8941–8944, 1987.

[Sar16] B. Sarabi, A. N. Ramanayaka, A. L. Burin, F. C. Wellstood, and K. D. Osborn, Projected Dipole Moments of Individual Two-Level Defects Extracted Using Circuit Quantum Electrodynamics, *Phys. Rev. Lett*, **116**, 167002, 2016.

[Säu21] M. Säubert, Einfluss von magnetischen Kernanregungen auf die dielektrische Funktion von amorphem Polyvinylchlorid bei tiefen Temperaturen, Bachelor's thesis, Heidelberg University, 2021.

[Sch75] M. v. Schickfus, S. Hunklinger, and L. Piché, Anomalous Dielectric Dispersion in Glasses at Low Temperatures, *Phys. Rev. Lett*, **35**(13), 876, 1975.

[Sch76] M. v. Schickfus and S. Hunklinger, The dielectric coupling of low-energy excitations in vitreous silica to electromagnetic waves, *J. Phys. C: Solid State Phys.*, **9**, L439, 1976.

[Sch78] M. v. Schickfus, B. Golding, W. Arnold, and S. Hunklinger, Coherent electric echoes in fused silica glass, *J. Phys. (Paris)*, (Colloque C6, supplément au n° 8, Tome 39), C6–959, 1978.

[Sch91] H. Scholze, Glass - Nature, Structure, and Properties, Springer-Verlag, (New York, Berlin, Heidelberg), 1991.

[Sch92] W. Schnauss, F. Fujara, and H. Sillescu, The molecular dynamics around the glass transition and in the glassy state of molecular organic systems: A ^{2}H-nuclear magnetic resonance study, *J. Chem. Phys.*, **97**(2), 1378–1389, 1992.

[Sch05] M. Schwoerer and H. C. Wolf, Organische Molekulare Festkörper: Einführung in die Physik von pi-Systemen, Wiley-VCH, (Weinheim), 1. edition, 2005.

[Sch07] Schott AG, Data sheet N-BK7, 2007.

[Sch14] Schott AG, Data sheet N-KZFS11, 2014.

[Sch16a] A. Schaller, Novel readout system and online analysis for dielectric polarisation echoes, Master's thesis, Heidelberg University, 2016.

[Sch16b] C. W. Scholz, Untersuchung der dielektrischen Eigenschaften von N-KZFS11 zwischen 300 K und 10 mK bei 25 MHz, Bachelor's thesis, Heidelberg University, 2016.

[Sch17] M. Schrodin, Low temperature dielectric properties of amorphous poly(vinyl acetate) and poly(vinyl chloride), Master's thesis, Heidelberg University, 2017.

[Sch18a] M. Schechter, P. Nalbach, and A. L. Burin, Nonuniverality and strongly interacting two-level systems in glasses at low temperatures, *New J. Phys.*, **20**, 063048, 2018.

[Sch18b] Schott AG, Infrared Chalcogenide Glasses IRG 22, IRG 24, IRG 25, IRG 26 and IRG 27, 2018.

[Sch18c] P. Schygulla, Investigations of the Impact of Nuclear Quadrupole Moments on the Low-Frequency Elastic and Dielectric Susceptibilities of a Polymer Glass at Low Temperatures, Master's thesis, Heidelberg University, 2018.

[Sch19] S. Schlör, J. Lisenfeld, C. Müller, A. Bilmes, A. Schneider, D. P. Pappas, A. V. Ustinov, and M. Weides, Correlating Decoherence in Transmon Qubits: Low Frequency Noise by Single Fluctuators, *Phys. Rev. Lett.*, **123**, 190502, 2019.

[Sig] Sigma-Aldrich, `https://www.sigmaaldrich.com/catalog/product/aldrich/430234?lang=de&region=DE`, Accessed: March 2021.

[Sim04] R. W. Simmonds, K. M. Lang, D. A. Hite, S. Nam, D. P. Pappas, and J. M. Martinis, Decoherence in Josephson Phase Qubits from Junction Resonators, *Phys. Rev. Lett.*, **93**(7), 077003, 2004.

[Sin16a] L. Singer, Untersuchung der dielektrischen Eigenschaften von amorphen PVC zwischen 10 K und 10 mK bei 40 und 140 MHz, Bachelor's thesis, Heidelberg University, 2016.

[Sin16b] M. Sinnwell, Dielektrische Polarisationsechos an HY-1 Glas bei tiefen Temperaturen, Bachelor's thesis, Heidelberg University, 2016.

[Smi71] J. A. S. Smith, Nuclear quadrupole resonance spectroscopy. General principles, *J. Chem. Educ.*, **48**(1), 39–48, 1971.

[Sta15] Z. H. Stachurski, Fundamentals of Amorphous Solids - Structure and Properties, Wiley-VCH, (Weinheim), 1. edition, 2015.

[Ste73] R. B. Stephens, Low-Temperature Specific Heat and Thermal Conductivity of Noncrystalline Dielectric Solids, *Phys. Rev. B*, **8**(6), 2896–2905, 1973.

[Ste76] R. B. Stephens, Intrinsic low-temperature thermal properties of glasses, *Phys. Rev. B*, **13**(2), 852–865, 1976.

[Sto13] N. Stone, Table of nuclear electric quadrupole moments, IAEA, Austria, (IAEA Nuclear Data Section, Vienna International Centre, P.O. Box 100, A-1400 Vienna, Austria), 2013.

[Str98] P. Strehlow, C. Enss, and S. Hunklinger, Evidence for a Phase Transition in Glasses at Very Low Temperature: A Macroscopic Quantum State of Tunneling Systems?, *Phys. Rev. Lett.*, **80**(24), 5361, 1998.

[Str00] P. Strehlow, M. Wohlfahrt, A. G. M. Jansen, R. Haueisen, G. Weiss, C. Enss, and S. Hunklinger, Magnetic Field Dependent Tunneling in Glasses, *Phys. Rev. Lett.*, **84**(9), 1938, 2000.

[Str18] M. R. Strohmaier, Thermalisierungsverhalten von amorphem Polyvinylacetat und Polyvinylchlorid bei tiefen Temperaturen, Bachelor's thesis, Heidelberg University, 2018.

[Sui06] B. H. Suits, Nuclear Quadrupole Resonance Spectroscopy, in D. R. Vij (Ed.), *Handb. Appl. Solid State Spectrosc.*, Chapter 2, 65–96, Springer US, 1st edition, 2006.

[Sze75] J. Szeftel and H. Alloul, Nuclear Spin-Lattice Relaxation Associated with Low-Energy Excitations in Glasses, *Phys. Rev. Lett.*, **34**(11), 657–660, 1975.

[Tsu17] S. V. Tsurkan, Two-pulse dielectric polarisation echo experiments on the multicomponent glasses N-KZFS11 and HY-1, Master's thesis, Heidelberg University, 2017.

[Ver94] D. E. Vernacotola, Alkali niobium and tantalum silicate glasses and ferroelectric glass-ceramics, *Key Eng. Mater*, **94-95**, 379–408, 1994.

[Vio18] P. C. Vioglio, P. M. J. Szell, M. R. Chierotti, R. Gobetto, and D. L. Bryce, $^{79/81}$Br nuclear quadrupole resonance spectroscopic characterization of halogen bonds in supramolecular assemblies, *Chem. Sci.*, **9**, 4555–4561, 2018.

[Vog92] W. Vogel, Glaschemie, Springer-Verlag, (Berlin, Heidelberg, New York), 3. edition, 1992.

[War41] B. E. Warren, Summary of work on atomic arrangement in glass, *J. Am. Ceram. Soc.*, **24**, 256–261, 1941.

[Web] Webelements, `https://www.webelements.com`, Accessed: April 2021.

[Wei85] V. R. Weidner, R. Mavrodineanu, K. D. Mielenz, R. A. Velapoldi, K. L. Eckerle, and B. Adams, Spectral Transmittance Characteristics of Holmium Oxide in Perchloric Acid Solution, *J. Res. Natl. Bur. Stand.*, **90**(2), 115–125, 1985.

[Wei95] R. Weis, Messung der dielektrischen Eigenschaften wechselwirkender Tunnelsysteme bei tiefen Temperaturen am Beispiel von KCl:Li, Doctoral thesis, Heidelberg University, 1995.

[Wer18] A. Werner, Dielektrische Permitivität des Glasses Br-DGEBA zwischen 10mK und 5K im MHZ-Bereich, Bachelor's thesis, Heidelberg University, 2018.

[Wes15] P. Wesp, Dielektrische Permittivität von N-KZFS11 Glas bei hoher Frequenz und tiefen Temperaturen, Bachelor's thesis, Heidelberg University, 2015.

[Wie87] S. A. J. Wiegers, R. Jochemsen, C. C. Kranenburg, and G. Frossati, Comparison of some glass thermometers at low temperatures in a high magnetic field, *Rev. Sci. Instrum.*, **58**(12), 2274, 1987.

[Woe63] K. E. Woessner and H. S. Gutowsky, Nuclear Pure Quadrupole Relaxation and Its Temperature Dependence in Solids, *J. Chem. Phys.*, **130**, 440–456, 1963.

[Woh01a] M. Wohlfahrt, Untersuchung der dielektrischen Tieftemperaturanomalien von Mehrkomponentengläsern in Magnetfeldern, Doctoral thesis, Heidelberg University, 2001.

[Woh01b] M. Wohlfahrt, P. Strehlow, C. Enss, and S. Hunklinger, Magnetic-field effects in non-magnetic glasses, *Europhys. Lett.*, **56**(5), 690–694, 2001.

[Wol14] M. H. Wolter, Two-pulse dielectric polarisation echo experiments on the multicomponent glasses BK7 and HY-1, Master's thesis, Heidelberg University, 2014.

[Wür02] A. Würger, A. Fleischmann, and C. Enss, Dephasing of Atomic Tunneling by Nuclear Quadrupoles, *Phys. Rev. Lett.*, **89**(23), 237601, 2002.

[Wür04] A. Würger, Dephasing of Coherent Echoes by Nuclear Quadrupoles, *J. Low Temp. Phys.*, **137**(3/4), 143–166, 2004.

[Xue93] X. Xue and J. F. Stebbins, ^{23}Na NMR Chemical Shifts and Local Na Coordination Environments in Silicate Crystals, Melts and Glasses, *Phys. Chem. Minerals*, **20**, 297–307, 1993.

[Yan86] C. Y. Yang, M. A. Paesler, and D. E. Sayers, First crystallization of arsenic trisulfide from bulk glass: The synthesis of orpiment, *Mater. Lett.*, **4**(5-7), 233–235, 1986.

[Zac32] W. H. Zachariasen, The Atomic Arrangement in Glass, *J. Am. Chem. Soc.*, **54**(10), 3841–3851, 1932.

[Zei15] A. Zeißner, Dieletrische Messungen im MHz-Bereich an HY-1 und Herasil zwischen 7 mK und 10 K, State examination thesis, Heidelberg University, 2015.

[Zel71] R. C. Zeller and R. O. Pohl, Thermal Conductivity and Specific Heat of Noncrystalline Solids, *Phys. Rev. B*, **4**(6), 2029–2041, 1971.

[Zhu78] A. P. Zhukov, L. V. Soboleva, and L. M. Belyaev, Niobium-93, Lanthanum-139, and Tantalum-181 pure NQR in rare earth orthoniobates and Lithium Tantalate, *Ferroelectrics*, **21**, 601–604, 1978.

[Zim81] J. Zimmermann and G. Weber, On the excess specific heat of vitreous silica at low temperatures, *Phys. Lett.*, **86A**(1), 32–34, 1981.

Acknowledgments

Zum Schluss möchte ich mich bei all jenen bedanken, die zum Gelingen dieser Arbeit beigetragen haben. Mein besonderer Dank gilt:

Prof. Christian Enss für die Möglichkeit an diesem interessanten Thema zu arbeiten, die Diskussionen über Messungen und Daten und die Freiheiten im Labor.

Prof. Heinz Horner für das Übernehmen des Zweitgutachtens.

Andreas Reiser für die tagtägliche Unterstützung im Labor und beim Interpretieren der Daten, für das Mitwirken bei den Experimenten und die Exkurse zur NQR Spektroskopie. Nicht zuletzt für die Ermöglichung von Homeoffice, auch vor Corona, und die Korrekturen und Anmerkungen beim Schreiben dieser Arbeit.

Andreas Fleischmann für die Diskussionen der Ergebnisse, anschaulichen Darstellungen und Erklärungen von unverstandenen Beobachtungen.

Prof. Sebastian Kempf, Andreas Reifenberger, Herrn Wolf und dem Reinraumteam für die schnelle Herstellung der mikrostrukturierten Resonatoren.

Rudi Eitel für die interessanten Geschichten der vor-Corona-Kaffeeecke und die nicht versiegende Heliumquelle.

Der Elektronikabteilung, Werkstatt und EDV, im besonderen Herrn Azeroth für die Unterstützung bei der Realisierung experimenteller Aufbauten und Umbauten am Kryostat, sowie an Doktorhüten.

Den langjährigen Büro und/oder Laborkollegen Benedikt Frey, Marcel Haas und Christian Ständer für die lustige Zeit und die gegenseitige Unterstützung.

"Meinen" Bachelor- und Masterstudent/-innen Matthias Sinnwell, Sergey Tsurkan, Anna Pollithy, Nicole Assmann, Robert Haase, Erik Weerda, Aljoscha Auer, Robin Strohmaier, Jan Arneth, Ansgar Lowack, Jan Blickberndt, Marcel Haas und Marius Säubert für die gute Zusammenarbeit.

Allen aktuellen und ehemaligen F345lern für die schöne Zeit und gute Atomsphäre in der Arbeitsgruppe und die interessanten Mittagspausen.

Meinen Eltern und Geschwistern für die Unterstützung über die Jahre und das Interesse am Vorankommen meiner Arbeit.

Meiner Frau und meinem Sohn für die Unterstützung, Motivation und das Korrekturlesen dieser Arbeit.